DEVELOPMENT AND APPLICATION OF THE ANALYZER-BASED IMAGING TECHNIQUE WITH HARD SYNCHROTRON RADIATION

Paola Coan

To cite this version:

Paola Coan. DEVELOPMENT AND APPLICATION OF THE ANALYZER-BASED IMAGING TECHNIQUE WITH HARD SYNCHROTRON RADIATION. Biological Physics [physics.bio-ph]. European Synchrotron Radiation Facility (ESRF), 2006. English. NNT : . tel-00174514

HAL Id: tel-00174514
https://theses.hal.science/tel-00174514
Submitted on 24 Sep 2007

EUROPEAN SYNCHROTRON RADIATION FACILITY
UNIVERSITE JOSEPH FOURIER - GRENOBLE I

THESE de DOCTORAT en PHYSIQUE
presentée et soutenue publiquement le 6 juillet 2006
par
PAOLA COAN

Pour obtenir le grade de
DOCTEUR de l'UNIVERSITE JOSEPH FOURIER

DEVELOPMENT AND APPLICATION OF THE ANALYZER-BASED IMAGING TECHNIQUE WITH HARD SYNCHROTRON RADIATION

Composition du jury

Professor Edoardo CASTELLI	Président
Professor Pekka SUORTTI	Rapporteur
Doctor Jürgen MOLLENHAUER	Examinateur
Professor MD François ESTEVE	Examinateur
Doctor José BARUCHEL	Co-directeur de Thèse
Doctor Alberto BRAVIN	Directeur de Thèse

Ai miei angeli

The important thing is not to stop questioning. Curiosity has its own reason for existing. One cannot help but be in awe when he contemplates the mysteries of eternity, of life, of the marvellous structure of reality. It is enough if one tries merely to comprehend a little of this mystery every day. Never lose a holy curiosity.

La cosa importante è di non smettere mai di interrogarsi. La curiosità esiste per ragioni proprie. Non si può far a meno di provare riverenza quando si osservano i misteri dell'eternità, della vita, la meravigliosa struttura della realtà. Basta cercare ogni giorno di capire un po' di quel mistero. Non perdere mai una sacra curiosità.

Albert Einstein

Acknowledgments

It is dutiful and a pleasure for me to thank all who have contributed in different ways to the completion of this Ph.D. Thesis, since without their support and encouragement this work would not have been possible.

I firstly wish to express my full gratitude to my supervisor Dr. Alberto Bravin; much of this work is due to his teachings and the passion for research he has been able to convey to me by working together. Thanks also for having borne my instinctive tendency of always questioning!

I would like to thank Dr José Baruchel, my "directeur de Thèse", for his encouragement and his constant positive disposition.

Special thanks to Dr. Jürgen Mollenhauer who introduced me into the Orthopaedics world. His contagious enthusiasm for his job and the research has been a real motor for the concerned part of this Thesis. I would really thank him for all the fruitful discussions and his teachings. Also thanks for the hospitality that he and his kind wife Christine gave me during my visits of the Department of Orthopaedics of Eisenberg.

I am very honoured that Prof. Pekka Suortti, Prof. Edoardo Castelli and Prof. François Esteve accepted to read and judge this work and I am grateful for their precious suggestions.

I particularly wish to thank all the extraordinary people from the Biomedical Beamline (ID17) who have daily helped me in my experimental and analysis work. Among all, I thank Christian Nemoz, for the informatics support and his humour which always cheers up the working environment, and Herwig Requardt and Thierry Brochard for their technical support during every beamtime.

For having taken care of "my" guinea pigs and the support in dealing with *in-vivo* experiments, thanks very much to Dominique Dallery, Geraldine Le Duc and Pierrick Regnard.

To this long list of acknowledgments, other people have to be added given their willingness to discuss and help me. They are: Dr. Peter Cloetens, incomparable mentor on phase contrast imaging, Dr. Claudio Ferrero, precious collaborator for the theoretical simulations of this Thesis, and last but not least Cyril Ponchut and Jean-Claude Labiche, minds of the FReLoN camera.

I then address a warm thank to the Finnish students team: Jani Keyriläinen, Liisa Porra and especially to Manuel Fernandez, companion of many DEI (or better ABI!) beamtimes as well as my personal Matlab guide. Gracias!

Among the staff of the Department of Orthopaedics of the University of Jena, I wish to also thank Dr. Andreas Wagner for helping in the interpretation of the results and for having made me attend some surgical operations. It was a unique and the most effective occasion for entering into the subject.

A special thanks to Dr. Angela Peterzol for the fruitful scientific discussions and her help in the data analysis.

For having introduced me to the Radiobiology field I wish to thank Dr. Nicolas Foray for the interesting discussions and in particular Dr. Wendy Renier for the care she had in teaching me the experimental and analysis aspects.

I now want to express all my gratitude to whom has always stood by me encouraging and bearing all my dumps.

Grazie di cuore a mia mamma per il suo affettuoso e costante sostegno e per l'impegno che mette nell'assencondare con amorevole rispetto i miei sogni nonostante la faticosa lontananza. Accanto a lei, desidero ringraziare tutta la mia famiglia composta di zii e cugini che mai mi fanno mancare il loro affetto.

Un grazie del tutto speciale ad Alessandro, l'ago della mia bussola, colui che con energica ed affettuosa determinazione sempre mi sprona a comunque assaporare la vita in ogni suo risvolto. Grazie per la tua insostituibile amicizia.

Desidero ancora ringraziare Elena e Riccardo, gli amici che sempre mi sono stati vicini in questi anni grenoblesi. A Riccardo un grazie per le prelibatezze che dispensa nelle sue cene e per l'allegria che sa regalare; ad Elena un grazie per la sua presenza, per le nostre belle chiacchierate, per l'aiuto materiale e no che mi ha sempre dato, per la sua squisita compagnia e la sua vivace intelligenza.

Finalmente, deseo especialmente dar las gracias a Lola, mi compañera de piso. Nos conocimos por casualidad y desde entonces hemos construido una gran amistad. Le agradezco haber aguantado mi forma de ser y por hacerme reir tanto. Lola, eres la pastilla del buen humor!

Many other people would deserve to be included in these acknowledgements; it is not possible to list here everybody, but each of them, in his heart, knows the way in which he supported me and he stood by me. Grazie!

Table of contents

Introduction en français

L'ostéoarthrite est un trouble dégénératif caractérisé par une perte du cartilage articulaire, l'épaississement de l'os subchondral et la formation des ostéophytes (excroissance de l'os).

L'étiologie de l' ostéoarthrite est multifactoriel avec des causes inflammatoire, métabolique, mécanique et génétique. L' ostéoarthrite est une maladie dont on sait peu et pour laquelle il n'existe encore aucun remède. Les principaux objectifs du traitement sont de contrôler la douleur, d'améliorer la fonctionnalité, et de réduire le handicap (Dougados, 2004).

A l'âge adulte, les capacités de réparation du cartilage sont très limitées et ceci entraîne une aggravation de l'arthrose. Dans les cas très sévères, la chirurgie est le seul traitement pour réduire la douleur et rétablir les fonctionnalités; les protocoles peuvent aussi intégrer le remplacement des articulations grâce à des implants artificiels.

C'est pour toutes ces raisons que les principaux points d'investigations pré-clinique et clinique sont orientés vers la compréhension des causes de l' ostéoarthrite et pour trouver de meilleurs traitements.

La surveillance de la progression de l' ostéoarthrite et des effets de la thérapie pendant les essais cliniques nécessitent l'usage de techniques fiables et suffisamment sensibles pour détecter les changements de condition des articulations.

Malheureusement, les outils conventionnels d'investigation de l' ostéoarthrite restent insatisfaisants.

Les facteurs dont on tient compte pour l'évaluation de l'arthrose et l'étude sur l'intervention des médicaments sont encore :

- L'observation clinique (douleur, inflammation, fonction de l'articulation)

1. L'imagerie avec des techniques conventionnelles dont radiographie, tomographie (CT), imagerie par résonance magnétique (IRM), ultrasons (UI), détection de marqueurs biologiques...

Ces deux modalités de diagnostic sont sensibles seulement dans les cas avancés d'ostéoarthrite, puisqu'elles ne permettent pas la visualisation ou la détection de signes de dégénérescence précoces et des processus d'ostéoarthrite du tissu cartilagineux ; elles présentent donc de graves limites.

Cette situation appelle à la découverte et le développement de nouvelles techniques d'imagerie médicale du cartilage articulaire, sensibles aux étapes précédant le point irréversible où le tissu cartilagineux est atteint. En d'autres mots, il existe des besoins importants d'imagerie à haute résolution, de diagnostic non-invasif, de techniques de surveillance permettant une détection précoce, ainsi que dans le suivi de la maladie, dans l'évaluation des traitements médicamenteux et dans l'évaluation de l'intégration osseuse des implants (Bellamy, Kirwan *et al.*, 1997; Gordon, Wu *et al.*, 2001; Wagner, Aurich *et al.*, 2005). **Tous ces points sont présentés dans le Chapitre 1.**

Dans ce cadre, les techniques d'imagerie en contraste de phase peuvent jouer un rôle important pour combler les lacunes dans la visualisation précoce de l' ostéoarthrite. L'intérêt de ces techniques dans les applications médicales est dû au fait qu'il est possible d'observer le contraste associé à la modulation de la phase du signal, même si l'amplitude de la modulation reste faible ou absente, avec une dose délivrée aux tissus similaire ou même réduite en comparaison à la radiographie d'absorption conventionnelle (Mollenhauer, Aurich *et al.*, 2002).

Les techniques de contraste de phase ont été appliquées avec succès dans les études de la mammographie, et ont mené à d'extraordinaires résultats en terme de visualisation de lésions précoces (Arfelli, Bonvicini *et al.*, 2000; Pisano, Johnston *et al.*, 2000; Keyriläinen, Fernández *et al.*, 2005).

L'imagerie en contraste de phase pourrait potentiellement être bien adaptée dans l'investigation des cartilages atteints, en améliorant la précision du diagnostic et en suivant la réaction au traitements innovants.

Des techniques diverses ont été développées pour exploiter les variations de phase dans les longueurs d'onde de rayonnement X.

Le travail de cette Thèse s'est concentré sur les techniques de phase, c'est-à-dire l'"Analyser-Based Imaging", (ABI), et la "Propagation-Based Imaging", (PBI). La première, ABI, utilise un cristal analyseur inséré entre l'échantillon et le détecteur. Un tel cristal peut être considéré comme un filtre angulaire pour réfracter les rayons X à travers l'échantillon. Le second, PBI, utilise simplement la propagation du faisceau de rayons X monochromatique et partiellement cohérent dans l'espace , sur une distance de quelques centimètres à plusieurs mètres. **La description complète de ces techniques est le sujet du Chapitre 2.**

Le travail préliminaire réalisé par les équipes de ID17 et ID19, et faisant partie de ma Thèse (Laurea in Fisica, University of Padova, 2002), a démontré que l'une ou l'autre technique devrait être choisie en fonction des caractéristiques de l'échantillon et des détails que l'on souhaite visualiser. En fait, les échantillons montrant de lentes modulations de phase, comme dans les cas de l'interface os-cartilage ou de la structure interne du cartilage, pourraient être bien étudiés par ABI plutôt que PBI, car ABI est plus sensible aux structures changeant lentement. Suite à ces réalisations, aussi bien sur le témoignage expérimental des études préliminaires réalisées sur le sujet (Mollenhauer, Aurich *et al.*, 2002; Muehleman, Majumdar *et al.*, 2004), seulement la technique ABI a été appliquée dans l'étude du tissu cartilagineux et dans l'investigation d'implants métalliques.

Bien que ces deux technique aient déjà de nombreuses applications (Yagi, Suzuki *et al.*, 1999; Suortti and Thomlinson, 2003), elles sont loin d'être implémentées dans l'environnement clinique (même si les essais cliniques pionniers dans le contraste de phase de la mammographie a récemment débuté à ELETTRA). Le principal obstacle est la nécessité d'utiliser un haut flux de rayons X avec des caractéristiques appropriées pour obtenir le contraste suffisant et pour permettre des expositions de courtes durées, ce qui est crucial pour des applications médicales *in-vivo*.

Approprié, dans ce contexte, signifie que les deux principales techniques utilisent le rayonnement monochromatique. Même si d'importants efforts ont été fournis ces dernières années dans le développement des sources quasi monochromatiques, compactes et intenses (Carroll, Mendenhall *et al.*, 2003), à ce jour seulement les sources de rayonnement synchrotron peuvent satisfaire les exigences du flux. Pour cette raison, et aussi pour la perspective de mettre en place une imagerie du cartilage de haute qualité, qui peut encourager encore plus loin la recherche dans le domaine des sources compactes intenses, les expériences ont été réalisées en utilisant des rayonnements synchrotron sur deux lignes de lumière ID17 et ID19 de l' European Synchrotron Radiation Facility (ESRF).

L'implémentation des techniques ABI et PBI sur ID17 et ID19, la caractéristique du détecteur utilisé pour la plupart des études et développé à l'ESRF (FReLoN camera) et les résultats de l'application ABI sur plusieurs spécimens humains et animaux sont rapportés dans les Chapitres 3, 4 et 5.

Depuis la première application, les techniques ABI et PBI sont étudiées et appliquées indépendamment et il n'a jamais été postulé en littérature qu'en utilisant une installation adéquate, il pourrait être possible de combiner les deux techniques *in-situ* pour produire des images de signaux mixtes de ABI et PBI. Néanmoins, en utilisant l'optique ondulatoire dans la description de la formation d'image on peut voir que, si les changements de phase se propagent librement dans l'espace avant d'être analysés par le cristal, l'analyseur analysera un signal composé de fréquences spatiales modifiées. En d'autres mots, la distance entre l'échantillon et le cristal analyseur devrait jouer un rôle dans la formation de l'image ABI. Il a été démontré expérimentalement dans cette Thèse, pour la première fois, que les techniques ABI et PBI peuvent être combinées ensemble pour produire des images montrant des caractéristiques originales (Hybrid imaging, HI) (Coan, Pagot *et al.*, 2005).

Les résultats expérimentaux ont été analysés grâce à l'utilisation du programme informatique DEIWAVE développé dans le cadre de la Thèse. Ce programme utilise la solution de Kato d'onde sphérique des equations de Takagi-Taupin pour décrire l’amplitude de l’onde diffractée par le crystal analyseur, et il est capable de produire des résultats en excellent accord avec les données expérimentales. DEIWAVE serait donc utilisé pour prévoir les résultats de futures expériences et pour optimiser encore plus la configuration expérimentale.

De plus, dans le but de simplifier l’exécution de ABI, la possibilité de réaliser des images ABI en utilisant un système des fentes comme analyseur a été étudié. Il a été découvert que la disposition des pixels de la caméra FReLoN décrite dans le Chapitre 4, placée à une distance adéquate de l’échantillon et correctement lu par l'électronique du détecteur peuvent analyser angulairement le faisceau de rayon X émergeant de l’échantillon ; pour cette raison la technique a été indiquée comme "detector-based analyser imaging" (DBA).

Plusieurs tests préliminaires ont souligné que la technique peut produire des images avec des caractéristiques similaires ou équivalentes à celles de ABI. De plus, la technique nommée DBA, dans ses premières réalisations montrent aussi des avantages par rapport à la technique ABI: la stabilité optique s’obtient plus facilement et les différents angles de réfraction peuvent simultanément être enregistres et analysés.

Cette technique a encore besoin d’être testée et analysée de manière expérimentale, mais elle reste très prometteuse dans la perspective de l'exploitation des techniques de phase avec de sources différentes du synchrotron.

La description de "Hybrid Imaging mode", les résultats des simulations réalisées en utilisant le programme DEIWAVE, la réalisation du "detector-based analyser imaging" (DBA) et ses premières applications sont décrites dans le Chapitre 6.

En bref, la Thèse est organisée dans la façon suivante:

Chapitre 1. Brève description de la maladie de l’ostéarthrite (causes, étiologie, effets sur le cartilage) et description des techniques conventionnelles utilisées pour visualiser le cartilage et les implants.

Chapitre 2. La formation de l’image; contraste de l’absorption versus contraste de phase. Description théorique de la propagation et des modalités de "analyser-based imaging".

Chapitre 3. La production (la source et les paramètres de base) du rayonnement synchrotron et les caractéristiques du faisceau de rayon X (énergie, polarisation, divergence, cohérence). Description détaillée de l’installation pour la "propagation-based" et l'"analyser-based phase contrast imaging" sur les lignes ID17 et ID19 de l’ESRF.

Chapitre 4. L’évaluation complète des performances de la camera CCD FReLoN munie de son optique à guide de lumière utilisée pour les expériences sur ID17: la fonction de transfert de

modulation (MTF), la densité spectrale de puissance de bruit normalisé (NNPS) et l'efficacité quantique de détection (DQE).
Une comparaison critique des performances de la camera FReLoN avec une sélection de détecteurs est présentée dans la littérature.

Chapitre 5. Les résultats expérimentaux obtenus en appliquant la technique "analyser-based imaging" (ABI) pour étudier le cartilage articulaire et l'évaluation de l'intégration des implants métalliques.
Les images d'ABI des spécimens humains et animaux excisés, et des expérience *in-vivo* sur des cochons d'Inde. Les techniques utilisées dans la reconstruction des images. Les résultats d'une campagne d'expériences radiobiologiques pour évaluer les effets biologiques du rayonnement sur les cellules du cartilage.

Chapitre 6. Les développements de la technique de "analyser-based imaging" (ABI): analyses qualitatives et quantitatives de la combinaison de ABI et PBI. Comparaison des résultats expérimentaux avec la réalisation de simulations avec un code écrit spécifique en utilisant l'approche de l'optique ondulatoire dans la formation d'image. Description de la possibilité d'utiliser la caméra FReLoN pour analyser les faisceaux de rayon X se réfracter et se diffracter à travers l'échantillon et rapport des résultats des expériences préliminaires.

Appendice. Brève description des résultats de la théorie dynamique de la diffraction des cristaux.

Introduction

Osteoarthritis (OA) is a degenerative disorder characterized by loss of articular cartilage, thickening of the underlying subchondral bone, and osteophyte (bone excrescence) formation. The etiology of OA is multifactorial, with inflammatory, metabolic, mechanical and genetic causes. OA is a poorly understood disease and, presently, no cure exists. The principal treatment objectives are to control pain adequately, improve function, and reduce disability (Dougados, 2004).

In adults, cartilage has very limited capability of repairing, and the situation is aggravated in OA conditions. In very severe cases, surgery remains the only remedy for reducing the pain and helping restore functions; protocols may also include the replacement of articulations with artificial implants.

For all these reasons, **understanding the causes of OA and finding better treatments are the major focuses of preclinical and clinical investigations.**

Monitoring the progression of OA and the effects of therapy during clinical trials requires the use of **valid and reliable** outcome **measurements that are sufficiently sensitive** to detect changes in articular joint conditions.

Unfortunately, tools conventionally used to investigate the OA disease remain unsatisfactory. For both OA assessment and drug intervention studies, the principal hallmarks are still:

- the clinical observation (pain, inflammation, joint function...)
- imaging with conventional clinical techniques, including planar radiography, CT, MRI, UI, biomarkers detection...

Both these diagnostic modalities can be sensitive only in case of advanced OA stages, since they do not allow the visualization or detection of very early degenerative signs and processes of OA in the cartilage tissue, or they present intrinsic severe limitations.

Poor imaging quality in practically all medical imaging technologies with respect to articular cartilage calls for the discovery and development of new techniques that are sensitive to stages preceding the point of irreversible damage of the cartilage tissue.

In other words, there is an important need of a high resolution, non-invasive diagnostic and monitoring technique allowing for the early detection and follow-up of OA, the evaluation of drug efficacy and the implant healing assessment (Bellamy, Kirwan *et al.*, 1997; Gordon, Wu *et al.*, 2001; Wagner, Aurich *et al.*, 2005). **All these points are presented in the Chapter 1.**

In this scenario, X-ray phase contrast modalities could play an important role in filling the gap in the capability of early and precise visualization of OA. The interest for phase sensitive techniques in medical applications resides in the fact that it is possible to observe contrast due to the phase modulation of the signal, even if the amplitude modulation is weak or absent, with a dose to the tissues similar or even reduced compared to conventional absorption radiography (Mollenhauer, Aurich *et al.*, 2002). Phase contrast techniques have been successfully applied to mammographic studies, leading to extraordinary results in terms of visualization of early lesions (Arfelli, Bonvicini *et al.*, 2000; Pisano, Johnston *et al.*, 2000; Keyriläinen, Fernández *et al.*, 2005).

Phase sensitive imaging could therefore be potentially well adapted for investigating cartilage damages, improving the accuracy in diagnosis and for following up the response to innovative treatments.

Various techniques have been developed to exploit the phase variations in the X-ray regime.

In this Thesis, the work has been focused on two phase-sensitive techniques, namely the Analyzer-Based Imaging (ABI) and the Propagation-Based Imaging (PBI). The first, ABI, uses an analyzer crystal, inserted in between the sample and the detector. Such crystal can be thought as an angular filter for the X-rays that have traversed the sample. The latter, PBI, simply uses the propagation (or Fresnel diffraction) of the monochromatic and partially coherent X-ray beam in free space, over a distance ranging from few centimeters to several meters. **The full description of the techniques is the subject of the Chapter 2.**

As part of a preliminary work performed by the ID17 and ID19 teams, which was also part of my Master Thesis (Laurea in Fisica, University of Padova, 2002), it has been demonstrated that one or the other technique should be chosen depending on the sample characteristics and the details to be visualized. In fact, samples showing slow modulations of the phase, like the cartilage-bone interface or the internal structure of damaged cartilage, might well be rendered by ABI rather than by PBI, ABI being more sensitive to slowly varying structures (Pagot, 2004). Following these achievements, as well as the experimental evidence of preliminary studies performed on the subject (Mollenhauer, Aurich *et al.*, 2002; Muehleman, Majumdar *et al.*, 2004), only the ABI technique has been applied for studying the articular cartilage tissue and investigating the metal implants healing.

Although these two techniques have already numerous applications (Yagi, Suzuki *et al.*, 1999; Suortti and Thomlinson, 2003), they are far from being implemented in a clinical environment (even if pioneering clinical trials of phase contrast mammography have recently started at ELETTRA). The main obstacle is the necessity of using a high X-ray flux with the appropriate characteristics to get sufficient contrast and allow short exposure times, which are crucial for *in-vivo* medical applications. Appropriate in this context means that both techniques primarily make use of a monochromatic beam separated from the continuous spectrum by a monochromator. Despite the fact that a large effort has been put in the recent years to develop compact, intense and intrinsically quasi-monochromatic sources (Carroll, Mendenhall *et al.*, 2003), to date only synchrotron radiation sources can satisfy the flux requirements. For this reason, and also in the perspective to set a gold standard of cartilage imaging, which can further stimulate the research at intense compact sources, the experiments have been performed using synchrotron radiation at the two long imaging beamlines ID17 and ID19, of the European Synchrotron Radiation Facility (ESRF).

The technical implementation of the ABI and PBI techniques at ID17 and ID19, the characterization of the detector used for most of the studies and developed at the ESRF (FReLoN camera) and the results of the application of the ABI to several human (*in-vitro*) and animal (*in-vivo*) specimens are reported in the Chapters 3, 4 and 5, respectively.

Since their first implementation, the ABI and the PBI techniques have been studied and applied independently, and it was never postulated in the literature that by using a suitable set-up it would be possible to combine the two techniques *in-situ* to produce images of mixed ABI and PBI signals. Nevertheless, using the wave optics approach in the description of the image formation, it can be seen that, if the phase shifts are let freely propagate in the space before being analyzed by the crystal, the analyzer will analyze a signal composed by modified spatial frequencies. In other words, the distance between the sample and the analyzer crystal should play a role in the ABI image formation. As part of this Thesis work it has been experimentally demonstrated, for the first time, that the ABI and PBI techniques can be combined to produce images showing original features (Hybrid imaging, HI) (Coan, Pagot *et al.*, 2005). The experimental results have also been simulated using the DEIWAVE computer program developed in the framework of this Thesis. This program, which uses the Kato spherical wave solution of the Takagi-Taupin equations to describe the wave amplitude diffracted by the analyzer crystal, is able to produce results which are in excellent agreement with experimental data. DEIWAVE will be therefore used for predicting results of future experiments and to further optimize the set-up.

In addition, with the aim of simplify the implementation of ABI, it has been studied the possibility of performing ABI imaging using a suitable slit system as the analyzer. It has been found that the array of pixels of the FReLoN camera described in the Chapter 4, placed at a suitable distance from the sample and suitably read-out by the detector electronics, could angularly analyze the X-ray beam emerging from a sample; for this reason the technique has been indicated as detector-based analyzer imaging (DBA). Several preliminary tests have highlighted that the technique can produce images with features similar or equivalent to the ABI ones. In addition, the DBA imaging, in its early implementation, also shows advantages with respect to the ABI: the stability of the optics is much easily obtained and several refraction angles can simultaneously be acquired and analyzed.

This technique needs further experimental analysis and tests but it is very promising also in the perspective of dissemination of the technique outside the Synchrotron Radiation sources.

The description of the Hybrid Imaging mode, the results of the simulations performed by using the DEIWAVE program, the implementation of the detector-based analyzer imaging (DBA) and its first applications are described in the Chapter 6.

In summary the Thesis is organized as follows.

Chapter 1. Brief description of the osteoarthritis disease (causes, etiology, effects on cartilage) and of the conventional techniques used to visualize the cartilage and implants.

Chapter 2. The image formation: absorption contrast versus phase contrast. Theoretical description of the Propagation and the Analyzer-based imaging modalities.

Chapter 3. The production (source and basic parameters) of synchrotron radiation and the X-ray beam characteristics (energy, polarization, divergence, coherence). Detailed description of the set-up for Propagation and Analyzer-based phase contrast imaging at the ID17 and ID19 ESRF beamlines.

Chapter 4. The full assessment of the imaging performance of the taper optics CCD "FReLoN" camera used for the experiments at ID17: modulation transfer function (MTF), normalized noise power spectrum (NNPS), and detective quantum efficiency (DQE). Critical comparison of the FReLoN camera perfomances with a selected number of detectors presented in the literature.

Chapter 5. The experimental results obtained by applying the analyzer-based imaging (ABI) technique to the study of join cartilage and metal implant healing evaluation. ABI images of excised human and animal specimens and *in-vivo* experiments on guinea pigs. Image reconstruction and processing methodologies. Results of a campaign of radiobiological experiments for the evaluation of the biological effects of radiation on cartilage cells.

Chapter 6. Developments of the analyzer-based imaging (ABI) technique: qualitative and quantitative analysis of the combination of ABI with PBI. Comparison of the experimental results with simulations performed with a specifically written code using the wave-optical approach of image formation. Description of the possible use of the FReLoN camera to analyze the X-ray beam refracted and diffracted by the sample and report of preliminary experimental results.

Appendix. Brief description of the results of the Dynamical theory of diffraction by crystals.

REFERENCES

F. Arfelli, V. Bonvicini, A. Bravin, G. Cantatore, E. Castelli, L. Dalla Palma, M. Di Michiel, M. Fabrizioli, R. Longo, R.-H. Menk, A. Olivo, S. Pani, D. Pontoni, P. Poropat, M. Prest, A. Rashevsky, M. Ratti, L. Rigon, G. Tromba, A. Vacchi, E. Vallazza and F. Zanconati (2000). "Mammography with synchrotron radiation: phase-detection techniques." Radiology **215** (1): 286-93.

N. Bellamy, J. Kirwan, M. Boers, P. Brooks, V. Strand, P. Tugwell and *e. al.* (1997). "Recommendations for a core set of outcome measures for future Phase III clinical trials in knee, hip, and hand osteoarthritis. Consensus development at OMERACT III." J Rheumatol **24**: 799-802.

F. E. Carroll, M. H. Mendenhall, R. H. Traeger, C. Brau and J. W. Waters (2003). "Pulsed, tunable monochromatic X-ray beams from a compact source: New opportunities." American Journal Roentgenology **181**.

P. Coan, E. Pagot, S. Fiedler, P. Cloetens, J. Baruchel and A. Bravin (2005). "Phase-contrast X-ray imaging combining free space propagation and Bragg diffraction." Journal of Synchrotron Radiation **12**: 241-245.

M. Dougados (2004). "Monitoring osteoarthritis progression and therapy." Osteoarthritis and cartilage **12**: S55-S60.

C. Gordon, C. Wu, C. Petrefy, J. Li, J. Duryea, C. Klifa and H. Genant (2001). "Automated measurement of radiographic hip joint space width." Med Phys **28:** 267-277.

J. Keyriläinen, M. Fernández, S. Fiedler, A. Bravin, M. L. Karjalainen-Lindsberg, P. Virkkunen, E. M. Elo, M. Tenhunen, P. Suortti and W. Thomlinson (2005). "Visualisation of calcifications and thin collagen strands in human breast tumour specimens by the diffraction-enhanced imaging technique: a comparison with conventional mammography and histology." European Journal of Radiology **53**: 226-237.

J. Mollenhauer, M. E. Aurich, Z. Zhong, C. Muehleman, A. A. Cole, M. Hasnah, O. Oltulu, K. E. Kuettner, A. Margulis and L. D. Chapman (2002). "Diffraction-enhanced X-ray imaging of articular cartilage." Osteoarthritis and cartilage **10**: 163-171.

C. Muehleman, S. Majumdar, A. Issever, F. Arfelli, R. Menk, L. Rigon, G. Heitner, B. Reime, J. Metge, A. Wagner, K. Kuettner and J. Mollenhauer (2004). "X-ray detection of structural orientation in human articular cartilage." Osteoarthritis Cartilage **12** (2): 97-105.

E. Pagot (2004). Quantitative comparison between two phase contrast techniques for mammography: diffraction enhanced imaging (DEI) and phase propagation imaging (PPI). Ph.D. Thesis, Université Joseph Fourier (Grenoble, France).

E. Pisano, R. Johnston, D. Chapman, J. Geradts, M. Iacocca, C. Livasy, D. Washburn, D. Sayers, Z. Zhong, M. Kiss and W. Thomlinson (2000). "Human breast cancer specimens: diffraction-enhanced imaging with histologic correlation--improved conspicuity of lesion detail compared with digital radiography." Radiology **214** (3): 895-901.

P. Suortti and W. Thomlinson (2003). "Medical applications of synchrotron radiation." Phys. Med. Biol. **48**: R1-R35.

A. Wagner, M. Aurich, M. Stoessel, N. Sieber, W. Wetzel, J. Mollenhauer, K. Schmuck, C. Muehleman, M. Lohmann, B. Reime, J. Metge, P. Coan, A. Bravin, F. Arfelli, L. Rigon and R. Menk (2005). Chance and limit of imaging of articular cartilage in vitro in healthy and arthritic joints - DEI (Diffraction Enhanced Imaging) in comparison with MRI, CT and ultrasound. SPIE Medical Imaging, SPIE.

N. Yagi., Y. Suzuki, K. Umetani, Y. Kohmura and K. Yamasaki (1999). "Refraction-enhanced X-ray imaging of mouse lung using synchrotron radiation source." Med. Phys. **26** (10): 2190-3.

1

Osteoarthritis and cartilage study

Contents

Pourquoi étudier les maladies des articulations? Qu'est-ce que l'ostéoarthrite? Comment repousser les limites techniques du diagnostic conventionnel? Ce chapitre introductif comporte une description (anatomique et structurale) des articulations, suivie d'une discussion sur les différentes causes de la maladie. Les techniques d'imageries conventionnelles utilisées pour le dépistage de l'arthrite sont également présentées. Les enjeux généraux et spécifiques pour la détection précoce et le suivi de l'évolution des maladies (y compris sous traitement) sont par ailleurs exposés dans cette section. Enfin, la nécessité de mettre en œuvre des techniques non invasives et plus sensibles pour le diagnostic est également soulignée.

Why studying joint diseases? What is Osteoarthritis? How intervening for overcoming the limitations of conventional diagnostic techniques? Besides a description of the joints and articular cartilage anatomy and architecture, disease causes are discussed and the imaging techniques conventionally used for osteoarthritis investigation are introduced. General and specific issues for early detection and monitoring of the disease and for therapeutical evaluation will be considered in this chapter, by also highlighting the need of new non-invasive and more sensitive diagnostic modalities.

1.1 Scientific case

Osteoarthritis (**OA**) is the most common type of **arthritis**, especially among older people. Sometimes OA is called "degenerative joint disease" or "osteoarthrosis". Statistics indicate that OA affects approximately 12% of the population in the seven major pharmaceutical markets (USA, Japan, France, Germany, Italy, Spain, and the UK)[1]. Almost 33 million American adults reported to have been told by a physician that they have some type of arthritis and, although arthritis is mainly a disease of adults, children may also suffer from OA (America Academy of Orthopaedics Surgeons[2]).

If one proceeds to a search engine like "Google" on Internet, as I did, and looks for websites about arthritis or osteoarthritis, the number of hits is 43.300.000 and 3.860.000 respectively. This somehow proves how great the general interest is in OA. In fact, OA is one of the most frequent causes of physical disability among adults and it hurts people in more that their joints: finances (cost of treatments, wages lost because of disability) and lifestyles (depression, anxiety, feelings of helplessness, limitation on daily and job activities) also are affected.

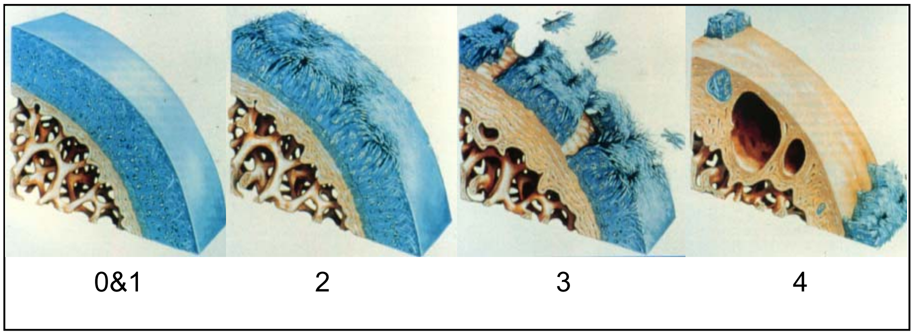

Figure 1.1. Cartilage degeneration process and its grading system (Collins grade (Collins, 1949)).

Osteoarthritis is a joint disease mostly affecting the cartilage. **Cartilage** is the smooth tissue that covers the ends of bones in a joint. Healthy cartilage allows bones to glide over one another, and the tissue also absorbs energy from the impact of physical movements. In OA, the surface layer of cartilage breaks down and is worn down (Figure 1.1). This tissue degradation determines subchondral bones to rub together, causing pain, swelling, and loss of motion of the joint. Over time, the joint may lose its normal shape. In addition, bone spurs - small growths called osteophytes - may grow on the edges of the joint. Bits of bone or cartilage may break off and float inside the joint space. This causes more pain and damage. People with OA usually have joint pain and limited movement. Unlike some other forms of arthritis, OA affects only joints and not internal organs. For example, **rheumatoid arthritis** - the second most common form of arthritis - affects other parts of the body besides the joints. The disease has a strong

---

[1] http://www.marketresearch.com/map/prod/843319.html

[2] http://www.aaos.org/

auto-immunological and chronic inflammatory component, may start at a younger age then OA, causes swelling and redness in joints, and may make people feel sick, tired, and (uncommonly) feverish. This disease can affect people of all ages and may involve many joints of the body at the same time causing pain even if the joint is not used.

Another important point is the fact **that OA presently has no cure**: so far, physician treatment strategies focus on treating the disease symptoms with minimal side effects.

In very severe cases, **the only solution for reducing the pain and helping restore functions is partial or complete joint replacement surgery**.

In the following paragraphs, basics of the OA and of the anatomy involved in the disease are presented. Afterwards, the diagnostic techniques that are conventionally used, their limitations as well as the peculiar issues of articular joint and metal implant healing studies will be discussed.

For the part concerning the cartilage tissue description, I refer to (Mollenhauer and Kuettner, 1997).

1.2 Osteoarthritis basics: the joint and its parts

Most joints—the place where two moving bones come together—are designed to allow smooth movement between the bones and to absorb stress and strain from movements like walking or repetitive motions. The joint is made up of:

- **Cartilage**: a hard but smooth coating on the end of each bone. Cartilage, which breaks down and wears down in osteoarthritis, is described in more detail in paragraph 1.3.
- **Joint capsule**: a tough connective tissue membrane that holds all the bones and other joint parts together.
- **Synovium**: a thin epithelial cell-based membrane inside the joint capsule.
- **Synovial fluid**: a fluid that lubricates the joint and keeps the cartilage smooth and healthy.
- **Ligaments, tendons, and muscles**: tissues that keep the bones stable and allow the joint to bend and move. Ligaments are tough, cord-like tissues that connect one bone to another. Tendons are tough, fibrous cords that connect muscles to bones. Muscles are bundles of contractile cells to produce movement when stimulated by nerves.

In Figure 1.2, the general scheme of a healthy joint and its components is presented and it is compared with an osteoarthritic articulation. In a healthy joint (a), the ends of bones are encased in smooth cartilage. Together, they are protected by a joint capsule with a synovial lining that produces synovial fluid; the capsule and fluid protect the cartilage, muscles, and connective tissue. With OA, the cartilage becomes worn down (b). Spurs grow out from the edge of the bone, and synovial fluid increases. Altogether, the joint feels stiff and sore.

Usually OA progresses slowly. Early in the disease, joints may ache after physical work or exercise. OA can occur in any joints, but the main targets are hands, knees, hips, or neck spine.

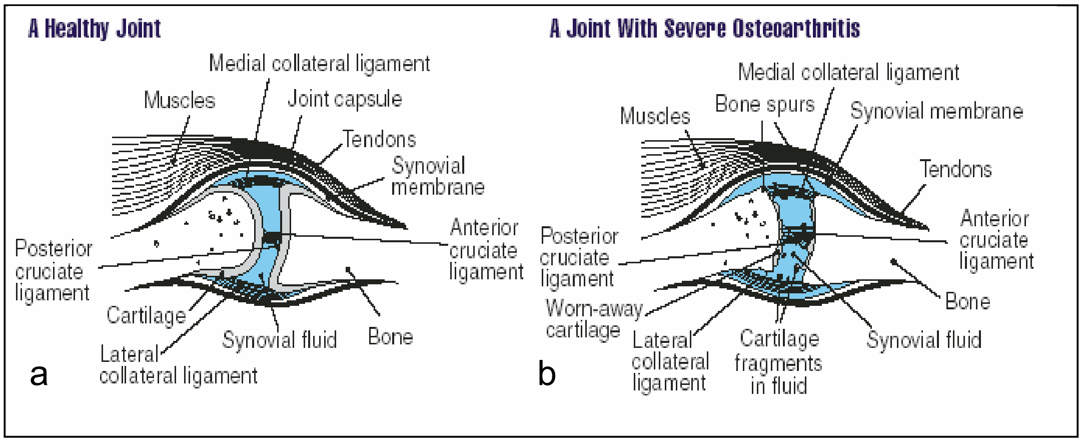

Figure 1.2 Joint architecture. Comparison between a healthy (a) and an osteoarthritic (b) joint.

1.3 Articular cartilage

The specific resident cell of the cartilage tissue is the **chondrocyte**. Typically, each chondrocyte is separated from the neighbouring cells by an **extracellular** hydrated **cartilage matrix,** which, in absence of vascular elements, is penetrated only by small biomolecules that provide nutrition and by regulatory biomolecules (i.e. tissue hormones). Chondrocytes are cells possessing different capabilities; besides normal cellular functions, these cells act as autonomous repair and self-defence units, and form the tissue matrix macromolecular framework from three classes of molecules (Figure 1.3): **collagens**, **proteoglycans**, and **noncollagenous proteins** (**glycoproteins**).

Cartilage tissue is an aneural and immunologically privileged tissue where the chondrocyte receives all the essential information for the control and maintenance of its extracellular matrix and for its intracellular activities from the biophysical (biomechanical) modulation of the tissue. This behaviour is governed by the physical properties of the extracellular matrix molecules and by ion fluxes that undergo alterations during mechanical loading. Therefore, the matrix protects the cells from injury resulting from normal joint use, determines the types and concentrations of molecules that reach the cells, acts as a mechanical signal transducer for the cells, and helps maintain the chondrocyte phenotype.

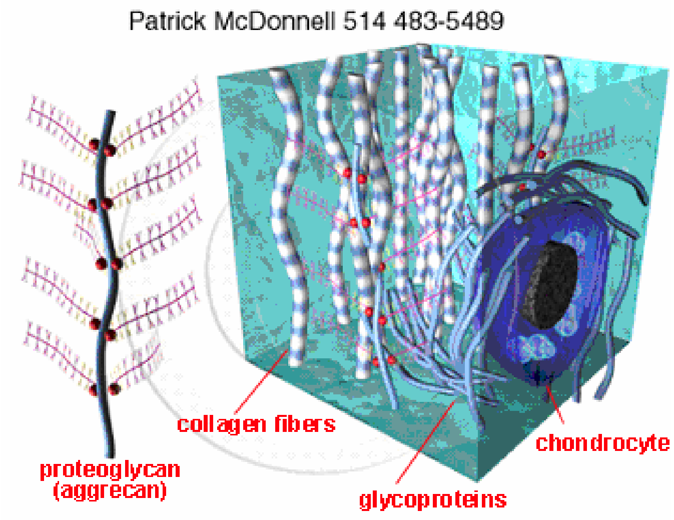

Figure 1.3. Molecular composition of the articular cartilage tissue.

Throughout life, articular cartilage undergoes internal remodelling as the cells replace matrix macromolecules lost through degradation. Aging decreases the ability of chondrocytes to maintain and restore articular cartilage and thereby increases the risk of degeneration of the articular cartilage surface.

A more detailed description of the molecular composition of the cartilage tissue is given in Appendix 1. The following paragraph presents the general tissue structure.

1.3.1 Tissue architecture

In adult articular cartilage four horizontal layers with different cell types and molecular composition can be distinguished (Figure 1.4):

1. the **superficial zone**
2. the **middle and deep zones**
3. the **tidemark**
4. the **calcified zone at the subchondral bone interface**

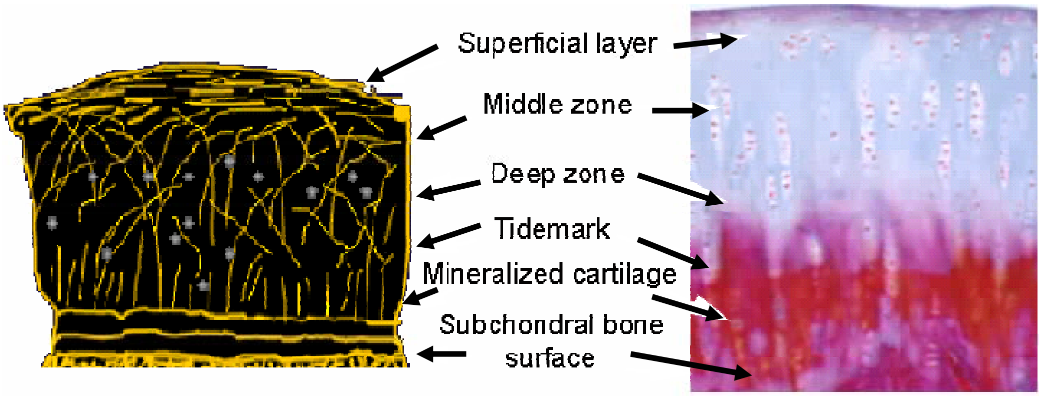

Figure 1.4. Scheme (left) and histological section (Azan stained) (right) of healthy intact cartilage. The different layers forming the tissue structure are indicated.

1. The **superficial zone** consists of one to three layers of flattened cells. These cells are less than 10% of all the cells in articular cartilage and they are different from the other cells of the tissue and produce their own particular subset of extracellular matrix proteins (including a very special *proteoglycan* - see Appendix 1). The superficial zone itself probably serves as a "basement membrane" equivalent that has the function to separate cartilage from the peripheral tissue and body fluid. Moreover, the superficial cells are very sensitive to irritation and they have capacities similar to those of macrophages.

2. The **middle and deep zones** consist of articular chondrocytes of spherical shape, surrounded by a distinct halo of "territorial" or "pericellular" matrix that has different properties and compositions than the "interterritorial" or "further removed" matrix. These cells are the major providers for the function of the articular cartilage and they represent and control most (over 80%) of the tissue. The chondrocytes of the deeper layers produce all the extracellular matrix components found in the articular cartilage: *collagens*, *proteoglycans*, *glycoproteins* and other substances needed for the tissue turnover.

Depending on the joint and the location within a joint, chondrocytes may exist either as single cells or as "chondrons" that are groups of two or several cells. **Chondrons** may be defined as functional subcompartments within the cartilage matrix hosting the chondrocytes and without any cellular junction between them. The matrix in which chondrons are embedded is both structurally and functionally different from the interterritorial matrix and it is equivalent to the territorial matrix of single chondrocytes.

3-4. The **tidemark** is a cell-free line of about 10 µm thickness at the border between the uncalcified and calcified cartilage, as shown by histological staining. The tidemark may mark the line of the most recent turnover of the calcified tissue, or a "sink" for metabolic (end)-

products, since it tends to migrate upward with age. The composition of this borderline is unknown except for some accumulated calcium-containing mineral deposits.

The deepest layers of the cartilage tissue are made of chondrocytes situated within a **calcified extracellular matrix**. These layers form a transitional tissue to the underlying bone but its calcification is sparse with respect to that one of the bone tissue. The function of the **calcified zone** is to prevent the diffusion of nutrients from bone to cartilage.

1.4 Osteoarthritis causes

Osteoarthritis affects each person differently. In some people, it progresses quickly; in others, the symptoms are more intense than in others. **Even if scientists do not know yet the ultimate causes of OA, there are several known risk factors, including overweight, the aging process, joint injury, and stresses on the joints from certain jobs and sport activities.**

Most cases of OA have no known cause and are referred to as **primary OA**. When the cause of the OA is known, the condition is referred to as **secondary OA**.

- **Primary OA** is mostly related to aging. With aging, the water content of the cartilage increases and the protein composition of cartilage degenerates. Repetitive over-use of the joints over the years irritates and inflames the cartilage. Eventually, cartilage begins to degenerate by flaking or forming tiny crevasses. In advanced cases, there is a total loss of the cartilage cushion between the bones of the joints. Studies show that occasionally OA can be found in multiple members of the same family, signifying that the susceptibility to cartilage breakdown may be partially genetic (Spector and MacGregor, 2004). Evidence of a genetic influence of OA comes from a number of sources, including epidemiological studies of family history and family clustering, twin studies, and exploration of rare genetic disorders. Classic twin studies have shown that the influence of genetic factors is between 39% and 65% in radiographic OA of the hand and knee in women, about 60% in OA of the hip, and about 70% in OA of the spine. Taken together, these estimates suggest a heritability of OA of 50% or more, indicating that half the variation in susceptibility to disease in the population is explained by genetic factors.
- **Secondary OA** is caused by another disease or condition including obesity, repeated trauma or surgery to the joint structures, abnormal joints at birth (congenital abnormalities), gout, diabetes, and other hormone disorders. Obesity causes OA by increasing the mechanical stress on the cartilage. In fact, next to aging, obesity is the most powerful risk factor for OA of the knees. Crystal deposits in the cartilage or in the joint space can cause cartilage degeneration, and OA. Uric acid crystals cause arthritis in gout. Some people are born with abnormally formed joints (congenital abnormalities) that are vulnerable to mechanical wear, causing early

degeneration and loss of joint cartilage. OA of the hip joints is commonly related to design abnormalities of these joints that had been present since birth. Hormone disturbances, such as diabetes and growth hormone disorders, are also associated with early cartilage wear and secondary osteoarthritis.

Convergence of these factors (primary and secondary) leads to the initiation of the disease state. Whether the factors that lead to disease initiation are the same that drive the disease from its initiation to any of its various outcomes, such as osteophyte formation, cartilage loss, and inflammation, has been the topic of much discussion. Further, some data suggest that the rate of progression of OA is variable; however, publications on the natural history of OA remain sparse. Literature reveals very few good quality studies that provide valid information on the rate of disease progression (Lohmander and Felson, 2004).

Longitudinal studies of OA are complicated by the fact that, generally speaking, during the period of a usually slow progression from a normal joint to end stage OA, patients age significantly.

In studies of OA incidence, patients are followed along a continuum progressing from a more or less normal state to a disease state. At some point, the patient crosses a borderline between what is recognized as absence of overt OA to presence of overt OA (Figure 1.5). It is important to note that the distinction between incident cases of OA and progression of prevalent cases depends on where along the continuum patients are considered to have overt OA. If, **for some reasons, medicine will become better at diagnosing OA, and overt OA is detected earlier, the definitions will change**, and then these criteria will change, perhaps even during the course of a long-term natural history study. Similarly, if OA is diagnosed later, cases formerly considered to be ‘progression cases’ will now be considered ‘incident cases.’ Thus, the definitions used to describe incident or prevalent cases of OA will critically depend on the criteria used to define OA. These considerations are important in developing a high-risk patient profile and in determining exactly what is being examined.

In summary, we do not yet fully know how risk factors interact to affect the incidence or the rate of disease progression in OA. Understanding these factors and the relationships between them are critical to designing studies that will ask the right questions and provide the answers necessary to develop effective means of treating and managing OA.

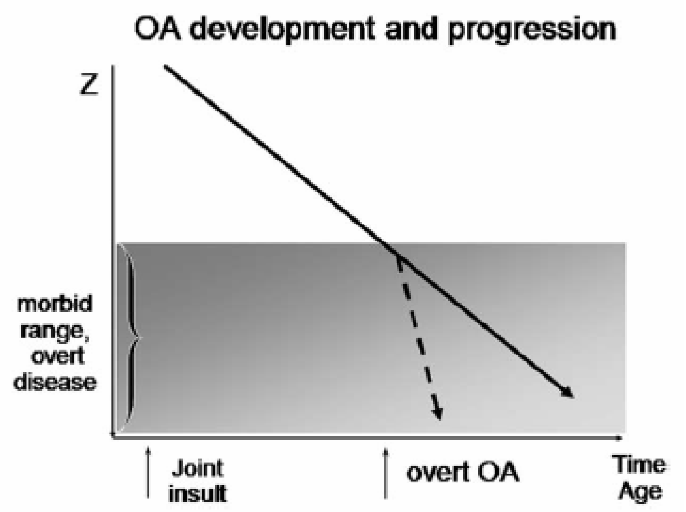

Figure 1.5. Graphic presentation of the 'background' progression (blue line) of osteoarthritis (OA) from 'no OA' to 'overt OA' (shaded zone) over time. A putative effect of a joint insult may cause an increase in the rate of disease progression (dashed line with steeper slope).

1.5 How is Osteoarthritis conventionally diagnosed?

A careful analysis of the location, duration, and character of the joint symptoms and the appearance of the joints helps the physician in diagnosing OA. Anyway, symptoms of OA vary greatly from patient to patient. Some patients become debilitated by their symptoms while others may have remarkably few symptoms in spite of dramatic degeneration of the joints. Symptoms also can be intermittent. It is not unusual for patients with OA of the hands and knees to have years of pain-free intervals between symptoms.

Because treatments that favourably influence clinical symptoms may at the same time have a deleterious effect on structural elements, international scientific committees have suggested that both symptomatic and structural variables of OA should be assessed in clinical studies (Bellamy, Kirwan *et al.*, 1997; Dougados, 2004).

Generally, a combination of the following methods is used to diagnose the OA disease and rule out other conditions.

- Among all, **imaging techniques** are so far the principal and most widely used tools for OA investigation. Nevertheless, their sensitivity is often insufficient for the detection of early stages of OA and its progression. Medical imaging techniques are based on physical (photon attenuation, temperature), mechanical (elasticity, dielectric coefficient...), electrical (conductivity, impedance), chemical, and biological (perfusion, protein expression...) properties of tissues.

The main diagnostic imaging modalities conventionally employed for OA detection are:

1. X-ray radiography
2. Computed Tomography (CT)
3. Magnetic Resonance Imaging (MRI)
4. Ultrasound
5. Arthroscopy

- Besides imaging modalities, more and more the **detection of biochemical markers** is used to evaluate OA presence and development. This procedure is based on the fact that alterations and destruction of the different components of the joint structure (cartilage, synovial tissue and bone), during progression of OA, release fragments or biological markers specific of these tissues in synovial fluids, blood and urine (Abadie, Ethgen *et al.*, 2004). There has been progress into the use of some of these markers for the prediction or measurement of progression of OA, as well as for the evaluation of response to pharmacological intervention with compounds of potential disease modifying OA drugs activity (Garnero, Ayral *et al.*, 2002; Bruyere, Collette *et al.*, 2003)). The potential for reliable and responsive markers is large. However, further work is still needed on how changes measured in some of these biochemical markers of cartilage turnover correlate with OA disease progression.

Hereafter the main imaging techniques used for OA diagnosis are described and the intrinsic limitations of these modalities are discussed in Paragraph 1.6. Particular attention will be paid to X-ray imaging modalities, since they represent the standard diagnostic tool for the OA study.

1.5.1 X-ray radiography

Radiography is the oldest and most frequently used form of medical imaging. Discovered more than a century ago, it can produce diagnostic images of the human body on film or digitally on a computer screen.

As X-rays penetrate most biological tissues with various attenuation properties according to the thickness, density, and atomic composition of the tissue traversed they provide a simple means to produce contrast between the different tissues. The principal interactions causing attenuation are the photoelectric absorption and non-resonant scattering. The radiographic image is formed by a distribution of photons transmitted through the sample and recorded by a receptor. Photoelectric absorption due to resonant scattering involves an excitation of the atom and a subsequent radiative (fluorescent) or non-radiative (Auger) transition via an intermediate state. Non-resonant scattering is either inelastic (Compton), where the incident photon energy is shared by a recoil electron and a scattered photon, or elastic, where the photon energy is conserved. The radiograph is due to variation on the photoelectric absorption, and in the intensity of the forward scattering recorded by the detector. Sample fluorescence, Compton scattering, and elastic scattering in particular carry detailed information about the composition and structure of the sample, as discussed later.

The radiograph is a projection of the attenuating properties of all the tissues along the path of the X-rays (Webb, 1988). It is a two-dimensional (2D) projection of the three-dimensional (3D) distribution of the X-ray attenuating properties of the tissue.

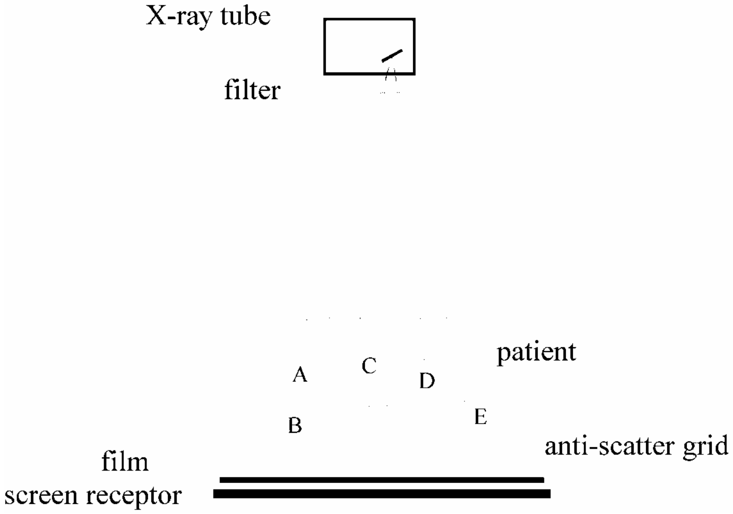

Figure 1.6. Components of the X-ray imaging system and the formation of the radiographic image. B and E represent photons passed through the patient without interacting; C and D are scattered photons; A is a photon absorbed by the sample.

– <u>The components of a typical X-ray imaging system</u> are shown in Figure 1.6. The photons emitted by the X-ray tube (with its cathode and anode element, see Paragraph 3.2) enter the patient, where they may be scattered, absorbed or transmitted without interaction. The primary photons recorded by the image receptor create the image, but the scattered photons produce a background signal, which degrades contrast. For this reason, generally these photons are removed by placing an anti-scatter device between the patient and the detector.

– <u>X-ray spectrum</u>. The spectrum shape and energy of X-ray photons generated are determined by the energy of the electrons, by the composition of the anode, and by filters placed along the X-ray beam path. Most commonly used anodes are molybdenum, rhodium, and tungsten. The choice for a particular target depends on the application or tissue probed and is a trade-off between acceptable radiation dose and achievable image contrast. For example, the characteristic X-ray photons emitted by molybdenum target are predominantly at 17.4 keV with

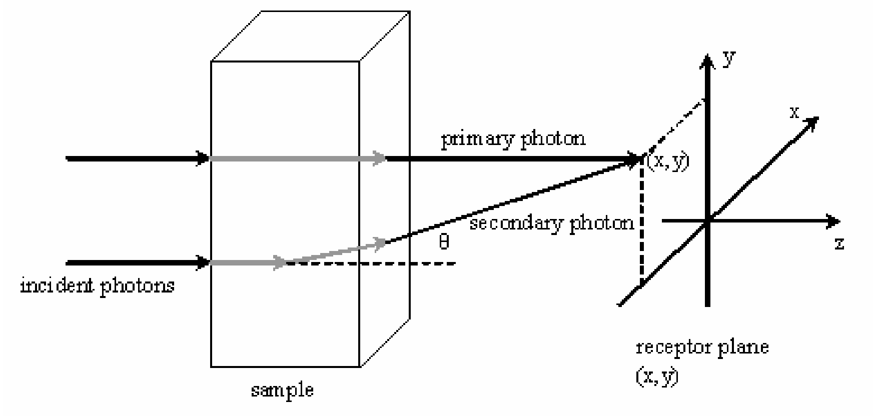

Figure 1.7. Simple model of the formation of the radiographic image showing both a primary and a secondary photon.

a smaller contribution from 19.7 keV, while tungsten has a characteristic emission at 59 keV with other low energy peaks.

– For describing the radiographic imaging process, it is useful to define a simple mathematical model (Webb, 1988). Let us consider a monochromatic X-ray source that emits photons of energy E and is sufficiently far from the sample so that the photon beam can be assumed parallel. Photons travel along the z direction and the image is recorded in the (x,y) plane. Let us also assume that each photon interacting in the receptor is locally absorbed and that the receptor response is linear, so that the image may be considered as a distribution of the absorbed energy. If $\varepsilon(E,\theta)$ is the energy absorption efficiency of the detector, and θ is the angle between the photon direction and the z direction (see Figure 1.7), the number of photons absorbed in the unit area of the detector centered on the point (x,y) is:

$$I(E,x,y) = I(E)\,\varepsilon(E,0)\,e^{-\int \mu_{att}(E;x,y,z)dz} + \iint \varepsilon(E,\theta)\,S(E;x,y,E_S,\Omega)\,dE_S d\Omega \qquad (1.1)$$

where $I(E)$ is the fluence (photons per area) of the incident radiation, $\mu_{att}(E;x,y,z)$ is the distribution of the linear attenuation coefficient of the sample, and $S(E;x,y,E_S,\Omega)\,dxdy\,dE_S d\Omega$ is the scatter distribution function that gives the number of photons in the energy range E to $E+dE$ and the solid angle range Ω to $\Omega+d\Omega$ which pass through the area $(x, x+dx; y, y+dy)$.

In equation (1.1), the first addend refers to primary photons while the second one to the secondary photons (the scattered ones). Since it is the first term that carries the useful information, and in practice it is the ratio R of the scattered to primary radiation that is either measured or calculated an appropriate form of the equation (1.1) is then:

$$I(E,x,y) = I(E)\,\varepsilon(E,0)\,e^{-\int \mu_{att}(E;x,y,z)dz}\left(1+R(E;x,y)\right) \qquad (1.2)$$

Moreover, the equation could further simplified, if one assumes $R(E;x,y)$ not depending on the position, that is $R(E;x,y) \approx R(E;0,0)$.

The number of photons recorded on the detector strictly depends upon the linear attenuation coefficient distribution of the tissues traversed by the radiation and the thickness of such tissues. In particular, the thicker is a feature and/or bigger the difference is in attenuation coefficients between the feature and the environment in which it is embedded, the better contrast is achieved on an image.

– The resolution of a radiographic device is determined by:

- the size and radiation intensity distribution of its focal spot (area of the anode emitting X-rays);
- the source-to-sample distance;
- the quality of the detector and its distance from the imaged detail.

Generally, another important parameter limiting the achievable image resolution is the acceptable dose to the tissue. In the case of joints radiography, this is anyway a less critical issue with respect other radiographic applications (for example mammography), since the targeted organs and tissues are in general not particularly radiosensitive.

– Many different types of image detectors are used in modern diagnostic radiography. They all form an image thanks to the absorption of energy from the X-ray beam but a variety of techniques are used to convert the resulting energy distribution into something that can be visualized by eyes. The most employed receptors are:

- **Screen-film combinations**. These receptors, based on the light conversion of fluorescent screens, are faster than direct-exposure films but do not have such good inherent resolution. They are, however, the detector of choice for many radiographic examinations where the dose reduction is more important than the loss of very fine details. The resolution (about 50-100 micron) in this case is mainly limited by the screen and in particular by the lateral spreading of the fluorescent light photons as they pass from screen to film. For this reason, good contact between screen and film is essential. The sensitivity of the system depends upon the X-ray absorption efficiency of the screen, the efficiency with which the energy deposited in the screen is converted to light, the sensitivity of the film and the development of the film.
- **Image intensifiers**. They are high-gain devices, so images need only very short exposure time. The radiation dose associated with their use for simple procedures is very low but the corresponding resolution and noise performances are inferior to those associated with screen-film systems. This receptor system is particularly valuable for

the study of processes that involve movement, flow or filling, for intra-operative control during surgery and for the fluoroscopic control of the insertion of catheters.

- **Digital detectors**. They mostly consist of photodiodes or photo-conductors (made of a semiconductor material) that are electrically coupled to a charge coupled device (CCD) camera. X-rays are absorbed in the shot-diode and converted into electric charge, which travels into the CCD and is read out by a computer.

Digital radiography systems are more expensive than conventional film or screen-film radiography systems, but they offer important advantages concerning different aspects:
i) image display.

Digital detectors are not affected by the very strict exposure requirements of the film-based radiography, where the *latitude* (range of exposure for which the receptor response is linear, outside this range the response of the film is very weak) is narrow. Digital detectors have a much wider dynamic range than film, with a linear response to X-ray exposure. The function that maps the digital image on to levels of brightness on a screen or film can completely controlled. The full range of density or brightness can be used to display just part of the range of pixel values, thereby enhancing the contrast in a region of interest.

ii) dose reduction.

In film-based radiography, the sensitivity of the image receptor and the film latitude determines the dose. In digital radiography, both these constraints can be relaxed. Moreover, thanks to complete control of the brightness range of an image, the risk of repeated acquisitions for optimizing the image exposure is extremely low.

iii) image processing.
Since the image is acquired and stored in a computer, the image can be enhanced digitally, and/or algorithms designed to detect subtle features may be employed.

iv) image storage and transfer.

Digital images are stored in a computer as standard binary files. This means that it is easy for hospitals and radiologists to share data for diagnostic purposes, since digital radiographs can be transmitted electronically. There is no chance of loss or damage of films, and an infinite number of backups can be made for each image with no degradation of the original.

A more extensive treatment on digital detectors will be presented in Chapter 4.

1.5.2 Computed Tomography (CT)

Conventional radiography provides no depth information, as the 3D body structure is projected onto a 2D image and makes it impossible to, for example, determine the three-dimensional position of a feature seen in a radiograph. A tomography is literally a cross-sectional image, a slice of an object. It can be obtained from different views around an axis of the object, each view being a projection of the object. A 3D-rendering of the object can be achieved by reconstructing several slices perpendicular to the object axis.

Mathematically, the solution to the problem of how to reconstruct a function from its projections dates back to the paper by Radon in 1917 (Radon, 1917), well before the first medical tomographic images were performed by Hounsfield in 1972 (Hounsfield, 1973). The reconstruction algorithms can be classified in two categories: the analytic methods by (Fourier) transformation and the iterative methods (algebraic and statistical).

Among the analytic methods, the *filtered backprojection* is the most commonly used one. It consists in convolving each projection with a filter function (which prevents the occurrence of the 'star artefact' in conventional backprojection) and reconstructing the slice by backprojecting the filtered projections along their original line-of-sight and summing up the relevant physical object quantity, i.e. the attenuation values in the case of X-ray tomography.

The underlying mathematics, as well as other reconstruction schemes are described in details in the books of Kak and Slaney (Kak and Slaney, 1988), Herman (Herman, 1980) and Born and Wolf (Born and Wolf, 1999).

Principles of reconstruction:

– Acquisition model

In the following, we consider the case of absorption X-ray imaging with a parallel beam geometry. In this case, the problem is reduced to the determination of the 2D object function $f(x,y)$ in a slice perpendicular to the rotation axis. For X-rays, this function is modelled by the two-dimensional spatial distribution of the X-ray linear attenuation coefficient $\mu(x,y)$.

A line integral represents the total attenuation of the X-ray beam as it travels in a straight line through the object. A projection is formed by the set of line integrals for a particular orientation θ. The coordinate system (t,l) is rotated by the angle of projection θ with respect to the fix coordinate system of the image (x,y) (Figure 1.8).

The function $p(t,\theta)$ represents the projection data:

$$p(t,\theta)=\int_L f(x,y)dl \tag{1.3}$$

The angle θ can be limited between $[0,\pi]$ as $p(t,\theta+\pi)=p(-t,\theta)$.

The points participating to the integration domain (*L*) for the point *t* of a projection at angle θ is given by:

$$t = x\cos(\theta) + y\sin(\theta) \tag{1.4}$$

in other words, $t = A\sin(\theta+\phi)$ with $A = \sqrt{x^2+y^2}$ and $\phi = \begin{cases} \arctan(x/y) & \mathit{for}\ y \neq 0 \\ \pi/2 & \mathit{for}\ y = 0 \end{cases}$ from which derives the expression **sinogram** of projections.

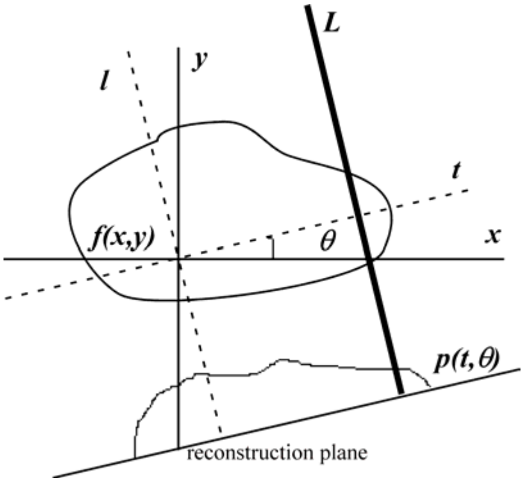

Figure1.8. Fix (*x*,*y*) and rotating (*t*,*l*) coordinate systems. θ is the rotation angle with respect to the *x*-axis. *L* is the direction along which the integration is performed.

– The simple backprojection

The easiest (but oversimplified) way to reconstruct is to project in the opposite sense the value of the line integral (*L*) the reconstruction plane. For a given angle θ, the value of $p(t,\theta)$ is assigned to each of the pixels that are along the integration line. The linear superposition of all backprojections forms the reconstructed image.
The backprojection can be formalized by:

$$f_{BP}(x,y) = \int_0^{\pi} p(t,\theta)d\theta \tag{1.5}$$

Most of the qualitative information of the initial distribution is preserved, however the image structures do not appear clearly. An exaggerated contribution of low frequencies perturbs the image and even a homogeneous distribution would show up as non-uniform.

– The Fourier slice theorem

The problem is to obtain a good estimate or reconstruction of $f(x,y)$ from the $p(t,\theta)$ values. For this, a theorem relates the 2D Fourier transformation of $f(x,y)$ to the 1D Fourier transformation of $p(t,\theta)$.

The 1D Fourier transformation, with respect to the spatial coordinate *t*, of the projection at angle θ_j is:

$$P(\omega,\theta_j) = \int p(t,\theta_j) e^{-i\omega t} dt \tag{1.6}$$

$$P(\omega,\theta_j) = \iint f(x,y) e^{-i\omega t} dl\, dt \tag{1.7}$$

where *t*, θ_j, *x* and *y* are related by $t = x\cos(\theta_j) + y\sin(\theta_j)$.

The point defined in polar coordinate by (ω,θ_j) can be expressed in an orthogonal coordinate system by:

$$\omega_x = \omega\cos(\theta_j) \tag{1.8}$$

$$\omega_y = \omega\sin(\theta_j) \tag{1.9}$$

The 2D Fourier transformation of the initial distribution is:

$$F(\omega_x,\omega_y) = \iint f(x,y) e^{-i(x\omega_x + y\omega_y)} dx\, dy \tag{1.10}$$

therefore $P(\omega,\theta_j) = F(\omega_x,\omega_y)$, i.e. the **1D Fourier transformation of a projection at a certain angle corresponds to the radial profile of the 2D Fourier transform of the initial function at this angle.** This constitutes the Fourier slice theorem, which enables, in principle, reconstruction with a direct method using the 2D inverse Fourier transform.

– The filtered backprojection

From the 2D inverse Fourier transform $F(\omega_x,\omega_y)$, one obtains $f(x,y)$:

$$f(x,y) = \frac{1}{4\pi^2} \int_{-\infty}^{+\infty}\int_{-\infty}^{+\infty} F(\omega_x,\omega_y) e^{i\omega t} d\omega_x\, d\omega_y = \frac{1}{4\pi^2} \int_{-\infty}^{+\infty}\int_{-\infty}^{+\infty} P(\omega,\theta) e^{i\omega t} d\omega_x\, d\omega_y \tag{1.11}$$

in a polar coordinate system:

$$f(x,y) = \frac{1}{4\pi^2} \int_{0}^{2\pi}\int_{0}^{+\infty} P(\omega,\theta)\, \omega e^{i\omega t} d\omega d\theta \tag{1.12}$$

As the point defined by (ω,θ) are the same than these defined by $(-\omega,\theta+\pi)$,

$$f(x,y) = \frac{1}{4\pi^2} \int_{0}^{\pi}\int_{-\infty}^{+\infty} P(\omega,\theta) \left|\omega\right| e^{i\omega t}\, d\omega d\theta \tag{1.13}$$

Let be $\hat{p}(t,\theta)$ defined by:

$$\hat{p}(t,\theta) = \frac{1}{2\pi} \int_{-\infty}^{+\infty} P(\omega,\theta) \left|\omega\right| e^{i\omega t} d\omega \tag{1.14}$$

thus, $f(x,y)=\frac{1}{2\pi}\int_0^{\pi}\hat{p}(t,\theta)d\theta$ which means that $f(x,y)$ can be obtained from the backprojection of $\hat{p}(t,\theta)$. If $|\omega|$ is neglected in equation (1.14), then one has a simple backprojection.

Let $\phi(t)$ be a function such that its Fourier transform is $|\omega|$ ($|\omega|=\int_{-\infty}^{+\infty}\phi(t)e^{-i\omega t}dt$), then the convolution of the projection $p(t,\theta)$ with this function gives:

$$p(t,\theta)*\phi(t)=\frac{1}{2\pi}\int P(\omega,\theta)|\omega|e^{i\omega t}d\omega=\hat{p}(t,\theta) \tag{1.15}$$

In other words, the initial projection data must be filtered by the function $\phi(t)$, before being backprojected.

– The filter function

The function $\phi(t)=\frac{1}{2\pi}\int_{-\infty}^{+\infty}|\omega|e^{i\omega t}d\omega$, which defines the filter function in the spatial domain diverges for t=0, if the integration domain is not limited. To limit the integration domain, the ramp function $R(\omega)=|\omega|$ is multiplied by a rectangular window:

$$\pi(\omega)\begin{cases}1 & if\ -\Omega<\omega<\Omega\\ 0 & otherwise\end{cases} \tag{1.16}$$

which finally gives $\phi(t)=\frac{1}{2\pi}\int_{-\Omega}^{+\Omega}|\omega|e^{i\omega t}d\omega$.

As the object is sampled at intervals equal to the distance between adjacent points of the projection Δt, the highest significant spatial frequency is given by $\Omega=\pi/\Delta t$.

The abrupt cut of the rectangular windows at the frequency Ω gives rise to oscillations at the edges of the object. This is known as the Gibbs phenomenon, whose effects can be reduced using other types of window, where a smoother transition is used.

1.5.3 Magnetic Resonance Imaging (MRI)

Magnetic Resonance Imaging (MRI), also referred to as Nuclear Magnetic Resonance imaging (NMR), is a technique involving magnetic fields and radiofrequency (RF) electromagnetic waves. Bloch and co-workers at Stanford and by Purcell at Harvard discovered it in 1946 independently. The idea to extend MRI to studies on humans dates back to Jackson, who in

1967 produced what are believed to be the first MR signals from a live animal; the first image of a live animal is instead due to Lauterbur in 1974.

In MRI, the patient is placed inside a strong magnetic field and nuclear magnetic resonance is utilised to obtain images as a function of proton spin density and relaxation times (or spectra of ^{31}P and ^{1}H in NMR spectroscopy). A detailed description of the technique is given by (Sorensen and Phelps, 1987).

– Common to the wide variety of MR instruments used to produce proton images of humans are the following basic components:

1. A magnet that has a bore size or gap large enough to accept the patient body, produces a stable homogeneous magnetic field (B_0) over the imaging volume of interest, and induces a weak magnetization (M) in the tissue as a result of alignment of fat and water proton magnetic dipoles with the field;
2. A gradient coil that creates pulsed magnetic field gradients, which are required for selecting the imaging slice (or slices) and for frequency and phase encoding of the magnetization within the slice;
3. A radiofrequency (RF) transmitter/receiver (transceiver) for generating the RF (B_1) pulses, which rotates M away from alignment with B_0, and for detecting the MR signal produced by precession of M;
4. A computing system for managing the magnet, transceiver, and gradient coil components, for processing and storing the MR signal, and for constructing, storing, and displaying the image.

• The magnet can be superconducting, resistive, or permanent. Superconducting magnets tend to have the highest magnetic field and therefore highest signal-to-noise values. Resistive and permanent magnets instead tend to have a more open architecture, allowing interventional MRI applications and tend to prevent claustrophobia.

• The gradients are resistive electromagnets consisting of metallic coils driven by a power amplifier. Gradient performance is measured in amplitude (milliTesla/meter) and rise time (microseconds): larger values of the former (>20 mT/m) and smaller values of the latter (<400 ms) being required for high-performance applications.

MRI principles

– When exposed to a static magnetic field, the randomly orientated magnetic moments (m_p) of the spinning nuclei of the sample align with the magnetic field. This phenomenon is explained by quantum mechanics: the external magnetic field B_0 creates two states for the proton (associated with a hydrogen nucleus) that are identified by the magnetic quantum number $m_p = \pm 1/2$, corresponding to 2*l*+1 (*l* spin quantum number) possible states, and the population of the states is governed by the Boltzmann distribution. The state with $m_p = 1/2$, in which the magnetic moment has a component parallel to B_0, has lower energy than the antiparallel state.

The interaction between each nucleus and B_0 causes the magnetic moment to precess around the magnetic field vector with the characteristic *Larmor frequency* (see Figure 1.9):

$$f_L = \frac{\gamma}{2\pi} B_0 \tag{1.17}$$

where $\gamma/2\pi$ is the gyromagnetic ratio characteristic of the nuclear isotope. For hydrogen nuclei in a magnetic field of B_0 = 1 Tesla, the precession frequency is 42.6 MHz. The hydrogen is favoured for MRI because of its abundance and sensitivity.

When a large number of nuclei in equilibrium are considered, the *xy*-component of m_p cancels out. However, the net magnetic component *M* will be aligned with B_0, i.e. the *z*-axis.

MRI is based on the resonance process, which is the induction of transitions between states of different energy ($m_p = \pm 1/2$ for protons). The energy required to produce such transitions equals the difference in energy between the lower and upper states, flipping magnetic moments from $m_p = 1/2$ to $m_p = -1/2$.

Application of a short pulse of circularly polarised radio frequency radiation, whose magnetic field vector is perpendicular to B_0, causes *M* to tilt away from the *z*-axis and rotate in the *xy* plane at frequency f_L. This represents a source of detectable radiation at the frequency f_L. The recovery of the *z* component gives rise to a signal, which is characterised by two decay mechanisms that are reflected in the **longitudinal** and **transverse relaxation times**, **T1** and **T2** respectively. T2 relaxation, which is usually considerably faster than T1 relaxation, is due to a loss in phase coherence between neighbouring nuclei, caused by local variations in the magnetic field. These arise from a local, tissue-dependent, variation in magnetic susceptibility as well as a non-uniform magnetic field. Unlike T1 relaxation, no energy is transferred from nuclei to the lattice in T2 relaxation. Nuclei in the excited and ground state may exchange energy with each other.

However, in biological tissues the main contribution to T2 is from the relatively static magnetic field from neighbouring protons. Large molecules, which tend to reorient more slowly than small molecules, promote T2 relaxation and have shorter T2 times. Free water has longer T2 than water associated with macromolecules. The magnetic field strength influences T2 much less than T1, at least under the conditions encountered in MRI. Typically, T2 in biological tissue ranges from approximately 50 to 100 ms.

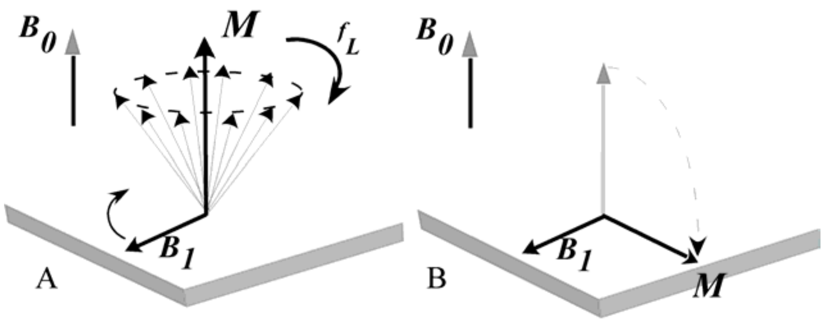

Figure 1.9. Tipping of longitudinal magnetization into transverse magnetization by a magnetic field B_1, associated with an RF wave or pulse. A) For appreciable tipping to occur, the B_1 field must rotate synchronously with the precessing transverse magnetization. This condition is met by circular polarized RF pulse at the Larmor frequency. B) All of the longitudinal magnetization is tipped into the transverse plane by an RF pulse that is strong enough and applied long enough to tip the magnetization 90 degrees.

T1 relaxation is a result of the precessing nuclei losing their associated potential energy due to coupling with the magnetic moments of surrounding nuclei. This energy transfer results in the individual magnetic moments returning to their equilibrium states such that M is again parallel to B_0. Because of the nature of the interaction, T1 provides information about vibrational motion in the lattice, which in biological tissues is usually water. It is a measure of the ability of water molecules in the neighbourhoods of the spins to tumble and rotate, which relates to the water content and to the degree to which water is bound or absorbed onto surfaces in the tissue. The frequency of rotation in medium-sized molecules, such as lipids, is closest to typical Larmor frequencies. Therefore, the magnetization associated with lipids relaxes faster than that associated with pure water or much larger molecules, such as proteins. Moreover, T1 relaxation times depend on magnetic field strength because the latter affects the Larmor frequency.

These relaxation times are characteristic of different tissue types and can be measured by applying suitable sequences of RF pulses and defining the radio frequency MR signals with a receiver coil. MR can be detected only if transversal magnetization (perpendicular to B_0) is created because this magnetization is time dependent and thus, according to Faraday's law of induction, generates a voltage in a receiver coil. The longitudinal magnetization in thermal equilibrium is static and therefore does not meet the criteria for magnetic induction.

Spatially resolved anatomical data sets are acquired by applying magnetic field gradients across the patient that result in a measurable gradient in the Larmor frequency in one plane, and a phase encoding gradient in the orthogonal plane.

MRI image arise from Fourier imaging, which is an efficient and versatile technique for identifying the location of MR signals originated from various regions of the body. It can create 2D and 3D MR images with various sizes and spatial characteristics. The images are calculated from digitized MR signals and they give a slice image of the plane of interest.

Among the reasons for the success of MRI as a diagnostic imaging tool are the relatively good high resolution (sub-mm), non-invasiveness and very low risk. Disadvantages are the high costs, bulkiness of the equipment, the requirement for the patient to remain motionless in the magnet for up to about half an hour, the problems associated with the presence of high magnetic fields and with the possible administration of contrasting agents such as iodine and gadolinium to enhance the image contrast.

1.5.4 Ultrasound

Current ultrasonic (UI) diagnostic imaging systems function mostly in the pulse-echo mode, where a single probe is used both for transmitting the signal and for receiving the echoes reflected or scattered back from tissues. To obtain the best resolution, the probe is excited by short and high frequency pulses of acoustic energy that are emitted into the patient body and experience reflection at boundaries between tissues of different characteristic impedance.

From the measurement of time delay and intensity of the reflected pulses (echoes), an image indicating tissue interfaces is reconstructed.

Depending on how the information is displayed, pulse-echo methods can be differently classified. The oldest and simplest type of UI instruments use a display of the echo amplitude as a function of depth of penetration, which is equal to $ct/2$ where t is the time of flight of the pulse, on a monitor. Other UI instruments use the echo amplitude to modulate the electron beam intensity of a cathode ray tube. If the intensity of the electron beam is modulated to be proportional to the echo amplitude, this type of display is called grey-scale B mode display.

Ultrasound imaging is considered to involve negligible risk provided that the incident intensities are sufficiently small. The relatively simple technology employed makes it also rather inexpensive as compared to other clinical imaging modalities.

The spatial resolution depends on many factors and is typically of the order of a millimeter.

Ultrasound frequencies typically range from 20 kHz to 15 MHz. The speed of sound in tissues follows the function:

$$c = \sqrt{\frac{K}{\rho_0}} \tag{1.18}$$

where K is the *bulk elastic modulus* and ρ_0 the tissue density. The average speed of sound in soft tissues is 1540 m/sec, with variations of about ±6 %. These variations are mainly due to changes in elasticity, rather than density, and are usually ignored in the reconstruction of images. As most biological tissues are effectively fluids, ultrasound waves are always longitudinal. The *characteristic acoustic impedance*, Z, of tissue is defined as:

$$Z = \rho_0 c \tag{1.19}$$

Hence, in analogy to Fresnel's formula in optics, the intensity of a sound beam reflected at a normal boundary between media with acoustic impedances *Z1* and *Z2*, relative to the incident intensity, is given by:

$$R = \left(\frac{Z_2 - Z_1}{Z_1 + Z_2} \right)^2 \tag{1.20}$$

The central component of an ultrasonic imaging system is the transducer. It converts electrical signals to sound waves, and vice-versa. Ultrasound transducers consist of one or several piezoelectric crystals coupled to the tissue via an impedance matching gel. In order to produce a 2D image, the transducer is either moved mechanically or an acoustic beam is steered by using interfering waves originating from an array of crystals. The physics and instrumentation of ultrasound imaging are covered in detail by (Shung, Smith *et al.*, 1992; Hedrick, Hykes *et al.*, 1995).

There are widespread clinical applications of diagnostic ultrasound systems. For musculoskeletal investigations, UI is a useful method to detect defects in muscles, tendons, ligaments, joints, and soft tissue, besides prenatal and coronary diagnostics.

1.5.5 Arthroscopy

Arthroscopy is a surgical technique whereby a viewing tube (arthroscope, containing a video camera) is inserted into a body cavity such as the joint space. Abnormalities of and damage to the cartilage and ligaments can be detected and sometimes repaired through the arthroscope. If successful, patients can recover from the arthroscopic surgery much more quickly than from open joint surgery.

1.6 Limitations of conventional imaging techniques in osteoarthritis detection and metal implants healing evaluation

Destruction and loss of articular cartilage is one of the key events in osteoarthritic disorders. Detection of very early stages of the tissue degeneration is extremely important for being able to intervene readily and effectively. At very advanced OA cases, when conservative measures fail to control pain and improve joint function, surgery is often considered

A crucial issue is the precise determination of the state of bone growth in the microscopic vicinity of metal implants. Even histological evaluation (in animal experiments only) suffers from the fact that it can only give information on very restricted portions of the implant because of the micrometer-scale thickness of individual sections.

The following paragraphs discuss the intrinsic limitations of diagnostic methods conventionally used for both OA detection and implant healing evaluation.

1.6.1 Osteoarthritis detection

- **Conventional radiography**

Among the different imaging techniques, conventional radiography has the highest spatial resolution and is the initial, most economical and most abundantly used imaging method in joint abnormalities.

The hallmark radiologic features for OA are:

- **joint space narrowing**, which is often irregular or asymmetric;
- **subchondral sclerosis**, which appears as an increased density in subchondral bone;
- **bony proliferation** with the presence of osteophytes/spurs;
- the presence of **cysts** in subchondral marrow adjacent to or sometimes remote from the joint (usually seen in later cases);
- **soft-tissue changes** (small effusions, calcification, and soft-tissue swelling).

Therefore, the radiographic evaluation of the disease severity and progression is made only **indirectly** and is mainly based on the measurement of the joint space narrowing that occurs between the ends of bones as cartilage is destroyed. Therefore, **conventional radiography** is **sensitive only in case of advanced disease**.

The cartilage tissue itself is not visible, and focal cartilage defects or structural abnormalities diagnostic of early stages of the degenerative joint disease are invisible on conventional radiographs or X-ray computed tomography.

In Figure 1.10, an example of conventional radiographs of a normal and an OA joint is presented. The detailed description of the features and of the limits of the projection imaging is given in the figure caption.

Moreover, even though radiographic measures of joint space width changes have been recommended as primary measure of efficacy for pharmacologic therapy (in particular for the so-called "disease modifying OA drugs"), and are commonly used for OA diagnosis, **precision of this measurement is quite variable and dependent on standardized radiographic techniques.** Small positional changes from one measurement to the other can jeopardize reproducibility of joint space width measurements. The degree of flexion of the knee determines the regions of cartilage taken into account for the measurements. Several methods including fluoroscopy, foot maps and positioning devices can be used to obtain satisfactory

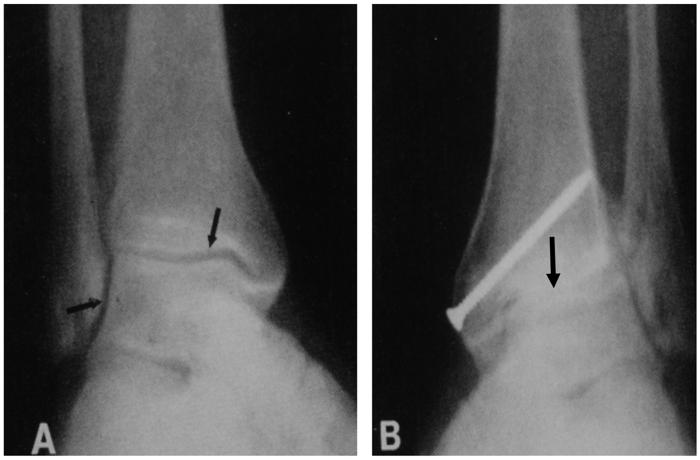

Figure 1.10. Conventional X-ray radiographs of a normal (A) and an osteoarthritic (B) ankle. In (B) an excess of mineralization and absence of a normal joint space is visible as hallmarks of OA (the screw is part of a joint fusion procedure). The only way to detect a cartilage disease or degeneration is to evaluate the narrowing of the joint space between the ends of the bones. In (A), the joint gap visible between the two bones means presence of cartilage tissue; therefore, it is a healthy joint. Nothing can be said about the status of the cartilage itself.

measurements, but despite standardization of radiographic techniques the rates of joint space narrowing can still vary widely (Brandt, Mazucca *et al.*, 2002; Mazucca, Brandt *et al.*, 2003) and lead to significant difficulties in the management of large sample size longitudinal clinical trials. Recent studies have also shown that alterations in the condition of the menisci (Gale, Chaisson *et al.*, 1999) could cause radiographic joint space narrowing independently of cartilage thinning. Measurements of joint space width at the hip seems less variable and more reproducible when using computer assisted methods (Conrozier, Lequesne *et al.*, 2001); (Gordon, Wu *et al.*, 2001).

- **Computed tomography (CT)**

It is a relatively expensive test. Relative to MRI, it gives poor definition of soft-tissue boundaries, giving rise to misleading cartilage thickness measurements. Computed tomography is particularly helpful in detecting fine details of cortical bone but it lacks sensitivity in early OA stages: degenerative signs of cartilage tissue and the entire tissue itself are not visible.

- **Magnetic resonance imaging**

MRI has been recognized as having potential for evaluation of joints in OA due to its ability to visualize the morphology and the integrity of the articular cartilage. It also provides a direct image of the soft tissues around the joint. Several studies have been performed in MRI to quantify the cartilage volume and thickness; in addition, *in-vivo* studies performed on knee joint have shown longitudinal cartilage volume losses in the range of 3 to 7% per year in OA patients (Biswal, Hastie *et al.*, 2002; Cicuttini, Wluka *et al.*, 2003; Pessis, Drape *et al.*, 2003; Raynaud, Kauffman *et al.*, 2003). However, other clinical trials did not detect any change in cartilage volume in patients with knee OA over a 3-year period (Gandy, Dieppe *et al.*, 2002). (Link, Steinbach *et al.*, 2003). More concerning is the fact that **no strong correlations have been shown between losses of cartilage volume measured by MRI over time and changes in X-ray joint space narrowing or in clinical symptoms**. Hence, larger longitudinal studies are still needed to clarify the clinical relevance of MRI measured cartilage volume in OA disease progression. Exploration of changes in the non-cartilage components of the OA joint (e.g. synovium and effusions, bone marrow 'edema') is also ongoing with MRI and may offer opportunities for the discovery of new parameters of interest (Link, Steinbach *et al.*, 2003).

However, the most promising MRI capabilities could well be the one developed to directly evaluate the changes in cartilage matrix components (e.g. *collagen* and *glycosaminoglycan*). These approaches could be of high interest to detect early changes in cartilage components in response to pharmacological intervention:

– several studies have shown that MRI T2 relaxation can be used as a qualitative assessment of collagen in the cartilage matrix (Mosher, Dardzinski *et al.*, 2000; Liess, Lussert *et al.*, 2002).

– one of the main constituents of cartilage which is lost in early OA, and which one would like to replace as part of therapeutic interventions, is the glycosaminoglycan (GAG) component. A new technique known as dGEMRIC (*delayed Gadolinium Enhanced MRI of Cartilage*) is being developed to directly image the GAG component in cartilage (Bashir, Gray *et al.*, 1999; Nieminen, Rieppo *et al.*, 2001; Tiderius, Olson *et al.*, 2003).

– another approach under investigation is sodium MRI. The rationale of this approach is based upon the fact that early stage of OA is primarily associated with a loss of proteoglycan (PG) and minimal changes in collagen. PG carries a negative fixed charge density due to its sulfate groups and thereby attracts sodium and potassium ions to maintain neutrality. Consequently, cation concentration can be used as an indirect measurement of PG content. Therefore sodium MRI of the knee has the potential for detecting early degenerative changes in cartilage (Regatte, Akella *et al.*, 2003).

Standard MRI is anyway considered costly and to have limitations in image resolution as to serve as a substitute, even though recent studies underscored its high diagnostic value (Wagner, Aurich *et al.*, 2005).

- **Ultrasound**

For ultrasound imaging, joint geometry and location often inhibit utilization of the method for most joints since the sound head **cannot resolve signals from structures that are not in straight geometry to and close connection to the microphone**.

- **Arthroscopy**

Although the arthroscopy technique appears reliable and sensitive to morphologic change at one, only the cartilage surface can be evaluated. Moreover, because this method is semi-quantitative and invasive, large multicenter studies would be difficult to conduct.

1.6.2 Metal implant healing evaluation

- **Conventional radiography**

Conventional radiology is limited in its use in bone/implant evaluation because of physical restrictions originating by the radiographic setup. Even though radiography allows the evaluation of an implant as a whole, at least along one axis of sight, it is finally hampered by **low local resolution caused by beam hardening based on the incident polychromatic light, thus, resulting in uncorrectable image errors** (example in Figure 1.11).

The first few hundred micrometers in the immediate vicinity of the metal surface are particularly prone to the image problems stated above.

- **Computed tomography (CT)**

Since metal objects are opaque to X-ray beams in the normal diagnostic energy range, their scannings yields incomplete projection data. CT pictures reconstructed from this incomplete data contain **imaging artefacts**, whose extent depends on the material type and volume of the implant. The artefacts make it difficult to determine the boundary between the implant, the cement, and the bone.

- **Magnetic resonance imaging**

The situation is aggravated in **patients with any kind of metal body parts**, ranging from pacemakers to artificial joints, because these patients **cannot be diagnosed by MRI**, since the technique uses magnetic fields. Unfortunately, a great proportion of the orthopaedic clientele is, from age and medical treatment history, particular prone to such limitations.

- **Ultrasound**

Ultrasound has **difficulty in penetrating bone and therefore can only see the outer surface of bony structures** and not what lies within and beyond bony features or metal implants. For this reason, the technique does not allow for investigations of inner parts of the sample and the border between bone and the implants cannot be visualized.

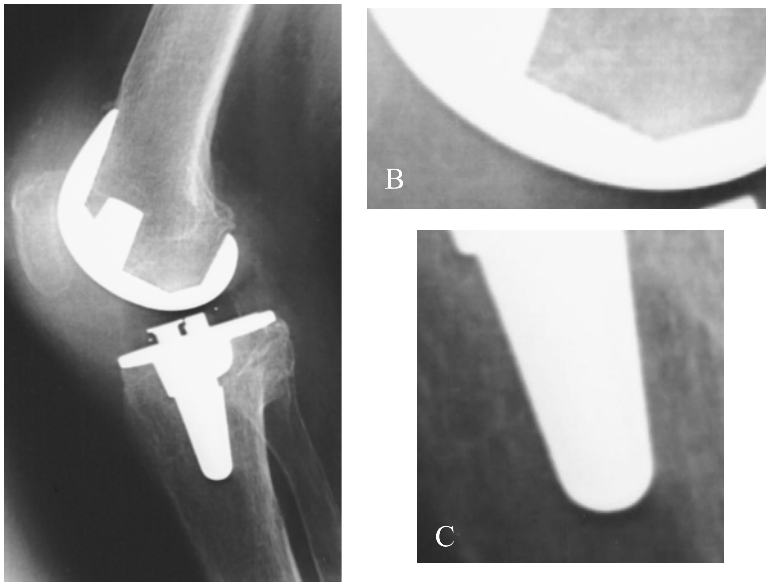

Figure 1.11. Conventional X-ray radiograph of a knee metal implant. Image artefacts caused by beam hardening false the information by creating an unsharped halo around the metal. Therefore nothing can be said about the first few hundred micrometers in the immediate vicinity of the metal surface. It is not possible in (B) and (C) to deduce whether or not the bone makes the desired contact with the implant surface.

1.7 Conclusions and research perspectives

Osteoarthritis (OA) is a degenerative disorder characterized by loss of articular cartilage, thickening of the underlying subchondral bone, and osteophyte (bone excrescence) formation. The etiology of OA is multifactorial, with inflammatory, metabolic, mechanical and genetic causes. A number of environmental risk factors, such as obesity, occupation, and trauma, may initiate various pathological pathways. In adults, cartilage has very limited capability of repairing, and the situation is aggravated in OA conditions. In very severe cases, surgery remains the only remedy for reducing the pain and helping restore functions.

OA is a poorly understood disease and, presently, **no cure exists.** The principal treatment objectives are to control pain adequately, improve function, and reduce disability.

For all these reasons, **understanding the causes of OA** and **finding better treatments** are the major focuses of preclinical and clinical investigations.

In the light of what presented in literature and discussed among the OA community, three major needs, and therefore tasks, for present and future research exist:

1. development of diagnostic markers and techniques for the **very early stages of OA** and for monitoring the **OA progression**;

2. development of methods and criteria for **evaluating therapeutic response** in the framework of cartilage-specific drugs innovation;
3. development of techniques for the **evaluation of metal (and low X-ray contrast bioresorbable) implant healing**.

Monitoring the progression of OA and the effects of therapy during clinical trials requires the use of **valid and reliable** outcome **measurements that are simple to perform and sufficiently sensitive** to detect changes in articular joint conditions.

Unfortunately, tools conventionally used to investigate the OA disease remain unsatisfactory. For both OA assessment and drug intervention studies, the principal hallmarks are still:

- the clinical observation (pain, inflammation, joint function...)
- the radiographic examination.

Both these diagnostic modalities can be sensitive only in case of advance OA stages, since they do not allow the visualization or detection of very early degenerative signs and processes in the cartilage tissue.

As described in the current chapter, many other imaging techniques are used (CT, MRI, UI, biomarkers detection...) but each of them presents intrinsic limitations (see Paragraph 1.6).

– Among all, the **'gold standard'** for measuring cartilage thickness remains the **radiographic method**, which allows the measurement of the narrowest joint-space width. Measurement of the joint-space width by standard radiography is used for both OA diagnosis and evaluation of drug effect even if it does not yield any information on the cartilage itself and provides only one measurement point. This fact considerably limits the statistical and clinical power of this technique in assessing cartilage degradation over time. Moreover, joint-space width, being a single-point evaluation of bone-to-bone distance, produces only an approximate measurement of the overall thickness of the articular cartilage and **gives no indication of its volume or any other structural changes associated with the disease process or with a therapeutical treatment.**

– Certain insights into early stages of arthritis derive from cell and tissue culture and experiments with normal cartilage and are linked to data from the more advanced stages obtained from surgical biopsy specimens. On the other hand, these studies do not allow any *in vivo* investigation since their destructive nature.

With such a scarcity of imaging indicators of early cartilage damage, the development of a modality that depicts initial phases of degeneration by harnessing different tissue characteristics in cartilage than those assessed through conventional X-rays radiography, MRI or ultrasound is warranted (Mollenhauer, Aurich *et al.*, 2002).

Poor imaging quality in practically all medical imaging technologies with respect to articular cartilage calls for the discovery and development of new techniques that are sensitive to stages preceding the point of irreversible damage of the cartilage tissue.

There is an important need of a high resolution, non-invasive diagnostic and monitoring technique allowing for the early detection and follow-up of OA, the evaluation of drug efficacy and the implant healing assessment.

In this scenario, phase contrast modalities have already largely demonstrated to possess higher sensitivity with respect to conventional techniques (Arfelli, Bonvicini *et al.*, 2000; Bravin, Fiedler *et al.*, 2002; Mollenhauer, Aurich *et al.*, 2002; Keyriläinen, Fernández *et al.*, 2005), without an increase of the delivered radiation dose. **In this work, it is demonstrated that the specificities of phase contrast techniques are able to fulfil many of the OA research requirements by improving the accuracy of the diagnosis and the sensitivity of the disease progression monitoring.**

REFERENCES

NIH Publication No. 02-4617 (2002). "National Institute of Arthritis and Musculoskeletal and Skin Disease - Osteoarthritis".

E. Abadie, D. Ethgen, B. Avouac, G. Bouvenot, J. Branco, O. Bruyere, G. Calvo, J. P. Devogelaer, R. L. Dreiser, G. Herrero-Beaumont, A. Kahan, G. Kreutz, A. Laslop, E. M. Lemmel, G. Nuki, L. Van De Putte, L. Vanhaelst and J.-Y. Reginster (2004). "Recommendations for the use of new methods to assess the efficacy of disease-modifying drugs in the treatment of osteoarthritis." Osteoarthritis and cartilage **12**: 263-268.

F. Arfelli, V. Bonvicini, A. Bravin, G. Cantatore, E. Castelli, L. Dalla Palma, M. Di Michiel, M. Fabrizioli, R. Longo, R.-H. Menk, A. Olivo, S. Pani, D. Pontoni, P. Poropat, M. Prest, A. Rashevsky, M. Ratti, L. Rigon, G. Tromba, A. Vacchi, E. Vallazza and F. Zanconati (2000). "Mammography with synchrotron radiation: phase-detection techniques." Radiology **215** (1): 286-93.

A. Bashir, M. Gray, J. Harke and D. Burstein (1999). "Nondestructive imaging of human cartilage glycosaminoglycan concentration by MRI." Magn Reson Med **41**: 857–865.

N. Bellamy, J. Kirwan, M. Boers, P. Brooks, V. Strand and P. Tugwell. (1997). "Recommendations for a core set of outcome measures for future Phase III clinical trials in knee, hip, and hand osteoarthritis.Consensus development at OMERACT III." J Rheumatol **24**: 799-802.

S. Biswal, T. Hastie, T. Andriacchi, G. Bergman, M. Dillingham and P. Lang (2002). "Risk factor for progressive cartilage loss in the knee." Arthritis Rheum **46**: 2884–2892.

M. Born and E. Wolf (1999). *Principles of optics: electromagnetic theory of propagation, interference and diffraction of light*. C. U. Press. Cambridge.

K. Brandt, S. Mazucca, T. Conrozier, J. Dacre, C. Peterfy and D. Provvedini (2002). "What is the best radiographic protocol for a clinical trial of a structure modifying drug in patients with osteoarthritis." J Rheumatol **29**: 1308-1320.

A. Bravin, S. Fiedler and W. C. Thomlinson (2002). "Very low dose mammography: new perspectives in Diffraction Enhanced Imaging (DEI) mammography." SPIE Medical Imaging, S. Diego, CA, SPIE.

O. Bruyere, J. Collette, O. Ethgen, L. Rovati, G. Giacovelli and Y. Henrottin (2003). "Biochemical markers of bone and cartilage remodeling in prediction of long term progression of knee osteoarthritis." J Rheumatol **30**: 1043–1050.

F. Cicuttini, A. Wluka, A. Forbes and R. Wolfe (2003). "Comparison of tibial cartilage volume and radiologic grade of the tibiofemoral joint." Arthritis Rheum **48**: 682–688.

D. H. Collins (1949). *Osteoarthritis. The Pathology of Articular and Spinal Diseases*. E. Arnold. London**:** 74-115.

T. Conrozier, M. Lequesne, H. Favret, A. Taccoen, B. Mazieres and M. Dougados (2001). "Measurement of the radiological hip joint space width. An evaluation of various methods of measurement." Osteoarthritis and Cartilage **9**: 281–286.

M. Dougados (2004). "Monitoring osteoarthritis progression and therapy." Osteoarthritis and cartilage **12**: S55-S60.

D. Gale, C. Chaisson, S. Totterman, R. Schwartz, M. Gale and D. Felson (1999). "Meniscal subluxation: association with osteoarthritis and joint space narrowing." Osteoarthritis and Cartilage **7**: 526–532.

S. Gandy, P. Dieppe, M. Keen, R. Maciewic, I. Watt and J. Waterton (2002). "No loss of cartilage volume over three years in patients with knee osteoarthritis as assessed by MRI." Osteoarthritis and cartilage **10**: 929–937.

P. Garnero, X. Ayral, J. Rousseau, S. Christgau, L. Sandell, M. Dougados and P. Delmas (2002). "Uncoupling type II collagen synthesis and degradation predicts progression of joint damage in patients with knee osteoarthritis." Arthritis Rheum **46**: 2613–2624.

C. Gordon, C. Wu, C. Petrefy, J. Li, J. Duryea, C. Klifa and H. Genant (2001). "Automated measurement of radiographic hip joint space width." Med Phys **28**: 267-277.

W. R. Hedrick, D. L. Hykes and D. E. Starchman (1995). *Ultrasound Physics and Instrumentation*. St. Louis, Mosby-Year Book.

G. T. Herman (1980). *Image reconstruction from projections*. New York, Academic Press.

G. N. Hounsfield (1973). "Computerized transverse axial scanning (tomography): Part I. Description of system." Br J Radiol **46**: 1016.

A. C. Kak and M. Slaney (1988). *Principles of Computerized Tomographic Imaging*. New York, IEEE Press.

J. Keyriläinen, M. Fernández, S. Fiedler, A. Bravin, M. L. Karjalainen-Lindsberg, P. Virkkunen, E. M. Elo, M. Tenhunen, P. Suortti and W. Thomlinson (2005). "Visualisation of calcifications and thin collagen strands in human breast tumour specimens by the diffraction-enhanced imaging technique: a comparison with conventional mammography and histology." European Journal of Radiology **53**: 226-237.

C. Liess, S. Lussert, N. Karger, M. Heller and C. Gluer (2002). "Detection of changes in cartilage water content using MRI T2 mapping in vivo." Osteoarthritis and cartilage **10**: 907–913.

T. Link, L. Steinbach, P. Ghosh, M. Ries, Y. Lu and S. Majumdar (2003). "Osteoarthritis: MRI imaging findings in different stages of disease and correlation with clinical findings." Radiology **226**: 373–381.

L. S. Lohmander and D. Felson (2004). "Can we identify a 'high risk' patient profile to determine who will experience rapid progression of osteoarthritis?" Osteoarthritis and cartilage **12**: S49-S52.

S. Mazucca, K. Brandt and K. Buckwalter (2003). "Detection of radiographic joint space narrowing in subjects with knee ostearthritis." Arthritis Rheum **48**: 385–390.

J. Mollenhauer, M. E. Aurich, Z. Zhong, C. Muehleman, A. A. Cole, M. Hasnah, O. Oltulu, K. E. Kuettner, A. Margulis and L. D. Chapman (2002). "Diffraction-enhanced X-ray imaging of articular cartilage." Osteoarthritis and cartilage **10**: 163-171.

J. Mollenhauer and K. E. Kuettner (1997). *Articular Cartilage. Principles of Orthopaedic Practice*. 2nd edition. New York, R. Dee, L.C. Hurst, M.A. Gruber, Stephen A. Kottmeier. McGraw Hill.

T. Mosher, B. Dardzinski and M. Smith (2000). "Human articular cartilage: influence of aging and early symptomatic degeneration on the spatial variation of T2." Radiology **214**: 259–266.

M. Nieminen, J. Rieppo, J. Toyras, M. Hakumaki, J. Silvennoinen and M. Hyttinen (2001). "T2 relaxation reveals spatial collagen architecture in articular cartilage: a comparative quantitative MRI and polarized light microscopic study." Magn Reson Med **46**: 487–493.

E. Pessis, J. Drape, P. Ravaud, A. Chevrot, M. Dougados and X. Ayral (2003). "Assessment of progression in knee osteoarthritis: results of a 1 year study comparing arthroscopy and MRI." Osteoarthritis Cartilage **11**: 361–369.

J. Radon (1917). "Berichte Sächsische Akademie der Wissenschaften, Leipzig." Math. Phys. Kl. **62**: 262.

J. Raynaud, C. Kauffman, G. Beaudoins, M. Berthaumie, J. de Guise and D. Bloch (2003). "Reliability of quantification imaging system using magnetic resonance images to measure cartilage thickness and volume in human normal and osteoarthritic knees." Osteoarthritis and Cartilage **11**: 351–360.

R. Regatte, S. Akella, R. Borthakur and R. Reddy (2003). "Proton spin-lock ratio imaging for quantification of glycosaminoglycans in articular cartilage." J Magn Reson Imaging **17**: 114–121.

K. K. Shung, M. B. Smith and B. Tsui (1992). *Principles of medical imaging*. San Diego, Academic Press.

J. A. Sorensen and M. E. Phelps (1987). *Physics in Nuclear Medicine*. Second Edition, Grune & Stratton.

T. D. Spector and A. J. MacGregor (2004). "Risk factors for osteoarthritis: genetics." Osteoarthritis and cartilage **12**: S39-S44.

C. Tiderius, L. Olson, P. Leander, O. Ekberg and L. Dahlberg (2003). "Delayed gadolinium-enhanced MRI of cartilage (dGEMRIC) in early knee osteoarthritis." Magn Reson Med **49**: 488–492.

A. Wagner, M. Aurich, N. Sieber, M. Stoessel, W. Wetzel, K. Schmuck , M. Lohmann, J. Metge, B. Reime, P. Coan, A. Bravin, F. Arvelli, G. Heitner, R. Menk, T. Irving, Z. Zhong, C. Muehleman and J. Mollenhauer (2005). "Options and Limitations of Joint Cartilage Imaging: DEI in Comparison to MRI and Sonography." Nucl. Instr. Meth. A **548**: 47-53.

S. Webb (1988). *The physics of medical imaging*. F. Mould. Avon, Iop.

2

The phase contrast imaging

Contents

Une alternative à la radiographie d'absorption est offerte par des techniques basées sur la détection du contraste de phase. Lorsque qu'une onde électromagnétique traverse la matière, sa phase peut être perturbée. L'enregistrement de ces phases produit des images fortement contrastées.

Le principe de la formation de l'image et les configurations expérimentales requises pour la mise en œuvre de la technique sont décrits dans ce chapitre. Les fondements théoriques sur le signal obtenu soit par l'intermédiaire d'un analyseur ou bien par propagation (les deux techniques ayant été étudiées dans ce travail de thèse) sont également présentés.

An alternative to conventional absorption-based radiography is offered by the so-called phase contrast imaging techniques. Besides X-ray attenuation, these techniques profit from the phase shifts occurring when an electromagnetic wave passes through the matter which can be recorded producing high sensitive and contrasted images.

In this chapter, the image contrast formation principles and the specific experimental configurations of the phase contrast techniques are presented. The theoretical basics of the signal of the Analyzer-based imaging and the Propagation-based imaging, the two modalities that have been studied and applied in this Thesis work, will be introduced and discussed.

2.1 Introduction

As already discussed in Chapter 1, in standard radiography the contrast results from variations in X-ray absorption arising from density differences and from variations in the thickness and composition of the specimen. The sensitivity of the technique is drastically decreased when the sample consists of low Z elements, for which the differences in the absorption coefficients are very small for hard X-rays (Henke, Gullikson *et al.*, 1993).

Weakly absorbing objects are often encountered in the life sciences, because organic matter is made mainly of carbon, hydrogen, oxygen and nitrogen. The difference in the absorption coefficient, for these elements, is of the order of 0.1-0.3 cm^{-1} (Förster, Goetz *et al.*, 1980) in the range of energies commonly used in radiology (10-60 keV).

A way for improving the image quality is the employ of high-efficiency and low-noise digital detectors, which allow to discriminate very weak signals, and the use of high collimated and monochromatic X-ray beams (Lewis, 1997).

In the last decade, a completely different approach has been proposed and developed. It consists in the application to the medical physics of the so-called **phase contrast techniques**, already largely used in other field of research in physics at lower energies. Such techniques are based on the recording of the phase variations occurring when X-rays pass through the matter. In fact, besides absorption, an X-ray beam traversing an object picks up information on its refraction properties that can also be utilized as a source of contrast for displaying the internal features of the sample.

The behaviour of X-rays as they travel through an object can be described in terms of a complex index of refraction (2.1) whose real part, δ, and imaginary part, β, are related to the electromagnetic wave phase shifts and to the X-ray attenuation in the object, respectively (Paragraph 2.2). In the energy range 10-60 keV, the phase term is orders of magnitude higher than the absorption one (Figure 2.1); therefore, radiographic techniques sensitive to variations of the δ term may potentially provide an increased image contrast with respect to those techniques based only on the X-ray absorption process.

In order to exploit the phase effects for imaging, different techniques have been developed (Fitzgerald, 2000). They include the propagation-based imaging (Snigirev, Snigireva *et al.*, 1995; Cloetens, Barrett *et al.*, 1996), the analyzer-based imaging (Förster, Goetz *et al.*, 1980; Davis, Gureyev *et al.*, 1995; Bravin, 2003) and the interferometric techniques (Momose, Takeda *et al.*, 1996; David, Nohammer *et al.*, 2002).

To be able to perform phase contrast imaging, the X-ray beam has to fulfil conditions concerning the temporal and spatial coherence properties of the radiation that are respectively linked to the

X-ray monochromaticity and to the angular source size. This topic will be discussed in Paragraph 3.6.

The introduced coherent imaging modalities, which will be described in the following paragraphs, have significant application in various fields such as material science (Cloetens, Ludwig *et al.*, 2002; Tsai, Hsu *et al.*, 2002), sub-micron imaging (Lagomarsino, Cedola *et al.*, 1997; Hignette, Cloetens *et al.*, 2003) and biomedical imaging (Arfelli, Bonvicini *et al.*, 2000).

In this Thesis work the phase contrast techniques which have been applied and investigated, are the **analyzer-based imaging** (ABI) and the **propagation-based imaging** (PBI); for this reason, they will be more extensively described.

2.2 Phase contrast versus absorption contrast

2.2.1 The refractive index

The propagation of X-rays in the matter is generally described with reference to the complex refractive index n, which can be expressed as (Jackson, 1975):

$$n = 1 - \delta + i\beta \tag{2.1}$$

– δ is the **refractive index decrement**, which determines the phase shifts of the electromagnetic wave in the matter and, therefore, its deviation from the incident direction due to the scattering with electrons of the medium (Azaroff, 1968);

– β is the **absorption index** which is linked to the photoelectric absorption of X-rays into the matter.

Under the influence of the electromagnetic field of the incident radiation, the polarization of the medium, for hard X-rays and far from the absorption edges, is well described by the free-electrons model where the electric susceptibility χ is proportional to the electron density ρ_e. The terms δ and β are related to the real and imaginary part respectively of χ by the following the expressions (Zachariasen, 1945):

$$\delta = -\frac{1}{2}\chi_{0r} \quad \text{and} \quad \beta = \frac{1}{2}\chi_{0i} \tag{2.2}$$

Such relations can be otherwise written as (Jackson, 1975):

$$\delta = \frac{r_e \lambda^2}{2\pi}\rho_e \tag{2.3}$$

$$\beta = \frac{r_e \lambda^3 \rho_e}{4\pi^2 c}\sum_j \frac{f_j \gamma_j}{Z} \tag{2.4}$$

where r_e is the electron radius, λ the X-rays wave length, f_j the number of electrons per atom with damping constant γ_j, and Z the atomic number that gives the total number of electrons per atom; the sum is over all the electrons of the atom.

ρ_e is linked to the macroscopic mass density of the medium ρ by the relation $\rho_e = Z/V = Z\,\rho\,N_A/A$ where *V* is the volume of reference, N_A the Avogadro's number and *A* the atomic weight.

The refractive index decrement, which is mainly due to Thompson scattering, can be generally expressed also as:

$$\delta = \frac{r_e\lambda^2}{2\pi V}\sum_j \left(Z + f_j^{'}\right) \tag{2.5}$$

with $f_j^{'}$ the real part of the wavelength-dependent dispersion correction of the atomic scattering factor.

Similarly, the absorption index β can be also written in terms of the imaginary part of the wavelength-dependent dispersion correction, $f_j^{"}$, as:

$$\beta = \frac{r_e\lambda^2}{2\pi V}\sum_j f_j^{"} \tag{2.6}$$

For energies far from the absorption edges, $f_j^{'}$ is approximately zero, whereas $f_j^{"}$ dominated by the absorption process, behaves with the energy as E^{-m}, with *m* between 3 and 4.

β is related to the linear absorption coefficient μ, through (Raven, Snigirev *et al.*, 1996):

$$\mu = \frac{4\pi\beta}{\lambda} \tag{2.7}$$

It has to be pointed out that the terms δ and β locally change inside the matter and therefore they have to be considered as functions of the spatial coordinates (*x*,*y*,*z*).

In the case of a crystalline medium, the scattering properties of the radiation are generally described by means of the structure factor (Appendix 1); if the Bragg reflection is not satisfied, the wave propagation is not influenced by the crystalline structure. In this case, the refractive index may be expressed in term of the (complex) structure factor F_0, as:

$$n = 1 - \frac{r_e\lambda^2}{2\pi}\frac{F_0}{V} \tag{2.8}$$

Numerically, *n* deviates only slightly from unity, δ and β being extremely small. The δ term is much larger than β in the energy range normally use in radiology and differs at least by three orders of magnitude as shown in Figure 2.1, where the ratio δ/β as function of the energy in the energy range 10 - 60 keV is reported.

This large difference between δ and β is the reason for the advantage of phase contrast imaging, the phase contribution being the sole source of contrast when the absorption counterpart is undetectable.

The energy dependence of the two terms δ and β, for energies far from the absorption edges and for low *Z* materials, is approximately given by (Eqs. (2.3) and (2.4)):

$$\delta \propto \frac{1}{E^2} \quad \text{and} \quad \beta \propto \frac{1}{E^4} \tag{2.9}$$

Since the phase φ is related to δ by the relation $\varphi \cong -2\pi\delta t/\lambda$, where *t* is the thickness traversed by X-rays, the energy dependence of the phase and of the linear attenuation coefficient may be expressed as:

$$\varphi \propto \frac{1}{E} \quad \text{and} \quad \mu = \frac{1}{E^3} \tag{2.10}$$

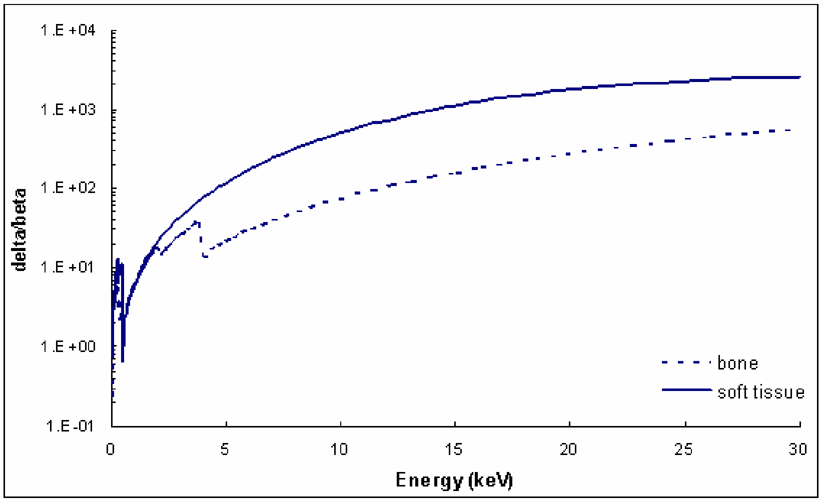

Figure 2.1. Ratio of the delta and beta terms in the energy range 10-30 keV for bone and soft tissue.

2.3 Phase contrast techniques

2.3.1 Interferometry

The principle of interferometry is to have a beam split into two separate coherent beams which can be recombined and interfere. The X-ray interferometry is owed to Bonse and Hart (Bonse and Hart, 1965) while its early application to the phase contrast imaging were performed by Ando et al. (Ando and Hosoya, 1972), in the early seventies. The technique is based on the use of the Bonse-Hart interferometer whose most commonly used configuration is the triple Laue (LLL), schematized in Figure 2.2. It utilizes Bragg diffraction by three perfectly aligned crystal slices cut out into a monolithic single silicon crystal. The first crystal acts as a coherent beam splitter, by diving the incident X-ray beam into a transmitted and a diffracted beam that are then deviated by the second crystal to allow for recombining them in the third crystal (or analyzer).

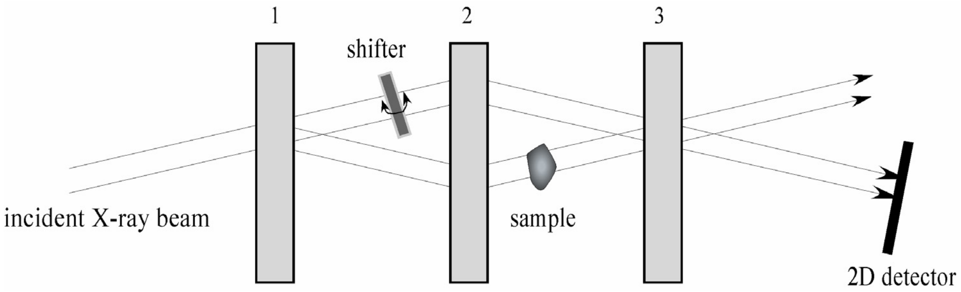

Figure 2.2. Scheme of a LLL interferometer. Details in the text.

Between the first two crystals, a phase shifter may be inserted and used to compensate for imperfections of the interferometer and to reconstruct the phase modulation introduced by the sample through the fringe scanning method. The sample is placed between the second and third crystal slice.

The image processing to quantitatively reconstruct the phase modulation introduced by the sample is rather simple. The phase modulation (with an uncertainty of 2π) is determined by recording a series of interference patterns (a minimum of 6 images per projection) with and without sample and for different settings of the phase shifter (Bonse and Busch, 1996). The phase ambiguity can then be eliminated by inspecting the radiographs and applying an appropriate phase unwrapping algorithm (Cusack, Huntley *et al.*, 1995).

Moreover, by measuring the phase shift in multiple directions by rotating the sample, a three-dimensional image mapping of the refractive index is obtained (phase tomography) (Momose, Takeda *et al.*, 1995).

There are several works, above all owed to Momose et al. (Momose, Takeda *et al.*, 1995; Momose, Takeda *et al.*, 1996; Momose, 2002), demonstrating the high potential and the advantages of this phase contrast technique with respect to the conventional absorption imaging. Nevertheless, the high complexity of the technique, mainly in terms of instrumental implementation, leads important limitations to its application that can be identified in the following points:

- **Set-up stability**

  The optical path length should be stable within a deviation smaller than the X-ray wavelength (~1 Å). A displacement at the atomic level between the different slices can jeopardize the fringe patter in such a way that no interference is observed. This is why the entire body of the interferometer is derived from a single block crystal and extreme mechanical, thermal or acoustical stability of the set-up have to be fulfilled.

- **Sample size**

  There is, therefore, a limit about the realizable dimensions of the apparatus and, consequently, the size of the sample to be investigated. The space available for the specimen is of few centimetres. To broaden the applicability of the technique, the field of view could be extended by the adoption of a two-crystal X-ray interferometer (Figure 2.3), the so called Laue skew-symmetric interferometer (Becker and Bonse, 1974), which has also be found to be considerably less affected by vibration than the single-crystal version. The latest version of this imaging system attained a 60 mm × 30 mm field of view (Yoneyama, Takeda *et al.*, 2004). Works using this two-crystal interferometry on biological samples are for instance (Momose, Yoneyama *et al.*, 1997; Yoneyama, Momose *et al.*, 1999; Yoneyama, Takeda *et al.*, 2004).

- **Sample environment**

  In order to avoid perturbations of the interference fringes due to phase discontinuities at the border of the sample, the latter has to be immersed in a liquid that matches the refractive index of the object.

- **Acquisition time**

  For reconstructing the phase map, several images are needed (at least six) to eliminate the incoherent contributions of the intensity and to avoid ambiguity on the sign of the phase. For this reason, the acquisition time can be up to several hours for performing interferometric tomography using a conventional X-ray source. The use of the high flux X-ray beams provided by synchrotron machine is, therefore, crucial for this kind of application.

- **Spatial resolution**

  The resolution is limited intrinsically by the passage of the beam through the analyser crystal. Dynamical diffraction occurring in this crystal spreads the energy of each point at its entrance over the Borrmann triangle whose width will limit the resolution. This typically limits the resolution up to about 15 μm (Beckmann, Bonse *et al.*, 1997). The volume of the interferometer implies a minimum distance between sample and detector, leading to some blurring due to the source size and Fresnel diffraction.

Contrary to other phase contrast techniques, interferometry does not have severe beam constraints. The beam incident on the sample, which is generally upstream monochromatized, is intrinsically monochromatic thanks to the Bragg diffraction in the slices of the interferometer.

Since the reference and the phase shifted beams derive from the same point of the original wave, the interference pattern is given by mutually coherent points and the incoming beam does not need to be highly laterally coherent itself.

Moreover, in the case of the interferometric technique, it is particularly convenient to work with small or smoothed phase gradient (low spatial frequencies), since the spacing of the fringes of interference is inversely proportional to the angular deflections of the X-rays inside the sample and the fringes are easily detected.

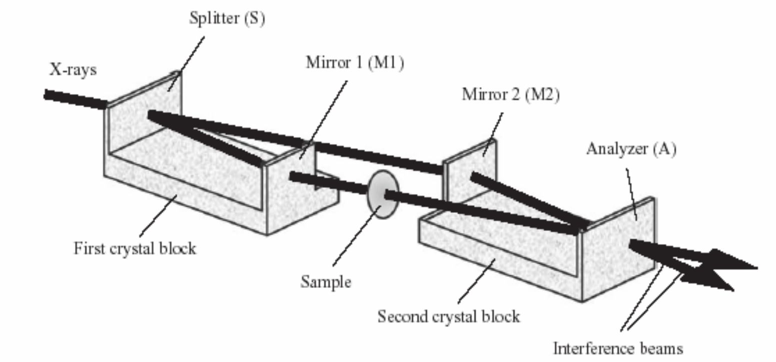

Figure 2.3. Scheme of a Laue two-crystal interferometer (Yoneyama, Takeda *et al.*, 2004).

2.3.2 Propagation-based imaging

In the propagation-based method, quasi-coherent radiation illuminates the object that can give rise to a spatially varying phase shift. As the radiation propagates from the sample, parts of the wavefront, which have experienced different deflections (Figure 2.5 (A)), interfere giving rise to a characteristic pattern that is then recorded by a detector set at a convenient distance (Figure 2.5 (B)) (Snigirev, Snigireva *et al.*, 1995; Cloetens, Barrett *et al.*, 1996). Thanks to the Fresnel diffraction, the phase shifts are therefore transformed in detectable intensity variations (Born and Wolf, 1999).

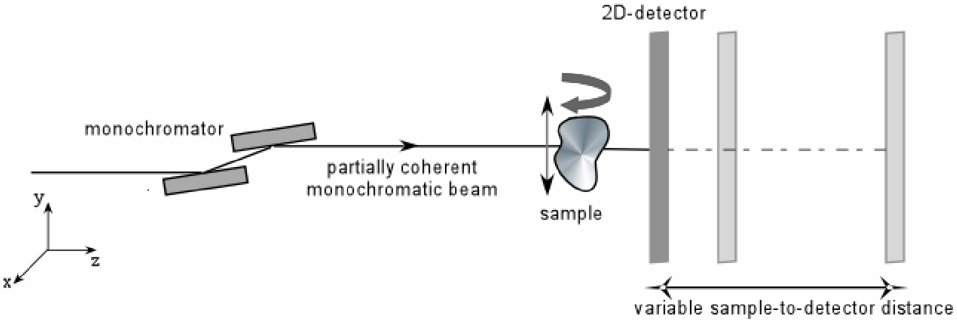

Figure 2.4. Scheme of the set-up of the propagation-based technique.

Among the phase contrast techniques, this imaging modality is characterized by a very simple set-up (Figure 2.4). The absence of optical elements implies that such an imaging method is intrinsically free from the usual aberrations, with achievable resolution depending largely, but not entirely, on the size of the source (Pogany, Gao *et al.*, 1997; Arhatari, Mancuso *et al.*, 2004).

Similarly to the analyzer-based technique that will be discussed afterwards, the propagation-based imaging is a differential phase imaging modality: a homogenous phase gradient, corresponding to an overall deflection of the beam, gives no contrast.

As mentioned, the contrast is associated to the angular deviations, $\Delta\alpha$, of the X-rays passed through the sample that, for a monochromatic plane wave travelling along the *z*-axis, can be expressed as:

$$\Delta\alpha(x,y) \simeq -\frac{\lambda}{2\pi}\vec{\nabla}_{x,y}\varphi(x,y;\lambda) \tag{2.11}$$

where φ and λ are the phase and the wavelength of the wave, respectively. This relation is valid if $|\nabla\varphi| << 2\pi/\lambda$, that is the so-called paraxial approximation. In particular, in the case of the propagation-based imaging, only features producing a non-zero laplacian of the phase variations may be visualized, as it will be described in Paragraph 2.4.

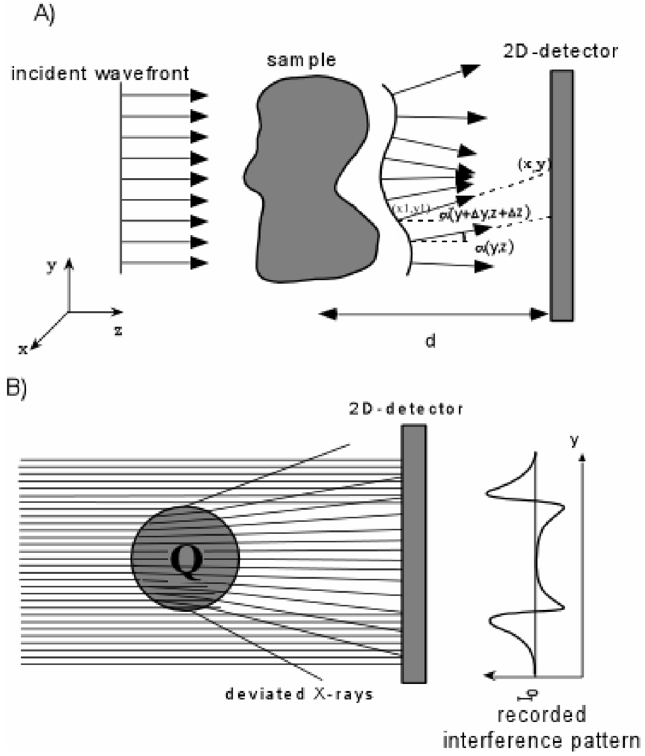

Figure 2.5. A) Angular deflection of the incident wavefront due to the refraction inside the sample; B) Recorded interference patter between parts of the incident wavefront affecting by different angular deviations.

There exists an important dependence on the sample-to-detector distance (*d*) of the phase contrast signal. By varying z and considering the transverse characteristic length scale *a* of the object and a monochromatic plane wave, three regimes may be distinguished (Snigirev, Snigireva *et al.*, 1995):

- $d \approx 0$ the **absorption regime**.
- $r_F^2 = \lambda d \le a^2$ the **edge detection** (or **near field diffraction**) **regime**: it is characterized by small propagation distances *d*. r_F is the radius in the object plane of the so-called **first Fresnel zone**. The latter represents the finite region in the object, which contributes significantly to the signal generated at a generic point *P* in the image. The contrast is formed locally around specific sample features characterized by high frequency components of the phase modulation. The boundaries of the object are strongly enhanced and a distinct interference pattern corresponds to every edge giving valuable geometrical information on the sample.
- $r_F^2 = \lambda d > a^2$ the **Fraunhofer** (or **far field diffraction**) **regime**: the interference fringes are very well resolved but they cannot no-more be associated to a given edge of the object. The shape of the sample is hardly recognizable and images give little direct information on the object itself.

Therefore, depending on the experimental conditions, the Fresnel diffraction pattern enhances different properties of the sample (edge-detection or far field diffraction). In general, for a given distance (*D*), the image is most sensitive to a specific frequency range. Being *f* the spatial frequency of a specific phase feature, one has that $D \approx 1/\left(2\lambda f^2\right)$. The defocusing distance *D* is determined by $D = d \cdot l/\left(d + l\right)$, where l and d are the source-to-sample and the sample-to-detector distance respectively. For $l >> d$, one has $D \simeq d$. As an example, for λ of 0.5 Å, in order to detect features of 10 μm (40 μm) size, the optimal distance would be 1 m (16 m). There is therefore a limit in the accessibility of low spatial frequencies (corresponding to smooth variations in the object's phase) due, essentially, to the experimental hutch dimensions.

Since at every propagation distance there are frequency components of the object that do not contribute to the image, the retrieval of the object phase cannot be simply performed with a single image without strong constraints on the object characteristics (Gureyev, Davis *et al.*, 2004). A way to retrieve phase is to acquire several images at variable distances and suitably combine them (Cloetens, 1999). Algorithms for quantitatively phase retrieval may be based on the Fresnel approximation of the Kirchoff diffraction formula (Op de Beeck, Dyck *et al.*, 1996) or on the transport-of-intensity equation (Gyreyev, Raven *et al.*, 1999). For certain types of objects, good results can however obtained through simple filtering and summation of the images (Cloetens, 1999).

▪ **X-ray source and detector influence on the propagation phase contrast signal**

– Particular requirements in terms of source size and beam monochromaticity are needed when performing phase contrast imaging (more details in Paragraph 3.6); this is one of the most important reasons why this technique emerged only recently with the advent of third generation synchrotron.

In particular**, the X-ray beam has to be (partially) laterally coherent and quasi-monochromatic**. The first condition, linked to the angular source size, is the more stringent in the case of the PBI technique and it is easily fulfilled by using synchrotron sources or microfocus X-ray tubes with source size of the order of 10 to 20 μm. With a classical laboratory X-ray source, the effect of the finite size of the source consists in the blurring of the interference patter. The degree of monochromaticity of the beam is instead less important as proven by Wilkins *et al.* who obtained PBI images even with a polychromatic spectrum generated by a conventional micro-focus X-ray tube (Wilkins, Gureyev *et al.*, 1996).

– The visualization of the PB signal has strong requirements in terms of detector spatial resolution. If I_p is the signal obtained with a point-like source, the recorded signal I_{det} can be written as the following convolution (Born and Wolf, 1999):

$$I_{\mathrm{det}}(x,y) = I_p(x,y) * h(x,y) * PSF(x,y) \tag{2.12}$$

where (*x*,y) is a point on the two dimensional detector plane, *h* a function expressing the projection of the angular source size $\alpha = S/L$ (*S* and *L* are the lateral source size and the source-to-sample distance respectively) scaled by the ratio d/L, and *PSF* is the Point Spread Function of the detector. The effect of this convolution chain is that of a low-pass filter removing the high frequencies of the interference image.

For untreated images and in edge-detection conditions, **the resolution is limited by the fringe spacing** to about $\sqrt{\lambda D}$, that corresponds to the radius of the first Fresnel zone (Born and Wolf, 1999).

The resolution in the PBI technique is also linked to **the image processing** and to the **sample thickness** (*t*). The latter contributes with a blurring equal to $\sqrt{\lambda t}$, that is 0.2 μm for a 1 mm sample and a λ of 0.5 Å, therefore this effect could be usually neglected since smaller than the pixel size (Cloetens, 1999).

In order to observe the interference fringes, a detector with a suitable spatial resolution is required. For instance, for a sample-to-detector distance of 5 m and a λ of 0.5 Å at least a resolution of ~16 μm is necessary. This fact determines an important drawback in consideration of possible clinical applications since the smaller the pixel size the higher is the dose required for achieving a given signal to noise ratio (defined in Chapter 6).

A more rigorous treatment of the formation of the propagation-based signal will be presented in Paragraph 2.4.

2.3.3 Analyzer-based imaging

This phase contrast imaging technique is based on the use of an analyser crystal placed between the sample and the imaging detector. As a highly collimated monochromatic beam traverses the sample, photons are deviated according to the gradient of the real part of the refractive index (Eq. (2.11). The analyser crystal acts as an angular filter, selectively accepting or rejecting such photons: only a narrow range of X-rays, those satisfying the Bragg law for the diffraction ($2d\sin\theta=\lambda$, where d is the crystal d-spacing, θ is the grazing angle of incidence to the crystal and λ the radiation wavelength), can reach the detector and then contribute to the image formation (Podurets, Somenkov et al., 1989; Bravin, 2003). The monochromator and analyzer form a non-dispersive pair of crystals, where the reflecting planes are parallel.. The filter function is given by the *rocking curve* (RC) (which actually corresponds to the convolution of the monochromator and analyzer reflectivity curves) of the crystal and typically features an acceptance window (given by the RC full-width at half maximum *FWHM*) of a few microradians or tens of microradians. As an example, the *FWHM* for the reflection 111 of the silicon spans the range 17.6–4.3μrad for the energy interval 15–60 keV (XOP[1]:). The crystal, placed between the sample and the detector, can be set either in Bragg (Förster, Goetz *et al.*, 1980; Somenkov, Tkalich *et al.*, 1991; Chapman, Thomlinson *et al.*, 1996; Bushuev, Beliaevskaya *et al.*, 1997) or Laue (Ingal et al., 1995) geometry (see Appendix 1).

The implementation of this technique was firstly reported by Förster (Förster, Goetz *et al.*, 1980) for measuring with micrometric precision the wall thickness of spherical plastic targets for laser nuclear fusion. Different authors have presented slightly varying versions of the same imaging modality by attributing it different names as well, as summarized in Table 2.1.

Refraction contrast radiography....................	(Förster, Goetz *et al.*, 1980)
Phase Dispersion Introscopy.........................	(Ingal and Beliaevskaya, 1997)
Diffraction Imaging.....................................	(Davis, 1996) (Bravin, 2003)
Phase contrast Imaging................................	(Davis, Gao *et al.*, 1995)
Analyzer-based phase contrast......................	(Pagot, Cloetens *et al.*, 2003) (Pavlov, Gureyev *et al.*, 2004) (Coan, Pagot *et al.*, 2005)
Schlieren Imaging..	(Förster, Goetz *et al.*, 1980)

Table 2.1. Different names present in literature for the phase contrast imaging with analyzer crystal.

---

[1] XOP: X-ray Oriented Program, Version 2.0, ESRF, Grenoble, France

The name "*Diffraction Enhanced Imaging*" has been introduced by Chapman *et al.* (Chapman, Thomlinson *et al.*, 1997) to indicate the algorithm for extracting the "refraction" and "apparent absorption" images (Paragraph 2.5) and used later on by other authors for indicating the imaging technique itself.
In this work, it has been chosen to utilize the name "*analyzer-based imaging*" (ABI), since it directly refers to the use of the analyser crystal, regardless the use of specific algorithm in the image processing.

ABI has been applied to X-rays and to neutrons, in the latter case for obtaining images of the magnetic field gradient in the gap of a permanent magnet and the distribution of magnetic domains in a ferrosilicon crystal plate (Podurets, Somenkov *et al.*, 1989). For a given sample, the contrast depends on:

- the rocking curve width of the analyser;
- the crystal composition and quality;
- the X-ray energy;
- the X-ray divergence and the diffraction order.

When all other parameters have been fixed, the contrast depends on the angular position of the analyser crystal with respect to the upstream crystals (monochromators).

The X-rays refracted from the sample deviate from their original direction by a small amount, which is proportional to δ (Eq. (2.5)). As previously shown (Paragraph 2.3.2), these angular deviations are linked to the object phase gradient through the relation (2.11). Conversely to the PBI technique, ABI is sensitive to deflections in only one direction that is the one parallel to the diffraction plane:

$$\Delta\alpha_y \simeq -\frac{\lambda}{2\pi}\frac{\partial\varphi(x,y;\lambda)}{\partial y} \qquad (2.13)$$

If X-rays arrive at the analyser within its angular acceptance they are diffracted with an intensity modulated by the intensity of the rocking curve at that point.
Besides absorption, the contrast formation arises from specific separate mechanisms:

- **the amplitude filtering property of the analyzer crystal**.
  - X-rays coming with angular deviations that are outside the small analyzer acceptance cannot be diffracted and do not contribute to the image formation. These missed scattered X-rays, which are always contributing to the blurring of the details in conventional images, appear in the diffraction images as absorbed X-rays, generating the so-called '**extinction contrast**'. When the analyser is set at the angle corresponding to the peak of the rocking curve, it diffracts the unrefracted X-rays with full efficiency. The images appear almost

  scatter-free, because only the small-angle scattering at angles within the rocking curve width can reach the detector.
  - When the analyser is set at one of the slopes of its rocking curve, the intensity of the X-ray beam diffracted by the analyser is changed by the refraction in the sample, giving rise to the ‘**refraction contrast**’.
  - By moving the analyser far off the Bragg angle, inverse contrast is observed: the analyser rejects the unrefracted X-rays whereas the scattered ones are recorded and contribute to the image formation (Zhong, 2000). This case is very interesting with samples producing a very large amount of small angle scattering (sponge-like tissues, for instance), where a visualization of the details can be achieved (Arfelli, Bonvicini *et al.*, 1999).
- **the phase inverting property of the analyzer crystal.**
  - The phase of the waves with negative spatial frequencies is shifted by 180°. This results in the inverted contrast behaviour observed at opposite angular positions of the analyzer.

An algorithm, called *diffraction enhanced imaging* (DEI) (Chapman, Thomlinson *et al.*, 1997; Zhong, Thomlinson *et al.*, 2000), has been proposed to separate refraction from apparent absorption (i.e. absorption and extinction) but neglects some effects owing to ultra-small-angle scattering.

New mathematical methods for image processing that deal more specifically with ultra-small-angle scattering have been recently introduced by (Oltulu, Zhong *et al.*, 2003; Pagot, Cloetens *et al.*, 2003; Rigon, Besch *et al.*, 2003; Wernick, Wirjadi *et al.*, 2003). Other procedures have instead been proposed for quantitatively computing mass-density maps from refraction-angle images (Hasnah, Parham *et al.*, 2005; Wernick, Yang *et al.*, 2006)

Nevertheless, for several kinds of applications, the exploitation of simply ABI images recorded at different angular positions of the analyzer may provide qualitative important information.

In general, the image formation can be described using either geometrical or wave optics. In geometrical optics, ray tracing of the radiation from the source to the detector can be performed by calculating, point by point, the refraction angle in the sample and by weighting the intensity of the refracted X-rays by the rocking curve of the analyser crystal calculated at the point $\theta + \delta\theta$, where θ is the analyser angular position and $\delta\theta$ is the refraction angle.

For simple objects this approach gives results that are generally in good agreement with the experimental data (Keyriläinen, Fernández *et al.*, 2002; Rigon, Zhong *et al.*, 2002). The wave optical approach provides more precise results because less stringent assumptions have to be considered (Bushuev, Beliaevskaya *et al.*, 1997). The use of the Takagi–Taupin equations to compute the intensity of the electric field outgoing a crystal is necessary for perfect and flat or cylindrically bent crystals; in these cases the equations even have analytical solutions (Authier, 2001). Gureyev *et al.* (Gureyev and Wilkins, 1997) have identified the general limits of utilization of the two approaches by differentiating the case of an area contrast (the contrast far from edges, where weak phase variation occurs) and of the edge contrast.

▪ **X-ray beam and resolution requirements**

– **X-rays** incident on the sample must be monochromatic with a typical $\Delta E/E$ of perfect crystal (~ 10^{-4}). The divergence in the diffraction plane has to be smaller than the angular deviations to be detected. Anyway, no particular restrictions have to be fulfilled by the beam arriving on the monochromator since the ABI set-up itself generally warrants the necessary beam collimation and coherence (see Paragraph 3.6). The advantage of the synchrotron radiation for the implementation of this technique mainly resides in the delivered high photon flux given the unavoidable loss of photons occurring in the monochromator/analyzer diffraction process.

– **The spatial resolution of the technique is intrinsically affected by the presence of the analyzer crystal**. In the geometrical-optics description, a point of the image (P', with reference to Figure 2.6) corresponds to an angularly deviated X-ray from a given point (P) of the projected object. In reality, when diffraction effects occur, either in a perfect or an imperfect crystal, the notion of wavefields which have definite propagation direction in the direct space (and which are represented by a tiepoint in reciprocal space) breaks down (Authier, 2001). Under the effect of an external field (incident X-rays), a perturbed electron density is developed in the crystal and it is the propagation of this perturbation that is associated with the electromagnetic wave in the crystal. In this dynamical approach, the relationship between the value of the amplitude and phase distribution at any point of the exit surface of the crystal is obtained by convolution of the Green-Riemann function (or *influence* function) with the amplitude and phase distribution on the entrance surface, expressed as a distribution of point sources (Pinsker, 1978; Förster, Goetz *et al.*, 1980; Authier, 2001). If the dynamical diffraction fringes are not disentangled, the resolution is limited to the width of the influence function, whose value (of the order of some microns) depends on the reflection geometry (Laue or Bragg geometry) and on the used photon energy.

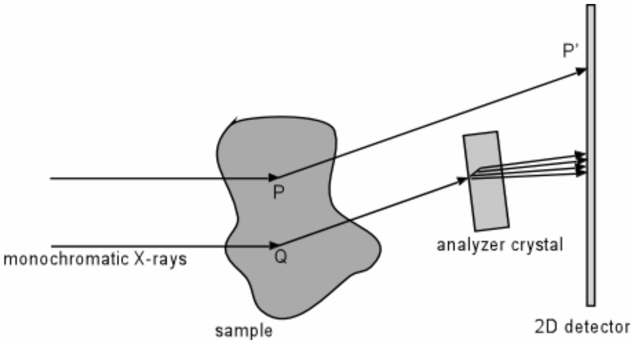

Figure 2.6. Effect of the diffraction from an analyzer crystal in Laue geometry (more details in the text).

Therefore an X-ray deviated at a generic point Q (Figure 2.6) in the object does not correspond any more to a unique point in the detector plane, but to a certain X-rays distribution.

– The effect of the finite resolution of the **detector** and of the finite size of the source can be considered by convoluting the signal with the point spread function of the detector and with the source distribution function as previously discussed (Eq. (2.12)). Moreover, image magnification is achievable in the diffraction plane by utilizing asymmetric crystals.

– **Fresnel diffraction occurring in the path between the sample and the detector** affects the spatial resolution of ABI images. In general, it is preferable to reduce as much as possible the analyzer-to-detector distance. **On the other hand, this typically undesirable effect has been demonstrated to be able to produce a signal to noise improvement in specific experimental conditions** (Coan, Pagot *et al.*, 2005). The experimental evidence of the possible advantages deriving from the combination of the propagation and diffraction from a crystal effects on the signal has been performed as part of this Thesis work (Chapter 6). Theoretical investigations on this subject have been realized by Pavlov *et al.* (Pavlov, Gureyev *et al.*, 2004) and (Bravin, Mocella *et al.*).

▪ ABI sensitivity and optics

The sensitivity of the ABI technique is strictly linked to the width of the analyzer rocking curve: the narrower the curve width the higher the extinction and refraction contrast.

As previously discussed, phase sensitive techniques are better suited to higher energies than conventional absorption X-ray imaging since the weaker energy dependence of the δ ($1/E^2$) term with respect to β ($1/E^4$). Among the others, the ABI technique particularly benefits from high energies since the rocking curve width for a given crystal reflection decreases linearly with increasing energy, and this partially compensates for the $1/E^2$ phase effect behaviour (Rigon, Zhong *et al.*, 2002; Bravin, 2003). Overall, ABI effectiveness is proportional to $1/E$.

– The fact that ABI sensitivity is inversely proportional to the rocking curve width encourages the quest for narrow rocking curves. The latter can be achieved utilizing **different crystal reflections** (Chapman, Thomlinson *et al.*, 1997; Zhong, Thomlinson *et al.*, 2000; Rigon, Zhong *et al.*, 2002). For instance, the use of the (333) reflection at 20 keV produces a rocking curve, which is about five times narrower that the one of the (111) reflection (Appendix 3). Therefore, the associated improvement in refraction contrast can be 5-fold.

– Recently, Protopopov *et al.* (Protopopov, Sobota *et al.*, 2002) proposed a special kind of **multilayer mirror** to analyse the refracted X-ray beam (technique referred as "dark field" imaging). For a given energy, the reflectivity curve of this multilayer has a resonant dip that is few microradians wide. If the multilayer is used as the analyser, it shows a minimum reflectivity for an unrefracted X-ray beam and, therefore, it acts as a perfect crystal with an ‘inverse’ rocking curve. The advantage of this set-up consists in the rejection of the direct beam, with only the pure refraction information being kept. At this stage of development, the width of the resonance is strongly energy dependent and therefore mirrors have to be adapted for single energy utilization; new developments on the mirror quality have been announced.

A different version of dark filed imaging was proposed by Ando *et al.* (Ando, Sugiyama *et al.*, 2001). The set-up in this case consisted in an asymmetric monochromator, a monolithic optics comprising a collimator and an analyzer, with the sample in between. The analyzer only accepts the angles containing the refraction information while eliminating the transmitted component by not reacting with it.

– Other optics implementations regard the use of **asymmetric crystals** as analyzer whose main advantages resides in the possibility of expanding in the diffraction plane and incident X-ray laminar beam. For small samples, this set-up does not require the simultaneous translation of sample and detector, which typically introduces blurring artefacts.

▪ **Comparison with other phase contrast techniques**

– The ABI experimental set-up is simplified with respect to interferometry and requirements on its stability are less stringent (angular stability should be about 0.2 μrad (Ingal and Beliaevskaya, 1996)). The monochromator and the analyzer are not parts of a monolith, and consequently more space is available for the sample and its environment. Nevertheless, the easiest set-up remains that of the propagation-based technique.

– As already mentioned, the ABI modality is sensitive only to phase variations along the diffraction direction while PBI is sensitive in both x and y directions.

– Moreover, as afterwards derived (in the theoretical description in Paragraph 2.4), the PBI requiresthat the second derivative of the phase shift is non-zero, while for the ABI techniques a non-zero gradient is sufficient.

2.4 Theoretical description of phase contrast formation

In this paragraph, the theoretical description of the propagation-based imaging and the analyzer-based imaging technique is presented in the elegant treatment developed by J.P Guigay (Guigay, Pagot *et al.*), under the approximation of an object with weak phase and amplitude modulations. In this approach, a unified formal description is used for both the techniques in terms of a wave propagator. The propagator forms specific for the two imaging modalities are independently derived.

The objective of this presentation is to show the different dependence of the PBI and ABI techniques on the phase shifts determined by the object and on the experimental parameters (X-ray wavelength, sample-to-detector distance etc.).

Let us consider a **monochromatic wave** which propagates along the z axis, $u_{inc}(x,y,z) = M(x,y)e^{2i\pi z/\lambda}$ (where M is the wave amplitude and λ the wavelength), and passing through a sample. If u_{trans} is the wave after the object, onto a plane perpendicular to the propagation direction one has (Born and Wolf, 1999):

$$u_{trans}(x,y) = T(x,y)u_{inc}(x,y,0) \tag{2.14}$$

$T(x,y)$ is the so-called **transmission function** of the object which depends on the projection of the refractive index of the sample. $T(x,y)$ is a complex function, since both the amplitude, $A(x,y)$, and the phase, $\varphi(x,y)$, of the wave may be altered on passing through the object. Its general expression is:

$$T(x,y) = A(x,y)e^{i\varphi(x,y)} \tag{2.15}$$

with

$$A(x,y) = e^{-B(x,y)} \quad \text{with} \quad B(x,y) = \frac{2\pi}{\lambda}\int \beta(x,y,z)\,dz = \frac{1}{2}\int \mu(x,y,z)\,dz \tag{2.16}$$

$$\varphi(x,y) = \frac{2\pi}{\lambda}\int \left[1-\delta(x,y,z)\right]dz = \varphi_0 - \frac{2\pi}{\lambda}\int \delta(x,y,z)\,dz \tag{2.17}$$

φ_0 is the phase modulation that would occur in the absence of the object and it is a non-relevant constant for a differential phase method. The integrations are performed along the propagation direction z over the maximum thickness t of the object.

In the case of a non-point like source and a detector with a finite resolution, the convolution of the signal with the source size and the detector point spread function (*PSF*) is necessary. For sake of simplicity, in the following description, the effect of the partial coherence of the radiation and of the detector spatial resolution will be neglected.

With P we indicate the wave propagator associated to the specific technique (PBI or ABI). For the moment, let us assume that such a propagator exists, it will be described in details afterwards. The wave recorded on the detector can be formally written in the real space and in the Fourier space respectively as:

$$u_{rec}(x,y) = u_{trans}(x,y) * P(x,y) \tag{2.18}$$

$$\tilde{u}_{rec}(f,g) = \tilde{u}_{trans}(f,g)\cdot \tilde{P}(f,g) \tag{2.19}$$

where '*' indicates convolution, $\tilde{u}_{rec}$ and $\tilde{P}$ are the Fourier transforms of u_{rec} and P, respectively, and *f* and *g* are the spatial frequencies associated to *x* and *y*.

Considering the case of a wave vector parallel to the *z*-axis (normal incidence), $u_{inc}(x,y,0)$ is a constant of real value *M* and the equation (2.19) can be then written as:

$$\tilde{u}_{rec}(f,g)=M\tilde{T}(f,g)\cdot\tilde{P}(f,g) \qquad (2.20)$$

In the generic case of an incident wave with non-zero component perpendicular to the *z*-axis, $\left(\frac{2\pi\delta_{0x}}{\lambda},\frac{2\pi\delta_{0y}}{\lambda}\right)$, the incident wave becomes $u_{inc}(x,y)=M(x,y)e^{2i\pi(k_{0x}x+k_{0y}y)}$ with $\mathbf{k}_0=(k_{0x},k_{0y})=\frac{1}{\lambda}(\delta_{0x},\delta_{0y})$ (case used for describing the change in angle of incidence with respect to the analyzer crystal in the ABI treatment).

For the sake of simplicity, the following notation is used: $\mathbf{x}=(x,y)$ and $\mathbf{f}=(f,g)$. The wave function after the sample in the real space and its Fourier transformation in the Fourier space are respectively: $u_{trans}(\mathbf{x})=MT(\mathbf{x})e^{i2\pi\mathbf{k}_0\mathbf{x}}$ and $\tilde{u}_{trans}(\mathbf{f})=M\tilde{T}(\mathbf{f}-\mathbf{k}_0)$.

The recorded wave intensity is given by $I_{rec}(x)=|u_{rec}|^2$ and its Fourier transformation by:

$$\tilde{I}_{rec}(\mathbf{f})=\int_{-\infty}^{+\infty}e^{i2\pi\mathbf{xf}}\left[u_{rec}\right]\cdot\left[u_{rec}^*\right]d\mathbf{x} \qquad (2.21)$$

where '*' denotes the complex conjugate. If **n** and **m** are a couple of two coordinates in the reciprocal space, then

$$\tilde{I}_{rec}(\mathbf{f})=\int_{-\infty}^{+\infty}e^{i2\pi\mathbf{xf}}d\mathbf{x}\int_{-\infty}^{+\infty}e^{i2\pi\mathbf{xm}}\tilde{u}_{rec}(\mathbf{m})d\mathbf{m}\int_{-\infty}^{+\infty}e^{-i2\pi\mathbf{xn}}\tilde{u}_{rec}^*(\mathbf{n})d\mathbf{n} \qquad (2.22)$$

Let us call $i_0=M^2$, the integration on **x** gives the Dirac function $\delta(-\mathbf{f}+\mathbf{m}-\mathbf{n})$ and one has:

$$\tilde{I}_{rec}(\mathbf{f})=i_0\int_{-\infty}^{+\infty}\tilde{P}(\mathbf{m})\tilde{T}(\mathbf{m}-\mathbf{k}_0)\tilde{P}^*(\mathbf{m}-\mathbf{f})\tilde{T}^*(\mathbf{m}-\mathbf{f}-\mathbf{k}_0)d\mathbf{m} \qquad (2.23)$$

In order to simplify this expression, the **approximation of weak phase and amplitude modulations** is assumed allowing for the following linearization

$$T(\mathbf{x})\simeq 1+i\varphi(\mathbf{x})-B(\mathbf{x}) \qquad (2.24)$$

With this assumption, the object transmission function in the Fourier space and its complex conjugate can be written as:

$$\begin{aligned}\tilde{T}(\mathbf{m})&=\int e^{-i2\pi\mathbf{xm}}\left(1+i\varphi(\mathbf{x})-B(\mathbf{x})\right)d\mathbf{x}=\delta(\mathbf{m})+i\tilde{\varphi}(\mathbf{m})-\tilde{B}(\mathbf{m})\\ \tilde{T}^*(\mathbf{m})&=\int e^{i2\pi\mathbf{xm}}\left(1-i\varphi(\mathbf{x})+B(\mathbf{x})\right)d\mathbf{x}=\delta(\mathbf{m})-i\tilde{\varphi}(-\mathbf{m})-\tilde{B}(-\mathbf{m})\end{aligned} \qquad (2.25)$$

By replacing the equations (2.25) in (2.23), the calculation of the integral gives, neglecting the second order terms:

$$\tilde{I}_{rec}(\mathbf{f}) = i_0 \left\{ \begin{array}{r} \delta(\mathbf{f}) \left| \tilde{P}(\mathbf{k}_0) \right|^2 + i\tilde{\varphi}(\mathbf{f}) \left[\tilde{P}^*(\mathbf{k}_0) \tilde{P}(\mathbf{k}_0 + \mathbf{f}) - \tilde{P}(\mathbf{k}_0) \tilde{P}^*(\mathbf{k}_0 - \mathbf{f}) \right] \\ - \tilde{B}(\mathbf{f}) \left[\tilde{P}^*(\mathbf{k}_0) \tilde{P}(\mathbf{k}_0 + \mathbf{f}) + \tilde{P}(\mathbf{k}_0) \tilde{P}^*(\mathbf{k}_0 - \mathbf{f}) \right] \end{array} \right\} \tag{2.26}$$

Assuming the approximation of weak phase and amplitudes modulations, one obtains a linear relationship between the spectrum of intensity of the recorded wave and the spectra of the phase and amplitude. This means that a given frequency component of the intensity is only determined by the same frequency component of the phase and amplitude modulations.

2.4.1 Propagation-based imaging

The theoretical framework for the PBI description is the Fresnel diffraction where the propagation of the wave over a certain distance *D* is expressed using the approximation of the Fresnel-Kirchhoff integral (Born and Wolf, 1999). In this context, the PBI propagator, P_D, is given by:

$$P_D(x, y) = \frac{1}{i\lambda D} \exp\left[i\pi \frac{x^2 + y^2}{\lambda D} \right] \tag{2.27}$$

and in the Fourier space:

$$\tilde{P}_D(f, g) = \exp\left[-i\pi\lambda D \left(f^2 + g^2 \right) \right] \tag{2.28}$$

Replacing this last expression in equation (2.26) and knowing that $\mathbf{k_0}$ is zero in the case of PB imaging, the intensity spectrum at distance *D* from the sample becomes:

$$\tilde{I}_D(f, g) = i_0 \left\{ \delta(f, g) + 2\sin\left[\pi\lambda D \left(f^2 + g^2 \right) \right] \tilde{\varphi}(f, g) - 2\cos\left[\pi\lambda D \left(f^2 + g^2 \right) \right] \tilde{B}(f, g) \right\} \tag{2.29}$$

This equation is valid if $\varphi(x + \lambda D f, y + \lambda D g) - \varphi(x, y) << 1$ (Guigay, 1977), which is a less restrictive condition than the weak phase approximation, and for $B(x, y) << 1$.

The two terms, containing the sine and cosine, are the contrast factors and they express the dependence of an image acquired at the propagation distance *D* on a given frequency component of the phase and amplitude, respectively. The behaviour of these two contrast factors as function of the normalized spatial frequency $\sqrt{\lambda D (f^2 + g^2)}$ and at a certain distance *D* is presented in Figure 2.7.

For a given frequency, at distances $D_p = p \big/ \left(\lambda (f^2 + g^2) \right)$ (with *p* integer) and $D_p = (2p + 1) \big/ \left(2\lambda (f^2 + g^2) \right)$ (with $p \neq 0$), the minima (maxima) and maxima (minima) of the phase (amplitude) contrast factor occur. At zero frequency, no information is available.

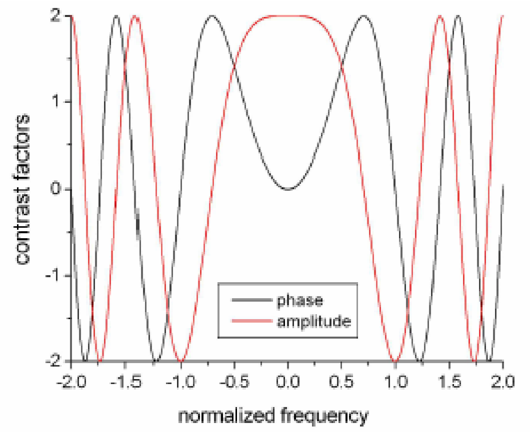

Figure 2.7. Contrast factors for the phase and amplitude modulations as a function of the normalized spatial frequency $\sqrt{\lambda D(f^2+g^2)}$. Simulation for 1 µm pixel size, an energy of 25 keV, and a sample to detector distance D = 8.8 m (Pagot, 2004).

Moreover, around the zeros of the contrast factors, only little information is given in the image for reconstruction of certain spatial frequencies. For this reason, a set of images taken at different distances has to be acquired for getting complete information on the object.

If $\pi\lambda D(f^2+g^2) << 1$, corresponding, for instance, to **weak defocusing conditions**, equation (2.29) becomes:

$$\tilde{I}_D(f,g) \approx i_0\left\{\delta(f,g)+2\tilde{\varphi}(f,g)\left[\pi\lambda D\left(f^2+g^2\right)\right]-2\tilde{B}(f,g)\right\} \tag{2.30}$$

$i_0\left(\delta(f,g)-2\tilde{B}(f,g)\right)$ can be considered as $\tilde{I}(f,g)$ that is the Fourier transformation of the intensity distribution $I_0(x,y) \approx i_0\left(1-2B(x,y)\right)$ at $D=0$. By using equations (2.16) and (2.14), it is possible to obtain: $I_0(x,y) = \left|A(x,y)\right|^2 = i_0 e^{-2B(x,y)} \approx i_0\left(1-2B(x,y)\right)$ and equation (2.30) can be approximated to:

$$\tilde{I}_D(f,g) \approx \tilde{I}_0(f,g) + 2i_0\left[\pi\lambda D(f^2+g^2)\right]\tilde{\varphi}(f,g) \tag{2.31}$$

and in the real space:

$$I_D(x,y) \approx I_0(x,y) + 2i_0\pi\lambda D\int\int_{-\infty}^{+\infty}\tilde{\varphi}(f,g)(f^2+g^2)e^{2i\pi(fx+gy)}df\,dg \tag{2.32}$$

For the phase and its 2D Laplacian, one has

$$\varphi(x,y) = \int\int_{-\infty}^{+\infty}\tilde{\varphi}(f,g)e^{2i\pi(fx+gy)}df\,dg \tag{2.33}$$

$$\Delta_{xy}\varphi(x,y) = \int\int_{-\infty}^{+\infty}\left[-4\pi^2(f^2+g^2)\right]\tilde{\varphi}(f,g)e^{2i\pi(fx+gy)}df\,dg \tag{2.34}$$

Therefore, the intensity at distance *D* depends on the laplacian of the phase through the equation:

$$I_D(x,y) \approx I_0(x,y) - i_0\frac{\lambda D}{2\pi}\Delta_{xy}\varphi(x,y) \tag{2.35}$$

This simple result gives the intensity distribution under the weak defocusing condition.

2.4.2 Analyzer-based imaging

The theoretical description of the ABI technique is based on the dynamical diffraction theory from perfect crystals (Zachariasen, 1945; Authier, 2001). In following description, the case of a thick non-absorbing crystal set in **symmetrical Bragg geometry** is considered and any propagation effect is neglected.

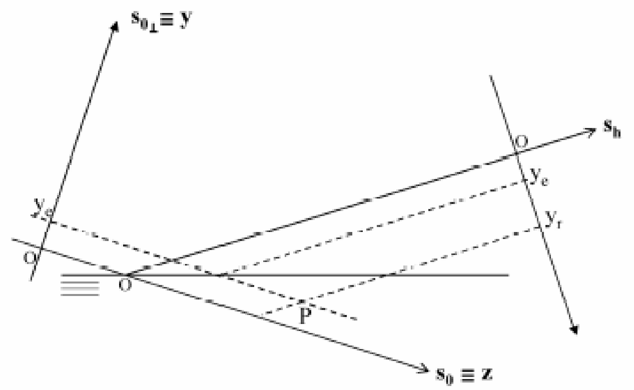

Figure 2.8. Reference system used in the ABI theoretical description here presented. s0 is the coordinate parallel to the incident beam and sh the coordinate parallel to the diffracted beam.

The oblique coordinates system (s_0, s_h), represented in Figure 2.8, will be used: s_0 is the coordinate parallel to z (incident beam direction) and s_h the coordinate parallel to the diffracted beam.

The action of the analyzer crystal is expressed by the one-dimensional Takagi propagator:

$$P_T(y) = i\frac{J_1(ay)}{y}H(y) \tag{2.36}$$

where J_1 is the first order Bessel function, H is the Heaviside function, $a = \omega_D \pi / \lambda = 2\pi|\chi_h| / (\lambda \sin 2\theta_B)$, θ_B is the Bragg angle, and χ_h is the crystal susceptibility. In the Fourier space, the propagator can be expressed as:

$$\tilde{P}_T(g) = ia\int_0^\infty e^{-2i\pi gy}\frac{J_1(ay)}{ay}dy \tag{2.37}$$

By introducing $b = \frac{2\pi}{a} = \frac{2\lambda}{\omega_D}$, $\tilde{P}_T(g)$ can be written as:

$$\tilde{P}_T(g) = \sqrt{\frac{\chi_h}{\chi_{-h}}}\left[bg + i\,\mathrm{sgn}(1+bg)\sqrt{1-(bg)^2}\right] \tag{2.38}$$

Two cases can be distinguished:

- for $|g| < \dfrac{1}{b}$ $$\tilde{P}_T(g) = \sqrt{\frac{\chi_h}{\chi_{-h}}}\left[bg + i\sqrt{1-(bg)^2}\right] = \sqrt{\frac{\chi_h}{\chi_{-h}}}e^{i\arccos(bg)}$$
- for $|g| > \dfrac{1}{b}$ $$\tilde{P}_T(g) = \sqrt{\frac{\chi_h}{\chi_{-h}}}\left[bg - \operatorname{sgn}(g)\sqrt{(bg)^2-1}\right]$$

The square modulus of $\tilde{P}_T(g)$ gives the theoretical reflectivity of the crystal $R(\theta)$: $R(\theta) = \left|\tilde{P}_T(g)\right|^2$. In particular, being $g = \theta/\lambda$, one has:

$$R(\theta) = \left|\frac{\chi_h}{\chi_{-h}}\right|\begin{cases} 1 & for\,|g| \le \dfrac{1}{b} \\ \left(bg - \operatorname{sgn}(g)\sqrt{(bg)^2-1}\right)^2 & for\,|g| > \dfrac{1}{b} \end{cases} \tag{2.39}$$

The Takagi propagator P_T depends only on the *y* coordinate (diffraction in the vertical plane), therefore the intensity of the spectrum $\tilde{I}_{out}$ is the Fourier transformation of $I_{out}(x,y)$ with respect to *y* only.

In the ABI case, the wave vector is given by $\mathbf{k}_0 = \left(0, \dfrac{\delta\theta}{\lambda}\right)$, where $\delta\theta$ represents the angular deviation of the analyzer from the Bragg angle and by using the equation (2.26), the intensity spectrum exiting from the analyzer crystal can be expresses as:

$$\tilde{I}_{out}(x,g) = i_0\left\{\begin{array}{l} \delta(g)\left|\tilde{P}_T\left(\dfrac{\delta\theta}{\lambda}\right)\right|^2 + i\tilde{\varphi}(x,g)\left[\tilde{P}_T^*\left(\dfrac{\delta\theta}{\lambda}\right)\tilde{P}_T\left(\dfrac{\delta\theta}{\lambda}+g\right) - \tilde{P}_T\left(\dfrac{\delta\theta}{\lambda}\right)\tilde{P}_T^*\left(\dfrac{\delta\theta}{\lambda}-g\right)\right] \\ \qquad - \tilde{B}(x,g)\left[\tilde{P}_T^*\left(\dfrac{\delta\theta}{\lambda}\right)\tilde{P}_T\left(\dfrac{\delta\theta}{\lambda}+g\right) + \tilde{P}_T\left(\dfrac{\delta\theta}{\lambda}\right)\tilde{P}_T^*\left(\dfrac{\delta\theta}{\lambda}-g\right)\right] \end{array}\right\} \tag{2.40}$$

Considering the case of **very low frequencies**, it is possible to write:

$$\tilde{P}_T\left(\frac{\delta\theta}{\lambda}+g\right) \approx \tilde{P}_T\left(\frac{\delta\theta}{\lambda}\right) + g\tilde{P}_T^{'}\left(\frac{\delta\theta}{\lambda}\right) \tag{2.41}$$

with $\tilde{P}_T^{'}$ derivate of $\tilde{P}_T$ with respect to *g*.

In order to simplify equation (2.40), let us write $\tilde{P}_T = |\tilde{p}|e^{i\phi}$, as a complex number with an amplitude term and a phase term and consider the following relations:

$$\tilde{P}_T^* \cdot \tilde{P}_T^{'} + \tilde{P}_T\tilde{P}_T^{*'} = \frac{d}{dg}\left(\left|\tilde{P}_T\left(\frac{\delta\theta}{\lambda}\right)\right|^2\right) = \frac{d}{d\theta}R(\delta\theta)\cdot\frac{d\theta}{dg} = \lambda\frac{d}{d\theta}R(\delta\theta) \tag{2.42}$$

$$\tilde{P}_T^* \cdot \tilde{P}_T^{'} - \tilde{P}_T \cdot \tilde{P}_T^{*'} = \left(\tilde{P}_T^*\right)^2 \cdot \left(\frac{\tilde{P}_T}{\tilde{P}_T^*}\right)^{'} = \left(\tilde{P}_T^*\right)^2 \cdot \left(e^{2i\phi}2i\phi^{'}\right) = \left(\tilde{P}_T^*\right)^2 \cdot \frac{\tilde{P}_T}{\tilde{P}_T^*} \cdot 2i\phi^{'} = 2iR\lambda\frac{d\phi}{d\theta} \tag{2.43}$$

By using this equations, the (2.40) becomes:

$$\tilde{I}_{out}(x,g)=i_0R(\delta\theta)\left\{\delta(g)+ig\lambda\frac{\dfrac{d}{d\theta}R(\delta\theta)}{R(\delta\theta)}\tilde{\varphi}(x,g)-2\left(1+ig\lambda\frac{d}{d\theta}\phi(\delta\theta)\right)\tilde{B}(x,g)\right\} \tag{2.44}$$

It can be seen that both contrast factors are complex, in particular the phase one is imaginary. Except the region where $dR(\delta\theta)/d\theta=0$ (the central flat-shaped part of the reflectivity curve), the phase contrast results to be proportional to the first derivative of the reflectivity with respect to θ, at the point $\delta\theta$. If g=0, the absorption contrast term is equal to -2, while, for $g\neq 0$ it depends by the derivative of the Takagi propagator phase term ϕ at $\delta\theta$.

It has to be pointed out that the lowest-order term with respect to *g* is of first order instead of second for the PBI case. Therefore, it is expected that the ABI technique is more sensitive to low spatial frequencies than the PBI technique.

Since $\tilde{I}_0(x,g)\simeq i_0\left(\delta(g)-2\tilde{B}(x,g)\right)$, as in the PBI case, equation (2.44) can be written as:

$$\tilde{I}_{out}(x,g)=\tilde{I}_0(x,g)R(\delta\theta)+ig\lambda\left\{\frac{d}{d\theta}R(\delta\theta)\tilde{\varphi}(x,g)-2R(\delta\theta)\frac{d}{d\theta}\phi(\delta\theta)\tilde{B}(x,g)\right\} \tag{2.45}$$

Transforming in the real space, one has:

$$I_{out}(x,y)=I_0(x,y)R(\delta\theta)+i\lambda\left\{\frac{d}{d\theta}R(\delta\theta)\int_{-\infty}^{+\infty}g\tilde{\varphi}(x,g)e^{2i\pi gy}dg-2R(\delta\theta)\frac{d\phi}{d\theta}\int_{-\infty}^{+\infty}g\tilde{B}(x,g)e^{2i\pi gy}dg\right\} \tag{2.46}$$

It is possible to simplify this equation by writing:

$$\nabla_y\varphi(x,y)=2i\pi\int_{-\infty}^{+\infty}g\tilde{\varphi}(x,g)e^{2i\pi gy}dg \tag{2.47}$$

$$\nabla_yB(x,y)=2i\pi\int_{-\infty}^{+\infty}g\tilde{B}(x,g)e^{2i\pi gy}dg \tag{2.48}$$

with $'\nabla_y'$ the gradient over y.

Therefore, the relation between the intensity of the wave exiting from the analyzer and the gradient of the phase can expressed as:

$$I_{out}(x,y)=I_0(x,y)R(\delta\theta)+\frac{i_0\lambda}{2\pi}\left[\frac{d}{d\theta}R(\delta\theta)\cdot\nabla_y\varphi(x,y)-2R(\delta\theta)\frac{d}{d\theta}\phi(\delta\theta)\cdot\nabla_yB(x,y)\right] \tag{2.49}$$

If the approximation $I_0(x,y)\approx i_0\left(1-2B(x,y)\right)$ is used, the cross terms are eliminated and the approximation of slowly varying amplitude is assumed (that means to eliminate the term proportional to $I_0(x,y)\nabla_yB(x,y)$) then, one gets:

$$I_{out}(x,y)=I_0(x,y)\left[R(\delta\theta)+\frac{\lambda}{2\pi}\frac{d}{d\theta}R(\delta\theta)\cdot\nabla\varphi(x,y)\right] \tag{2.50}$$

Reminding that $\nabla\varphi(x,y)=2\pi\Delta\theta_y/\lambda$ (equation (2.13)), a similar expression to that one obtained by Chapman with a first Taylor approximation of the reflectivity (paragraph 2.5) can be derived:

$$I_{out}(x,y)=I_0(x,y)\left[R(\delta\theta)+\frac{d}{d\theta}R(\delta\theta)\cdot\Delta\theta_y(x,y)\right] \tag{2.51}$$

The difference between equation (2.49), obtained without the approximation of slowly varying amplitude) and the Chapman one (equation (2.51)) consists essentially in the additional term related to the phase of the propagator P_T and the difference between i_0 and I_0, as the weak amplitude object approximation has been assumed.

- **Further remarks**

A comparison of the different behaviours of the phase and amplitude contrast factors for the PBI (equation (2.29)) and the ABI (equation (2.40)) techniques, as function of the normalized frequency $\sqrt{\lambda D f}$, is shown in Figure 2.9. The contrast factors were simulated for a 7.46 μm pixel size detector, for a Si (111) analyzer crystal with an angular deviation corresponding to $\omega_D/2$ $(\eta=1)$ (see Appendix 1) in the ABI case, and for a sample-to-detector distance of 8.8 m for the PBI case.

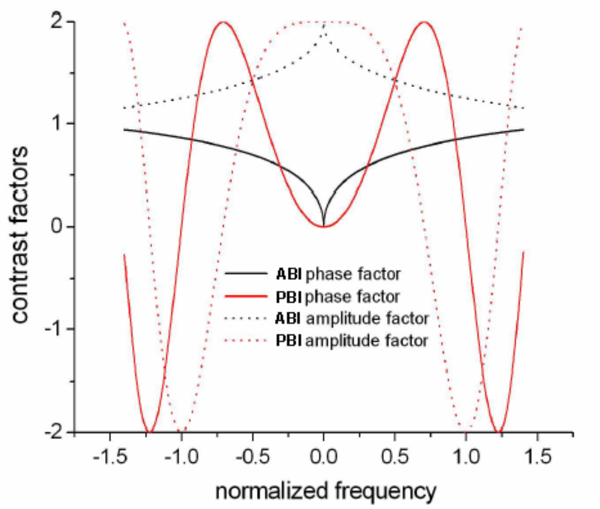

Figure 2.9. Phase and amplitude contrast factors for both PBI and ABI techniques as a function of the normalized frequency $\sqrt{\lambda D f}$ (Pagot, 2004). The parameters of the simulation are: 7.46 μm pixel size, an energy of 25 keV, the 111 reflection and η = 1 in the ABI case and a sample to detector distance of 8.8 m in the PBI case.

2.5 The Diffraction Enhanced Imaging (DEI) algorithm

As extensively discussed in the previous paragraphs, the contrast on ABI images originates not only from absorption but from the refraction and diffraction properties of the sample as well. Considering the scale of rocking curve widths, the X-rays involved in the image contrast formation are those refracted by macroscopic features and determining the average deviation, and those affected by the ultra small angle scattering (USAXS) produced by very small and unresolved structures and broadening the rocking curve.

In first approximation, small-angle scattered X-rays (SAXS) are rejected since, in the range of hard X-rays, they are deviated at angles of the order of milliradians which are larger than the microradians range of the rocking curve widths. Therefore, these photons will be neglected in the following discussion (Chapman, Thomlinson *et al.*, 1997).

This is the approximation behind the DEI algorithm proposed by Chapman *et al.* (Chapman, Thomlinson *et al.*, 1997) for extracting quantitative information in ABI. It has to be underlined that this algorithm fails in case of samples producing large amount of SAXS and for this reason new and more accurate algorithms have been proposed and tested (Wernick, Wirjadi *et al.*, 2002; Pagot, Cloetens *et al.*, 2003), also in developed as part of this Thesis work. Nevertheless, for historical reasons, I will here describe the DEI algorithm in detail.

The DEI algorithm is based on recording two images on both sides of the rocking curve at $\pm FWHM/2$ and suitably combining them for obtaining two new images mapping the "refraction" and the "apparent absorption" of the sample.

Let I_R be the intensity of the transmitted beam from the sample, $\Delta\theta(x,y)$ the angle at which the incident photons are refracted in the vertical plane (*x*,*y*) and let $\delta\theta$ be the angular deviation of the analyzer with respect to the incident direction, that is with respect to the Bragg angle θ_B. The intensity $I(x,y)$ reaching the detector can therefore been expressed as:

$$I(x,y)=I_R(x,y)R\left(\theta_B+\delta\theta+\Delta\theta(x,y)\right) \tag{2.52}$$

where R is the rocking curve of the analyzer and $\theta_B+\delta\theta+\Delta\theta(x,y)$ is the angle between the lattice planes of the analyzer crystal and the direction of the considered photons.

Two images are acquired on the slopes of R, at the angular positions $\theta_L=\theta_B-(\alpha\cdot FWHM)$ and $\theta_H=\theta_B+(\alpha\cdot FWHM)$ with $\alpha\geq 0$ and $FWHM$ of the analyzer rocking curve. In particular, in the Chapman's algorithm, $\alpha=1/2$. Equation (2.52) can be rewritten specifically for these two cases as follows:

$$I_{L,H}(x,y)=I_R(x,y)R\left(\theta_{L,H}+\Delta\theta(x,y)\right) \tag{2.53}$$

By linearly fitting the flanks of R and taking into account that $\Delta\theta(x,y)$ is small compared to $FWHM/2$, the first order Taylor approximation of the rocking curve at the two angular positions $\theta_{L,H}$ gives:

$$I_{L,H}(x,y)=I_R(x,y)\left[R\left(\theta_{L,H}\right)+\frac{dR\left(\theta_{L,H}\right)}{d\theta}\cdot\Delta\theta(x,y)\right] \tag{2.54}$$

The system of equations (2.54) can be solved in the two unknown I_R and $\Delta\theta$:

$$I_R(x,y)=\frac{I_L(x,y)\dfrac{dR(\theta_H)}{d\theta}-I_H(x,y)\dfrac{dR(\theta_L)}{d\theta}}{R(\theta_L)\dfrac{dR(\theta_H)}{d\theta}-R(\theta_H)\dfrac{dR(\theta_L)}{d\theta}} \tag{2.55}$$

$$\Delta\theta(x,y)=\frac{I_H(x,y)R(\theta_L)-I_L(x,y)R(\theta_H)}{I_L(x,y)\dfrac{dR(\theta_H)}{d\theta}-I_H(x,y)\dfrac{dR(\theta_L)}{d\theta}} \tag{2.56}$$

The two last equations are applied pixel-by-pixel to the diffracted images from the high and low angles at the slopes of the analyzer rocking curve.

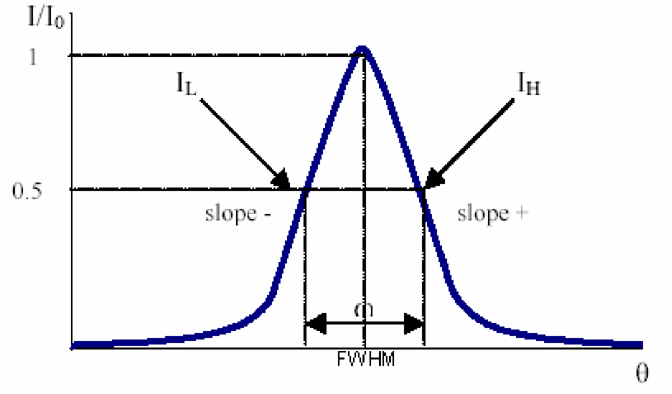

Figure 2.9. Angular positions for acquiring the two ABI images to be used in the DEI algorithm.

The two calculated images are:

- $I_R(x,y)$, the so-called **apparent absorption image**. It features not only the conventional absorption contrast but also an additional extinction contrast (paragraph 2.3.3).
- $\Delta\theta(x,y)$, the **refraction image**. It is a map of the vertical component of the refraction angle of the photons emerging from the sample.

- **Limitations of the DEI algorithm**

The DEI algorithm relies on the hypothesis that the pixel size of the detector is small enough compared to the structure of the object, so that each pixel is focused on a well-defined feature of the sample, where a certain refraction angle is expected.

In the case of objects featuring a fine refractive structure, which is not resolved by the spatial resolution of the detector, the fundamental requirements for the applicability of the DEI algorithm are not fulfilled.

In order to overcome this limitation, Rigon *et al.* (Rigon, Besch *et al.*, 2003) has proposed a new algorithm that takes into account this particular case. Formally, this algorithm closely resembles the classical DEI algorithm, the main difference is the utilization of the images acquired at the top and at the tail of the rocking curve (rather than on the slopes) and the use of the second derivatives of the rocking curve (rather than the first derivatives). In particular, the new algorithm measures the width of the refraction distribution of the photons passing through the object. A new couple of post-processed images are obtained, which can provide quantitative information on the *absorption* and *refraction* characteristics of the sample including structures in the sub-pixel length scale.

2.6 The statistical method

A different approach for quantitatively extracting the information contained in ABI images has been proposed by our group (Pagot, Cloetens *et al.*, 2003). This method allows to separate refraction information from absorption and USAXS and is based on a statistical processing of the ABI images (a similar statistical approach has been introduced by Wernick *et al.* (Wernick, Wirjadi *et al.*, 2002) but it will not discussed here).

This method assumes that locally the angular distribution of the diffracted intensity is the convolution of the object angular spectrum with the monochromator/analyzer system rocking curve (*R*): $I(\theta) = R(\theta) * S(\theta)$, with $S(\theta)$ the angular intensity distribution of the X-rays emerging from the object.

Using a series of *N* images taken along the analyzer rocking curve (RC), the method considers the individual RCs corresponding to each of the pixels of the detector. In this case, two series of images are acquired, one with sample and one without sample, giving, respectively, for each individual pixel, an *object* RC and a *reference* RC (see Figure 2.10).

For each pixel, the algorithm calculates the zero-, first-, and second-order moments:

$$M_i = \sum_{j=1}^{N} \left(\theta_j\right)^i \cdot I\left(\theta_j\right) \qquad \left(i = 0,1,2\right) \tag{2.57}$$

and the maximum of both the object and reference rocking curves. $I\left(\theta_j\right)$ is the intensity recorded in the considered pixel for the angular position θ_j.

In particular, one has that (Frodesen, Skjeggestad *et al.*, 1979):

– the zero$^{\text{th}}$ moment M_0 is equal to the integrated intensity;

– the first moment gives the position of the mass center $\theta_0 = M_1 / M_0$;

– the second order moment gives the standard deviation $s = \left(M_2 / M_0 - \theta_0^2\right)^{1/2}$;

– as maximum, it is considered $m = I\left(\theta_0\right)$

The following four images are therefore derived, whose meaning is, with also reference to Figure 2.10:

1) $I_{abs} = M_{0,obj} / M_{0,ref}$: the *integrated absorption* image (absorption and small angle scattering rejection). It is the ratio of the integrated intensity under the object RC with respect to the reference RC one.
2) $\Delta\theta_0 = \theta_{0,obj} - \theta_{0,ref}$: the *integrated refraction* image (average angular deviation in the plane of refraction). It is the angular displacement of the object RC mass center with respect to the reference RC one.
3) $\sigma = \left(s_{obj}^2 - s_{ref}^2\right)^{1/2}$: the *ultra small angle scattering* image (spread around the average angular deviation). It is the standard deviation of the object RC deconvolved with the standard deviation of the reference RC.
4) $I_m = m_{obj} / m_{ref}$: the *maximum absorption* image. It is the ratio of the maximum intensity of the object RC with respect to the reference RC one.

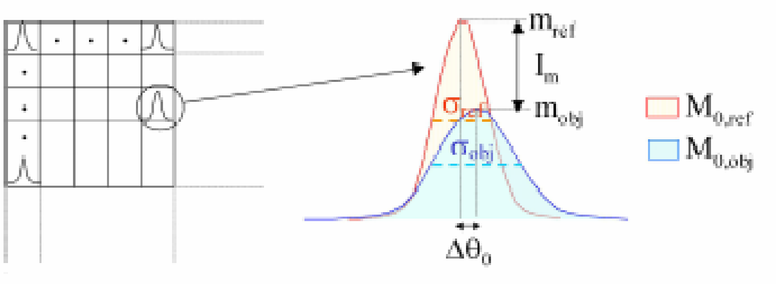

Figure 2.10. In each pixel of the detector, the local RCs with object and without (reference) are recorded. The modifications in height, area, position and width of this curve yield the information intrinsic to the object: the local absorption, refraction and ultra small angle scattering.

The statistical method is well suited for imaging with a 2D radiation field compared to a one-dimensional acquisition geometry (line beam), for which the recording of many points on the RC would be time consuming and prone to errors due to analyzer drifts. By comparing local object and reference RCs, the statistical method is a means to correct inhomogeneities in the image due to deformations of the crystals. Although the accumulated dose when acquiring a long image series could hamper applications in life sciences, good results may be obtained with as few as three images.

REFERENCES

M. Ando and S. Hosoya (1972). Proc. 6th Intern. Conf. on X-ray Optics and Microanalysis. Tokyo, Univ. of Tokyo Press, eds. G. Shinoda, K. Kohra and T. Ichinokawa.

M. Ando, H. Sugiyama, A. Maksimenko, W. Pattanasiriwisawa, K. Hyodo and Z. Xiaowei (2001). "A new optics for Dark-field imaging in X-ray region 'owl'." Jpn. J. Appl. Phys. **40**: L844-L846.

F. Arfelli, V. Bonvicini, A. Bravin, G. Cantatore, E. Castelli, L. Dalla Palma, M. Di Michiel, M. Fabrizioli, R. Longo, R.-H. Menk, A. Olivo, S. Pani, D. Pontoni, P. Poropat, M. Prest, A. Rashevsky, M. Ratti, L. Rigon, G. Tromba, A. Vacchi, E. Vallazza and F. Zanconati (2000). "Mammography with synchrotron radiation: phase-detection techniques." Radiology **215** (1): 286-93.

F. Arfelli, V. Bonvicini, A. Bravin, G. Cantatore, E. Castelli, L. Dalla Palma, R. Longo, R.-H. Menk, A. Olivo, S. Pani, P. Poropat, M. Prest, F. Rashevsky, L. Rigon, G. Tromba, A. Vacchi and E. Vallazza (1999). Improvements in the field of radiological imaging at the SYRMEP beamline. Medical Applications of Penetrating Radiation, Denver, USA.

B. D. Arhatari, A. P. Mancuso, A. G. Peele and K. A. Nugent (2004). "Phase contrast radiography: Image modeling and optimization." Rev. Sci. Instrum. **75** (12): 5271-5276.

A. Authier (2001). *Dynamical theory of X -ray diffraction*. New York, Oxford Press.

L. Azaroff (1968). *Elements of X-ray crystallography*. New York, Mc Graw-Hill.

P. Becker and U. Bonse (1974). "The skew-symmetric two-crystal X-ray interferometer." J. Appl. Cryst. **7**: 593-598.

F. Beckmann, U. Bonse, F. Busch and O. Günnewig (1997). "X-Ray microtomography (µCT) using phase contrast for the investigation oforganic matter." J. Computer Assist. Tomography **21**: 539.

U. Bonse and F. Busch (1996). "X-ray computed microtomography (microCT) using synchrotron radiation (SR)." Prog Biophys Mol Biol: **65** (1-2): 133-169.

U. Bonse and M. Hart (1965). "An X-ray interferometer." Applied Physics Letters **6** (8): 155-156.

M. Born and E. Wolf (1999). *Principles of optics: electromagnetic theory of propagation, interference and diffraction of light*. C. U. Press. Cambridge.

A. Bravin (2003). "Exploiting the X-ray refraction contrast with an analyser: the state of the art." Journal of Physics D: Applied Physics **36**: A24-A29.

Bravin, A., V. Mocella, C. Ferrero, P. Coan, S. Fiedler and W. Thomlison "A wavefront propagation approach to Diffraction Imaging." **In preparation**.

V. Bushuev, E. Beliaevskaya and V. Ingal (1997). "Wave optical description of x-ray phase contrast images of weakly absorbing non crystalline objects." Il Nuovo Cimento **19D**: 513-520.

D. Chapman, W. Thomlinson, F. Arfelli, N. Gmur, Z. Zhong, R. Menk, R. Johnson, D. Washburn, E. Pisano and D. Sayers (1996). "Mammography imaging studies using a Laue crystal analyzer." Rev Sci Instrum **67** (9): 1-5.

D. Chapman, W. Thomlinson, R. Johnston, D. Washburn, E. Pisano, N. Gmur, Z. Zhong, R. Menk, F. Arfelli and D. Sayers (1997). "Diffraction enhanced x-ray imaging." Phys Med Biol **42** (11): 2015-25.

P. Cloetens (1999). Contribution to Phase Contrast Imaging, Reconstruction and Tomography with hard Synchrotron Radiation. Principles, Implementation and Applications. Vrije Universiteit. Brussel.

P. Cloetens, R. Barrett, J. Baruchel, J. Guigay and M. Schlenker (1996). "Phase objects in synchrotron radiation hard X-ray imaging." Journal of Physics D: Applied Physics **29**: 133-146.

P. Cloetens, W. Ludwig, E. Boller, F. Peyrin, M. Schlenker and J. Baruchel (2002). Image Anal. Stereol. **21 (Suppl 1)**: S75-S85.

P. Coan, E. Pagot, S. Fiedler, P. Cloetens, J. Baruchel and A. Bravin (2005). "Phase-contrast X-ray imaging combining free space propagation and Bragg diffraction." Journal of Synchrotron Radiation **12**: 241-245.

R. Cusack, J. M. Huntley and H. T. Goldrein (1995). "Improved noise-immune phase-unwrapping algorithm." Appl. Opt. **34**: 781.

C. David, B. Nohammer, H. Solak and E. Ziegler (2002). "Differential X-ray phase contrast imaging using a shearing interferometer." Applied Physics Letters **81** (17): 3287-3289.

T. Davis (1996). "X-ray diffraction imaging using perfect crystals." Journal of X-ray Science and Technology **6**: 317-342.

T. Davis, D. Gao, T. Gureyev, A. Stevenson and S. Wilkins (1995). "Phase-contrast imaging of weakly absorbing materials using hard X-rays." Nature **373**: 595-598.

T. Davis, T. Gureyev, D. Gao, A. Stevenson and S. Wilkins (1995). "X-ray image contrast from a simple phase object." Phys. Rev. Lett. **74** (16): 3173-3176.

R. Fitzgerald (2000). "Phase sensitive X-ray imaging." Physics Today **53**: 23.

E. Förster, K. Goetz and P. Zaumseil (1980). "Double crystal diffractometry for the characterization of targets for laser fusion experiments." Kristall Technik **15**: 937-945.

A. G. Frodesen, O. Skjeggestad and H. Tofte (1979). Probability and statistics in particle physics. Universitetsforlaget, Bergen-Oslo-Tromso.

J. P. Guigay (1977). Optik **49**: 121.

J. P. Guigay, E. Pagot and P. Cloetens "Fourier optics approach to X-ray analyzer-based imaging." Submitted.

T. Gureyev and S. Wilkins (1997). "Regimes of X-ray phase-contrast imaging with perfect crystals." Il Nuovo Cimento **19 D** (2-4): 545-552.

T. Gureyev, T. J. Davis, A. Pogany, S. C. Mayo and S. W. Wilkins (2004). "Optical phase retrieval by use of first Bornand Rytov-type approximations." Applied Optics **43** (12): 2418-2430.

T. Gyreyev, C. Raven, A. Snigirev, I. Snigireva and S. Wilkins (1999). "Hard x-ray quantitative non-interferometric phase-contrast microscopy." J Phys D: Appl Phys **32**.

M. O. Hasnah, C. Parham, E. D. Pisano, Z. Zhong, O. Oltulu and D. Chapman (2005). "Mass density images from the diffraction enhanced imaging technique." Med. Phys. **32** (2): 549-552.

B. Henke, E. Gullikson and J. Davis (1993). "X-Ray Interactions: photoabsorption, scattering, transmission and reflection at E= 50-30000 eV, Z= 1-92." Atomic Data Nuclear Data Tables **54**: 181-342.

O. Hignette, P. Cloetens, W. Lee, W. Ludwig and G. Rostaing (2003). "Hard X-ray microscopy with reflectiong mirrors status and perspectives of the ESRF technology." Journal de Physique IV **104**: 231-234.

V. Ingal and E. Beliaevskaya (1996). "Phase dispersion radiography of biological objects." Physica Medica **XII** (2): 75-81.

V. Ingal and E. Beliaevskaya (1997). "Phase Dispersion Introscopy." Surface Investigation **12**: 441-450.

J. Jackson (1975). *Classical Electrodynamics*. Wiley. New York.

J. Keyriläinen, M. Fernández and P. Suortti (2002). "Refraction contrast X-ray imaging." Nucl Instr Meth A **488**: 419-427.

S. Lagomarsino, A. Cedola, P. Cloetens, S. Di Fonzo, W. Jark, G. Soullié and C. Riekel (1997). "Phase contrast hard X-ray microscopy with submicron resolution." Applied Physics Letters **71** (18): 2557-2559.

R. Lewis (1997). "Medical applications of synchrotron radiation X-rays." Physics in Medicine & Biology **42**: 1213-1243.

A. Momose (2002). "Phase-contrast X-ray imaging based on interfometry." J Synchrotron Rad **9**: 136-142.

A. Momose, T. Takeda and Y. Itai (1995). "Phase-contrast x-ray computed tomography for observing biological specimens and organic materials." Rev Sci Instrum **66** (2): 1434-1436.

A. Momose, T. Takeda, Y. Itai and K. Hirano (1996). "Phase-contrast X-ray computed tomography for observing biological soft tissues." Nat Med **2** (4): 473-5.

A. Momose, A. Yoneyama and K. Hirano (1997). "Operation of a Two-Crystal X-ray Interferometer at the Photon Factory." J. Synchrotron Rad **4**: 312.

O. Oltulu, Z. Zhong, M. Hasnah, M. N. Wernick and D. Chapman (2003). "Extraction of extinction, refraction and absorption properties in diffraction enhanced imaging." J. Phys. D: Appl. Phys. **36**: 2152–2156.

M. Op de Beeck, D. V. Dyck and W. Coene (1996). "Wave function reconstruction in HRTEM: the parabola method." Ultramicroscopy **64**: 167-183.

E. Pagot (2004). Quantitative comparison between two phase contrast techniques for mammography: diffraction enhanced imaging (DEI) and phase propagation imaging (PPI). Ph.D. Thesis, Université Joseph Fourier (Grenoble, France).

E. Pagot, P. Cloetens, S. Fiedler, A. Bravin, P. Coan, J. Baruchel, J. Härtwig and W. Thomlinson (2003). "A method to extract quantitative information in analyser-based X-ray phase contrast imaging." Applied Physics Letters **82** (20): 3421-3423.

K. M. Pavlov, T. E. Gureyev, D. Paganin, Y. I. Nesterets, M. J. Morgan and R. A. Lewis (2004). "Linear systems with slowly varying transfer functions and their application to x-ray phase-contrast imaging." J. Phys. D: Appl. Phys. **37**: 2746–2750.

Z. Pinsker (1978). *Dynamical scattering of X-rays in crystals*. **5**. Springer Series in Solid State Physics, Berlin.

K. Podurets, V. Somenkov and S. Shilstein (1989). "Refraction-contrast radiography." Sov Phys - Tech Phys **34** (6): 654-657.

A. Pogany, D. Gao and S. Wilkins (1997). "Contrast and resolution in imaging with a microfocus x-ray source." Rev. Sci. Instrum. **68** (7).

V. Protopopov, J. Sobota, A. Tremsin, O. Siegmund and Y. Platonov (2002). X-ray imaging of microobjects using dark field refraction-contrast method with resonantly absorbing multilayer mirrors. SPIE Medical Imaging, S. Diego, SPIE.

C. Raven, A. Snigirev, I. Snigireva (1996). "Phase-contrast microtomography with coherent high-energy synchrotron X rays." Appl. Phys. Lett. **69** (13): 1826-1828.

L. Rigon, H. Besch, F. Arfelli, R. Menk, G. Heitner and H. Plothow-Besch (2003). "A new DEI algorithm capable of investigating sub-pixel structures." J. Phys. D: Appl. Phys. **36**: A107-A112.

L. Rigon, Z. Zhong, F. Arfelli, R.-H. Menk and A. Pillon (2002). Diffraction Enhanced Imaging Utilizing crystal reflections at Elettra and NSLS. SPIE Medical Imaging, S. Diego, SPIE.

A. Snigirev, I. Snigireva, V. Kohn, S. Kuznetsov and I. Schelokov (1995). "On the possibility of X-ray phase contrast microimaging by coherent high-energy synchrotron radiation." Rev. Sci. Instrum. **66** (12): 5486-92.

V. Somenkov, A. Tkalich and S. Shilshtein (1991). "Refraction contrast in X-ray introscopy." Sov. Phys. Tech. Phys. **36** (11): 1309-1311.

W. Tsai, P. Hsu, Y. Hwu, C. Chen, L. Chang, J. Je, H. Lin, A. Groso and G. Margaritondo (2002). "Building on bubbles in metal electrodeposition." Nature **417**: 139.

M. Wernick, O. Wirjadi, D. Chapman, O. Oltulu, Z. Zhong and Y. Yang (2002). Preliminary investigation of a multiple-image radiography method. IEEE International Symposium on Biomedical Imaging, Whashington.

M. N. Wernick, O. Wirjadi, D. Chapman, Z. Zhong, N. P. Galatsanos, Y. Yang, J. G. Brankov, O. Oltulu, M. A. Anastasio and C. Muehleman (2003). "Multiple-image radiography." Phys Med. Biol. **48** (23): 3875-3895.

M. N. Wernick, Y. Yang, I. Mondal, D. Chapman, M. Hasnah, C. Parham, E. Pisano and Z. Zhong (2006). "Computation of mass-density images from X-ray refraction-angle images." Phys Med. Biol. **51**: 1769-1778.

S. Wilkins, T. Gureyev, D. Gao, A. Pogani and A. Stevenson (1996). "Phase-contrast imaging using polychromatic hard X-rays." Nature **384**: 335-338.

A. Yoneyama, A. Momose, E. Seya, K. Hirano, T. Takeda and Y. Itai (1999). "Operation of a separated-type x-ray interferometer for phase-contrast X-ray imaging." Rev. Sci. Instrum. **70**: 4582–4586.

A. Yoneyama, T. Takeda, Y. Tsuchiya, J. Wu, T. T. Lwin, A. Koizumi, K. Hyodo and Y. Itai (2004). "A phase-contrast X-ray imaging system with a 60×30 mm field of view based on a skew-symmetric two-crystal X-ray interferometer." Nucl. Instrum. Methods **A523**: 217–222.

W. Zachariasen (1945). *Theory of X-ray diffraction in crystals*. J. Wiley & Sons Inc New York.

Z. Zhong (2000). "Using a prism to reject or select harmonic reflections in an X-ray monochromator." Journal of Applied Crystallography **33**: 1082-1087.

Z. Zhong, W. Thomlinson, D. Chapman and D. Sayers (2000). "Implementation of diffraction-enhanced imaging experiments: at the NSLS and APS." Nucl Instr and Meth A **450**: 556-567.

3

The X-ray source and experimental methods

Contents

Ce chapitre détaille les caractéristiques du rayonnement synchrotron en soulignant les particularités qui en font un outil puissant pour l'imagerie comparativement aux autres sources de rayons X. Les dispositifs expérimentaux utilisés sont aussi décrits dans ce chapitre avec une présentation des lignes de lumière où ont été réalisées les expériences : l'une dédiée aux recherches biomédicales (ID17) et l'autre à la tomographie et topographie (ID19).

In this chapter, the synchrotron radiation (SR) characteristics and the experimental facility are described and compared with other X-ray sources, highlighting the peculiarities that make the SR a so powerful tool for imaging. The Biomedical (ID17) and Tomography & Topography (ID19) beamlines are introduced and the experimental set-ups used for measurements performed for this Thesis are presented.

3.1 Introduction

The science of X-ray production and application is now a little more than a century old (Röntgen, 1895) but is still an active field of research and development (Bushber, 1994).

Historically, X-rays for imaging and crystallography have generally been produced through the use of *bremsstrahlung* and characteristic lines from electrons impinging on a metallic anode (X-ray tubes). Such sources are inexpensive, simple, and robust but provide little control over the X-rays produced.

During the past three to four decades, synchrotron radiation (SR) sources have had a revolutionary impact on fields of science and technology extending from material science to biomedical imaging.

The peculiar geometrical and spectral characteristics of the SR beam allow overcoming the intrinsic limitations of the conventionally produced X-rays thanks to the high brilliance, collimation, and wide energy range of the produced radiation.

Unfortunately, synchrotrons are large, expensive facilities and are therefore not entirely practical for routine imaging applications. The excellent results of experiments with monochromatic sources (Suortti and Thomlinson, 2003) show the desirability of improving on the current broadband X-ray sources. No alternative has existed for experiments that need to operate at various X-ray energies and under particular coherence conditions. The availability of tabletop, intense monochromatic sources may fundamentally change the practice of X-ray imaging and can largerly extend the application of imaging techniques that are presently confined into SR facilities. Recent developments in this sense are represented by Compact Light Sources (CLS).

In this chapter after having introduced the different X-ray sources, I will describe more in detail the physical characteristics of the SR focusing on the European Synchrotron Radiation Facility (ESRF) where I have performed the experiments, then I will introduce peculiarities of the installations available at ID17, the Biomedical beamline, and at ID19, the Tomography & Topography beamline of the ESRF.

The second part of the chapter will be dedicated to the description of the experimental set-up used for the Propagation-based and Analyzer-based imaging techniques.

3.2 X-ray sources

3.2.1 X-ray tubes

X-ray radiation for medical diagnostic procedures or for research purposes are conventionally produced by X-ray tubes. The basic principle of an X-ray tube has not changed significantly since Röntgen's 1895 discovery. Current applied to a metal cathode produces free electrons which are accelerating with a high voltage towards a metal target (anode). X-rays are produced when the electrons are suddenly decelerated upon collision with the target; these X-rays are commonly called *brehmsstrahlung* or "braking radiation". If the bombarding electrons have sufficient energy, they can knock an electron out of an inner shell of the target metal atoms (ionization process). Then electrons from higher states drop down to fill the vacancy, emitting X-ray photons with precise energies determined by the electron energy levels. These X-rays are called *characteristic X-rays*. The energy E of a X-ray photon and its wavelenght are related by the equation $E = hc/\lambda$, where h is the Planck's constant and c the speed of light.

Actually, most of the energy in the electron beam is deposited in the target in the form of heat, and one of the problems faced by tube designers is how to limit the heat deposition in the target area and how to remove it. The use of slit source of electrons helps by spreading out the target area and this idea can be extended by using a rotating anode so that the target area (effective focal-spot) is spread out over the periphery of the disc (anode). The shape of the X-ray spectrum will depend upon the target material, the potential and the waveform applied to the tube and the effects of any filters placed in the X-ray path.

3.2.2 Synchrotron radiation sources

Whenever a relativistic charged particle (electron or positron) passes through a magnet field, its path is bent and a sharply collimated radiation is emitted tangentially to the curved trajectory of the accelerated particle. Such electromagnetic waves are the so-called synchrotron radiation (SR) and it is emitted in a narrow cone with a typical natural opening angle of about $1/\gamma$ ($\gamma = 1/\sqrt{1 - v^2/c^2}$, v is the electron velocity). The beam geometry is shown in Figure 3.1.

Historically, SR research is truly an outgrowth of high-energy physics research. In the very beginning, most SR programs operate primarily in parasitic mode, using the radiation produced during high-energy physics operations of storage rings. Since '80s an increasing number of fully dedicated SR facilities have been built all around the world.

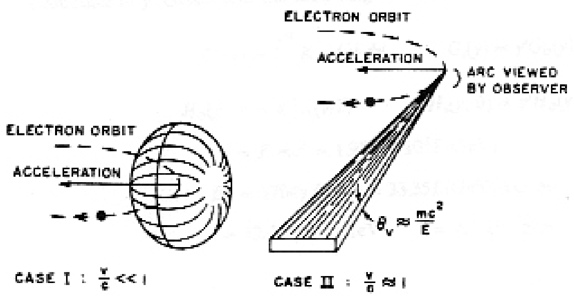

Figure 3.1. Geometry of the radiation emitted by a no-relativistic and a relativistic particle.

Electrons used in synchrotron machines are produced in bunches of about 10^{11} particles by means of an electron gun (by heating a cathode) with a frequency up to 10 Hz. After preacceleration using disc-loaded wave guides (Brefeld and Gurtler, 1991) in a linear accelerator (*LINAC*), electrons are then injected into an additional accelerator (*booster*) where their energy is "ramped" to the final energy. In the first and second generation SR machines, the booster was made to operate as a synchrotron and as a storage ring at the same time. In the new generation of SR facilities, electrons are transferred to a second ring, called *storage ring*, where magnetic elements are positioned all along the electron orbit. Magnetic dipoles are used to define the closed orbit of the particles and, in storage rings, dipoles are one type of SR light source.

A closed, continuous high-vacuum chamber extends through the various booster and storage ring elements including:

(1) bending magnets (dipoles);

(2) radiofrequency cavities which accelerate electrons (in the booster) or replenish the energy lost by the particles into SR (in the storage ring);

(3) vacuum pumps to evacuate the chamber;

(4) straight sections with elements for the injection of the electrons from another accelerator (LINAC-to-booster, booster-to-storage ring).

Other important components are the quadrupoles magnets; suitably combined, they provide focusing forces that keep the electron-beam transverse dimensions small. Sextupoles are instead employed to compensate for loss of beam chromaticity around the electrons revolution.

The electrons run in ultra high vacuum (less of 10^{-8} mbar) in order to minimize the probability of collisions with residual gas.

In the curved sections are installed the already mentioned bending magnets which produce a continuous spectrum of SR. In the straight sections are installed special *insertion devices*, that can be either **wigglers** and **undulators**, which are alternative more powerful X-ray sources.

They consist of a sequence of dipole magnets of alternating polarities. The magnetic fields force the electron to oscillate around a straight-line trajectory and the cones of light emitted at each bend superimpose.

- In the case of undulators, the electron beam deflection is inferior to $1/\gamma$, so that the beams emitted by individual poles can interfere coherently. This leads to a spectrum with strong peaks at a specific energy and its harmonics.
- In the wiggler case, the total divergence is much larger than the natural opening angle of the radiation and no more interference occurs. The final beam emitted by the device is the incoherent sum of the beams emitted at each pole, and the X-ray spectrum exhibits a continuous distribution.

Tangential beam channels (*beamlines*) starting from the storage ring permit the synchrotron radiation to enter experimental halls. Since many beam channels can be installed all along the ring, and some of them can even be split in more branches by means of mirrors or crystals, a large number of simultaneous experiments are possible.

A more detailed and formal description of the main parameters characterizing the SR light and machine are presented in Paragraph 3.3

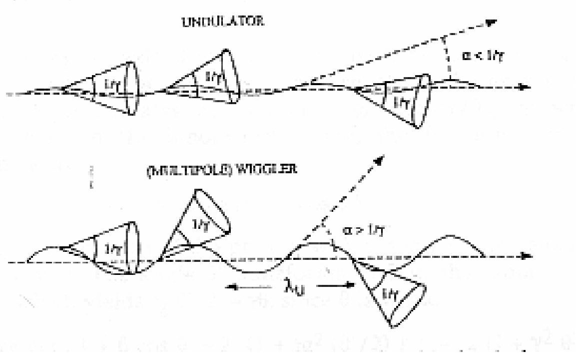

Figure 3.2. Schematic comparison of the SR emissions from an undulator and a wiggler.

– Geometrical and spectral comparison between X-ray tubes and the SR beams

Figure 3.3 shows the different geometries of the beams produced by a X-ray tube and a SR source. X-ray tubes emit radiation in all directions and the sample is normally close to the source. The operator can change the magnification $M = (z_1 + z_2)/z_1$ of the image by varying the distance between the focal spot and the sample z_1 and the distance between the sample and the detector z_2.

Thanks to the large sample to source distance at synchrotron facilities, the SR beam is almost parallel at the sample position. This property is particular suited when performing tomography imaging but, on the other hand, the magnification *M* is much smaller than in conventional sources if additional optics is not installed.

Figure 3.4 presents the comparison between the X-ray beam spectrum produced with X-ray tubes with that produced by a SR wiggler device. In the first case, the spectrum is given by a continuous *brehmsstrahlung* background from where the characteristic X-ray emissions stand out; SR wiggler beams are instead characterized by a continuous emission in a wide energy range which is orders of magnitude more intense than the strongest characteristic lines from X-ray tubes.

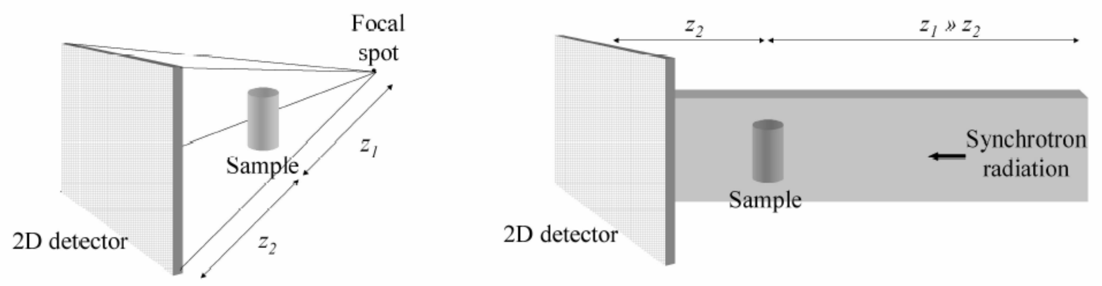

Figure 3.3. Schemes of the set-ups for X-ray tubes and SR imaging and of the different geometries of the related X-ray beams.

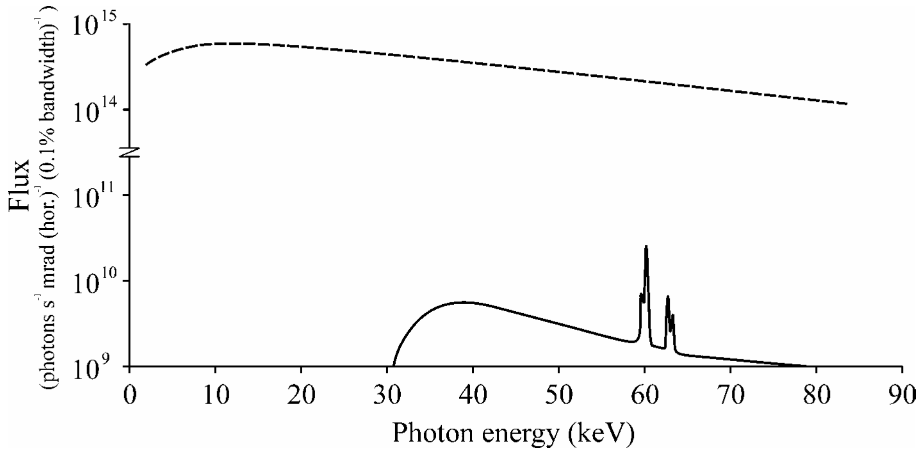

Figure 3.4. Comparison between a wiggler X-ray beam spectrum (dashed line) (ESRF. ID17 at 200 mA ring current) and an X-ray tube (110 kVp - 2.5 mm Al @ 1 meter/source).

3.2.3 Compact hard X-ray sources

There is a great interest in developing high brilliant X-ray compact sources, which can replace the large and "costly" synchrotron machines especially for some specific applications (e.g. crystallography and high-resolution imaging). Delivery of 2D beam of hard, tunable, high-brightness monochromatic X-rays suitable for rapid medical imaging is a long-sought goal. In fact, a device to produce X-rays in a clinical environment has to be relatively compact and capable of delivering (i) X-ray energies that encompass the useful diagnostic range and (ii) a cone-geometry X-ray beam allowing single-shot imaging over a broadly tunable range at variable bandwidths.

Several groups are simultaneously working in investigating compact light sources (CLS). For such machines, different solutions have been proposed, but most of them are based on the same physical process: **the inverse Compton scattering**.

Inverse Compton scattering basically consists of the head-on collision of an energetic (20-50 MeV) electron beam with an intense beam of light. Therefore, a CLS machine essentially integrates a laser with a linear accelerator (usually a photocathode RF gun combined with a X-band accelerating tubes system). Both beams, electrons and light from laser respectively, are focused to an exceptionally small spot size at the point of collision. Light scatters off the electrons, picking up some of their energy and being deflected back out of the interaction zone as X-ray photons along an axis almost collinear with the path of the electron beam (see Figure 3.5 (A)). By exploiting this process, high-brilliance hard X-ray beams with a laboratory-scale facility can be produced.

Literature on CLS projects is still relatively limited. Interesting works on hard-X-ray CLS calculations and design have been presented, for example, by Fukasawa (Fukasawa, Iijima *et al.*, 2001), Carroll (Carroll, Mendenhall *et al.*, 2003) and by the Lyncean Technologies enterprise[1].

Unfortunately, there are not yet scientific publications produced with such a source. Nevertheless, given the importance of the development of sources alternative to the SR for clinical applications of phase contrast techniques, I will report the key features of the Carroll's and co-workers' project in the rest of the paragraph.

They have developed a tabletop-terawatt laser-based Compton backscattering system, which uses few-joule pulses from a 1.052-nm laser to collide with a 20- to 50-MeV electron beam to produce an intense pulse of narrowband X rays. The entire system is 4 m wide by 10 m long, and it requires no shielding vault. It produces X rays in a small angle cone-beam geometry in the 10 to 50 keV range, with up to 10^{10} photons in an 8-ps pulse, which is a marginally sufficient flux for medical and industrial imaging to be performed in a single shot.

---

[1] http://www.lynceantech.com/index.html

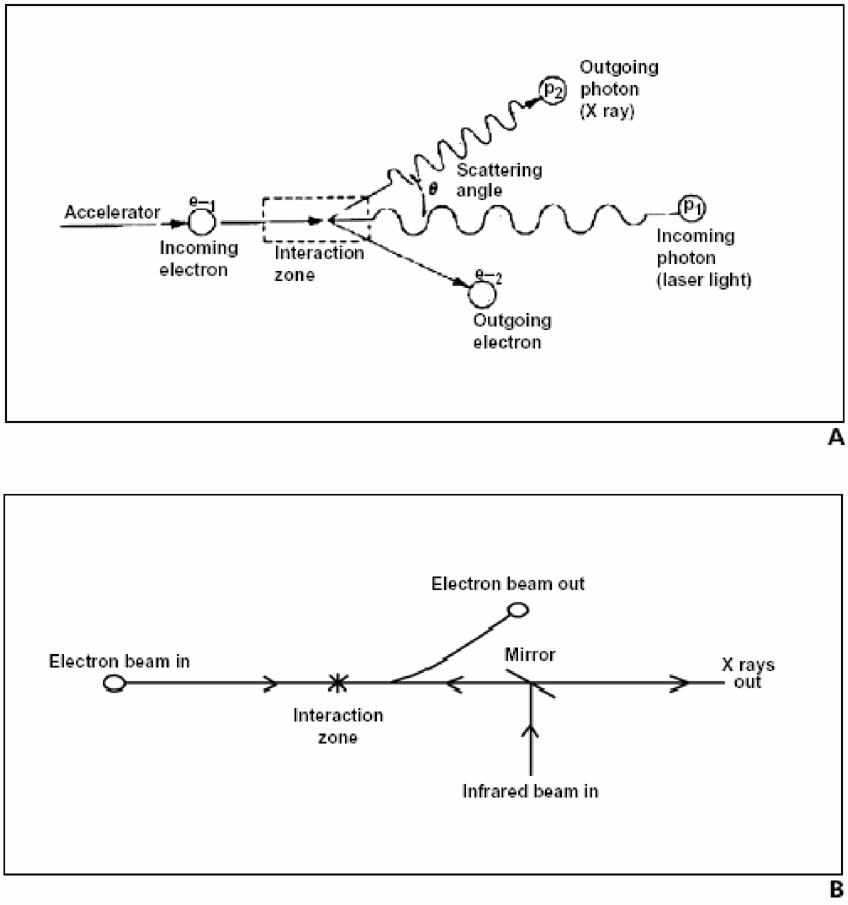

Figure 3.5. Theory and practice of inverse Compton scattering process used in Compact Light Sources (CLS) (Carroll, Mendenhall *et al.*, 2003). A) Diagram of the theory: an energetic beam collides head-on with focused intense infrared beam, resulting in X-rays propagating almost collinearly with electron beam direction. B) General scheme of a CLS machine.

The system consists of several basic subcomponents. In fact, the unit produces an electron beam, an infrared light beam, and an X-ray beam (see Figure 3.5 (B)).

- The electron beam. A neodymium:yttrium lithium fluoride (Nd:YLF) laser, pulse compressor, and frequency quadrupler provide up to 200 μJ of 263-nm light in 5-ps pulses that strike a copper photocathode. A radiofrequency drive system and bare copper photocathode electron gun–linear accelerator produce a high-brightness electron beam. A superconducting solenoid focusing magnet is used downstream from the linear accelerator to focus the electron beam to its point of interaction with the infrared light beam.
- The infrared beam. A 200 fs Ti:Sapphire seed laser runs at 1.052 nm and drives a stretcher–regenerative amplifier combination, which produces a 480-Hz train of 200 μJ pulses stretched to approximately 1 ns. This laser seeds both the Nd:YLF laser used to generate the electron beam and a multistage Nd: glass amplifier. This Nd: glass laser and

pulse compressor provide up to 10 J of 1.052-nm light compressed to 8-ps infrared pulses for the collision with the electron beam. This infrared beam is focused on the interaction zone after being deflected by a beryllium mirror pointed upstream into the linear accelerator.

- The X-ray beam. An interaction zone and beam alignment system are used where the electron beam and photon beam collide head-on in a 50 µm spot. The X rays produced traverse the infrared beryllium mirror, and a thin beryllium exit window is used to allow the X rays out of the vacuum beam line into the imaging area.

Preliminary results of imaging by using the hard tunable high-peak brightness monochromatic X -ray produced by this compact source are promising. Moreover, pico-second pulses become valuable for studying physical, chemical, or mechanical processes that occur on the X-ray beam's picosecond time scale. Because a machine of this type is easily scaled to higher photon energy by simply lengthening the LINAC, it should be simple to adapt this technology for other applications. Because the X-ray photon energy increases as the square of the electron beam energy, doubling the LINAC length quadruples the X-ray energy, and shortening it can make it useful for other applications in medicine and biologic research.

Thanks to their high brightness, short pulses, and a variable bandwidth X-ray beam, compact light source machines have a high potential to become, in the future, the reference source for high resolution and sensitive clinical programs for the diagnosis and treatment of everyday human medical applications.

3.3 The European Synchrotron Radiation Facility (ESRF)

The European Synchrotron Radiation Facility (ESRF) at Grenoble is the most powerful third-generation synchrotron of Europe (Figure 3.6). ESRF is the result of an international consortium of eighteen countries founded in 1988 for scientific and technological research by means of high brilliant hard X-rays.

The machine consists of: i) a LINAC that accelerates the electron beam, produced by an electron gun, up to an energy of 200 MeV; ii) a booster of 290 meters of circumference where two radiofrequencies at 10 Hz accelerate the electrons bunches up to the maximum energy of 6 GeV; iii) and a 844 meters circumference storage ring composed by bending magnets and straight sections, where electron bunches turn at a frequency of 352 MHz given rise to a current that can reach 200 mA.

Forty specialized beamlines are installed by the storage ring (Figure 3.7). These beamlines are designed for research in areas as diverse as engineering, physics, chemistry, crystallography, earth science, biology and medicine, surface and materials science. Several Collaborating Research Groups ("CRG") made up of institutes from countries participating in the ESRF, are building and operating beamlines at the ESRF with independent funding.

Experimental data presented in this Thesis have been acquired at the two long beamlines of the ESRF: the Biomedical (ID17) beamline and the Topography & Tomography (ID19) beamline. Before giving a general description of these two wiggler based-experimental stations, in the following paragraphs the synchrotron and X-ray beam parameters will be presented.

Figure 3.6. Aerial view of the European Synchrotron Radiation Facility (ESRF) at Grenoble. On the right side of the picture, the external buildings hosting the two long beamlines ID17 and ID19 of the facility are visible.

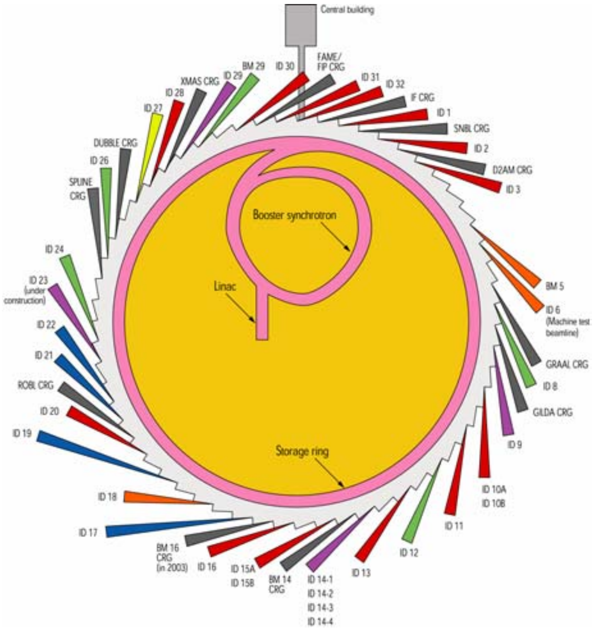

Figure 3.7. Scheme of the ESRF structure. Tangentially to the storage ring, thirty eight beamlines are installed.

3.4 The storage ring electron beam and the machine parameters

The electron orbit and beam size in the storage ring are influenced by the presence of bending magnets, quadrupoles, sextupoles and insertion devices placed all along the circumference. In order to keep a circular electron trajectory of radius ρ, the magnetic field (*B*) of magnets, which is perpendicular to the horizontal orbital plane, has to fulfil the relation (Hercules, 1993) $\rho[\mathrm{m}] = 3.32\,E[\mathrm{GeV}]/B[\mathrm{T}]$, where E is the electrons energy. Therefore, the emission of radiation by accelerated electrons, determines a loss of energy and consequently spatial fluctuations of electrons along their orbit.

For this reason, a **transverse dimension distribution** and an **angular deviation distribution** are associated to the electron beam; the related standard deviations are indicated by σ_x and σ_z, $\sigma_x^{'}$ and $\sigma_z^{'}$ respectively (the coordinate system is shown in Figure 3.8).

The electron beam **emittances** $\varepsilon_x = \sigma_x \sigma_x^{'}$ and $\varepsilon_z = \sigma_z \sigma_z^{'}$ are characteristic constants of the storage ring, while the beam size and divergence vary along the ring (Liouville's theorem). The shapes of the emittance ellipses are given by functions β_x and β_z (ESRF, 1987)

$$\beta_x = \frac{\sigma_x}{\sigma_x^{'}} \quad \text{and} \quad \beta_z = \frac{\sigma_z}{\sigma_z^{'}} \tag{3.1}$$

and accordingly

$$\sigma_x = \sqrt{\varepsilon_x \beta_x} \quad \text{and} \quad \sigma_z = \sqrt{\varepsilon_z \beta_z} \tag{3.2}$$

$$\sigma_x^{'} = \sqrt{\frac{\varepsilon_x}{\beta_x}} \quad \text{and} \quad \sigma_z^{'} = \sqrt{\frac{\varepsilon_z}{\beta_z}} \tag{3.3}$$

The electron motions in the vertical and horizontal planes are coupled; in fact there are always misalignments of the directions of the magnetic fields, or of their gradients, as well as local field inhomogeneities, which result in a **coupling coefficient,** q^2, between the vertical and horizontal emittances:

$$\varepsilon_z = q^2 \varepsilon_x \tag{3.4}$$

q^2 mainly depends on the machine characteristics and, in the ESRF case, it is about 1%.

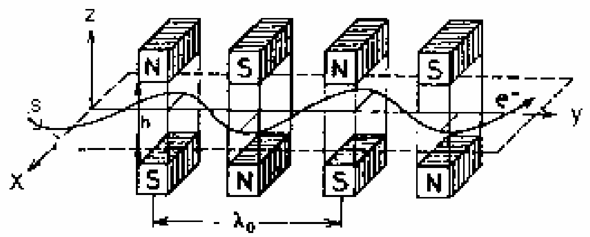

Figure 3.8. Trajectory of electrons inside a wiggler and definition of the coordinates system.

The beam characteristics of electrons passing through an insertion device influence the produced X-ray beam properties. Depending on experimental requirements, small source size and high divergent beam or, conversely, large source size and a little divergent beam can be desiderable. In the former case, a wiggler is used and installed in a section where the β function has a minimum (*low beta* sections), while in the latter case an undulator is used and installed in section where β is maximum (*high beta* sections).

In the case of ID17 and ID19, the radiation source is a *low beta* wiggler.

Energy	6 GeV
Average circumference	844 m
Horizontal emittance	3.9×10^{-9} m
Vertical emittance	3.9×10^{-11} m
Horizantal dimension σ_x	4.42×10^{-5} m
Vertical dimension σ_z	1.032×10^{-5} m
Horizontal divergence $\sigma_x^{'}$	8.83×10^{-5} rad
Vertical divergence $\sigma_z^{'}$	3.78×10^{-6} rad

Table 3.1 ESRF storage ring and electron beam parameters at a low β section.

3.5 Synchrotron radiation from a wiggler

In a wiggler or undulator, the periodic structure of the magnetic field forces the relativistic electrons to oscillate perpendicularly to their direction of motion. As already mentioned, the sum of radiation emitted at each individual wiggle is incoherent in the case of a wiggler and partially coherent for an undulator.

The distinction between these two regimes is not unique; for this reason, the so-called **deflection parameter** *K* has been introduced. It is defined as:

$$K = \delta\gamma \tag{3.5}$$

where δ is the maximum electron deflection angle and $\gamma = E/mc^2$ (*E*, m are the electron energy and mass respectively, and *c* the light speed). Wigglers have $K >> 1$, while undulators $K \leq 1$.

The radiation pattern produced in an insertion device is sharply peaked in the direction of electron motion. The half-angle of the radiation cone is in the vertical plane

$$\sigma_{\psi}^{'} \approx 1/\gamma \tag{3.6}$$

and in the horizontal plane

$$\delta = K/\gamma \tag{3.7}$$

The *K* values can be modified by changing the distance between the magnetic poles of the insertion device (*gap*). In Figure 3.9, the dependence of *K* upon the device gap for the ID17 case is presented, while the the main Fourier components of the magnetic field of the ID17 wiggler are reported in Table 3.2

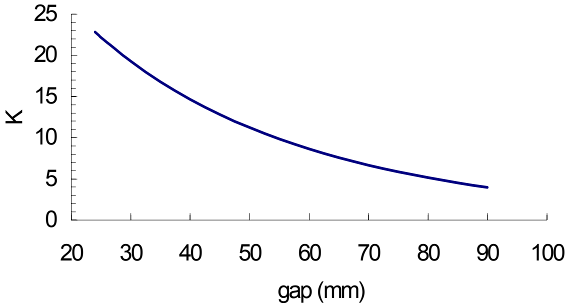

Figure 3.9. *K* as function of the wiggler gap at ID17.

Let us define *s* the coordinate along an electron trajectory inside a wiggler (see Figure 3.8). The deviation angle $\alpha(s)$ of the electron is given by:

$$\alpha(s) = \frac{K}{\gamma}\cos\left(\frac{2\pi s}{\lambda_u}\right) \tag{3.8}$$

where λ_u is the period of the magnetic field. Then, by integrating (3.8), the transverse displacement in the orbit plane is:

$$x(z) = \frac{K}{\gamma}\frac{\lambda_u}{2\pi}\sin\left(2\pi\frac{z}{\lambda_u}\right) \tag{3.9}$$

3.5.1 Critical wavelength and energy

The wavelength value that devides the total emitted radiation power into two equal parts is called the **critical wavelength** λ_c; in a similar way the **critical energy** E_c is defined. At the center of the beam, we have:

$$\lambda_c = \frac{4\pi\rho}{3\gamma^3} \quad \text{and} \quad E_c = \frac{3hc\gamma^3}{2\rho} \tag{3.10}$$

Here ρ is the minimum bending radius of the electron orbit.

Because of the sinusoidal variation of the magnetic field, these parameters vary as function of the angle θ in the orbit plane as:

$$\lambda_c(\theta)=\frac{\lambda_c(\theta=0)}{\sqrt{1-(\theta/\delta)}} \quad \text{and} \quad E_c=E_c(\theta=0)\sqrt{1-(\theta/\delta)^2} \tag{3.11}$$

In Figure 3.10 I have reported critical energy values as function of the ID17 wiggler gap.

The **total radiated power from a wiggler**, if *N* is the number of magnetic periods, is given by:

$$P_T=\frac{N}{6}Z_0Ie\frac{2\pi c}{\lambda_u}\gamma^2K^2 \tag{3.12}$$

with *I*, electron beam current, $Z_0=377\,\Omega$ and λ_u is the magnetic field period.

With reference to equations (3.12) and (3.5), it possible to see that the power of the emitted radiation depends on the fourth power of the particle (electron or positron) energy and on the inverse fourth power of its mass.

High values for the critical energies are achievable only in "high" energy synchrotron like Spring8 (Japan, $E=6$ GeV), APS (USA, $E=7$ GeV), and ESRF (France, $E=6$ GeV).

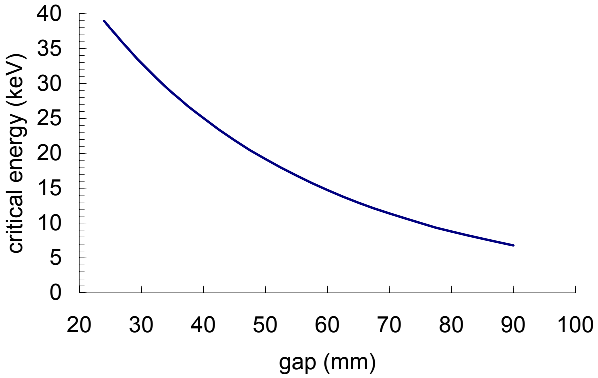

Figure 3.10. Critical energy in the central wiggler axis as function of the gap of the ID17 wiggler.

3.5.2 Energy distribution of the radiation emitted by a single electron

At each dipole of a wiggler, the angular distribution of the radiation emitted by electrons is expressed by:

$$\frac{d^2\Phi}{d\theta d\psi}=\frac{3\alpha}{4\pi^2}\gamma^2\frac{\Delta\omega}{\omega}\frac{I}{e}y^2\left(1+X^2\right)\left[K_{2/3}^2(\xi)+\frac{X^2}{1+X^2}K_{1/3}^2(\xi)\right] \tag{3.13}$$

where Φ is the number of photons per second, α the fine-structure constant, ω the angular frequency of a photon, *I* the electron beam current, $y=\varepsilon/\varepsilon_c$, $X=\gamma\psi$, $\xi=y\left(1+X^2\right)^{3/2}/2$, $K_{2/3}^2(\xi)$ and $K_{1/3}^2(\xi)$ are the modified Bessel functions of the second kind.

Equation (3.13) and the previous ones defined a gaussian distribution for the X-ray beam emitted by a wiggler both in the horizontal (*x*) and vertical (*z*) direction.

3.5.3 The polarization of the synchrotron radiation

The two addends in the squared bracktes of equation (3.13) correspond to two orthogonal states of polarization; in particular, to the horizontal plane (*xy*) and to the vertical plane (*xz*) respectively.

– The amplitude of the vertical polarization is zero at $\psi = 0$, meaning that for an observer in the orbit plane, the radiation emitted by a single dipole is 100% linearly polarized in the acceleration direction, while it is elliptical for $\psi \neq 0$.

– When considering the case of several dipoles, like a wiggler, equations written above have to be multiplied by 2*N*, where *N* is the number of periods of the magnetic field. The polarization in the $\psi = 0$ plane is still linear; for $\psi \neq 0$, radiations emitted from two adjacent half-period of the magnetic field are elliptically polarized but with opposite signs. However, the phase difference is arbitrary, so that outside the orbit plane the beam consists of a linear component and unpolarized component.

3.5.4 The divergence of the synchrotron radiation

The angular distribution of the X-ray beam can be well approximated by a gaussian both in the orbit plane and in the perpendicular one (in reality it is a composition of Bessel functions as described in Paragraph 3.5.2). The standard deviations of such distributions are given by:

$$\Sigma'_{x,z} = \sqrt{\sigma'^2_{x,z} + \sigma'^2_{\theta,\psi}} \tag{3.14}$$

where the first term is the standard deviation of the electron beam divergence (equation (3.2)), and the second term is the angular divergence of the photon beam defined by equations (3.6) and (3.7) and deducible by equation (3.13). In Table 3.2, the calculated values of the standard deviations of the divergence for a point-like source and a real source are reported.

Parameter	Photon beam divergence (μrad)
σ'_θ	730
σ'_ψ	84.6
Σ'_x	735
Σ'_z	84.7

Table 3.2. Standard deviations of the photon beam divergence calculated for an electron energy *E*=6 GeV and wiggler gap of 60 mm for a point-like (σ') and real (Σ') source.

3.5.5 The source size

The radiation source can be assumed a two-dimensional gaussian distribution whose standard deviations (Σ_x and Σ_z) depend upon both the radiation and electron beams characteristics.

In particular, the factors that influence the coherence properties (Paragraph 3.6) of the X-rays beam are:

- Electron distribution along the insertion device;
- The length of the insertion device;
- The electron maximum deflection (δ) in the orbit plane (see equation (3.5)) inside the insertion device.

The standard deviations of the photons source distributions in the vertical and in the horizontal (orbit) plane are expressed, respectively, by (Cloetens, 1999):

$$\Sigma_z = \sqrt{\sigma_z^{\,2} + \frac{\left(L\theta_{oss-z}\right)^2}{12}} \tag{3.15}$$

$$\Sigma_x = \sqrt{\sigma_x^{\,2} + \frac{\left(L\theta_{oss-x}\right)^2}{12} + \left(\frac{K}{\gamma}\frac{\lambda_u}{\pi}\right)^2} \tag{3.16}$$

σ_x and σ_z (equations (3.1)) are the standard deviations of the spatial distribution of the electrons, θ_{oss-z} and θ_{oss-x} are the angles at which an observer looks at the insertion device with respect to its axis in the two transverse directions; here *L* is the length of the wiggler.

It is important to highlight that Σ_z and Σ_x, as defined above, do not give the real spatial aperture of the photon source, but they express the optical source size. The terms appearing in the equations (3.15) and (3.16) are the ones influencing the degree of coherence of the source itself and therefore the quality of images when exploiting the phase contrast (as it will be discussed in Paragraph 3.6.1).

Table 3.3 reports the values of the standard deviations of the source distributions in the two directions calculated for a wiggler gap of 60 mm, an X-ray beam size of 100 x 1 mm^2 and for an observer placed at a distance of 156 m from the source (maximum wiggler source-detector distance at ID17. See Paragraph 3.8).

The optical source size defines also the brilliance properties of the insertion device. In Table 3.4, some figures of merit (Spectral Flux, Central Brightness and Brilliance) characteristic of the radiation are presented.

In Table 3.5, are instead reported the main parameters of the source (*low* β wiggler) of ID17 (values are the same for the ID19).

	$\theta_{oss\text{-}x} = \theta_{oss\text{-}z} = 0$	$\theta_{oss\text{-}x} = 320\ \mu\text{rad}$ $\theta_{oss\text{-}z} = 3.2\ \mu\text{rad}$
Σ_x (μm)	56.26	158.37
Σ_z (μm)	10.32	10.42

Table 3.3. Standard deviations of the photon source distributions in the vertical and in the horizontal (orbit) plane calculated for a wiggler gap of 60 mm on the axis of the beam (second column) and at the edges of a beam of 100 x 1 mm^2 with the observer at a distance of 156 m from the source (ID17 case) (third column).

Figure of merit	Definition	Units
Spectral Flux	$\frac{d^2n}{dtd\theta\, d\lambda/\lambda}$	$\text{photons} \cdot \text{s}^{-1} \cdot \text{mrad}^{-1} \cdot (0.1\%\ \text{bandwidth})^{-1}$
Central brightness*	$\frac{d^3n}{dtd\theta d\psi\, d\lambda/\lambda}$	$\text{photons} \cdot \text{s}^{-1} \cdot \text{mrad}^{-2} \cdot (0.1\%\ \text{bandwidth})^{-1}$
Brilliance	$\frac{d^5n}{dtd\theta d\psi dxdy\, d\lambda/\lambda}$	$\text{photons} \cdot \text{s}^{-1} \cdot \text{mrad}^{-2} \cdot \text{mm}^{-2} \cdot (0.1\%\ \text{bandwidth})^{-1}$

Table 3.4. Definition of some figures of merit of the radiation and their units. *Central brightness calculated for $\theta = \psi = 0$.

low β wiggler at ID17	
Number of poles	21
Length	1.6 m
Maximum magnetic field B_0	1.5 T
Magnetic period λ_u	150 mm
Minimum gap	24.8 mm
Maximum critical energy E_c	38.1 keV
Maximum deflection parameter K	19.6
Total emitted power at 200 mA	14.3 kW
Max. vert. divergence	3.3 x 0.1 mrad^2 (HxV) FWHM
Magnetic field calculated for the ID17 wiggler	$B_0 = 2.78 \cdot e^{-0.02535 \cdot gap} + 0.8425 \cdot e^{-0.07538 \cdot gap} - 0.087 \cdot e^{-0.081 \cdot gap} - 0.487 \cdot e^{-0.16 \cdot gap}$

Table 3.5. Some characteristics of the ID17 wiggler.

In Figure 3.11, are reported some calculations I made by using the XOP software. In particular, I have investigated how the central brightness varies by changing the energy (A) and wiggler gap (B), and how the X-ray beam profile (C) and vertical dimension (D) change depending on gap and horizontal position with respect to the wiggler axis, respectively. For further details concerning the parameters used in calculations, please refer to the figure caption.

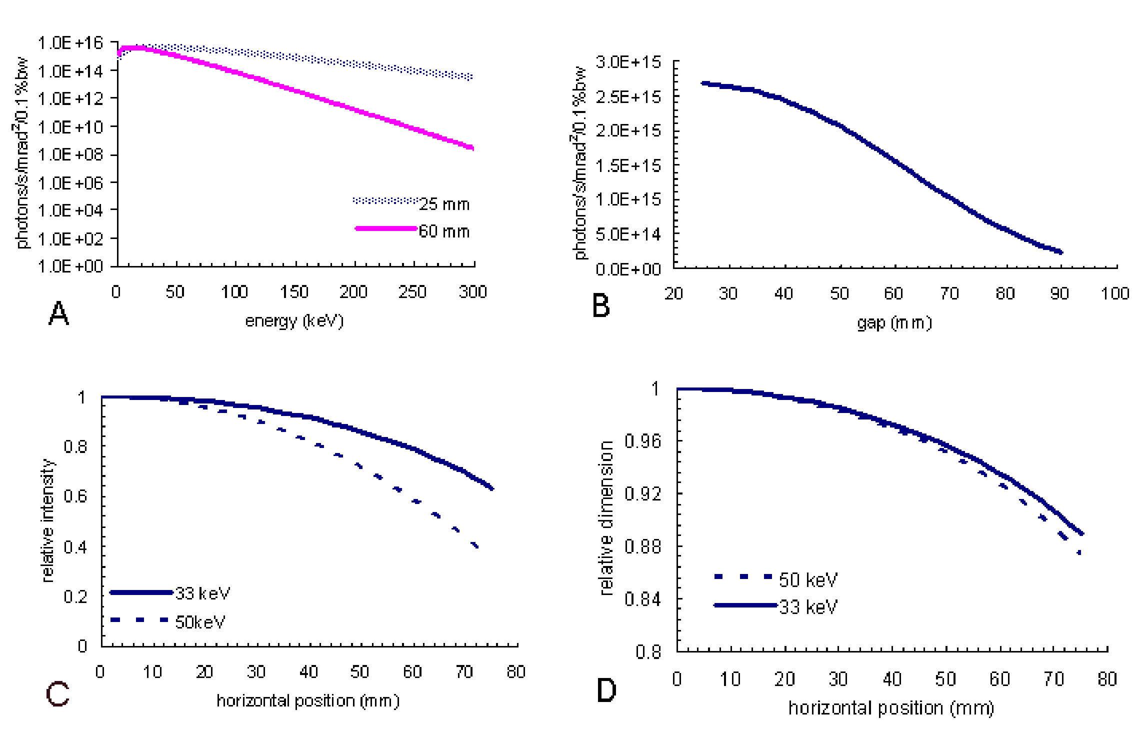

Figure 3.11.
A) Central brightness for an electron current of 200 mA, and a wiggler gap of 25 mm e 60 mm.
B) Central brightness as function of the wiggler gap calculated using parameters values reported in Table 3.5.
C) Horizontal beam profile for $\psi = 0$, a wiggler gap of 60 mm and for photon energies of 33 and 50 keV. The axis origin corresponds to the wiggler axis.
D) X-ray beam dimension in the vertical plane (*yz*), as function of the horizontal position, calculated with respect to its (maximum) value at $\theta = 0$, for a wiggler gap of 60 mm and at 33 keV. The axis origin corresponds to the wiggler axis.

3.6 X-ray coherence properties

X-ray waves emitted by each electron in the storage ring are individually coherent, but waves produced by the different electrons are mutually incoherent. Empirically, "coherence" can be defined as the property that makes a wave capable to produce *observable* interference and diffraction effects on a screen (Margaritondo, Hwu *et al.*, 2001).

Only a point-like single-wavelength source can be defined as a coherent source. But what happens if the source is no longer monochromatic, or no longer point-like, or either, as a real source? The interference fringes will be blurred and, beyond a certain point, they are no longer visible.

The coherence properties of a wave field can be described by time and space dependent correlation functions (Born and Wolf, 1999), respectively linked to the X-ray monochromaticity and to the angular source size. The following definitions are used.

– **Temporal (longitudinal) coherence** implies a phase relationship between the wave $u(t)$ and the wave $u(t+\Delta t)$ separated by a short time delay. The distance covered by the wave during a time delay over which the correlation remains high is called the longitudinal coherence length $l_l = \lambda^2/\Delta\lambda$ where λ is the wavelength. It is associated to the monochromaticity ($\Delta\lambda/\lambda$) of the beam.

– **Spatial (transverse) coherence** indicates the correlation of the amplitudes of waves between different points transverse to the direction of propagation (between the wave $u(x)$ and the wave $u(x+\Delta x)$ in two points separated by a distance Δx). This property is usually expressed in term of lateral (or transverse) coherence length $l_t = \lambda/2\alpha$, where $\alpha = S/L$, L and S are the source-object distance and the dimension of the source, respectively. This properties is associated to the directionality of the beam.

In a more formal treatment, in the case of a quasi-monochromatic beam, a complete description of the spatial coherence is given in terms of *mutual intensity* (Born and Wolf, 1999) $J(x_1,x_2) = \sum u(x_1)\cdot u^*(x_2)$, which expresses the correlation of the wavefield (u) in two different points (x_1,x_2). The *degree of coherence* is obtained by normalizing $J(x_1,x_2)$

$$\gamma^c(x_1,x_2) = \frac{J(x_1,x_2)}{\sqrt{I(x_1)\cdot I(x_2)}} \tag{3.17}$$

with $I(x_1)$ and $I(x_2)$ the intensities of the wavefield at the two considered locations. The degree of coherence is by definition equal to 1 when the two points coincide and it describes the coherence that remains between the two points when they are separated. Moreover, $\gamma^c(x_1,x_2)$ is the Fourier transformation of the source distribution *S*: $\gamma^c(x_1,x_2) = \tilde{S}\left((x_1-x_2)/\lambda z_1\right)$. In terms of degree of coherence, l_t can also be defined as the distance at which $\left|\gamma^c(x_1,x_2)\right| = 1/2$.

3.6.1 Coherence requirements for the phase contrast imaging

To be able to perform phase contrast imaging, the X-ray beam has to fulfil conditions concerning the temporal and spatial coherence properties.

The **temporal coherence** condition ($\Delta\lambda/\lambda \ll 1$) is usually a strong requirement in the case of the analyzer-based imaging technique, but it is easily satisfied in SR facilities using perfect crystal monochromators ($\Delta\lambda/\lambda \le 10^{-4}$). In the case of propagation, even a polychromatic spectrum generated by a conventional micro-focus X-ray tube can be used (Wilkins, Gureyev *et al.*, 1996).

On the contrary, the need of **spatial coherence** is more stringent for propagation-based phase contrast imaging. If the detail set on the object-plane has dimensions smaller (or of the same order) than l_t, it will see the X-ray beam as coherent and it could produce observable phase effects by an appropriate choice of the sample to detector distance (*d*) and of the spatial resolution of the detector. In fact, in the case of small angular source sizes, *d* can be varied at will in the meter range without appreciable blurring of the image ($d \cdot \alpha$).

Concerning the analyzer-based imaging technique, the requirement is that α, as seen by the sample, is smaller than the Darwin width of the crystal-analyzer (see Appendix 1). If the initial beam already satisfies this condition, there is no loss of intensity by the monochromatization/collimation process upstream the sample.

For long SR beamlines such as ID19 at the ESRF (~145 m), the transverse coherence length can be as high as 140 μm at 25 keV in the vertical direction; in the case of a microfocus tube with a typical source size of 20 μm, l_t=0.6 μm for *d*=0.5 m.

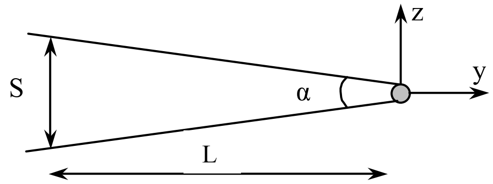

Figure 3.12. Coordinate system and quantities used for defining coherence properties. $\alpha \cong S/L$ **is the source angular dimension,** ***L*** **is the source-object distance and** ***S*** **the source dimension.**

3.7 Why synchrotron radiation is a so interesting tool for X-ray imaging?

Summarizing, the peculiar properties of the synchrotron radiation include:

- high intensity
- broad spectral range
- high degree of polarization
- pulsed time structure
- natural collimation

All these characteristics make the synchrotron light a unique and powerful source for a wide variety of scientific and technological applications. In detail, the SR properties listed above are particularly suited for X-ray imaging for the following reasons:

- A high photon flux, emitted in a small cone and from a small source. Therefore a high spectral brilliance, which enables to reduce considerably the exposure time.

The brilliance of the beam can be as large as 10^{21} photons s^{-1} m^{-2} $mrad^{-2}$ (0.1% bandwidth)$^{-1}$ in the 3rd generation machine.

- The small opening angle of the X-ray beam enables to position the sample at large distances from the source, while preserving a high incident intensity. This plays an essential role for coherent imaging, where the large source-to-sample distance (*L*) and small source size (*S*) are crucial to achieve a high degree of coherence (see Paragraph 3.6). The small source size enables to achieve a good geometrical resolution $R = S \cdot d/L$ (*d* is the sample to detector distance) and a large transversal coherence length, $l_{coh}^{t} \approx \lambda L/2S$ (Paragraph 3.6), of the emitted X-rays.
- The continuous spectrum allows either to select a particular wavelength with a monochromator or, in the special case of X-ray topography (Bragg diffraction imaging), to work in 'white beam' mode, which allows simultaneously recording several diffraction spots of a Laue diffraction pattern, at the same moment.
- The polarisation of the beam, which may be changed, can give access to specific information on the sample, for example through magnetic dichroism.
- The pulsed-time structure can be exploited for time resolved experiments.

3.8 The Biomedical (ID17) and the Tomography & Topography (ID19) beamlines at the ESRF

In this section, I will introduce the ID17 and ID19 beamlines, where the experimental data for this Thesis have been acquired.

– The mission of the **ID17** bio-medical beamline is to take advantage of 3rd generation SR features for biomedical research, and more in particular to carry out pre-clinical and human studies in imaging and radiation therapy. Different kinds of programs have been or are presently performed, including: human coronary angiography, cerebral computed tomography, phase contrast imaging techniques, bronchography, brain perfusion studies, preclinical Microbeam Radiation Therapy (MRT) and Photon Activation Therapy (PAT), and radiobiology investigations.

– **ID19** is mainly devoted to X-ray imaging in general: topography (Bragg diffraction imaging), high-resolution diffractometry, absorption and phase contrast radiography or micro-tomography are the main investigation techniques.

3.8.1 Beamline designs

The main features for the beamline design derive from specific experimental requirements. The X-ray beam, in fact, has to possess:

- spectral and spatial homogeneity
- high coherence (especially at ID19)
- suitable dimensions at the sample position
- high flux
- large energy spectrum for tuning the energy depending on the sample characteristics.

These requirements lead to the choice of long beamlines. ID17 and ID19 experimental hutches are located in separate buildings outside the hall of the storage ring, at 150 m (ID17) and 145 m (ID19) from the source, respectively.

The X-ray sources of the two beamlines are respectively:

- ID17. A multipole wiggler magnet with adjustable gap (21 poles, period 15 cm, max field 1.6 T at the minimum allowed gap - 24.8 mm) with a maximum critical energy at 38.1 keV (unfiltered). The X-ray source size, calculated at gap 60 is 132 × 24 μm^2, as Full Width at Half Maximum (FWHM) (HxV) (See Paragraph 3.5.5). For imaging programs the wiggler is typically operated at a gap of 60 mm (field 0.6 T, critical energy 14.7 keV), which provides a good compromise between the flux available and the contributions of the higher energy harmonics to the beam spectrum. The monochromator systems can extract X-ray beams in the range 18-100 keV.
- ID19. An 11-pole variable-field wiggler (Bmax=1.4 T,period 15 cm, 11 poles, maximum critical energy of 32 keV). The long source-to-sample distance in combination with the very small dimensions of the source (25(V)×125(H) μm^2, expressed as (FWHM)), leads to a highly coherent X-ray beam. Monochromatic X-ray beams are available between 6 and 120 keV for the experimental programs.

The general structures of the two beamlines are very similar. All optical components were designed and manufactured (polished windows, filters, reductions of small monochromator vibrations, etc.) to avoid, as much as possible, spurious images, and /or losses of coherence on the X-ray path, and/or beam inhomogeneities at the sample.

ID17 and ID19 layout consists of:

- A first Optics Hutch (OH1), located just after the front-end at about 30 m from the source, and containing a first set of diaphragms, slits, filters, and shutters for the spectral and geometrical definition of the X-ray beam;

- A long tunnel (100 m long) that connects the OH1 with the satellite building located outside the storage ring hall. In this concrete and lead shielded tunnel, the radiation is transported in a vacuum pipe;
- A second Optics Hucth (OH2 or Monochromator hucth), where are installed a second set of slits, absorbers, beam monitors and the main monochromators (see Paragraph 3.8.2). At ID17, the hutch also contains a fast shutter and a chopper. The latter, in particular, synchronized with the taper optics FReLoN camera, prevents the camera from being exposed during the read out time (see Chapter 4). At ID19, the hutch instead comprises a "stroboscopic shutter", which allows optimisation of the heat load on the sample when working with white beam.
- An Experimental Hutch (EH) and a control room where the different experiment set-ups are installed (including special optical elements, high precision linear or rotating motors for the sample positioning and movement, etc.) and all beamline and experimental elements are remotely controlled. At ID17, in this hutch is possible to have only monochromatic beam, while at ID19 a monochromatic or white beam can be alternatively used. For this reason ID19-EH is a rather highly shielded hutch (Pb thickness shielding is typically 30 mm).

A scheme of the ID17 layout is shown in Figure 3.13. Concerning ID17, it has to be added that the OH1 acts also as experimental hutch for Microbeam Radiation Therapy experiments. When the beam is taken in the second optics hutch (OH2) and experimental hutch (EH) in the satellite building, a flying pipe assures the vacuum continuity. Since a few months, a monochromator system (a fixed-exit monochromator based on two bent Si crystals in the Laue geometry; the energy range, after the preliminary commissioning tests, is 31–120 keV) has been installed in the OH1, so that a white or monochromatic beam can be used in this first hutch.

Annexed to ID17, ia the Biomedical Facility (BMF) where there are ancillary laboratories including e.g. the animal house, the cell laboratory, the sample preparation laboratory, and the molecular biology laboratory for the sample/animals preparation and manipulation.

3.8.2 Monochromators

At ID17 and ID19, energy selection of the X-rays is performed by using silicon crystal monochromators in single crystal or double-crystal configurations. ID19 is also equipped with a multilayer device. The choice between one system or the other depends on the required energy resolution ($\Delta E/E$) for the specific experimental program.

For the experimental data acquired in the framework of this Thesis, double-crystal system monochromators have been used both at ID17 and at ID19.

A brief introduction into the dynamical theory of X-ray diffraction is presented in Appendix 1.

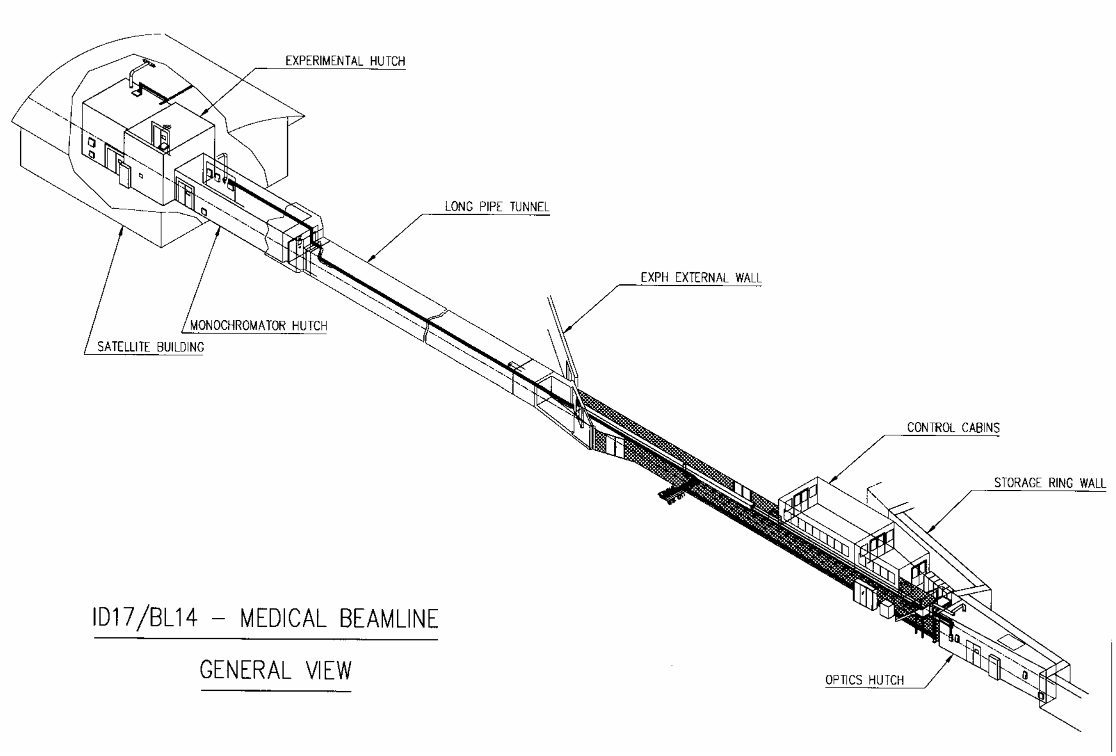

Figure 3.13. The general layout of the ID17 beamline, from the first optics hutch to the satellite building.

In the following Paragraphs I will describe the monochromators used for the acquisition of the experimental results in this Thesis (at ID17 and ID19, respectively).

– ID17

Two monochromator systems are presently operational: 1) a single crystal monochromator (also called "angiography monochromator") and a double crystal monochromator ("CT monochromator") for fixed-exit applications. Both systems run in oxygen-free helium filled chambers, at atmospheric pressure.

- The computed tomography monochromator uses two water-cooled bent Si crystals in Laue geometry producing a monochromatic beam parallel to the incident white beam with a vertical offset of 40 mm. The central part of the crystals is 1 mm thick, 150 mm wide and 12 mm high, cut with an asymmetry angle of 15°. The energy range is 15 to 95 keV.

– ID19

At ID19, both silicon monochromators are based on flat crystal in Bragg geometry configuration. The systems in operation are:

- The horizontal monochromator, located at the beginning of the EH, and consisting of a single crystal diffracting in the horizontal plane.
- The vertical monochromator, which is the main system in use, consisting of a water-cooled fixed-exit double crystal silicon (111) monochromator operating in Bragg diffraction in the vertical plane that provides an X-ray beam of up to 14(V)×40(H) mm^2 at the sample position. It is maintained in a helium flow. The two crystals are set in a non-dispersive arrangement. The symmetrical Bragg setting is chosen because it does not introduced additional divergence in the diffraction plane and consequently does not degrade the coherence properties of the beam. A good monochromaticity degree ($\Delta\lambda/\lambda = 1.8 \cdot 10^{-4}$) is achievable.

3.8.3 The X-ray detectors used at ID17 and ID19

I will here list the different types of detectors used at ID17 and ID19 respectively. In particular, a full description and characterization of the detector I used at ID17 for most of the results presented in this Thesis and the basics of CCD detectors will be given in Chapter 4.

– ID17

- Germanium detector. It is made from a monolithic high purity p-type Ge (B doped with a rate of 10^{18} ion/cm^3) crystal 2 mm thick, 160 mm long, 10 mm high and electrically segmented into two rows of 432 parallel strips each (0.35 mm pitch) (Figure 3.14). It is protected by a 0.5 mm thick beryllium window and cooled at liquid nitrogen temperature (Eurisys Mesures) (Elleaume, Charvet *et al.*, 1999). The 16-bit electronics works in charge integration mode. The efficiency is of nearly 100 % at 33 keV and 45 % at 90 keV (Peterzol, Bravin *et al.*, 2003). In all the K-edge subtraction (KES) imaging methods, the two X-ray beams coming from the angiography monochromator are detected by the dual-line Ge detector. This detector is also used in preclinical brain perfusion experiments, bronchography, low resolution DEI, as well as in bone imaging. In addition, it is a very suitable instrument for beamline alignment purposes and is also routinely used as photon counter to calculate the dose for radiotherapy experiments.

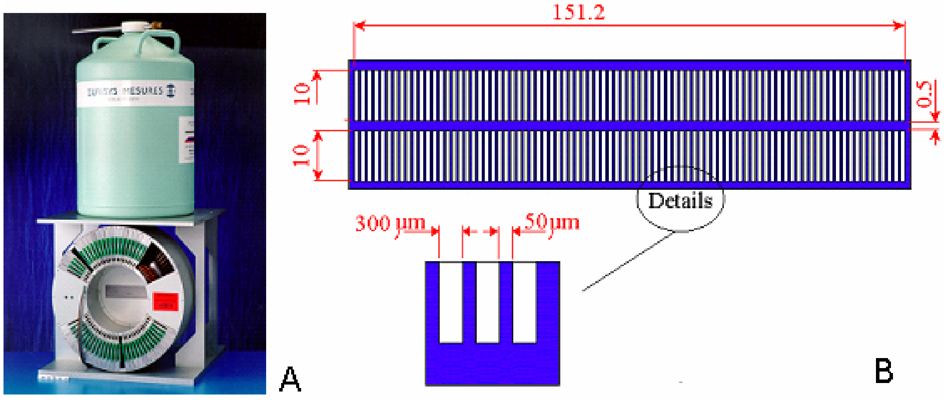

Figure 3.14. A) Picture of the ID17 high purity Ge detector with above its liquid nitrogen cooling system. B) Scheme of the electrical segmentation into two rows of 432 parallel strips each (0.35 mm pitch) of the 160 mm long, 10 mm high Ge crystal.

- Taper optics FReLoN camera. The FReLoN 2000 (Fast Read-out Low-Noise, 2kx2k pixels) taper optics CCD camera is permanently installed in the EH1 (Figure 3.15). Its field of view is 93x93 mm^2 and the pixel size is 46 µm. It is equipped with exchangeable fluorescent screens to optimize the X-ray detection with the X-ray energy. It is routinely applied in CT-DEI mammography and cartilage studies, high resolution Cerebral Blood Value (CBV), bone and palaeontology studies. In addition, a recent development in the detector control system has made it possible to simultaneously acquire two beams for Dual Energy imaging applications.
- High resolution FReLoN optics (operational since 2005). In order to cope with the users requirement for high resolution microCT (for microvasculature and cartilage studies), a 7.5 µm optics has been recently commissioned to be used in combination with an ESRF FReLoN electronics (either 1kx1k or 2k×2k). This is the same kind of FReLoN camera later on described for ID19.

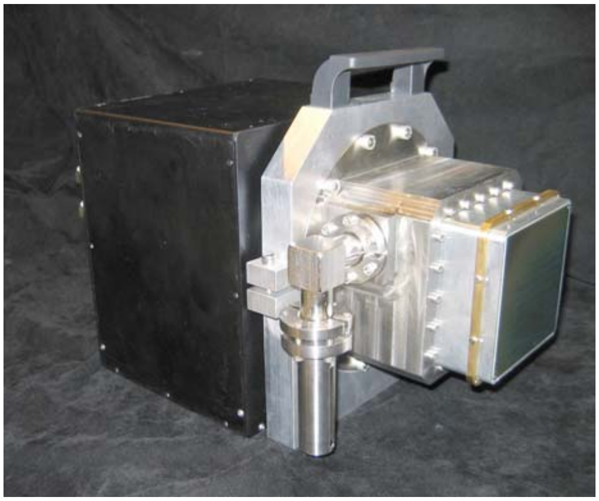

Figure 3.15. The ID17 taper optics FReLoN camera.

– ID19

- Photographic films. They can be: i) standard resolution (SR) films (grain size of 4-5 μm); ii) high resolution (HR) films (grain size smaller than 1 μm); or nuclear plates (grain size 1-2 μm). Besides in the resolution, these devices differ in their exposure time and developing process. Despite the low dynamic range and non-linearity, films offer the advantage of having large field of view and high spatial resolution.
- FReLoN CCD based X-ray detector (see Figure 3.16). Actually, two models of this detector are available: the 1024×1024 pixels CCD chip with 19 μm pixel size and the 2048×2048 pixels CCD chip with 14 μm pixel size. Different kinds of fluorescent screens and coupled visible light optics (and therefore different spatial resolutions) can be used. In particular, six different optical systems consisting in magnifying or de-magnifying lenses are available. The configurations used for some images presented in this Thesis are:

  - "the 10 μm pixel optics" with a 10 μm thick Gadox powder scintillation screen (see Chapter 4), resulting in an effective pixel size of 7.5 μm in the image (with a spatial resolution of about 16 μm (Cloetens, 1999)) and providing a maximum field of view of 15.3×15.3 mm^2.
  - "the 40 μm pixel size optics", combined with a 50 μm thick Gadox powder scintillation screen, generating an effective pixel size of 30.30 μm with a maximum field of view of 31×31 mm^2.

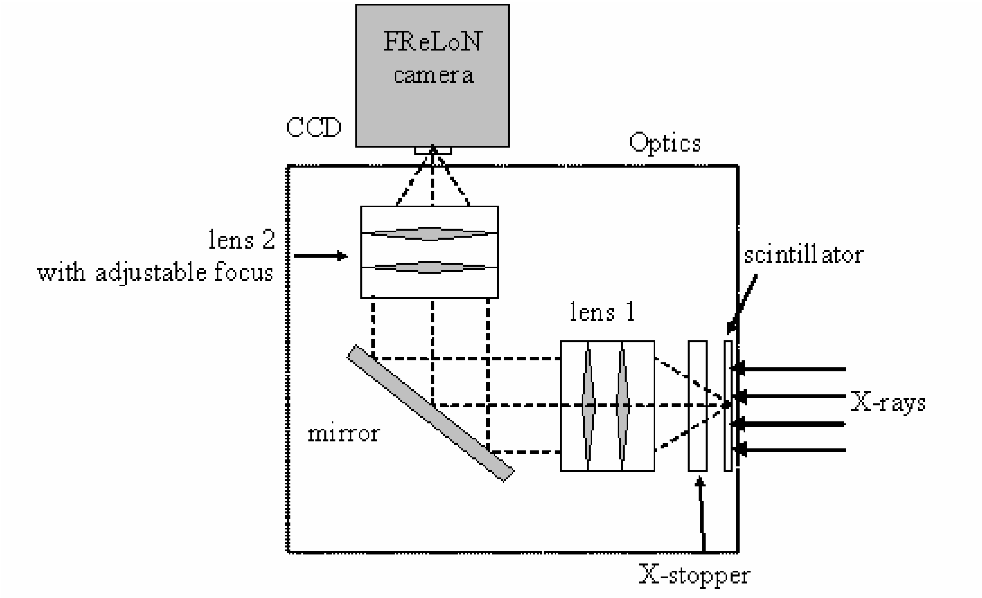

Figure 3.16. Principle of the ID19 FReLoN camera detector including an X-ray/visible light converter (scintillator), optical lens coupling and a cooled CCD camera.

3.8.4 Beamline control system

All elements and motors of the beamlines, the large amount of data and images acquired during an experiment are remotely controlled in the ESRF standard way, using the software package SPEC (University of Wisconsin). This Unix-based program for instrument control and data acquisition is widely used for X-ray and neutron diffraction at synchrotrons and various laboratories. Special macros that facilitate and, in same cases, automate the beamline alignment and data acquisition are available.

The data are then transferred and stored on an ESRF central computer NICE (Networked Interactive Computing Environment). NICE permits the manipulation and processing of large data volumes and the image processing with shared software such as Matlab, IDL or Python for example.

3.9 Experimetal set-ups for the PBI and ABI techniques

The ABI experimental acquisitions presented in the framework of this Thesis have been performed both at ID17 and at ID19, while the PBI only at ID19. The set-ups used at the two beamlines are hereafter separately described.

The SR beam that impinges on the sample in both cases, is monochromatized by the main monochromator that are the fixed-exit double (111) silicon crystal system respectively in Laue (ID17) and Bragg (ID19) geometry.

3.9.1 ABI instrumentation at ID17

The ABI set-up of ID17 is schematically shown in Figure 3.17, while a photograph is reported in Figure 3.18.

All instruments are placed on a very stiff optical table in the experimental hutch at about 155 m from the source. The table efficiently decouples the optics from the floor for increased stability. The beam coming in the hutch from the Laue crystal is monochromatized to narrower band-pass by a Si Bragg crystal (n° 1 in Figure 3.17). The monochromator, as well as all the other instruments, is placed on high-resolution stages, which are remotely controlled for alignment and acquisition purposes. The sample (n° 3) is vertically scanned through the beam for projection images, whereas it sits on a rotation stage for CT imaging.

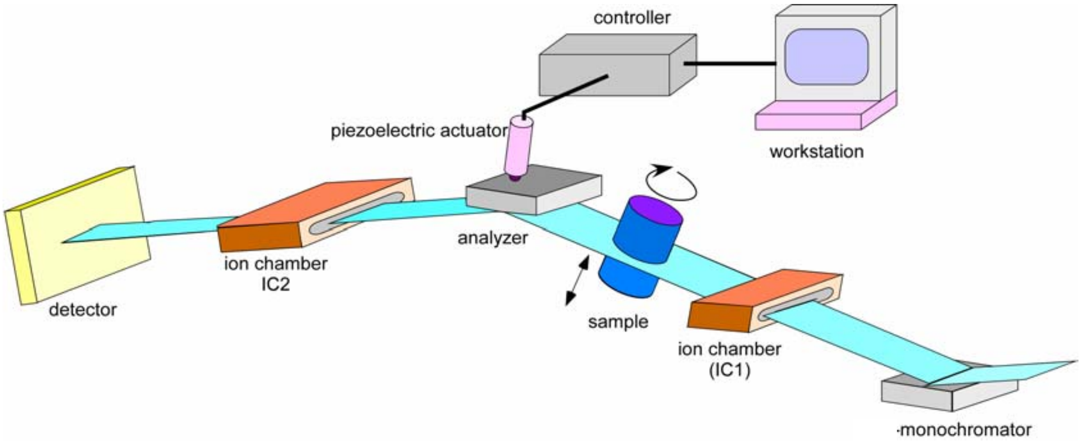

Figure 3.17. Scheme of the ABI set-up at ID17.

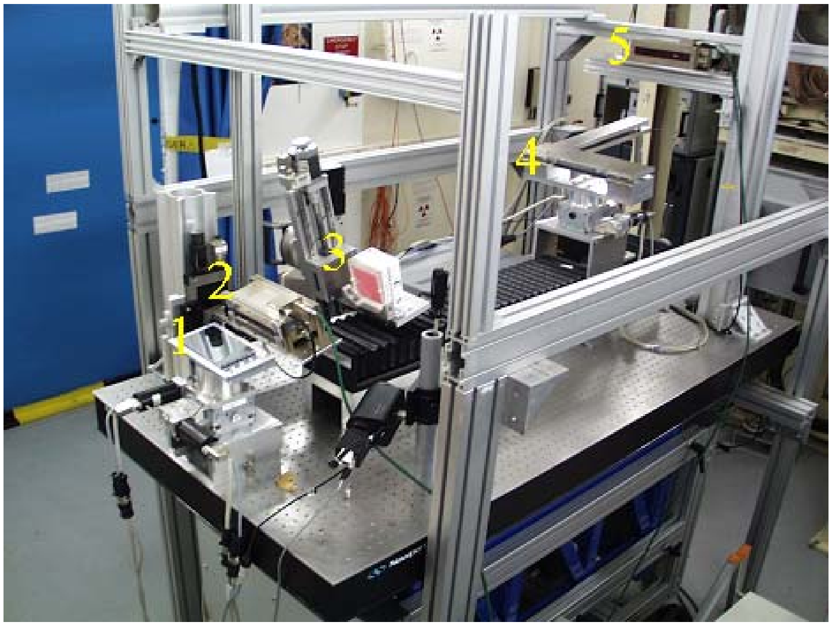

Figure 3.18. Photograph of the ABI set-up at ID17.

A Si crystal (n° 4), which is identical to the first one (and set at the same reflection cut), is used to analyze the beam emerging from the sample. Two ionization chambers are used to control the incoming X-ray beam intensity. The first is in front of the sample (n° 2) and the second is placed behind the analyzer (n° 5-in the Figure, it is not in the X-ray beam). The latter is used both to align the analyzer and to control the beam intensity on the detector.

<u>More in detail:</u>

- The <u>monochromator crystal stage</u>, presented in Figure 3.19(A), consists a tower bearing the crystal (n° 3) and mounting on a "theta" (n° 1) and "roll" (n° 2) tilt motors. In particular, "<u>theta</u>" indicates the angle with respect to the X-rays propagation direction and "roll" the angle with respect the perpendicular direction. The two tilt motors have a resolution of 0.25x10^{-3} degrees. In the same figure the first ionization chamber (IC1 - n° 4) is visible.

- The sample stage, for both projection and CT imaging, is mechanically decoupled from the optical table, in order to not transmit vibrations from the sample motors to the crystals during motors movements and acquisition scans. Figure 3.19(B) shows the sample stage, which is anchored to a transverse bar directly fixed on the floor. The sample stage consists of:

  - a high resolution vertical (*z*) translation motor (n° 2), used for scanning the sample through the laminar SR beam. The motor resolution is 1 μm.

  - a horizontal (*y*) translation motor (n° 1) (motion perpendicular to the X-rays direction) for centering the sample with respect to the center of the beam and put it in/out of the beam for reference images acquisitions (motor resolution = 0.1 μm).

  - a rotation stage (n° 3) for tomographic imaging (resolution = 0.01 degrees).

  - a "theta" tilt motor (n° 4) for angularly aligning the sample with respect to the X-ray beam direction, in particular to position the object to image perpendicular to X-rays (resolution = 0.01 degrees).

  - a "roll" tilt motor (n°5) for sample alignment purposes (resolution = 0.25x10^{-3} degrees).
- The analyzer crystal stage is shown in Figure 3.20. It is fixed on a 50 cm long arm which is angularly controlled by means of a piezoelectric motor (n° 2) (resolution 0.1 μrad) by determining the analyzer tuning. Like for the monochromator, the tower bearing the analyzer crystal is placed on a double cradle (" theta" (n° 3) and "roll" tilts (n° 4)) for alignment and acquisition purposes. The entire stage can be moved along the beam direction (n° 1) in order to keep a fixed exit when varying the energy of the beam.
- The optical table is equipped with a vertical translation motor which allows to align the whole set-up with respect to the X-ray beam.

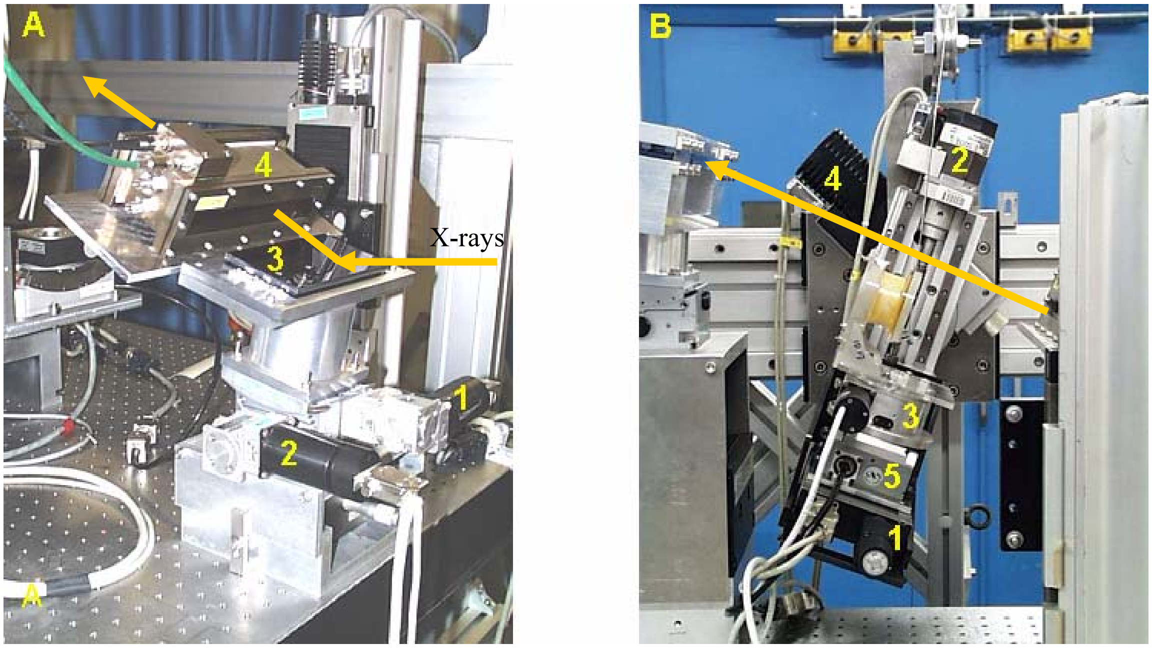

Figure 3.19. A) The pre-monochromator stage (n° 1, 2, 3) and the IC1 (n° 4). B) The sample stage (n° 1-5).

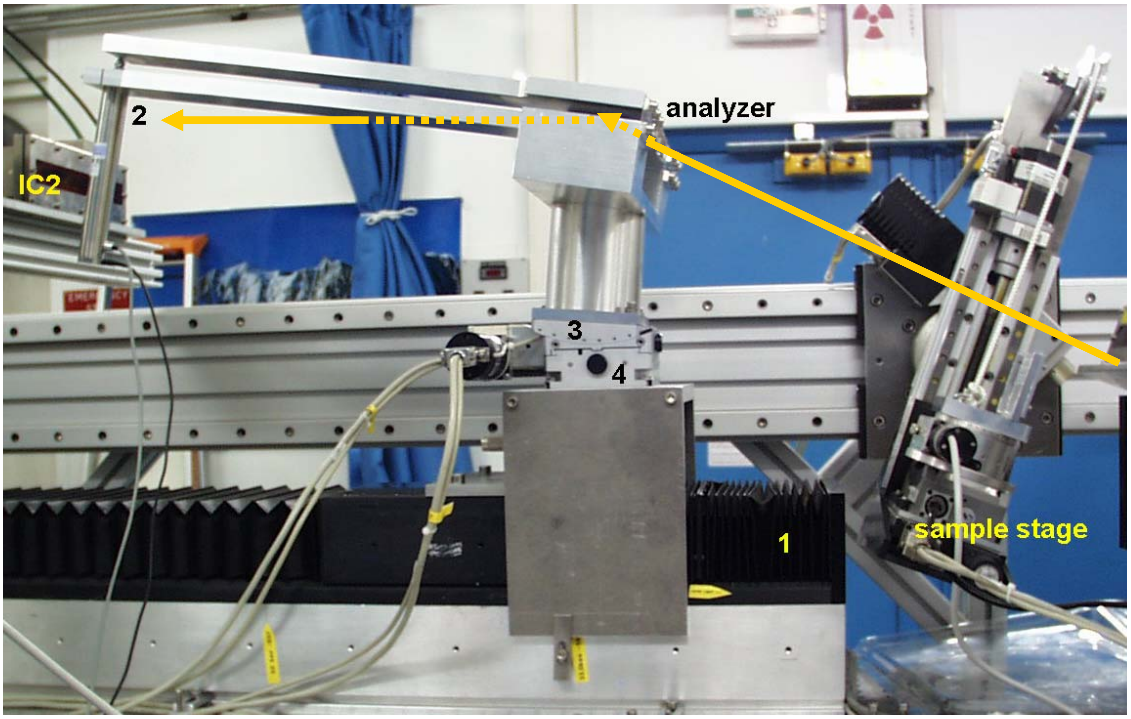

Figure 3.20. The analyzer stage (n° 1-4) (IC2 is out of the X-ray beam).

- A laser, installed upstream at the entrance of the X-ray beam in the EH, and aligned with the beam, serves as indicator for the positioning of the different optical elements and of the sample. For a finer control of the X-ray beam position, "burn" paper (Kodak® linagraph direct print paper) sensitive to X-rays is used.
- The pre-alignment of all optical elements is made by using a level and a theodolite.

- When "low" energies (18-30 keV) are used, a vacuum pipe is installed between the EH entrance and the monochromator in order to reduce the X-ray attenuation and scattering before the sample (Figure 3.21).

Figure 3.21. The vacuum pipe which is installed in the EH at ID17 when working a low energies (18-30 keV).

<u>Set-up limitations and improvements</u>

- The actual ID17 ABI set-up is quite compact. All optical elements are installed in the same table and the sample support is located between the IC1 and the long horizontal stage of the analyzer (n° 1 in Figure 3.20). The space available for the sample is limited and in case of big samples (e.g. animals etc.) even insufficient; it could be sometimes impossible to scan the whole sample through the beam.

In order to overcome this limitation, a solution could be to put the monochromator and the IC1 on another vibration-free optical table.

- Due to the very small acceptance of the analyser crystal, the main challenge in this kind of experiment is the insurance of the overall stability of the whole system. Dedicated mechanical systems have been developed to eliminate vibrations coupled to the floor.

A Monochromator Controller (MOCO) developed by the Instrument Support Group of the ESRF has been recently successfully integrated in the ABI set-up (scheme in Figure 3.22). This device permits to tune dynamically the analyser piezo actuator as a function of the measured intensity of the beam and its stabilization by means of a feedback system. In particular, the ratio between the intensity measured by IC1 and a diode placed after the sample in a portion of the beam that has not passed through the sample is controlled and kept constant during the acquisition.

- The crystals fixation is a really critical point of the set-up, in particular for the analyzer in this case. The actual system is based on screw clamps at the edges of the crystal. If not sufficiently tightly but strain-free fixed, crystals may vibrate and/or drift, or be distorted respectively causing beam dishomogeneities or gradients. An optimized fixation system is under study.

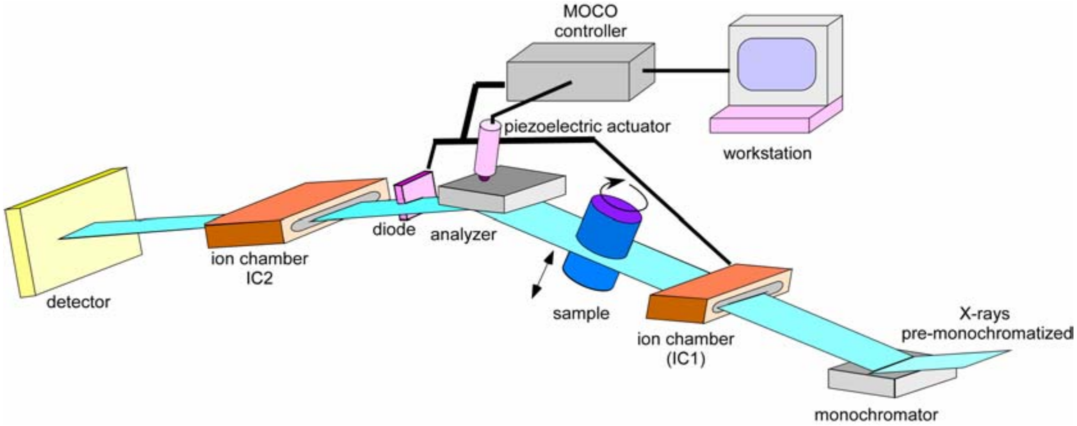

Figure 3.22. Scheme of the analyzer crystal feedback control system.

3.9.2 The PBI and ABI instrumentation at ID19

The instrumentation for PBI and ABI set-ups is identical except the additional optical component for the ABI set-up, which is the analyzer crystal.

Since the high stability requirements of the analyzer crystal, the ABI instrumentation is put on a light frame KB table (Figure 3.23). This table is mainly implemented to support a Kirkpatrick-Baez (KB) mirror set-up. Its good stability is due to its low mass and high rigidity. Pneumatic airpads allow to move and perform a pre-alignment of the table.

- The analyzer crystal stands on a support attached to a high precision rotation (angular resolution: 0.9 μrad) (n° 2 in Figure 3.23). In this way, a series of images can be very conveniently and rapidly acquired along the rocking curve. The resolution of the rotation can be increased using an appropriated electronics, which is adapted to the stepping motor driver and allows to control the motor in a microstep range. This system was used when working with the 333 reflection.
- A horizontal translation under the rotation stage allows to bring the center of the crystal at the exact beam position, or to remove the crystal completely from the beam path in order to switch to the PBI mode.
- Vertically, to reach the height of the beam, a bench supporting the rotation device was added and fixed to the table.
- A tilt of 5 μrad resolution, inserted under the crystal and fixed to the rotation plate enables to perform "theta" alignment of the crystal in a parallel way with respect to the beam geometry and

therefore to correct for misalignment in the horizontal direction.

- For large samples, a long range translation stage in vertical and horizontal directions, enables to move the specimen at the desired position or remove it from the beam to take a series of reference images.

Other details:

- To switch from one set up to the other one is actually easy: the crystal is horizontally translated in or out of the beam and the detector unit is moved close or far away from the sample. The maximum sample-to-detector distance attainable in the hutch is 8.8 m.
- The incident beam on the samples is monitored by a large, nitrogen filled ionization chamber that possesses two thin Kapton® foils on the entrance and exit sides.

Monitoring each measurement is necessary to account for the decreasing intensity that follows the decay of the synchrotron radiation storage ring current. The monitor is calibrated for the different X-ray energies with a standard PTW 23342 ion chamber and a high precision electrometer (PTW UNIDOS dosimeter).

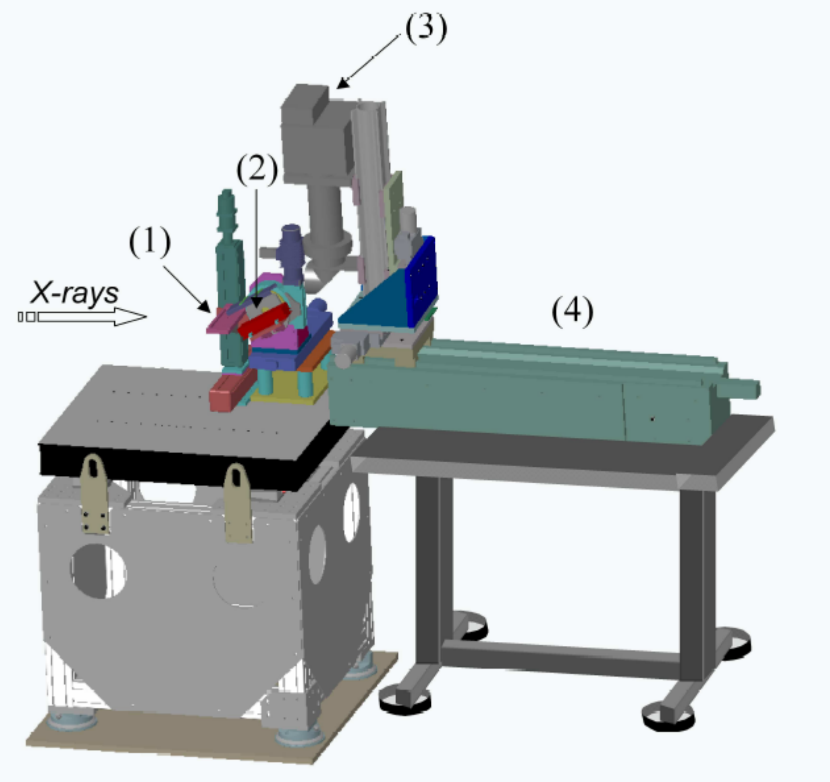

Figure 3.23. Drawing of the experimental station used for ABI and PBI set-up, in the case of large samples. (1) sample stage, (2) analyzer stage for ABI, (3) detector unit with the FReLoN CCD camera, (4) table with detector translation along the beam for ABI.

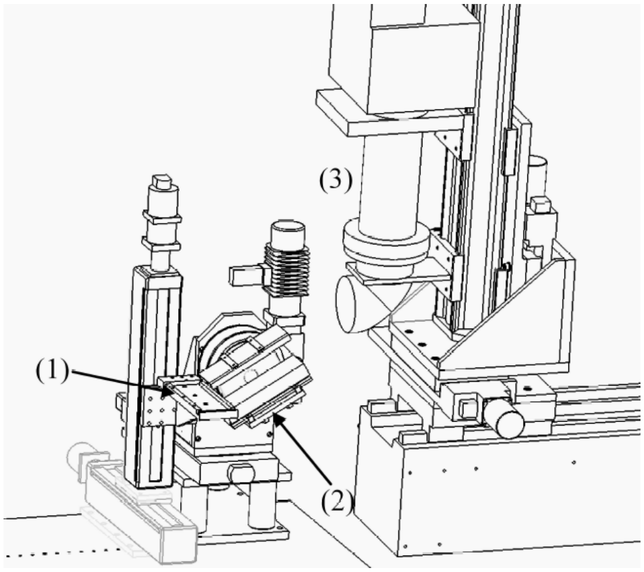

Figure 3.24. Zoom on the central part of the ABI set-up: (1) Sample stage with horizontal and vertical motorized translation, (2) crystal analyzer stage for ABI, with a horizontal motorized translation, allowing to align the centre of the crystal with the beam or remove it from the beam path in the PBI case, (3) detector system with a vertical motorized translation, permitting to adjust the detector with the height of beam.

REFERENCES

M. Born and E. Wolf (1999). *Principles of optics: electromagnetic theory of propagation, interference and diffraction of light*. C. U. Press. Cambridge.

W. Brefeld and P. Gurtler (1991). *Synchrotron Radiation Sources. Handbook on Synchrotron Radiation*. S. Ebashi, M. Koch and E. Rubenstein. Amsterdam, Elsevier Sience Publishers. **4:** 269-296.

J. Bushber (1994). *The essential physics of medical imaging.* Baltimore, Williams & Wilkins.

F. E. Carroll, M. H. Mendenhall, R. H. Traeger, C. Brau and J. W. Waters (2003). "Pulsed, tunable monochromatic X-ray beams from a compact source: New opportunities." American Journal Roentgenology **181**.

P. Cloetens (1999). Contribution to Phase Contrast Imaging, Reconstruction and Tomography with hard Synchrotron Radiation. Principles, Implementation and Applications. Vrije Universiteit. Brussel.

H. Elleaume, A.-M. Charvet, P. Berkvens, G. Berruyer, T. Brochard, Y. Dabin, M. Dominguez, A. Draperi, S. Fiedler, G. Goujon, G. Le Duc, M. Mattenet, C. Nemoz, M. Perez, M. Renier, C. Schulze, P. Spanne, P. Suortti, W. Thomlinson, F. Esteve, B. Bertrand and J.-F. Le Bas (1999). "Instrumentation of the ESRF medical imaging facility." Nucl. Instr. and Meth. A **428**: 513-527.

ESRF (1987). Foundation phase report. Grenoble.

A. Fukasawa, H. Iijima, M. Uesaka, J. Urakawa, T. Higo, M. Akemoto and H. Hayano (2001). "Compact hard X-ray source via inverse Compton scattering based on the X-band LINAC." Proceedings of the Second Asian Particle Accelerator Conference (China).

Hercules (1993). *Neutron and sunchrotron radiation for condensed matter studies*. J. Baruchel, J. Hodeau, M. Lehmann, J. Regnard and C. Schlenker. Berlin, Springer Verlag. **I**.

G. Margaritondo, Y. Hwu and G. Tromba (2001). "Synchrotron light: from basics to coherence and coherence-related applications." Lezioni della VI scuola nazionale di luce di sincrotrone S. Margherita di Pula, Italy.

A. Peterzol, Bravin, A., Coan, P. and H. Elleaume (2003). "Image quality evaluation of the angiography imaging system at the European synchrotron radiation facility." Nucl. Instr. Meth. A **510**: 45-50.

W. Röntgen (1895). Über eine neue Art von Strahlen. Sitzungberichte der physikalisch-medizinischen Gesellschaft. Würzburg, Germany, Physics and Medical Society of Würzburg**:** 132-141.

P. Suortti and W. Thomlinson (2003). "Medical applications of synchrotron radiation." Phys. Med. Biol. **48**: R1-R35.

S. Wilkins, T. Gureyev, D. Gao, A. Pogani and A. Stevenson (1996). "Phase-contrast imaging using polychromatic hard X-rays." Nature **384**: 335-338.

4

FReLoN camera characterization

Contents

Une caméra optique CCD appelée FReLoN est un détecteur utilisé couramment sur ID17. Dans ce chapitre, son optique de conversion est évaluée à travers la fonction de transfert de modulation (MTF), la densité spectrale de puissance de bruit normalisé (NNPS) et l'efficacité quantique de détection (DQE). Les mesures ont été effectuées pour plusieurs énergies monochromatiques entre 20 et 86 keV avec un écran à base de gadolinium variable en épaisseur. L'acquisition et l'analyse des données ont été réalisées en adaptant les protocoles utilisés pour les faisceaux coniques ordinaires à la géométrie plane du faisceau synchrotron. A la fin de cette section, les caractéristiques de la caméra FReLoN sont comparées avec les performances de détecteurs recensés dans la littérature.

In this chapter the full assessment of the imaging performance of the taper optics CCD "FReLoN" camera, an indirect conversion detector routinely used at ID17, is presented in terms of modulation transfer function (MTF), normalized noise power spectrum (NNPS), and detective quantum efficiency (DQE). Measurements were made at various monochromatic energies in the range 20-86 keV for a gadolinium-based fluorescent screen varying in thickness; data acquisition and analysis were made by adapting to the synchrotron beam laminar geometry protocols used for conventional cone beams. At the end of the chapter the results of the FReLoN characterization will be compared with a selected number of detectors presented in the literature.

4.1 Introduction

The presently developed SR imaging techniques require a detector of sufficient field of view for small animal imaging (~10 cm), with a pixel size suitable for high resolution imaging (50 μm or smaller). In-vivo projection and tomographic studies require a low noise and fast readout system adapted to a laminar beam. In addition, the detector must maintain a high efficiency over a wide energy range, to minimize the dose delivered to the sample and to minimize the imaging time.

Detectors specifically developed for SR imaging are extremely rare (only (Yagi, Katsuaki *et al.*, 2004) and (Yagi, Yamamoto *et al.*, 2004)). However, several commercial detectors for X-ray medical imaging exist on the market, highlighting simultaneously one or several of such characteristics, but unfortunately do not feature all at the same time.

Literature on medical radiology has mainly focused on amorphous Selenium (a-Se) or amorphous Silicon (a-Si) Flat-Panel (FP) and charge-coupled device (CCD) detectors coupled to different kind of scintillators. In most of the cases, detectors with a large field of view are generally characterized by rather large pixel sizes (~0.1-0.2 mm) (Granfors and Aufrichtig, 2000; Samei, 2003; Samei and Flynn, 2003). Higher spatial resolutions and good performances in terms of DQE (although strongly energy-dependent) are offered by a-Se and a-Si FPs coupled to gadolinium oxysulphide (GOS) screens, and by CCDs coupled to thallium-doped caesium iodide (CsI:Tl) screens (Goertzen, Nagarkar *et al.*, 2004). Nevertheless, the field of view, and/or the readout speed do not always fit the specific needs of the different medical imaging applications performed at SR facilities.

A more detailed discussion on detectors presented in the literature is reported in Paragraph 4.7.

To match the specific requirements of SR medical imaging, the Detector Pool of the ESRF in collaboration with ID17 scientists has developed a taper optics CCD Fast Readout Low Noise "FReLoN" detector, whose evaluation is presented here. The FReLoN camera is characterized by a specific optics, which has been tailored for medical imaging purposes. The electronics and the data acquisition system, also developed at the ESRF, have been incorporated in several cameras (>10) used at different ESRF beamlines, each one coupled to a beamline-tailored optics.

The large-area transfer characteristic, the Modulation Transfer Function (MTF), the Noise Power Spectrum (NPS) and the Detective Quantum Efficiency (DQE) have been calculated at different beam energies and for two different X-ray converters (fluorescent screens).

Unlike conventional sources, there is no established standard procedure for a complete evaluation of the detector performances when a laminar X-ray beam is used; neither is there any reference in the literature on this subject.

It is also presented in detail how I have adapted to this case the image quality assessment procedures used for conventional sources.

This work on the characterization of the FReLoN camera detector has been reported in a publication:

– P. Coan, A. Peterzol, S. Fiedler, C. Nemoz, C. Ponchut, J. C. Labiche, A. Bravin, "Evaluation of image performance of a taper optics CCD "FReLoN" camera designed for medical imaging", *Journal of Synchrotron Radiation*, Vol.13, 260-270, 2006.

4.2 The "FReLoN" camera detector

The Fast Readout Low Noise (FReLoN) CCD camera coupled to a fiberoptical taper used at ID17 has been developed at the ESRF for a broad range of applications; its specifications were initially tailored for Computed Tomography applications in Diffraction Enhanced Imaging mammography (Bravin, Fiedler *et al.*, 2003).

The FReLoN taper optics shows an active input surface of 94 x 94 mm^2 where X-rays are converted to visible light by a fluorescent screen; this secondary radiation is then guided by a fiberoptic taper with a 3.2:1 reduction ratio and extra-mural absorption (Schott) onto the 2048 x 2048 pixel^2 14 x 14 µm^2 CCD (Atmel Corp, USA). This reduction allows an effective pixel size of about 46 x 46 µm^2 to be achieved.

Thanks to a careful design of the electronics and to a Peltier-type cooling of the CCD (standard operation at –18 ºC), both readout and dark signal levels are kept low (1.4 ADU/pixel rms, respectively 0.01 ADU/(pixel*s) rms without binning[1]). At the same time, a maximum readout

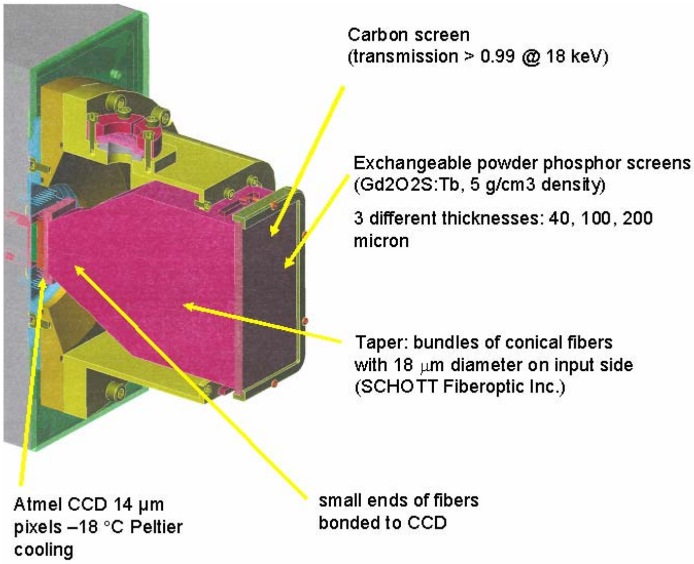

---

[1] Analogical to Digital Unit (ADU) and root mean square (rms)

Figure 4.1. Structure of the taper optics FReLoN camera.

speed of 20 Mpixels/s through four outputs provides the possibility of high frame rate imaging (4.2 frames/s) in full size image mode without binning (Figure 4.1). The gain is constant and it is 23 electrons/ADU; the maximum analogical-to-digital readout of 2^{14} bits corresponds to $3*10^4$ electrons whatever the binning applied.

The fluorescent screen can be easily exchanged in order to optimize the X-ray conversion with the different experimental applications and the selected energy. The camera can be coupled to powder phosphor screens ($Gd_2O_2S:Tb$, 5 g/cm^3 density) of 40 μm, 100 and 200 μm thicknesses. The thin screen favors the spatial resolution at the expense of absorption efficiency, whereas the thicker screen provides the opposite compromise. Both screens consist of an active phosphor layer deposited on a thin plastic film substrate, the active layer being in direct contact with the fiberoptic taper input surface.

Taking into account the phosphor screen light yield, the optical coupling efficiency and the CCD quantum efficiency, the system quantum conversion ratio with the 40 μm screen is 6-7 electrons per absorbed 10 keV photon.

4.2.1 The "FReLoN" camera read out system

The camera offers a set of acquisition/readout modes adapted to various experimental conditions. The CCD lines can be read independently or binned either horizontally and vertically.

In the so-called "full frame mode", used for projection imaging, the sample must be scanned through the fan beam while the detector is moved in the same direction. At the end of the scansion, the whole CCD is electronically split in four quadrants, each read out by a channel at 206 μs per line (Figure 2). Small regions of interests (ROIs) can also be selected and, if this is the case, the read out time is proportionally reduced.

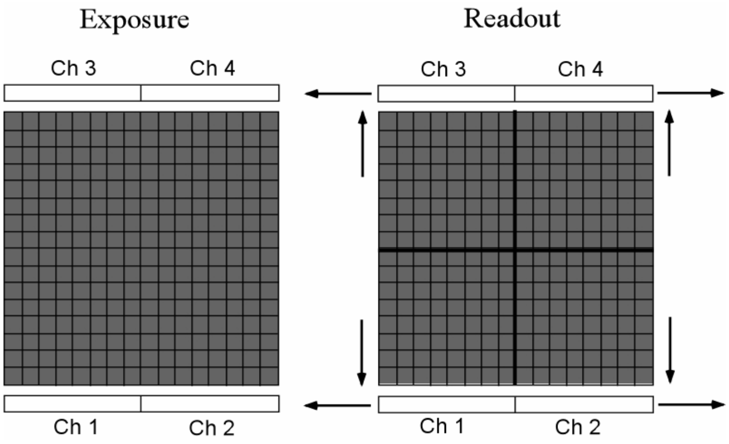

Figure 4.2. Full frame mode. Readout starts at the end of the exposure; each of the four quadrants (1024x1024 pixel2) is readout by a channel.

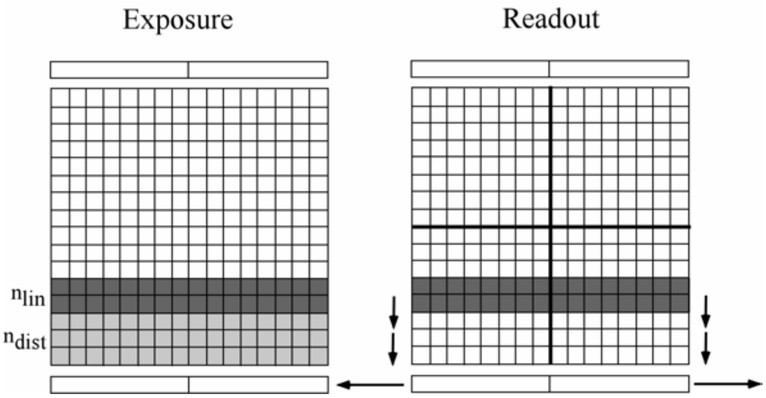

Figure 4.3. Pipeline mode. The image size is reduced to nlin lines at ndist (in the figure: nlin =2 and ndist =3) from the nearest output channels. This image is then sequentially treated as in the full frame mode, but only two channels on one side of the CCD are used for the readout.

The “pipeline mode” is used for Computed Tomography imaging. The sample is scanned in front of the detector that is kept stationary: the same lines are thus continuously exposed (their number depends on the beam height on the camera). The image is performed by illuminating nlin lines at ndist pixels from the nearest output channel. Each part of the image is then shifted towards the closest serial outputs (10 µs per line) where each line is read out (206 µs per line) (Figure 3).

The total dead time is given by:

$$Dead\ time = \left(n_{dist} + n_{lin}\right) \cdot 10\,\mu s + \left(n_{lin}/bin\right) \cdot 206\,\mu s \tag{4.1}$$

where bin corresponds to the chosen binning factor.

The number of lines that can be recorded in this mode is limited only by the RAM memory of the acquisition computer.

A variation of the "pipeline" mode (called “concatenate mode”) consists in the read out of a ROI between two movements of the sample without moving the detector; the image is then reconstructed from cumulated ROIs. This last variant has been used for the acquisition of the edge profiles (Edge Spread Function) for the calculation of the MTF.

The maximum possible binning for these modes is 2(H) x 2(V) line^2 for the “full frame mode”, and 2(H) x 1024(V) line^2 for the “pipeline” and the “concatenate” modes.

A further acquisition mode, the so called “hybrid mode” has been implemented for faster CT imaging. As in the pipeline mode, the detector is stationary and each projection is made of few lines (nlin). After being illuminated, the lines are shifted towards the two farthest outputs, to fill the CCD. This new "image", made of elementary parts, is then read out as in the full frame mode (Figure 4). This procedure reduces the dead time between two projections but their maximum number is limited to 2048/nlin.

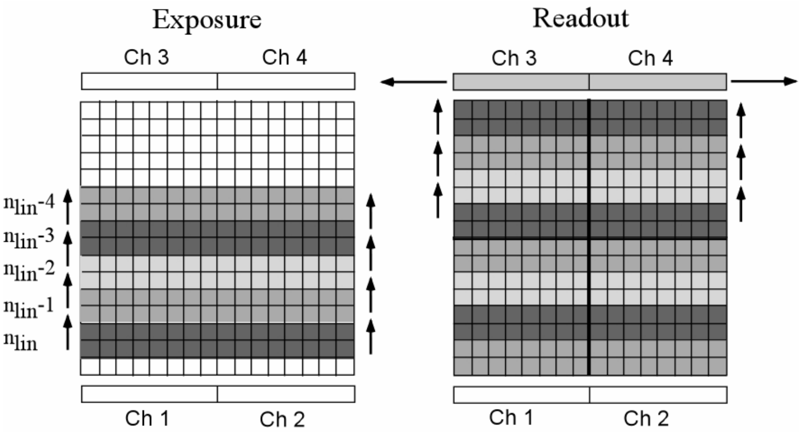

Figure 4.4. Hybrid mode. The full frame is filled by elementary "pipeline mode" images, then the readout of the CCD is performed.

4.3 The reference detector: the germanium pixel detector

The measurements of the detector exposure were performed by using the high-purity germanium detector (HPGe) operating at the liquid nitrogen temperature (already introduced in Paragraph 3.8.3).

This receptor allows a highly efficient detection (Peterzol, Bravin *et al.*, 2003) of X-rays in the energy range used for the characterization of the FReLoN camera. The germanium detector and the FReLoN camera are installed on top of each other on a same remotely controlled support that can vertically translate; in this way, the two detectors can be alternatively positioned in the beam, allowing a constant distance from the source.

4.4 Detector performance assessment parameters

4.4.1 Large-area transfer characteristic

The linearity of the digital system has been verified in the exposure range used for the NPS measurements. The verification of the system linearity response is necessary to allow for the direct use of digital pixel value in the rest of the analysis; in this way the linear-system approach can be applied to characterize the detector performances in the spatial-frequency domain (Cunningham, 2000). A large-area transfer characteristic curve has been determined by measuring the detector output in terms of pixel values versus the input photon fluency. In the NPS study, ten flat-field images per energy and per exposure level have been acquired in pipeline mode. For each image set, the mean pixel value has been calculated by averaging the ten mean values obtained from a same central part of each image over an area of 1280(H) x

512(V) pixel^2 (~ 59 x 23 mm^2). The number of incoming photons was varied by means of a set of plexiglas attenuators and evaluated as described in Paragraph 4.4.4.

4.4.2 Modulation Transfer Function (MTF)

The MTF is defined as the two-dimensional Fourier transform amplitude of the point spread function (PSF), which is the system response to a delta-shape input signal; it is typically used to characterize the resolution properties of an imaging system in the spatial-frequency (*u*) domain. In order to access the one-dimensional MTF in both horizontal and vertical directions, I have chosen to calculate the MTF as the one-dimensional Fourier transform of the line spread function, as detailed later.

The crucial point in the calculation of the MTF is the fineness of the sampling of the signal: if the spatial frequencies are not sampled closely enough to avoid aliasing, the system is no longer adequately described by the linear-system model. If this is the case, the fundamental requirement of spatial invariance fails (Dobbins, 2000). Many different techniques have been developed to determine the MTF of a detection system. In the literature, the MTF is experimentally determined by imaging a bar pattern test phantom, which gives the system response to a square-wave input signal (Johns and Cunningam, 1971; Borasi, Nitrosi *et al.*, 2003). Alternatively, it is indirectly determined from the line spread function (LSF) or from the edge spread function (ESF) which is measured by imaging narrow slits (Fujita, Doi *et al.*, 1985) and opaque edges (Samei, Flynn *et al.*, 1998), respectively. To overcome aliasing effects, it is possible to slightly tilt the slits (or the edge) in order to obtain more finely sampled LSF or ESF and the presampling MTF (Samei, Flynn *et al.*, 1998; Dobbins, 2000; Greer and van Doorn, 2000).

For the determination of the MTF, I have chosen the edge method by using a 50 x 50 mm^2, 0.3 mm-thick tungsten foil for all the energies. The ESF was measured in both the horizontal and vertical directions by acquiring an image of the edge phantom with a 2 μm scanning step (*a*). Each MTF is the average of the MTFs calculated by several determinations of the ESF (~70 for the vertical direction and ~20 for the horizontal). The horizontal ESFs were reconstructed by shifting each data row of a relative interval of 23 pixels (=horizontal pixel size/scanning step). From the ESF profiles, LSFs have been calculated by the finite-element difference method:

$$LSF(x_j) = ESF(x_{j+1}) - ESF(x_j) \tag{4.2}$$

where $LSF(x_j)$ is the jth value of the LSF and $ESF(x_j)$ and $ESF(x_{j+1})$ are the adjacent values of the ESF. As the differentiation process reduces the SNR (Cunningham and Fenster, 1987), the ESFs have been smoothed before LSF calculation by using the Matlab "cubic smoothing spline" function. Finally, the MTF has been determined as the modulus of the discrete Fourier transform of the LSF using a discrete spatial frequency interval (*u*) given by $1/Na$, where N is the number of sample points of the ESF. The presented MTF values have been normalized with respect to the MTF at zero frequency (MTF(0)) (the scheme of the procedure is shown in Figure 4.5).

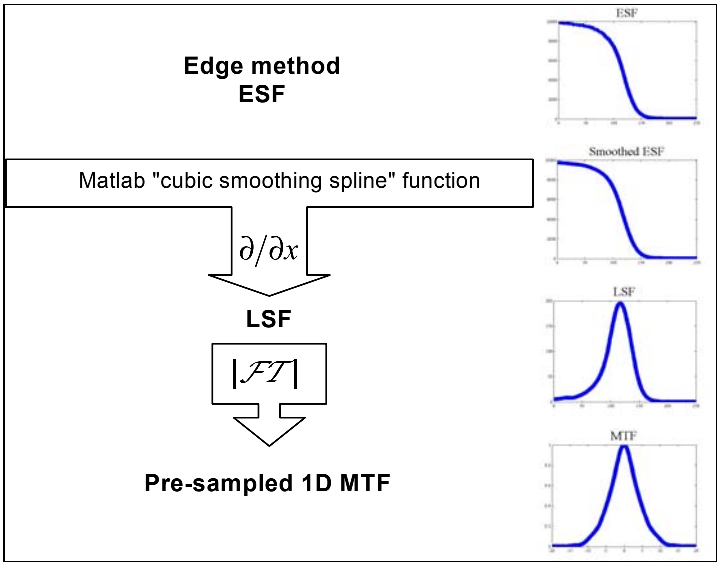

Figure 4.5. Scheme of the MTF evaluation procedure.

4.4.3 Noise Power Spectrum (NPS)

The NPS represents a spectral decomposition of the variance of the image since it provides an estimation of the spatial frequency dependence of the pixel-to-pixel fluctuations originating both from the quantum noise of the X-ray beam and from any noise introduced in the electronic chain between detector input and output (Williams, Mangiafico *et al.*, 1999). In practice, it describes the different noise sources in a detection system and quantifies the effects of parameters, such as the exposure level and the energy, on the magnitude and texture of the noise. The two-dimensional digital NPS (Cunningham, 2000) has been determined as:

$$NPS\left(u_i, v_j\right) = \frac{\Delta x \Delta y}{N_x N_y} \left\langle \left| DFT2\left(n_{ij}\right) \right|^2 \right\rangle \tag{4.3}$$

where x and y are the pixel spacing, N_x and N_y the image dimensions in the x- and y- directions, n_{ij} is the two-dimensional noise image, and *DFT2* is the discrete 2D Fourier transform.

Experimentally, ten 550 x 2048 pixels^2 flat field images have been acquired for each evaluation of the NPS (at a given energy and exposure) by using the pipeline mode. Because the values along a column are affected mainly by temporal variations of the signal, a new "noise image" was calculated from each of the 10 original images, by subtracting, from each pixel, the average pixel value of its relative column. With this operation, long-range (low frequency) background trend and deterministic variability in the image due to detector and/or beam spatial nonuniformity have been discarded; it has to be underlined that this procedure is not capable of removing the temporal fluctuations along the vertical direction.

In the analysis, we considered a central portion of 1280(H) x 512(V) pixel^2 for each of the 10 noise images.

This area should be then subdivided into horizontally and vertically half-overlapped regions (Figure 4.6) (IEC, 2002). Actually, there is always a trade-off when choosing the size and the number of these sub-regions. The larger the size of the sub-regions, the finer the frequency resolution of the resulting NPS, but also the fewer the number of regions available for averaging the NPS determinations (Dobbins, Ergun *et al.*, 1995). In our case, we used 27 sub-regions of 256 x 256 pixel^2 each.

In order to compare NPS at different input fluxes, the Normalized Noise Power Spectrum (NNPS) has been used:

$$NNPS\left(u_i, v_j\right) = \frac{NPS\left(u_i, v_j\right)}{\left\langle P\right\rangle^2} \tag{4.4}$$

with $\left\langle P\right\rangle$ the mean pixel values related to the sub-region over which the NPS was calculated. Each of the NNPSs presented in this paper is the average of the 270 normalized spectra obtained from the NPS calculated over the 270 sub-areas.

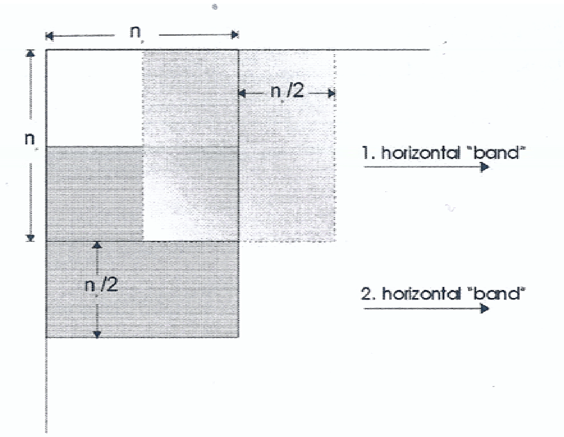

Figure 4.6. Scheme for definition of ROIs on a noise image for NPS calculation

4.4.4 The calculation of the incoming photon flux

The incoming photon flux has been calculated with the germanium detector. Ten flat fields have been acquired for each combination of energy and attenuators used in the NPS calculation. The pedestal noise has been first subtracted from each flat field and then the average image counts were calculated. For these determinations, a 173-pixel large ROI (60.55 mm) has been preliminarily selected on the germanium detector matching with the horizontal portion of the beam illuminating the ROI on the FReLoN camera. From the mean counts (expressed in bits) the number of the incoming photons per unit of area, time and storage ring electron beam current has been calculated as (Corde, 2002):

$$\frac{photons}{s\cdot m^2\cdot A}=\frac{bits\cdot n_0\left[photons/bit\right]}{\tau\left[s\right]\cdot\left(p\cdot h\right)\left[m^2\right]\cdot I\left[A\right]\cdot G} \tag{4.5}$$

where n_0 is the bit-photon conversion factor corresponding to the number of photons integrated by the germanium per bit at a given gain (G=1, for all measurements); τ is the integration time, p the horizontal pixel size, h the measured X-ray beam height and I is the ring current (to which the photon flux is linearly proportional). The air-kerma (K) has been calculated as:

$$K\left[Gy\right]=bits\cdot K_E\left[Gy/m\cdot bit\right]\frac{\tau_{Fr}\left[s\right]\cdot pxla_{Fr}\left[m^2\right]\cdot I_{Fr}\left[A\right]}{\tau_{Ge}\left[s\right]\cdot h_{Ge}\left[m\right]\cdot I_{Ge}\left[A\right]\cdot G}\cdot\frac{\mu_{air}}{\mu_{water}} \tag{4.6}$$

where K_E, is a factor including all the energy-dependent terms like the energy itself, the water mass attenuation coefficient and the horizontal pixel size (p). The subscripts indicate the detector used and *pxla* is the FReLoN camera pixel area, while μ_{air} and μ_{water} are the air and water mass attenuation coefficients, respectively.

4.4.5 Detective Quantum Efficiency (DQE)

Once the MTF, the NPS and the input Signal-to-Noise Ratio (SNR) of the X-ray beam used to measure the NPS are known, the DQE can be calculated assuming a linear, shift-invariant detection system. The DQE is a paradigmatic performance parameter of digital X-ray detectors since it is a frequency-dependent measure of the efficiency of the system in reproducing the information contained in the incident X-ray signal.

In other words, this parameter expresses the degradation in the SNR introduced by the processes of detection and conversion of the X-ray signal and it is defined as the square of the ratio of the SNR at the detector output to that at its input. Experimentally, the calculation of the frequency-dependent DQE of a linear system can be deduced from the measured presampling MTF and NNPS (Cunningham, 2000):

$$DQE\left(u\right)=\frac{MTF^2\left(u\right)}{NNPS\left(u\right)}\frac{1}{q} \tag{4.7}$$

where q is the mean number of incident quanta per unit of area and corresponds to the input squared SNR. The DQEs of the system have been computed for one-dimensional spatial frequencies in the horizontal and vertical directions by using the one-dimensional NNPS projections.

4.5 Results

The energy dependence of the detector performances has been investigated by measuring MTF, NNPS and DQE for several energies and three different fluorescent screen thicknesses as reported in Table 4.1.

Screen (μm)	Energy (keV)
40	20, 25, 33
100	25, 33, 51.5
200	70, 86

Table 4.1. Energies considered in this work for the three fluorescent screens.

4.5.1 Photon flux and exposure calculations - Linearity verification

In Table 4.2, values of the bit-photon conversion factor (n_0), the K_E parameter, and the air and water mass attenuation coefficients (μ_{air} and μ_{water}) are reported for the six energies considered in this study. In column 6 of the same table, the measured beam height for the beam used at each energy is shown. The determination of beam height has been performed on full-frame images of the beam acquired with the FReLoN camera after deconvolution with the related MTF.

A detailed description of the experimental parameters used for the image acquisition and for all calculations made is not essential to understand the results. For this reason, I decided to put in Table 4.3 the main parameters and their range of work for acquisitions performed with the germanium detector and the FReLoN camera respectively; in fact the photon flux and exposure values obtained by using equations 4.5 and 4.6 are anyway presented in the graphs in Figure 4.7 on linearity verification and in the NNPS and DQE graphs (Figures 4.12-4.16).

Energy (keV)	n_0 (photons/bit)*	K_E (Gy/m·bit)	μ/ρ (cm^2/g) air	μ/ρ (cm^2/g) water	beam height (mm)**
20	238.40	$1.25\cdot10^{-7}$	0.539	0.550	0.553
25	190.72	$6.15\cdot10^{-8}$	0.346	0.353	0.225
33	144.49	$2.63\cdot10^{-8}$	0.154	0.156	0.190
51.5	96.33	$9.45\cdot10^{-9}$	0.039	0.130	0.220
70	89.77	$8.20\cdot10^{-9}$	0.027	0.029	0.262
86	97.41	$1.02\cdot10^{-8}$	0.024	0.026	0.270

Table 4.2. Parameters used for the photons flux and exposure calculation with the germanium detector through equations 4.5 and 4.6.
*** At G=1; ** Beam height is accurate within 5%.**

In order to justify the use of the theory for linear systems, the linearity of the system response has been verified over the exposure range considered in the rest of the evaluation. The results are shown in Figure 4.7 where the large area transfer characteristic curves of the FReLoN camera are presented for the different energies and the three screens. In all the cases (except the 40 µm screen at 25 keV, where $R^2 = 0.98$), the linear fit of the experimental data has an R-squared coefficient of 0.99.

Parameter	Germanium detector	FReLoN camera
Pixel size (mm^2)	0.350 (H) x 10 (V)	0.046 (H) x 0.046 (V)
Integration time (ms)	100 (50 for 33 keV)	42
Ring current (mA)	164 ÷ 172	133 ÷ 175

Table 4.3. Experimental parameters used for the image acquisition with the germanium detector and the FReLoN camera.

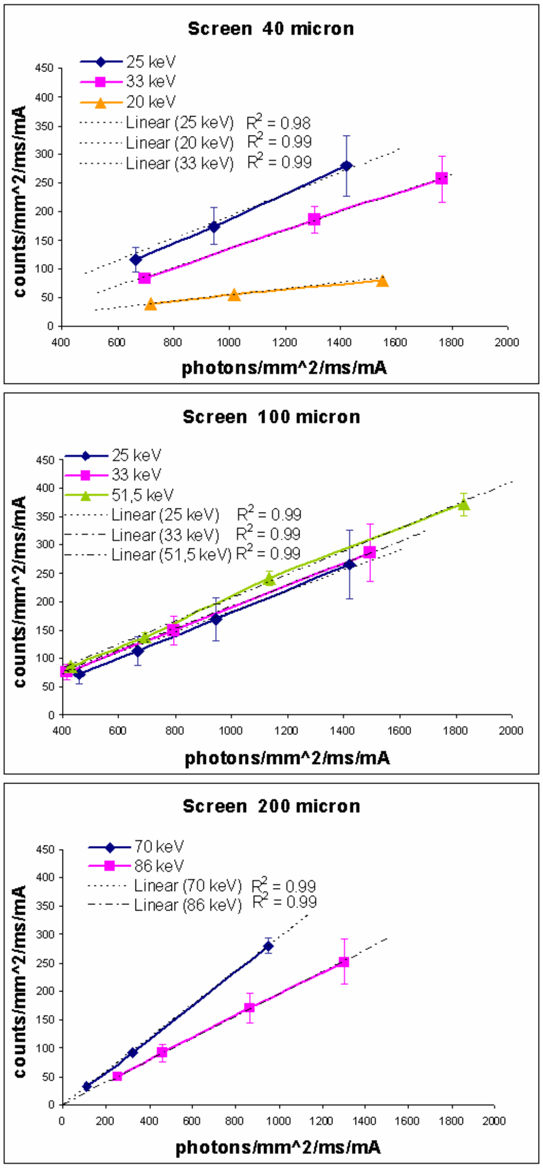

Figure 4.7. Large-area transfer characteristics for the three screens at 20, 25, 33, 51.5, 70 and 86 keV. Counts of the FReLoN versus the calculated number of photons are reported, normalized per unit of area, time and storage ring electron beam current.

4.5.2 MTF

Figure 4.8 illustrates the presampling MTF measured in both directions. For a given fluorescent screen, the MTF slightly changes with the energy but the MTF curves are almost overlapping. In Table 4.4 the spatial frequencies corresponding to 50%, 10% and 5% of the MTF are reported. In most of the cases, the MTF values in the vertical direction are slightly higher than in the horizontal. Figure 4.9 shows the MTF curves at 25 and 33 keV for the three fluorescent screens. As expected, the MTF worsens when the thickest screen is used.

Figure 4.10 shows how the MTF is influenced by the acquisition and readout modes (concatenate and the pipeline modes at binning 1, 4 and 8).

Screen thickness (μm)	Energy (keV)	50%		10%		5%	
		H	V	H	V	H	V
40	20	3.7	4.0	8.2	9.0	10.0	10.7
	25	3.9	4.1	8.5	9.0	10.1	10.6
	33	4.1	4.0	8.5	9.2	9.9	10.6
100	25	3.7	3.6	7.8	8.0	9.6	10.2
	33	3.7	3.8	7.8	8.6	9.8	10.1
	51.5	3.5	3.4	7.6	7.8	8.9	9.5
200	70	1.9	2.4	4.1	4.5	5.1	6.2
	86	1.9	2.5	4.0	5.0	5.0	5.8

Table 4.4. Spatial frequencies (1/mm) corresponding to 50%, 10% and 5% of the MTF in the horizontal (H) and vertical (V) directions. Each value is affected by an error estimated in 0.2 1/mm.

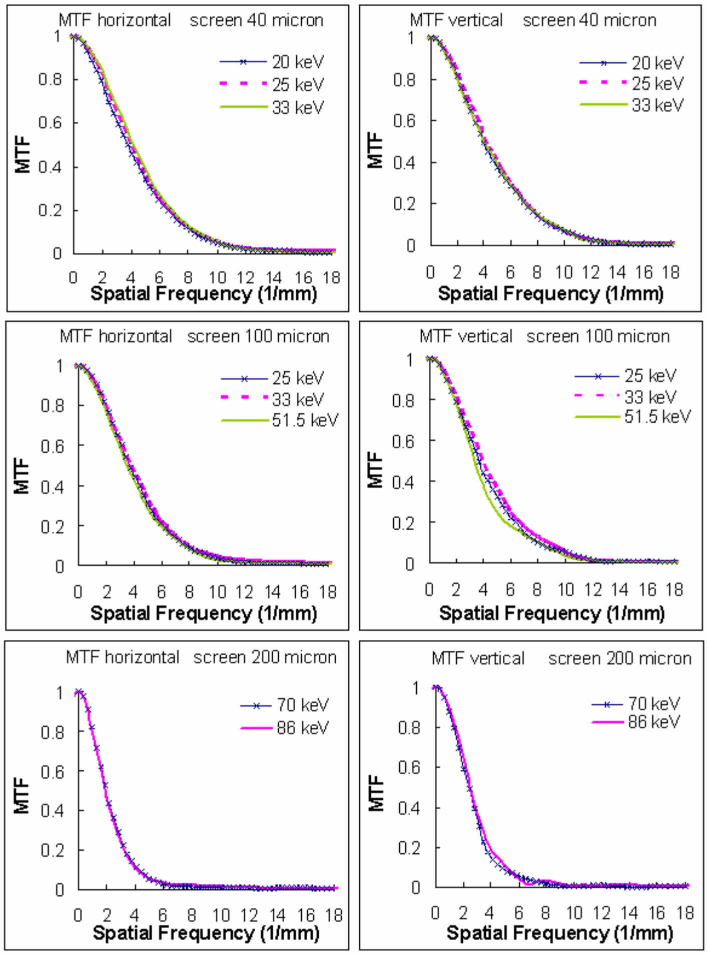

Figure 4.8. MTF along the horizontal and vertical directions for the 40, 100, and 200 µm thick screens.

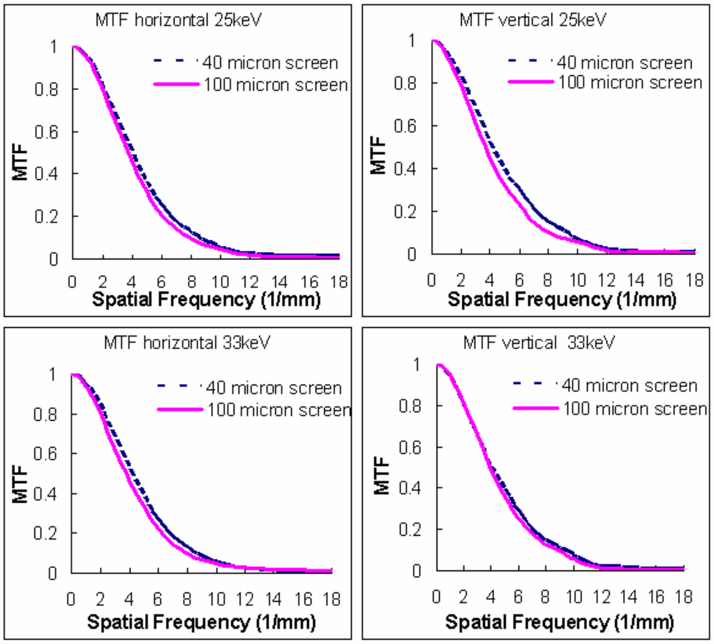

Figure 4.9. Comparison of the horizontal and vertical MTFs at 25 and 33 keV for the 40 and 100 µm fluorescent screens.

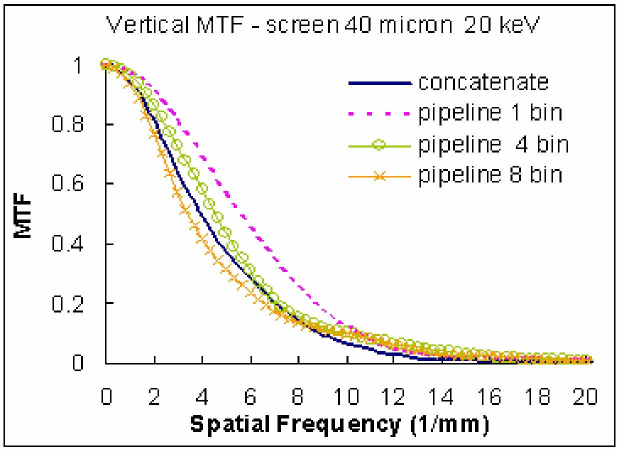

Figure 4.10. Measured MTFs in "concatenate" and "pipeline" acquisition modes at 20keV for the 40 µm screen.

4.5.3 NNPS

In Figure 4.11 an example of the two-dimensional NNPS for the 40 µm fluorescent screen at 33 keV (air-kerma of 1.36 mGy) is presented. This figure reveals that there are artefacts at very low frequency. In fact, as known in the literature (Tapiovaara and Wagner, 1993), such a noise along the axes depends on deterministic noise processes in the imaging chain.

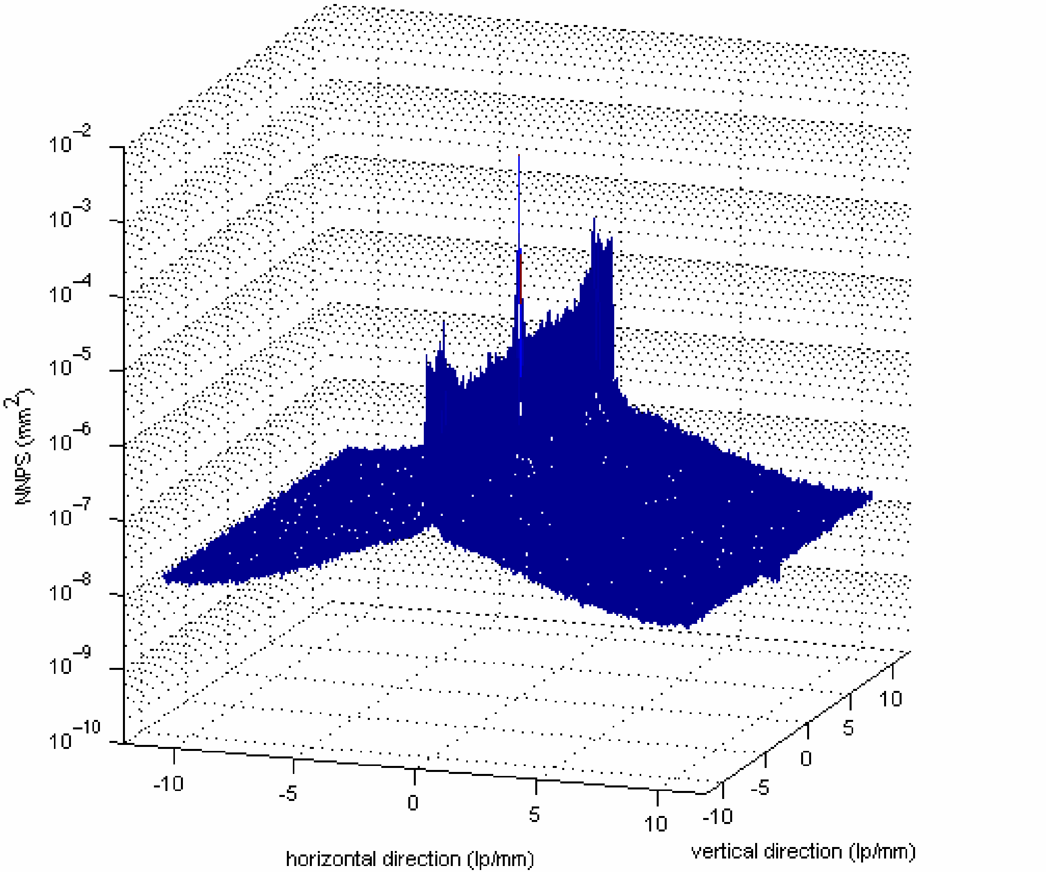

Figure 4.11. Two-dimensional NNPS for the 40 µm fluorescent screen at 33 keV (air-kerma = 1.36 mGy).

For this reason, as recommended by the IEC, we report in Figures 4.12, 4.13 and 4.14 the one-dimensional cuts of the NNPS along the two directions after having averaged a few rows/columns on both sides of the axes, and having omitted the axes themselves.

As expected, due to the weaker contribution of the stochastic (quantum) noise, the normalized noise power decreases when the exposure level increases. For all the energy-exposure cases, the NNPS projections show different behaviours: in the horizontal direction the NNPS systematically decreases as the spatial frequency increases, while in the vertical (temporal) direction the NNPS has a flat profile with, in many cases, some larger fluctuations at high frequencies where the quantum noise prevails.

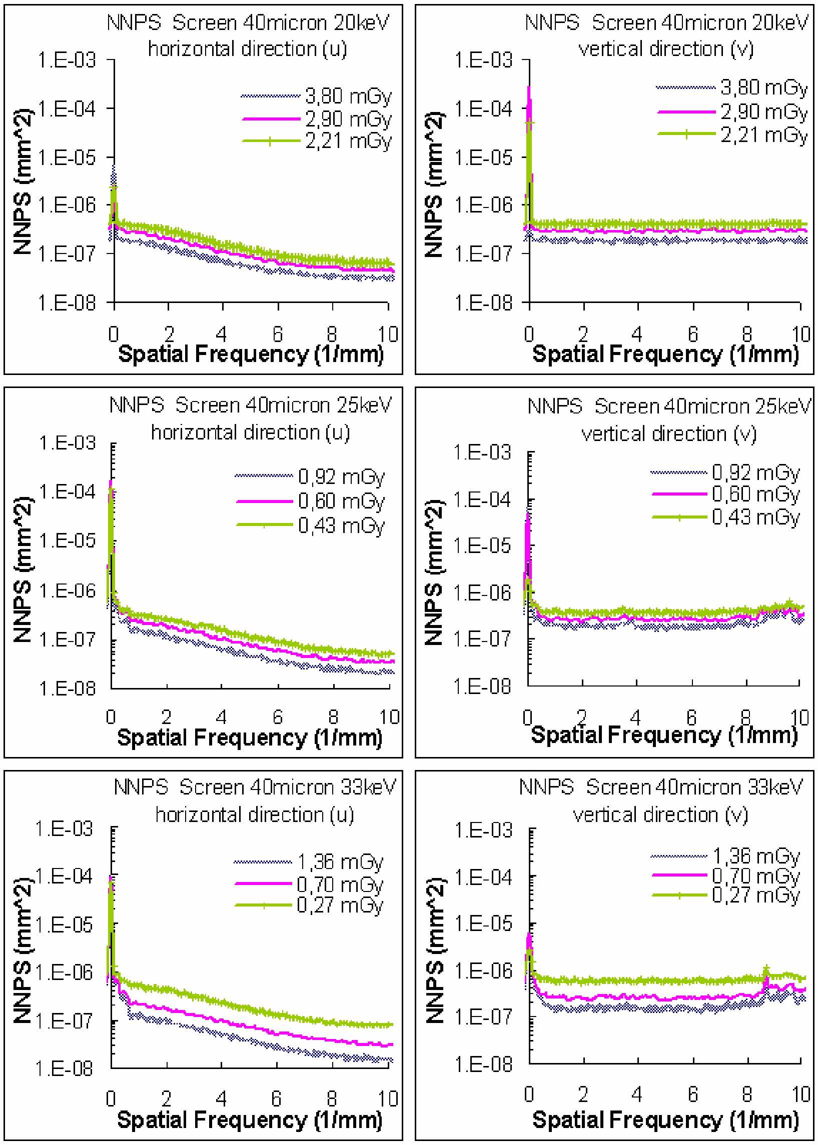

Figure 4.12. NNPS in the horizontal and vertical directions for the 40 µm thick screen at 20, 25 and 33 keV.

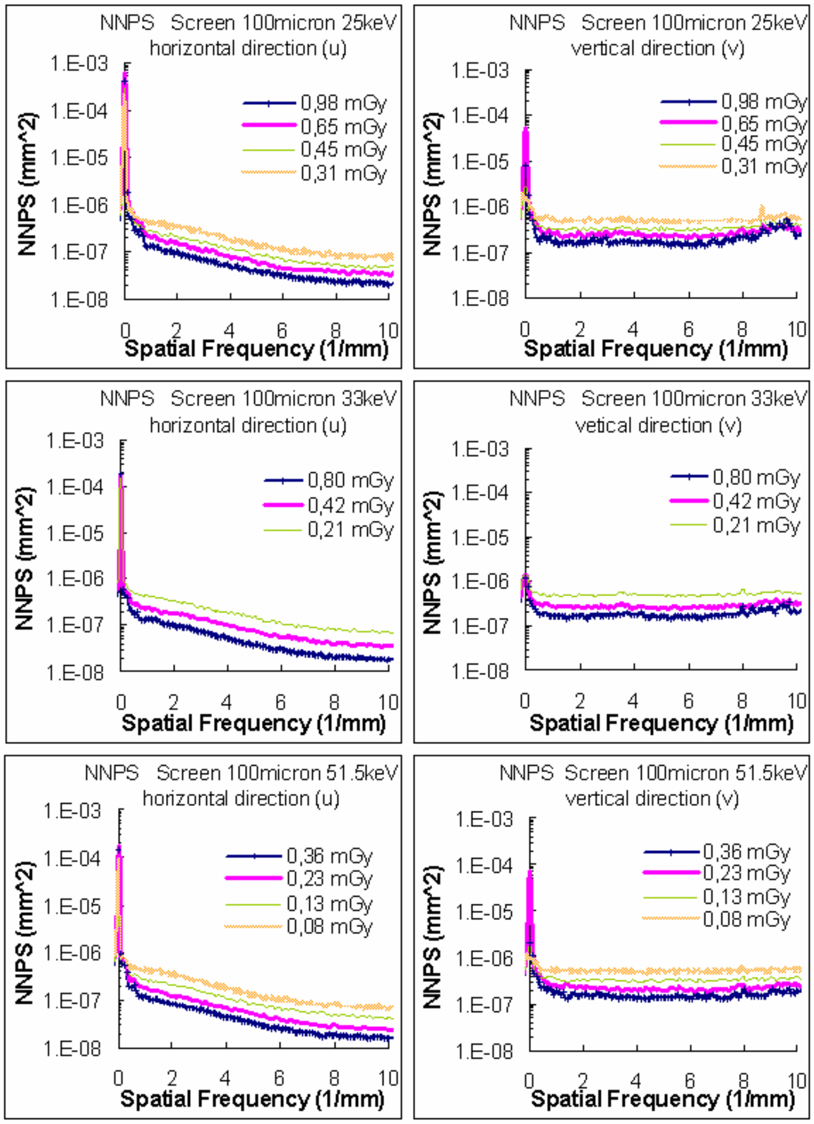

Figure 4.13. NNPS in the horizontal and vertical directions for the 100 µm thick screen at 25, 33 and 51.5 keV.

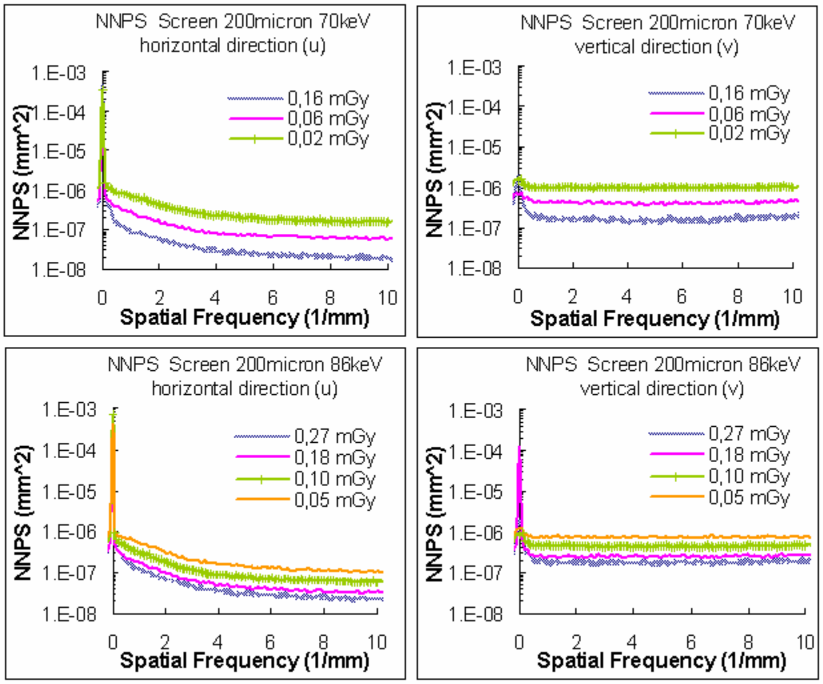

Figure 4.14. NNPS in the horizontal and vertical directions for the 200 µm thick screen at 70 and 86 keV.

4.5.4 DQE

Figure 4.15 and 4.16 illustrate the DQE for the 40 and 100 µm screens. Data for the 200 µm screen are not reported because of the impossibility of calculating the correct number of incoming photons due to:

i.) inaccuracy of values of the conversion factors (n_0, K_E) for the germanium detector at high energies;

ii.) the low spatial resolution of the screen that does not allow determining the exact beam height necessary for the calculation (many artefacts when deconvolving images).

For an ideal linear detector, characterized by the absence of any additive (or multiplicative) system noise, the DQE does not depend on q (Cunningham, 2000). This kind of behaviour is also shown in the results of the present study for the investigated q range. For a given fluorescent screen and at a fixed energy, the DQEs determined at different exposures overlap over almost the entire frequency interval considered here. Deviations from the ideal case concern the low frequency values that are largely affected by the NNPS artefacts, and the DQE in the vertical direction, because of temporal fluctuations of the X-ray beam. Moreover, the vertical DQE is slightly smaller than the horizontal, because the vertical NNPS is larger than the horizontal.

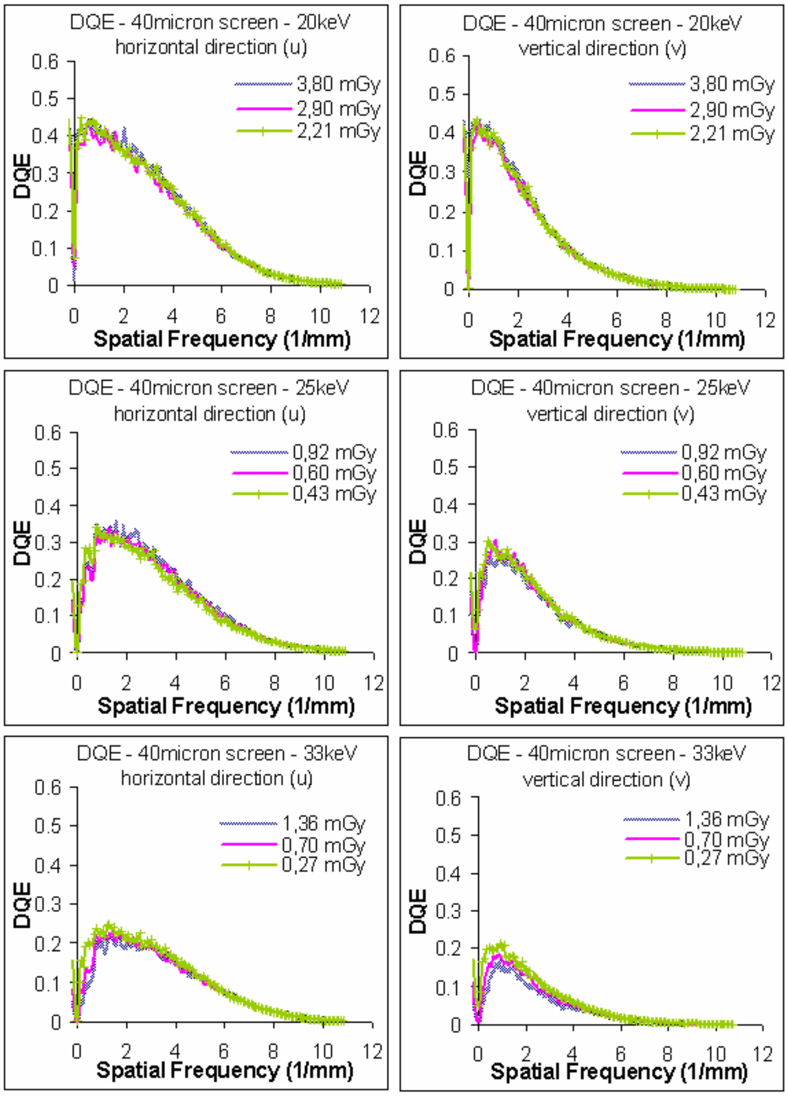

Figure 4.15. DQE in the horizontal and vertical directions for the 40 µm thick screen at 20, 25 and 33 keV.

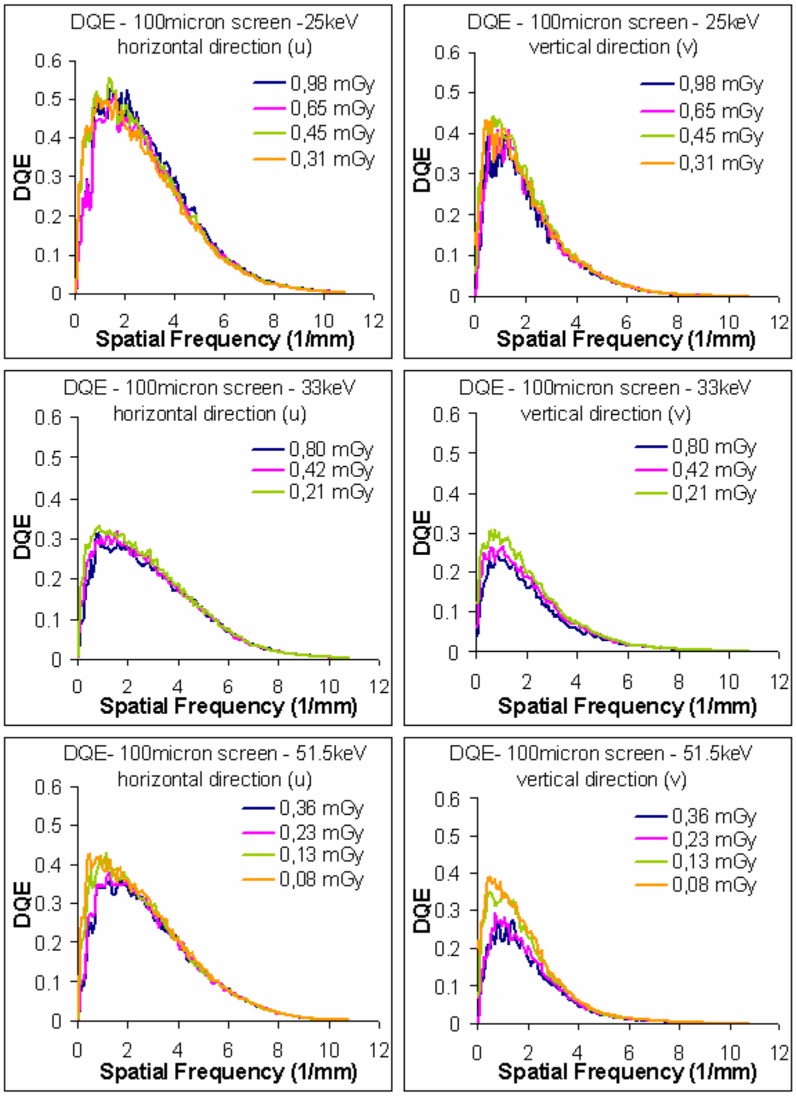

Figure 4.16. DQE in the horizontal and vertical directions for the 100 µm thick screen at 25, 33 and 51.5 keV.

4.6 Discussion of the results

The resolution (presampling MTF), the noise (NNPS) and the signal-to-noise ratio (DQE) properties of the FReLoN camera have been investigated.

- MTF

The presampling MTF was determined by using an edge analysis, since several studies have demonstrated that, in comparison to the slit technique, it is a simple and accurate method for measuring the low- and mid-frequency response of a system and it provides adequate results also at the high-frequency domain (Cunningham and Fenster, 1987; Samei, Flynn *et al.*, 1998).

- **The comparison of the presampling MTFs for the three fluorescent screens at the same energy shows that, by increasing the screen thickness, the spatial resolution worsens because of the increased scattering of the visible light.**

  As reported in literature (Borasi, Nitrosi *et al.*, 2003), increasing the energy (for a given fluorescent screen thickness) should result in a spatial resolution improvement since the mean photon-gadox screen interaction point is deeper and therefore light scattering inside the fluorescent screen is limited. This behaviour is theoretically true in the X-ray energy range where the linear attenuation coefficient monotonically decreases with the energy. Besides, in an energy interval containing a fluorescent screen absorption edge, an opposite trend should be observed among X-ray energies below and above the edge. The latter behaviour was experimentally verified here in terms of MTF worsening at 51.5 keV (just 0.5 keV higher than the Gadolinium K-edge) with respect to the 33 keV MTF. Experimentally, the horizontal MTF at 10% is 7.8 at 33 keV and 7.6 at 51.5 keV, while the vertical MTF at 10% is 8.6 at 33 keV and 7.8 at 51.5 keV for the 100 μm screen (Table 4.4).
- **The slight difference between the MTFs in the two directions (higher values in the vertical direction)** may be related to the readout electronics bandwidth; in fact, it can be attributed to a small residual charge left on the register pixel when the signal moves horizontally during the read out.
- Not surprisingly, the comparison of the MTF curves obtained by different detector acquisition-readout modes (Figure 4.10) reveals that the **best spatial resolution is achieved when operating without binning.**

- NNPS

- Also as expected, **the NNPS is exposure dependent (higher at lower exposures);** this behaviour is related to the Poisson distribution of the quantum noise component of an X-ray image.
- In addition, in all the considered exposure-energy cases, **the NNPS presents significant higher values near the zero frequency, where the deterministic noise component prevails.** The low frequency effects are less evident at low exposures as they are masked by the stochastic contributions.
- **The trend of the NNPS along the horizontal and vertical direction is different**, as shown in Figures 4.12, 4.13 and 4.14. In the horizontal direction, the NNPS constantly decreases as it moves towards the high frequency domain. This behaviour is typical of detectors based on indirect conversion and is determined by the spatial correlation between adjacent pixels that read the same signal because of the light scattering of the

screen (Samei and Flynn, 2003). On the contrary, the vertical NNPS is almost flat. Along this direction, the noise spectrum depends mainly on the time variations of the X-ray beam and therefore at high frequencies the graphs show an increase of the NNPS values. At low exposures this increase is less evident because the stochastic (quantum) noise component dominates. In the case of the 200 μm thick screen, the fluctuation of the NNPS at high frequencies seems to disappear. A possible explanation is that the blurring of the signal caused by the scattering of light in the screen prevails over the deterministic component of the NNPS.

- DQE

- **The high contribution of the deterministic component of the NNPS at high exposures affects the DQE shape in the vicinity of the zero-frequency**.
- **For the 100 μm screen, the DQEs at 51.5 keV (just above the K-edge of the Gadolinium based fluorescent screen) present values similar or even higher than those at 33 keV.** This result is explained by the abrupt increase in the photon interaction cross section at the K-edge of the element, which therefore increases the light yield production of the screen.
- As shown, **the DQE values for the 40 μm screen are of the same order of those for the 100 μm** since the 40 μm phosphor screen is optimized for spatial resolution and not for DQE.

Several factors contribute to limiting the DQE:
– The phosphor screen conversion yield certainly plays an important role; thicker screens would be more efficient in particular at high energies, but the detriment of the spatial resolution would not be acceptable for applications like mammography (Bravin, Fiedler *et al.*, 2003).
– A second important role is played by the low efficiency of the CCD (about 25% (Atmel, 2002)) which registers only a fraction of visible photons emitted by the screen.
– Of importance is also the fact that the choice made in the detector construction, i.e. to permit an easy change of the fluorescent screen, prevents the optimization of the optical contact between the fluorescent screen itself and the taper (the present layout makes it difficult to avoid air gaps in between).
Higher DQE values would be of particular importance for *in-vivo* imaging when the dose delivered to the sample has to be kept as low as possible. In the new version of this detector prototype, presently under development, work to reduce efficiency losses, by using a more efficient CCD and by improving the screen-taper contact.

4.7 Comparison of the "FReLoN" camera performances with other X-rays detector in literature

In order to better appreciate the characteristics and performances of the taper optics FReLoN camera, they are compared (Table 4.5) with X-ray imaging detectors presented in the literature, by focusing our attention on the field of view, pixel size, MTF, DQE and readout speed. For the FReLoN camera we have chosen to report results for the 100 µm thick screen only.

It should be noted, however, that care should be taken when interpreting such a table. The different experimental conditions, under which each of these detectors has been characterized (reported in the table when available), make the comparison difficult and often unfair; in fact performances strongly depend on the energy used for the characterization and on the applied binning. In addition, specific detector layouts (like the availability of different readout modes for the FReLoN camera) are not mentioned in the literature on other detectors. Such features may play a critical role in the detector choice. Despite these limitations, data reported in Table 4.5 lead to considerations reported in the paragraph on what it is available today, and where FReLoN is positioned with respect to SR medical imaging needs.

The most commonly used devices for high-resolution imaging are CCDs and FPs. CCDs are typically characterized by low noise, a small pixel size (typically tens of microns or less) and a large pixel number (up to ~ $3.0*10^7$ so far); on the other hand, CCDs are easily damaged by X-rays and their readout is limited by the charge-transporting method. This is why CCD-based detectors are generally combined with tapered optical fibers and/or with indirect lens-coupling or intensifier (Vedantham, Karellas *et al.*, 2000; Yagi, Katsuaki *et al.*, 2004).

Amorphous silicon detectors (for instance n° 9 in Table 4.5), are another important category of solid state detectors; they are built on a photodiode array with an active TFT (thin-film transistor) matrix readout which can be quite big (n° 9, 10). Their sensitivity to X-rays is achieved by using amorphous selenium as the converting medium (X-rays to electrons) or by coupling them with a scintillator (X-rays to visible light conversion). In general, even if this kind of detector can achieve high efficiency, it has severe limitations in terms of spatial resolution (pixel size >100 µm) and noise. A good compromise is offered by the amorphous-Se direct detector Thermotrex Inc. (n° 11); it presents a pixel size of 66 µm, good spatial resolution and DQE compared to other detectors in the same category (n° 9, 10). A point which remains to be verified is the readout speed that is not reported in the literature. Another example in the same category is the amorphous-Si flat panel coupled to thallium-doped Cesium iodide (CsI:Tl) (GE, n° 9) that presents a readout speed faster than the FReLoN, but a much worse spatial resolution.

An alternative is the CMOS (Complementary Metal-Oxide Semiconductor) FP. Hamamatsu Photonics (n° 8 in Table 4.5) has an active area larger than the FReLoN and the same pixel size. Moreover, the direct deposition of the scintillator on the taper allows to increase the spatial resolution of the CMOS FP, resulting in a very competitive device. The weak aspect is the low readout speed, which is half of the FReLoN readout speed.

Other CCD-based detectors reported in literature are presented in Table 4.5 (lines 1-7). Among them, the FReLoN has one of the largest areas and fastest readout.

Very fast readout (291 frames/s) is achieved by the C7770 Hamamatsu Photonics KK detector (n° 5) which is based on three CCDs alternatively read and coupled to an X-ray image intensifier; the pixel size is only 9.9 µm but the detector dimensions are too small for in vivo medical imaging (6.5 x 4.9 mm^2).

A relatively large active area (49 x 86 mm^2) and small pixel size (12 µm) characterize the Philips FTF7040 CCD (n° 6); it also presents good values for both MTF and DQE. The readout speed is nevertheless quite limited for medical imaging (0.14 frames/s).

In his paper, Goertzen reported the evaluations of two Dalsa-Medoptics CCDs (Goertzen, Nagarkar *et al.*, 2004): the first one (CCD1) (n° 2) is coupled to a fiberoptic taper with a 3:1 demagnification and gadolinium oxysulphide (GOS) phosphor screen converter; the second CCD (CCD2) is coupled to a fiberoptic taper with a 2:1 demagnification and to a changeable scintillator that can be either a GOS (n° 3) or a CsI:Tl (n° 4) screen. For the CCD2, the CsI:Tl screen results in nearly twice the DQE with respect to the GOS screen (0.4 versus 0.24 at 0 mm^{-1}); the CCD2 shows MTF values nearly identical to CCD1 when the GOS screen is used.

The pixel size for both these two CCD-based devices is comparable to that of the FReLoN camera; nevertheless, since the number of pixels is limited to 1024x1024, the resulting detector area is smaller than the FReLoN. In addition, considering that the MTF and DQE values of these CCDs have been measured with a 21 keV-equivalent X-ray beam, it is possible to conclude that the FReLoN camera offers similar or even better performances (see also Table 4.4 and Figure 4.12 for data at 20 keV) both in terms of spatial resolution and efficiency in a rather wide energy range (the readout speed values are not available).

This comparison shows that the performances of the FReLoN camera in its present version position it very well in the X-ray imaging detector world. Not one of the detectors presented exceeds the FReLoN camera in all parameters simultaneously; this is the outcome of the compromise made in the camera layout to fit with the SR medical imaging needs. In addition, the camera offers the advantage of data acquisition modes specifically tailored to a SR laminar beam. Very likely, its performances will be improved even further, in terms of efficiency, in the newest version currently under development.

Detector	Dimensions (mm^2)	Number of pixels	Pixel size (µm)	10% MTF (mm^{-1})	DQE At 0 mm^{-1}	X-ray beam energy (keV)	Readout speed (frames/s)	Reference
1- FReLoN coupled to 100 µm Gadox screen*	94x94	2048x2048	46x46	8.0 8.6 7.8	~ 42 % ~ 30 % ~ 35 %	25 33 51.5	4.2	This work
2- Dalsa-Medoptics CCD with a 3:1 fiber taper and GOS screen	69x69	1024x1024	67.55x67.55	~ 8.0	~ 30 %	~21***	-	(Goertzen *et al.* 2004)
3- Dalsa-Medoptics CCD with a 2:1 fiber taper and GOS screen	49x49	1024x1024	48.23x48.23	~ 8.0	~ 24 %	~21***	-	(Goertzen *et al.* 2004)
4- Dalsa-Medoptics CCD with a 2:1 fiber taper and (CsI:Tl) screen	49x49	1024x1024	48.23x48.23	~ 9.3	~ 40 %	~21***	-	(Goertzen *et al.* 2004)
5- C7770 Hamamatsu Photonics KK +prism+3CCDs with intensifier	6.5x4.9	656x494	9.9x9.9	-	-	-	291	(Yagi *et al.*, 2004)
6- Philips FTF7040 CCD with Gadox screen	49x86	4096x7168	12x12	~ 16 (2x2 binning)	~ 65 % (2x2 binning)	12****	0.14	(Phillips *et al.*, 2002)
7- CCD Senovision, GE Medical Systems	61x61	4096x4097	15x15 30x30 (binned)	~ 10	~ 40 % ÷ 28 % (depending on exposure)	28kV Mo filter	-	(Vedantham *et al.*, 2000)
8- CMOS flatpanel imager from Hamamatsu Photonics (C7942)	120x120	2240x2368	50x50	~ 6.5 ~ 10.0 **	-	20	2	(Yagi *et al.*, 2004)
9- amorphous-Si flat panel coupled to CsI:Tl scintillator, (Revolution XQ/i G.E. Medical Systems)	410x410	2048x2048	200x200	~ 1.6 (at 50% MTF)	~ 66 %	~50***	8	(Granfors and Aufrichtig, 2000)
10- amorphous-Se flatpanel, Direct Radiography Corp. (Hologic) DR-1000 (DRC)	350x350	2560x3072	139x139	~ 6.4	~ 38 %	~50***	-	(Samei and Flynn, 2003)
11- amorphous-Se Thermotrex Inc.	67.5x54.9	1024x832	66x66	~5.5 (at 50% MTF)	~ 55 %	~21***	-	(Goertzen *et al.*, 2004)

* MTF and DQE (column 5 and 6 respectively) correspond to results calculated in the vertical direction.

** Modified version of the CMOS flatpanel imager from Hamamatsu Photonics (C7942) obtained by direct deposition of the scintillator (CsI:Tl) on the photodiode array.

*** Mean energy in keV has been estimated from the HVL values given in the paper

**** Mean energy declared in the paper

Table 4.5. Selected characteristics of the FReLoN camera compared to some other detectors used in X-ray imaging. Values here reported have been extracted from graphs shown in the reference papers (column 9). The energy refers to the X-ray beam used for the detector characterization; in absence of notes, SR monochromatic beams have been used.

4.8 "FReLoN" camera combined to a chopper

In order to improve the FReLoN camera performances, a chopper has been designed to be used in combination with the camera. This instrument has been developed and built at ID17 (Renier, Fiedler *et al.*, 2005) and it is particularly suited when imaging in a laminar beam geometry (the beam is extended horizontally over all rows of the CCD but vertically only one or a few lines are covered), where images are rapidly acquired line by line during continuous exposure and the object to be imaged is translated or rotated synchronously through the laminar beam (pipeline mode).

Charges created during the readout time of each individual line are blurring the image and hamper exact quantitative analysis. In addition the chopper protects the camera from unnecessary exposure by blocking the wide X-ray beam during the readout time of the camera. Moreover, for *in vivo* measurements, it is essential to minimize the measuring times in order to avoid motion artifacts and to optimize radiation dose. The minimum sampling time depends on the maximum frame rate of the detector system in a given readout mode. If the readout time is long with respect to the frame lifetime, the exposure during the readout will degrade the performance of the system.

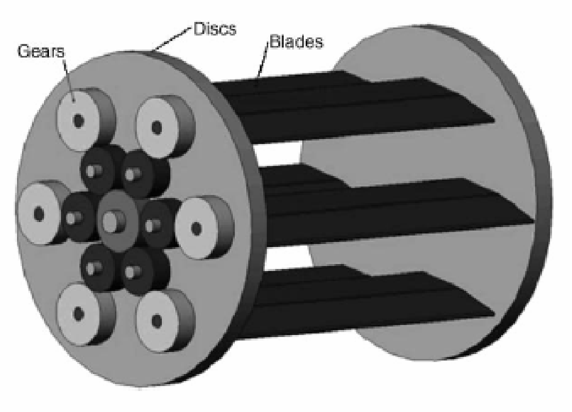

Figure 4.17. Chopper layout.

The apparatus is based on the rotation of planetary blades mounted between two large discs (Figure 4.17). The planetary blades (which are in the number of 6 in the schematics but 12 in the prototype) are kept permanently parallel to each other thanks to a series of gears, which also allow changing their orientation. The gears are fixed to the rotating discs and are made of polyoxymethylene (DelrinTM). A brushless motor rotates the two discs at variable speed. As the discs are rotated the blades alternatively interrupt the transmission of the beam so that a pulsed beam emerges. It is the orientation of the blades that permits the adjustment of the duty cycle, whilst the speed of rotation of the supporting discs modifies the frequency of the beam interruption. The two parameters (duty cycle and frequency) are therefore controlled independently and in a remote manner. For a better understanding of the operation, the two extreme cases should be considered. In the first case, (Figure 4.18 above) the blades are kept vertical: the beam is interrupted most of the time. The resulting duty cycle is therefore minimum (around 5%). In the second case, (Figure 4.18 below) the blades are kept horizontal: the chopper transparency is maximized. The duty cycle reaches 90%. All the intermediate angular blade positions are also possible, allowing for continuously variable duty cycle.

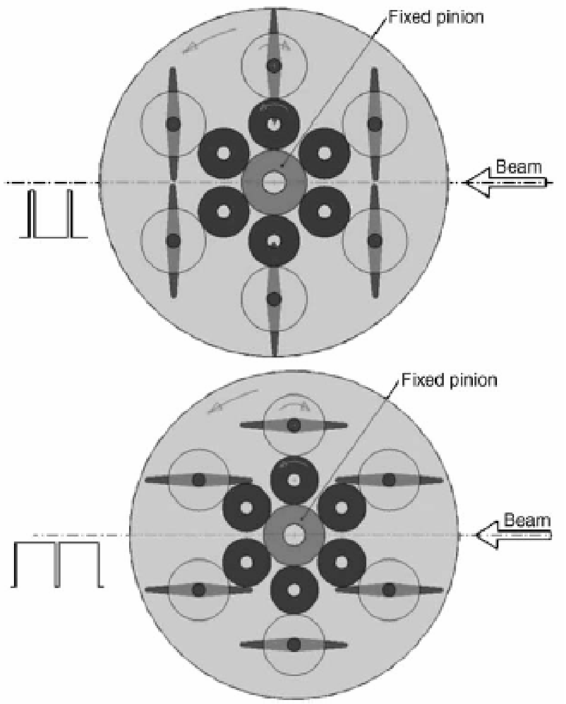

Figure 4.18. The two extreme cases. Upper figgure: blades kept vertical. Lower figure: blades kepts horizontal.

Parallel work (Renier) has proven that, depending on the application , the use of the chopper is able to:

(1) reduce the noise in the images, thanks to the suppression of the irradiation during readout time;

(2) considerably increase the dynamic range as a consequence of avoiding early saturation of the detector;

(3) reduce the X-ray dose to the sample proportionally to the duty cycle;

(4) allow for improved quantitative analysis even in K-edge subtraction (KES) mode.

4.8.1 Chopper control principle

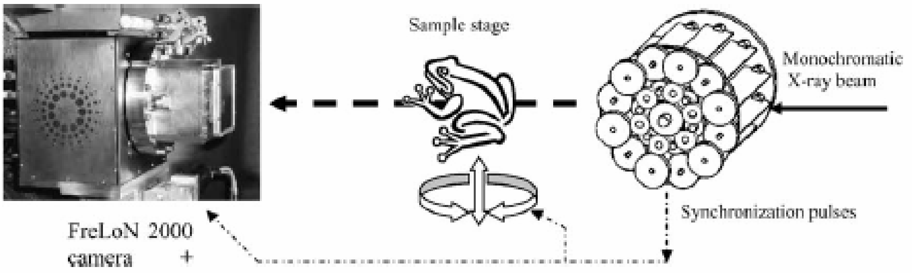

Figure 4.19. Control principle

When imaging in pipeline mode and without chopper, it is desirable to operate the system with a large duty cycle (the ratio of the integration time to the total period of a single frame) in order to minimize blurring effects. Obviously, this is particularly disadvantageous when fast and repeated acquisition are needed. With the chopper in operation, the beam is stopped during the readout period, preventing any mixing of the signal so that short integration times can be chosen. This is valid both for planar radiography and for computed tomography. The latter can profit in two ways by the system if the laminar beam covers several lines of the CCD vertically. Since their signal can be used to process the same number of tomographic slices in parallel, an important gain in acquisition time for larger sample volumes can be achieved.

In our design (Figure 4.19), the chopper generates the TTL pulses that will be used to synchronize the FReLoN 2000 camera and the sample stage rotation. A perforated disk coupled to an optical sensor and driven by the chopper main shaft generates the pulses. The brushless motor speed of rotation is adjusted from 0 to 6000 rpm that correspond to 0 to 300 Hz for the chopping frequency. The duty cycle is adjusted independently from the speed of rotation by a simple stepper motor.

4.8.2 MTF evaluation of the "FReLoN"- chopper combination

The assessment of FReLoN performances when used in combination with the chopper have been evaluated and presented hereafter.

The MTF has been calculated for two different acquisition modes: (1) concatenate, (2) pipeline. In Figure 4.20, results are compared with the MTF of the system without chopper for two fluorescent screens of different thicknesses (54 μm and 100 μm) and an energy of 33 keV. Moreover for the 100 μm screens, MTF obtained at 51.5 keV are also presented. Results show that the chopper does not introduce a significant change in the MTF under this operation conditions.

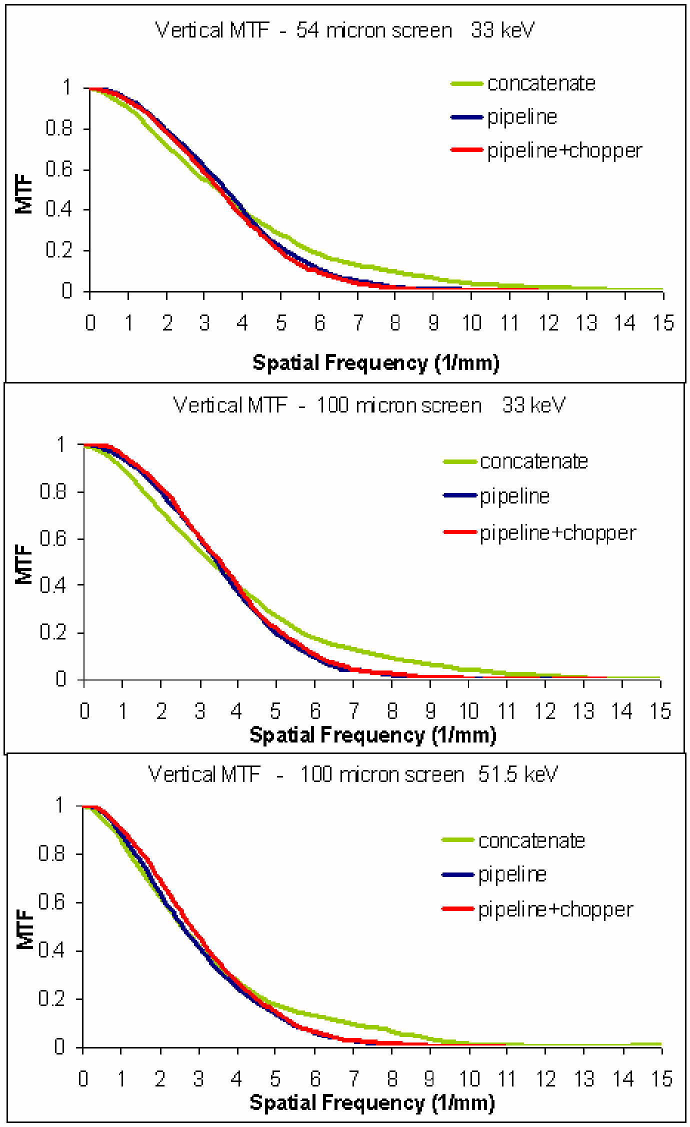

Figure 4.20. Comparison of the MTF of the FReLoN camera calculated for two different acquisition modes: concatenate and pipeline with and without chopper.

REFERENCES

G. Borasi, A. Nitrosi, P. Ferrari and D. Tassoni (2003). "On site evaluation of three flat panel detectors for digital radiography." Med. Phys. 30 (7): 1719-1731.

A. Bravin, S. Fiedler, P. Coan, J.-C. Labiche, C. Ponchut, A. Peterzol and W. Thomlinson (2003). "Comparison between a position sensitive germanium detector and a taper optics CCD "FRELON" camera for Diffraction Enhanced Imaging." Nucl. Instr. Meth. A 510: 35-40.

S. Corde (2002). Enhancement of the photo-electric effect with pharmacological agents in synchrotron radiation based anti cancer radiotherapy: a methodological study. Grenoble, Université J. Fourier.

I. Cunningham (2000). *Applied Linear-Systems Theory*. *Handbook of Medical Imaging, Medical Physics and Psychophysics*. Washington, SPIE. 1 (Chapter 2): 79-159.

I. Cunningham and A. Fenster (1987). "A method for modulation transfer function determination from edge profiles with correction for finite-element differentiation." Med. Phys. 14 (4): 533-537.

J. T. III Dobbins (2000). *Image Quality Metrics for Digital Systems. Handbook of Medical Imaging, Medical Physics and Psychophysics*. Washington, SPIE. 1 (Chapter 3): 161-221.

J. T. III Dobbins, D. Ergun, L. Rutz, D. Hinshaw, H. Blume and D. Clark (1995). "DQE(f) of four generations of computed radiography acquisition devices." Med. Phys. 22 (10): 1581-1593.

H. Fujita, K. Doi and M. Giger (1985). "Investigation of basic imaging properties in digital radiography. 6.MTFs of II-TV digital imaging systems." Med. Phys. 12 (6): 713-720.

A. L. Goertzen, V. Nagarkar, R. A. Street, M. J. Paulus, J. M. Boone and S. R. Cherry (2004). "A comparison of X-ray detectors for mouse CT imaging." Phys Med. Biol. 49: 5251-5265.

P. R. Granfors and R. Aufrichtig (2000). "Performance of a 41x41cm2 amorphous silicon flat panel X-ray detector for radiographic imaging applications." Med. Phys. 27 (6): 1324-1331.

P. Greer and T. van Doorn (2000). "Evaluation of an algorithm for the assessment of the MTF using an edge method." Med. Phys. 27 (9): 2048-2059.

IEC (2002). IEC 62220-1. Medical electrical equipment. International Electrotechnical Commission. San Diego.

H. Johns and J. Cunningam (1971). *The physics of radiology*. Springfield.

A. Peterzol, A. Bravin, P. Coan and H. Elleaume (2003). "Image quality evaluation of the angiography imaging system at the European synchrotron radiation facility." Nucl. Instr. Meth. A 510: 45-50.

W. C. Phillips, A. Stewart, M. Stanton, I. Naday and C. Ingersoll (2002). "High-sensitivity CCD-based X-ray detector." J Synchrotron Radiat 9: 36–43.

M. Renier, S. Fiedler, C. Nemoz, H. Gonzalez, G. Berruyer and A. Bravin (2005). "A mechanical chopper with continuously adjustable duty cycle for a wide X-ray beam." Nucl. Instr. Meth. A 548: 111-115.

E. Samei (2003). "Image quality in two phosphor-based flat panel digital radiographic detectors." Med. Phys. 30 (7): 1747-1757.

E. Samei and M. Flynn (2003). "An experimental comparison of detector performance for direct and indirect digital radiography system." Med. Phys. 30 (4): 608-622.

E. Samei, M. Flynn and D. Reiman (1998). "A method for measuring the presampled MTF of digital radiographic systems using an edge test device." Med. Phys. **25** (1): 102-113.

M. Tapiovaara and R. Wagner (1993). "SNR and noise measurements for medical imaging: I. A practical approach based on statistical decision theory." Physics in Medicine & Biology **38**: 71-92.

S. Vedantham, A. Karellas, S. Suryanarayanan, I. Levis, M. Sayag, R. Kleehammer, R. Heidsieck and C. D'Orsi (2000). "Mammographic imaging with a small format CCD-based digital cassette: Physical characteristics of a clinical system." Med. Phys. **27**: 1832–1840.

M. Williams, P. Mangiafico and P. Simoni (1999). "Noise power spectra of images from digital mammography detectors." Med. Phys. **26** (7): 1279-1293.

N. Yagi, I. Katsuaki and T. Oka (2004). "CCD-based X-ray area detector for time-resolved diffraction experiments." J Synchrotron Radiat **11**: 456-461.

N. Yagi, M. Yamamoto, K. Uesugi and K. Inoue (2004). "A large-area CMOS imager as an X-ray detector for synchrotron radiation experiments." J Synchrotron Radiat **11**: 347-352.

5

Analyzer-based imaging technique applied to the articular joints study and dose effect investigation

Contents

Ce chapitre inclut les résultats expérimentaux obtenus par la technique de contraste de phase à travers un analyseur (ABI) pour l'étude de cartilages et l'évaluation de la guérison après pose d'implants métalliques. Les images ABI obtenues pour des échantillons *post mortem* humains et animaux, ainsi que les expériences impliquant des animaux vivants sont présentées. Les méthodes de reconstruction et traitement des images sont également décrites. Enfin, une étude radiobiologique conduisant à l'évaluation de la dose délivrée est présentée.

In this chapter, the experimental results obtained by applying the analyzer-based imaging (ABI) technique to the study of joint cartilage and evaluation of metal implant healing are presented. ABI images of excised human and animal specimens and in-vivo experiments are discussed. Image reconstruction and processing methodologies are described as well. In the last part of the chapter, the results of radiobiological experiments for dose effect evaluations are also discussed.

5.1 Introduction

As extensively discussed in Chapter 1, plain X-ray radiography is still the clinical technique having the highest resolution and currently being the most economical, readily available and accepted method to detect joint abnormalities. Nevertheless, because of its intrinsic limitations, in some cases planar radiology is not sufficiently sensitive.

There are two major directions of radiological analysis where advancements in X-ray technology could be particularly beneficial for orthopaedics:

- **imaging of soft tissue joint components, such as cartilage and ligaments**

  Gathering information on the structure of normal cartilage and the ways in which this tissue (with limited or no ability to repair) changes after damage or in pathological conditions is essential for the development of rational treatment strategies.
- **imaging metal implant healing in bones**

  Even though radiography allows the evaluation of an implant as a whole, at least along one axis of sight, it is finally hampered by low local resolution caused by beam hardening based on the incident polychromatic light, thus, resulting in uncorrectable image errors. Histological evaluation, by contrast, suffers even in animal studies from the fact that it can only give information on very restricted portions of the implant because of the micrometer-scale thickness of individual sections.

In this chapter, I will present the results obtained by applying the Analyzer-based imaging (ABI) technique to the study of articular cartilage tissue and of metal implant healing.

The results will demonstrate the high potential of the ABI technique for this kind of application and its ability both of non-invasively detecting cartilage abnormalities, especially in the initial stages of degenerative joint disease (OA) or early in its progression, and of evaluating the status of ingrowth of bone tissue into the implant surface.

The scientific value of the ABI images presented in this chapter is highlighted by the comparison with results produced with conventionally used diagnostic techniques (histology, magnetic resonance (MRI), ultrasound (UI), and conventional tomography (CT)) of the same samples.

This consequent parallel analysis represents also the peculiarity and the originality of this work, which is the fruit of the synergy of complementary competences specific of two different disciplines: Physics and Medicine.

The real engine of this research has been the collaboration between the ID17 (ESRF) team, offering the physical, technical and data processing support, and the research department of the Department of Orthopaedics of the University of Jena for the medical and clinical aspects (choice and supply of samples, image interpretation, and imaging with conventional techniques). In particular, I had the possibility to profit by the experience of Dr. Mollenhauer who, as the first, showed that the ABI technique could be a powerful tool in diagnostic orthopaedics (Mollenhauer, Aurich *et al.*, 2002).

Contrary to other fields, when applying Physics to medical investigations, a different attitude has to be assumed: Physics is in service of the Medicine. This means that:

- the purpose of research is defined by specific medical issues
- it is the physician who indicates the target since he knows what is most important to look for from a medical point of view
- investigation modalities have to be adapted to the particular biological samples in terms of
  - experimental conditions (temperature, humidity, etc.)
  - sample position and orientation
  - control of the delivered dose
- data processing and presentation should be the most suitable to physicians' requirements and habits.

In the light of these considerations, the study I performed has mainly aimed to obtain images useful and meaningful from a diagnostic point of view. At this stage, the objective was essentially to verify the feasibility and the potential of the technique with respect to the techniques conventionally used in the study of cartilage and bone. Efforts were addressed to produce "good" images from a number of samples both in projection and tomographic (CT) mode. The specific image processing modalities applied in order to improve the quality and the interpretation of ABI images will be also described in this chapter.

Starting from tomographic ABI slices, a **three dimensional rendering** of an articulation has been realized allowing, by a manual segmentation, the separation of cartilage from the entire structure of the articular joint. An example of such volumetric reconstruction will be reported and the preliminary results obtained in a couple of pioneering ***in-vivo*** experiments on animals, successfully performed at ID17, will be shown.

The last part of the chapter is dedicated to the presentation of the work I performed (in collaboration with W. Renier and N. Foray[1]) on chondrocytes in order to identify potential radiation damage as a consequence of the X-ray irradiation during image acquisition with the ABI technique.

---

[1] INSERM unit 647-RSRM, Grenoble, France

5.2 Investigated samples

5.2.1 *In-vitro* experiments

In-vitro experiments for articular cartilage disease study and for implant healing evaluation have been performed on excised human specimens and metal implants in sheep bones, respectively.

- **Samples from patients** were acquired in the course of surgical procedures such as joint replacement surgery and amputations, and from organ donors (through the auspices of the Gift of Hope Organ and Tissue Donor Network[2]). Patient consent and institutional approval have been obtained for each sample. The specimens were immediately fixed in 4% paraformaldehyde solution and stored in 1% paraformaldehyde prior use in order to minimize storage artefacts and allow for subsequent extensive histological examination.

The samples investigated in this work are:

- human femoral heads from patients with hip osteoarthritis or necrosis of the femoral head;
- human ankle joint;
- human big toe joints;

- **Implants** are made from sand blasted Ti_6Al_4V alloy coated with a 55 μm-thick layer of hydroxyapatite (HA) with an average grain size of 5 μm. Implants consist of a cylinder with 10 mm diameter and 15 mm height (Figure 5.1) containing different profiles to test for the response of bone to various geometries. In particular, the surface contains a ring shaped groove of 4 mm width x 1 mm depth and three longitudinal indentations 3 mm wide x 1 mm deep of round, respectively rectangular, cross section. The longitudinal axis contains a threaded hole closed during implantation by two screws. The thread serves as an anchorage for a pull-out device. These specific kinds of implants have been used to be implanted in the tibia head of sheep. In addition, always one of the cylinder pair (the one in the left tibia usually) has been coated with bone morphogenetic protein 2 (BMP-2) in order to enhance bone formation.

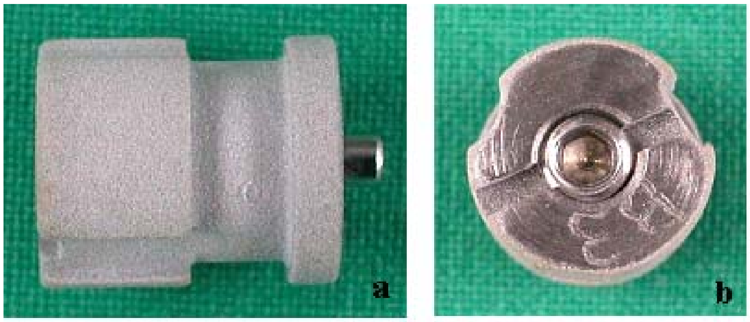

Figure 5.1. Lateral (a) and axial (b) views of the metal implants implanted in sheep bones.

---

[2] http://www.giftofhope.org/

After implantation, animals were maintained for up to 20 weeks before sacrificing. Bones containing the implants were cut into segments, fixed with paraformaldehyde and submitted to ABI examination. The differentially treated implants resulted in variations in ingrowth speed and completeness generating various tissue conditions to be monitored by X-rays.

5.2.2 *In-vivo* and radiobiological experiments

- For the pioneering ***in-vivo* experiments** on live animals performed in the framework of this thesis, the guinea pig animal model has been chosen. The reasons for this choice are in the fact that certain inbred guinea pigs are genetically prone to develop osteoarthritis starting at about six months (unfortunately, for this study not all animals develop the disease!) and that they are of acceptable size for the experimental set-up. Anatomical targets have been the hip (femoral head) and the knee (Figure 5.2).

"Retired breeder" DUNKIN HARTLEY guinea pigs have been purchased (Charles River Laboratories) and are currently hosted at the ID17 Animal facility in order to follow the development of the arthritic status.

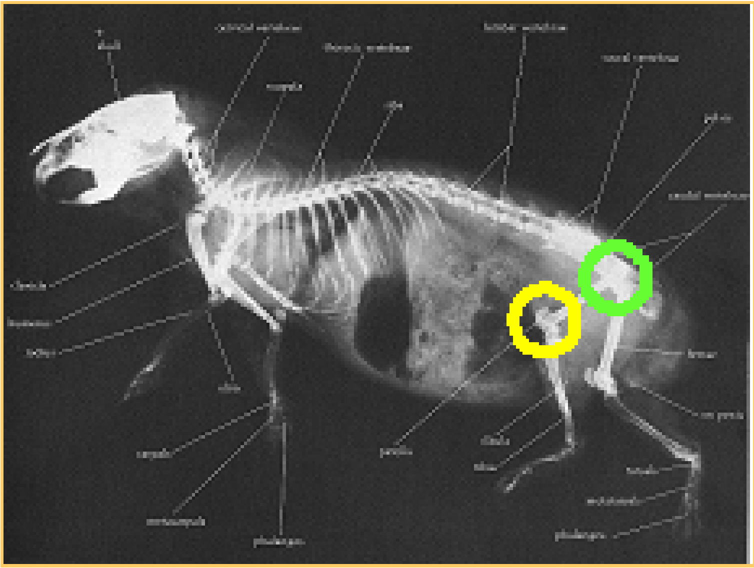

Figure 5.2. Skeletal conventional radiograph of a guinea pig. The two ring circumscribe the investigated target: in yellow the knee and in green the hip.

- **Radiobiological investigations** were made on primary human chondrocytes (HCH-c) derived from hip joints (PromoCell GmbH). Further details will be given in Paragraph 5.8.

5.3 Experimental methods

5.3.1 ABI experimental configurations

The set-up used for the ABI acquisition presented in this chapter has been already described in Paragraph 3.9.

Energies used are 33 keV and 51.5 keV (just above the K-edge of the Gadolinium, which is the main component of the fluorescent screen of the FReLoN camera - Chapter 4) and the monochromator and analyzer crystal reflection is the (333) for all the shown images. By varying the energy, the characteristics of the reflectivity curve of each crystal (Appendix 1) change and, in particular, its angular acceptance reduces. In order to keep the height of the beam emerging from the crystals fixed when changing the X-ray energy, the experimental configurations have to be modified appropriately. Experimentally, the monochromator-to-sample distance was always about 30 cm, while other distances were set as reported in Table 5.1. In the same table, the theoretical *FWHM* (Full Width at Half Maximum) of the reflectivity curves for a Si (333) crystal and the related Bragg angles at the considered energies are also reported.

	30 keV	**51.5 keV**
pre-monochromator-to-analyzer distance (cm)	54.30	90.50
analyzer-to-detector distance (cm)	131.70	95.50
FWHM (μrad)	2.40	1.45
Bragg angle (rad)	0.18	0.11

Table 5.1. Experimental details at the two energies used: distances between optical elemenets; FWHM of the reflectivity curve of a Si (333) crystal; Bragg angles.

5.3.2 Image acquisition

The imaging modalities employed for the acquisition of the images presented in this work are:

1. the projection mode,
2. the tomographic (CT) mode.

In both cases, the acquisition procedure is determined by the laminar shape of the SR X-ray beam and images are recorded at different angular positions of the analyzer crystal.

1. **The projection mode** consists of a vertical scan of the sample through the laminar beam. Depending on the detector operating mode (see Chapter 4), the sample movement, synchronized with the detector acquisition, can be continuous or discrete (in the latter case the sequence is: movement, acquisition, movement etc.). In these two cases, the movement speed or the step, respectively, is regulated to have squared pixelated images. Images are

then reconstructed by combining the lines of pixels of the detector illuminated at each acquisition during the sample movement (scan).

2. **The CT acquisition** consists in acquiring *sinogram* images and using specific software for the three-dimensional slice reconstruction. A number n of sinograms are acquired, where $n=h_{roi}/h_{pixel}$, (h_{roi} is the total height of the sample to image and h_{pixel} is the vertical pixel size of the detector). Each of these n sinograms corresponds to a given horizontal slice of the sample and is obtained by combining projections acquired at different angular orientation of the sample (which rotates around an axis perpendicular to the incident X-ray beam). Images are reconstructed using the **HST** (High Speed Tomography) program, which utilizes a direct filtered backprojection algorithm. Filtering is performed internally in the reconstruction subprogram provided by the SciSoft group[3]. However it is possible to disable this feature by selecting a sinogram filter other than the internal filter.

   The acquisition can be made in two modes:

   - Full mode: the rotating sample must be fully included in the Field Of View (FOV) of the detector in such a way the side pixels record only white field.
   - Half mode: it is used for samples wider than the detector. In half mode, it is possible to enlarge the FOV up to a factor of 2 by displacing laterally the center of rotation. The acquisition is made over 360 degrees (half the object is in the FOV from 0-180 degrees and the other half is in the FOV between 180 and 360 degrees. The second half of the sinogram is then reversed and “glued” to the 0-180 degrees sinogram; in such a way a complete 0-180 degrees sinogram of up to twice the FOV is available for reconstruction.

5.4 Image processing and correction

In this paragraph, the image processing performed to correct both projection and tomographic images is described. Such corrections are necessary for the different kind of detector noise and distortions. Since the characteristics of noise depend on its source, specific procedures have to be designed and applied for eliminating linear and/or non-linear noise components.

5.4.1 Correction of taper deformations

Each (*raw*) image acquired by using the taper FReLoN camera has to be corrected for the image distortions of the camera itself, for example deformations arisen from the imperfections of the

---

[3] For further details on the HST software, refer to http://www.esrf.fr/computing/scientific/FIT2D/HST/hst.html

camera optics (aberrations and deformations of the taper, imperfections in the coupling of the taper with the CCD etc.)

By using images of a periodic object (a grid), it was possible to quantitatively calculate pixel by pixel the distortion introduced by the camera and to calculate the corrections to be applied (C. Nemoz, private communication).

In Figure 5.3 (A) an image of a grid (holes distance: 2.5 mm) is shown as acquired with the FReLoN camera and also overlapped to its mathematical reproduction (smaller points). As a result, a two-dimensional correction matrix (of same dimensions as the raw image) has been written. Each element of the matrix contains the shifts to be applied to each image pixel in both horizontal and vertical direction in order to obtain the *true image* of the object. The corrected image of the grid is presented in Figure 5.3 (B).

The taper-correction procedure has been implemented in the IDL software routinely used at ID17 for the image processing.

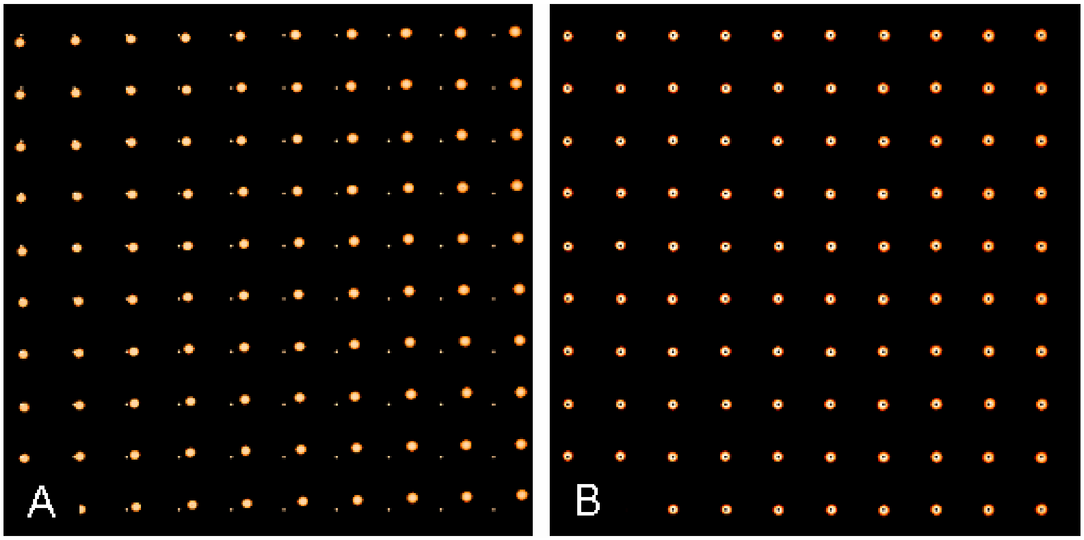

Figure 5.3. (A) Image of a grid overlapped with its mathematical reproduction. The displacement of each hole from its theoretical position is due to the imperfections of the camera optics. (B) The corrected image.

5.4.2 Image normalization

The signal of an image (raw image) is always the result of the interaction of the radiation with the sample under investigation plus a series of other contributions (signal fluctuations) that can degrade in different ways the image quality.

Possible sources of these intensity fluctuations within images are:

1. temporal instability of the incident X-ray beam.

   Causes: machine current decreased with time, and vibrations or thermal drift of optical elements (filters, slits, crystals) may occur along the X-ray path.

2. spatial instability of the incident X-ray beam.

   Causes: angular position of the X-ray beam from the wiggler and defects or deformations of optical elements.

3. detector response inhomogeneities.

   Causes: electronic noise (dark current); pixels with different gain.

In order to correct images by eliminating or reducing these spurious contributions, a *normalization* procedure is applied. Depending upon the experimental set-up and acquisition modalities, the image normalization has to be suitably defined.

Two supplementary images have to be acquired:

- a *dark-noise image*, which is recorded without exposure to X-rays. The signal consists only in the electronics noise of the detection chain (additive noise).
- a *white-field image*, which is registered in the same conditions as the raw image to normalize but without the sample in the X-ray beam. Therefore, this image is an image of the beam itself (multiplicative noise) and the detector response.

Since the white-field is degraded by the electronic noise as any image, the normalization procedure can be schematized as

$$normalized\ image = \frac{raw\ image - darknoise}{whitefield - darknoise} \tag{5.1}$$

When a laminar beam is employed, as is the case at ID17, the image is obtained as a sum of the different series of illuminated lines of pixels of the detector while the sample is scanned through the X-rays. Therefore, after subtracting the dark-noise image from the raw image and the white-field, respectively, normalization is achieved by dividing each pixel value of a column of the raw image by the average of the pixel values of the related column of the white-field.

In the case of a broader X-ray beam able to cover the entire sample, combined with an area-detector, the normalization procedure is obtained by applying the equation (5.1) pixel by pixel. This last case concerns acquisitions performed at ID19 and presented in Chapter 6.

Spatial inhomogeneities due to misalignment of the crystals of the monochromator/analyzer system (such as the presence of a tiny horizontal tilts between them or other possible instrumental distortions like dynamical deformations of the crystals (lattice curvature)), may still remain in the corrected images. These inhomogeneities could give a small spectral gradient in the final image meaning that different areas in the image may be illuminated with slightly different X-ray wavelengths.

5.4.3 Correction of line and ring artefacts

Images can be sometimes affected by inhomogeneities that are quite but not perfectly regular and/or constant with time. This is, for instance, the case for artefacts due to low intensity of the X-ray beam or of vibrations of the optics caused by the (monochromator) cooling systems. These disturbances generate horizontal lines that cannot always be normalized by procedures described above.

In some cases, normalizing the image by selecting bands of pixels on the image itself (in regions not covered by the sample) can partially solve the problem. In fact, vertical or horizontal (depending on the direction of the inhomogeneities) bands of pixels can be chosen close to the detail of interest, averaged and used in image normalization. This may sometimes work, especially on small areas. When it is not possible to model the noise by linear calculations and reduce it with simple normalization methods, other more complex procedures are needed.

Working in the frequency domain can often simplify the task. For this reason, the Fourier transformation is used in a wide range of applications, such as image analysis, image filtering and reconstruction. It is used to access the geometric characteristics of a spatial domain image.

The Fourier transformation produces a complex-number valued output image which can be displayed by two images, either with the *real* and *imaginary* part or with *magnitude* and *phase*.

In image processing, often only the magnitude of the Fourier transformation is displayed since it contains most of the information on the geometric structure of the spatial domain image.

In most implementations, the Fourier image ($F(u,v)$, with u and v spatial frequencies in the two perpendicular directions) is shifted in such a way that the image mean ($F(0,0)$) is displayed in the center of the image. The further away from the center an image point is located, the higher its corresponding frequency will be.

Generally, an image contains components of all frequencies, but their magnitude gets smaller with higher frequencies. Hence, low frequencies carry most of the information.

The image mean is by far the largest component of the Fourier transformed image, as shown in the 2DFT (discrete Fourier transformation) images in Figure 5.4 (b) and 5.5 (b). Moreover, there are two dominating directions in the Fourier image, one passing vertically and one horizontally through the center. These directional features originate from the regular patterns in the background of the original image that could also be due to particular noise inhomogeneities.

Additive noise is, in many cases, evenly distributed over the frequency domain and therefore it is dominant at high frequencies. Its effects can be reduced using some kind of *low-pass* filter. Multiplicative or non-linear noise would be much more difficult to model and would require complicated mathematical treatment.

For frequency filtering, the Fourier-transformed image can be used and combined with suitable *frequency-mask images* for reducing spatial fluctuations. After having identified the frequencies of the noise signal, it is possible to set those frequency components to zero by means of a mask image.

In order to reduce the line artefacts sometimes affecting images acquired for this Thesis, the procedure hereafter schematized has been written in Matlab language and applied (examples of images of a biological sample and a plastic phantom are presented in Figure 5.4 (a) and 5.5 (a) respectively):

1. **Two-dimensional Fourier transformation** *F(u,v)* of the image *I(x,y)* (Figure 5.4 (b), 5.4 (b));
2. Creation of a **mask**, *b(u,v)*, consisting of 'zeros' at the frequencies of the noise artefacts and 'ones' elsewhere. An example of such an image is shown in Figure 5.4 (c) and 5.5(c). Depending on the distribution of the noise frequencies the mask pattern can be modified by changing the parameter n_u and n_v, the width and the length of the "zeros" region, respectively (see figure). When the line artefacts are horizontally oriented, in the Fourier domain the related frequencies lie on the vertical axes, while the opposite is the case for artefacts vertically oriented;
3. **Noise frequencies elimination** by multiplying the Fourier transformation *F(u,v)* of the image by the mask *b(u,v)* (results in Figure 5.4 (d) and 5.5 (d)). The Fourier transformation of the corrected image is given by $F_{cor}(u,v) = F(u,v) \bullet b(u,v)$;
4. The corrected image in the spatial domain is obtained by applying the inverse two-dimensional Fourier transformation of $F_{cor}(u,v)$ (Figure 5.4 (e) and 5.5 (e)).

In this analysis, two aspects have to be highlighted.

- As already mentioned, Fourier transformation produces complex-numbered images that can be displayed by a couple of images representing the magnitude (real) and the phase (imaginary) components, respectively. In image processing (and in the figures presented here as well), often only the magnitude of the Fourier transformation is displayed, as it contains most of the information of the geometric structure of the spatial domain image. However, if the Fourier image has to be re-transformed into the spatial domain after some processing in the frequency domain, both magnitude and phase of the Fourier image must be preserved.
- Moreover, the dynamic range of the Fourier coefficients (*i.e.* the intensity values in the Fourier image) is too large to be displayed on a screen. Therefore, a logarithmic transformation has to be applied to the image.

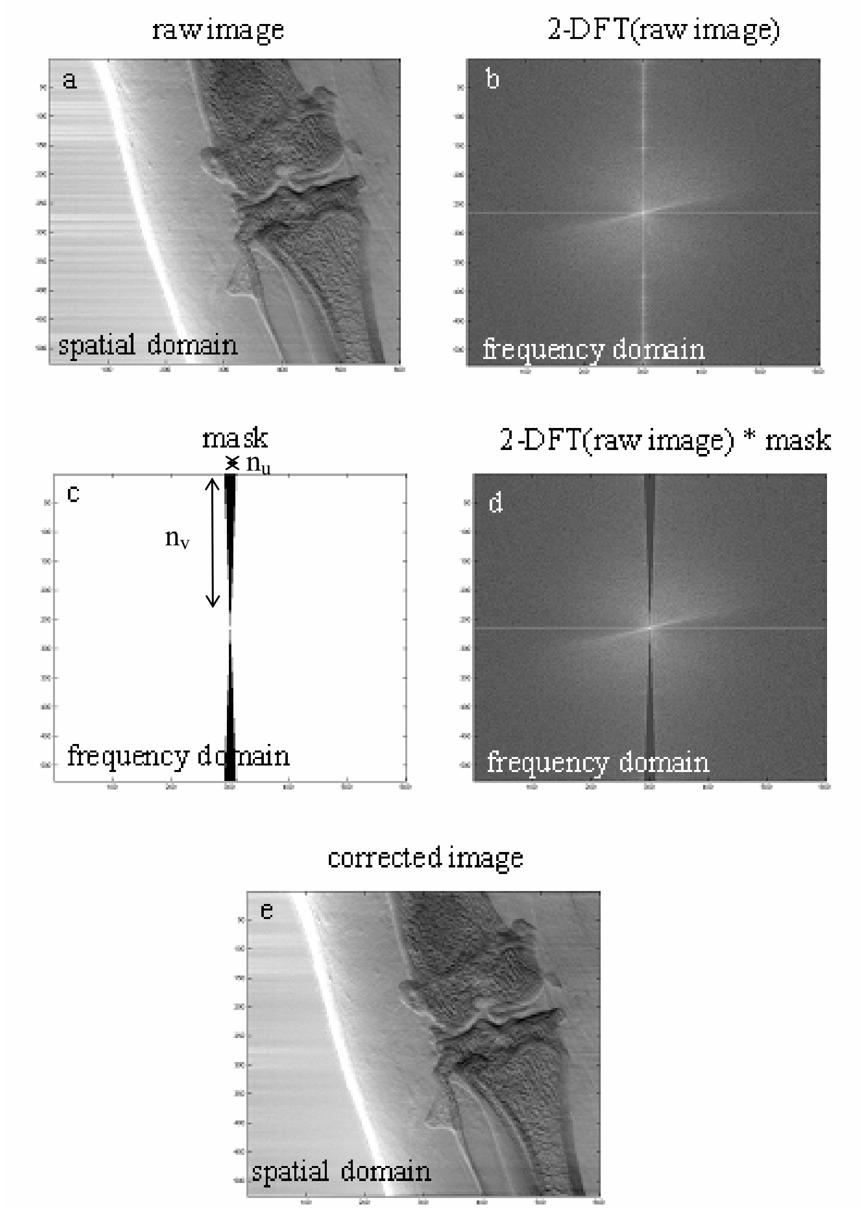

Figure 5.4. Images of a biological sample (knee articulation of a guinea pig) representing the intermediate and final results of the different steps of the line artefacts correction procedure.

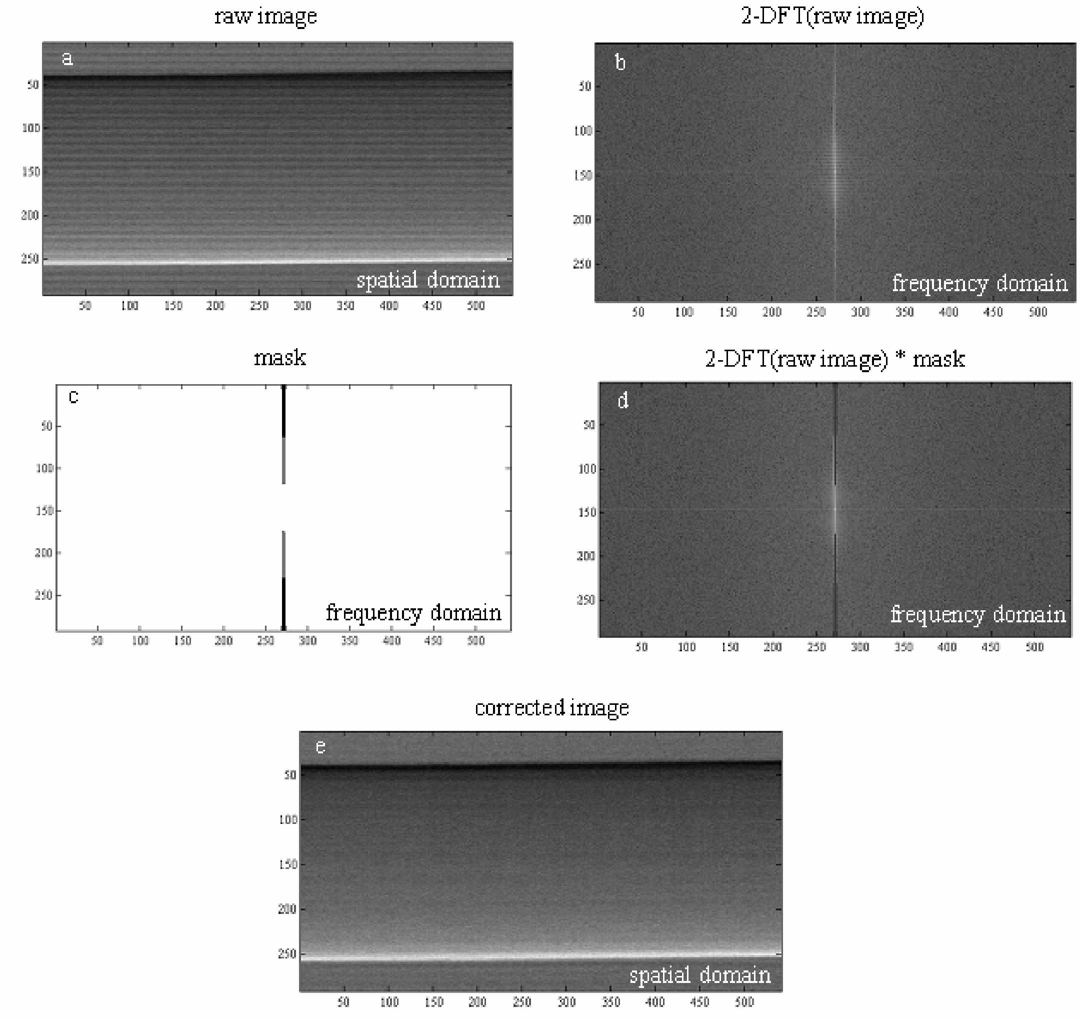

Figure 5.5. Images of a plastic phantom representing the intermediate and final results of the different steps of the line artefacts correction procedure.

- When applying this correction method some frequency components of the image are cancelled, thus modifying the geometrical structure of the original spatial domain image. Since the noise frequency pattern in most cases is at least partially mixed up with the image frequency pattern, this operation always eliminates some image frequencies together with the noise frequencies. For this reason, if quantitative measurements have to be performed on the considered images, particular attention has to be paid in the frequencies cut-off.
- This procedure has been shown to be particularly useful for correcting ring artefacts in tomographic images (originating by noisy or dead detector pixels in the sinograms).

5.4.4 Deconvolution with detector spatial resolution

The image ($I_{cor}(x,y)$) recorded by a detector is always the result of the convolution of the incident signal $I_{inc}(x,y)$ (the real, unknown image) with the *Point Spread Function* (*PSF(x,y)*) of the acquisition system (Dainty and Shaw, 1974). Therefore it is possible to write in the spatial domain:

$$I_{rec}(x,y) = I_{inc}(x,y) * PSF(x,y) \tag{5.2}$$

More in detail, since acquisitions are performed in our case with a laminar X-ray beam that illuminates a linear ROI (region of interest) of the detector (often just one line), the problem can be treated in a one-dimensional approach and the signal recorded by the detector can be expressed as (Hasegawa, 1990):

$$I_{rec}(y) = \frac{1}{p}[I_{inc}(y) * LSF(y) + n(y)] \cdot \Pi\left(\frac{y}{p}\right) \tag{5.3}$$

with *p* being the detector pixel size (corresponding to the sample scanning step), *LSF* the Line Spread Function (=*PSF* integrated along the scan direction), $p^{-1}\Pi(y/p)$ the sampling (comb) function and *n* the noise (here represented as an additive function).

As already mentioned in Chapter 4, the effect of convolution with the detector *PSF* in the spatial domain (or multiplication in the Fourier space) is that of a low-pass filter that cuts off the image high frequencies. A detector is considered to possess a high resolution when it does not substantially modify the incoming signal since its *PSF* has a FWHM narrower than the width of the signal variations or oscillations.

The convolution effect is a relevant smearing of the signal, but lost information can be at least partially recovered off-line by means of a deconvolution algorithm. This off-line processing receives as inputs the acquired signal and the detector *PSF* (or *LSF*), which has to be measured separately, and produces as output an image with increased spatial resolution.

As for the line artefacts correction, once again passing in the Fourier space allows simplifying the task since convolution of functions (deconvolution) in the spatial domain turns into multiplication (division) of the related Fourier transformation in the frequency domain and *vice versa*.

Expressing the detector resolution in terms of Modulation Transfer Function, *MTF(v)*, (see Chapter 4) which is the Fourier transformation of the *LSF(y)*, the (5.3) becomes:

$$F_{rec}(v) = [F_{inc}(v) \cdot MTF(v) + N(v)] * \Pi(pv) \tag{5.4}$$

with $F_{rec}(v)$, $F_{inc}(v)$ and $N(v)$ being the Fourier transformations of the recorded signal, the incident signal and the noise, respectively.

The effect of the convolution with the comb function $\Pi(pv)$ is the replication with the frequency *1/p* along the entire *v* axis of the spectrum:

$$\widetilde{F}_{rec}(v) = [F_{inc}(v) \cdot MTF(v) + N(v)] \tag{5.5}$$

If such a spectrum is not limited to frequencies lower than $(2p)^{-1}$, this leads to the well-known *aliasing* error (Dainty and Shaw, 1974): all frequencies higher than $(2p)^{-1}$ will not be reproduced in the image, and an overestimation of the Fourier coefficients may occur at all frequencies. These errors are strictly correlated to the necessity of sampling the signal, and therefore unavoidable. Due to this fact, we neglect the spectrum replication and the correction procedure will be directly applied to equation (5.5). This procedure is strictly exact if the spectrum is limited to frequencies lower than or equal to $(2p)^{-1}$ (Nyquist theorem); otherwise it will result in an approximation which becomes less and less effective as the limiting frequency is increased. In principle, $F_{inc}(v)$ can be estimated from equation (5.5) as:

$$F_{inc}(v) = \frac{\widetilde{F}_{rec}(v) - N(v)}{MTF(v)} \tag{5.6}$$

The real image $I_{inc}(x, y)$ can then be estimated by inverse Fourier transforming $F_{inc}(v)$. It is clear that such estimation is correct only in the ideal case of $N(v) = 0$; in fact, noise sources are always present in an acquired image (there are at least the quantum fluctuations).

I have calculated correct images by simply neglecting the noise and applying the equation:

$$I_{inc}(y) = F^{-1}\left(\frac{\widetilde{F}_{rec}(v)}{MTF(v)}\right) \tag{5.7}$$

with F^{-1} denoting the inverse Fourier transformation.

I have used the *MTF* curves of the FReLoN camera I measured and presented in Chapter 4. In Figure 5.6 the vertical *MTF* for the 100 µm thick fluorescent screen at 51.5 keV is shown.

As examples, results of the deconvolution of two different images are displayed in Figure 5.7 (same two images considered for the line artefacts correction in the previous paragraph). For the calculation, the *MTF* of Figure 5.6 has been used (both images were in fact acquired at 51.5 keV).

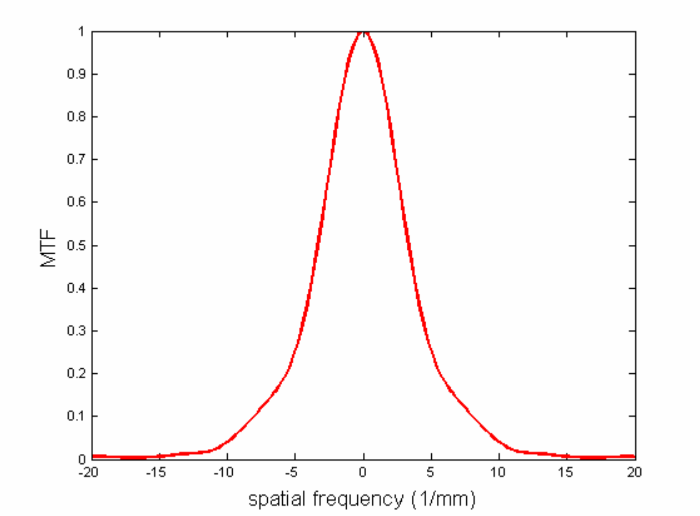

Figure 5.6. FReLoN camera vertical MTF for the 100 μm thick fluorescent screen at 51.5 keV.

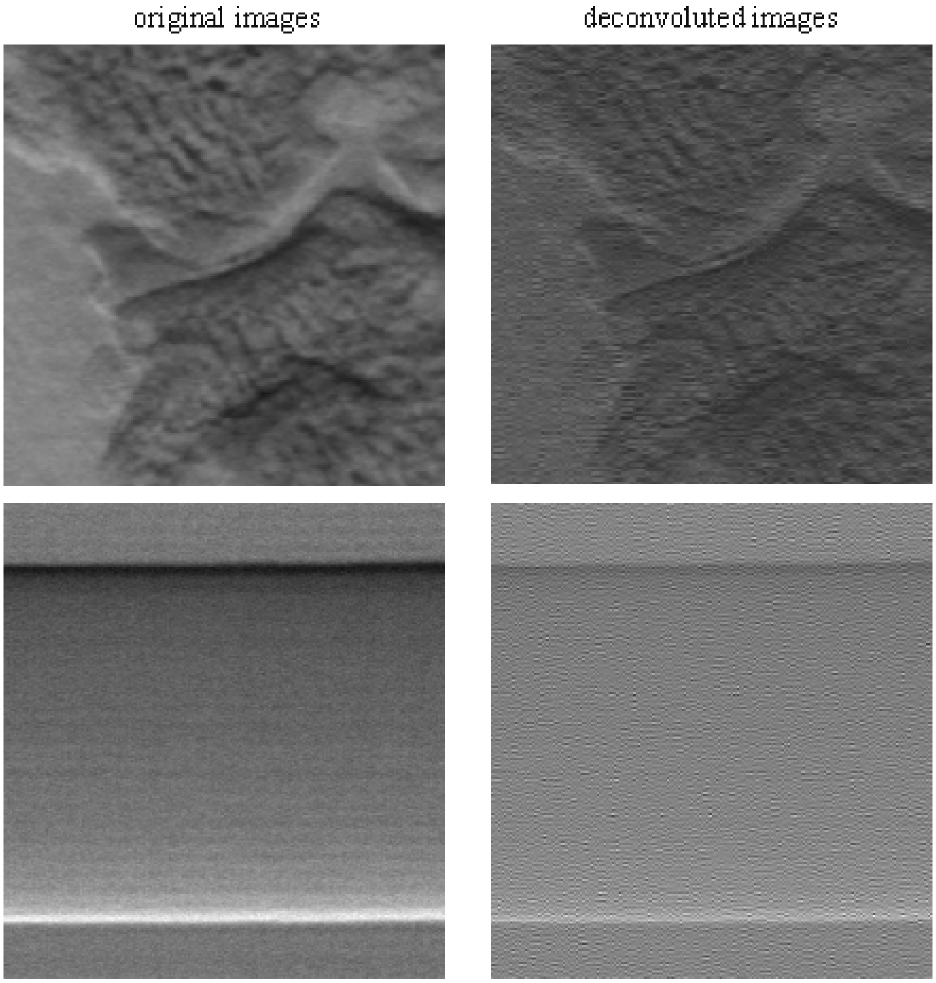

Figure 5.7. Raw images acquired with the taper FReLoN camera (left) and the same images deconvoluted with the measured *MTF* of the detector by using equation (5.7) (right). Image have been acquired with the 100 μm thick fluorescent screen at an energy of 51.5 keV.

By looking at the deconvoluted images of Figure 5.7, it is possible to notice that the applied correction algorithm introduces a lot of evenly distributed background that heavily spoils the image quality. As discussed in some literature (Olivo, Rigon *et al.*, 2000), this background originates from the low intensity of the high frequency components of the *MTF*. In fact, the ratio *N/MTF* (in equation (5.6)) becomes extremely high for those frequencies where $MTF \rightarrow 0$, even when the noise is very low. Thus, it is necessary to apply some filtering.

Different filtering functions can be used. It is, for instance, possible to multiply both members of the equation (5.6) by a function $\xi(v)$ such as: $\xi(v) \rightarrow 1$ for $F_{inc}(v) \gg N(v)$ and $\xi(v) \rightarrow 0$ for $F_{inc}(v) \ll N(v)$ (Olivo, Rigon *et al.*, 2000). As seen in the previous paragraph, noise dominates the image at high frequencies, therefore $\xi(v)$ has to be a sort of a low-pass filter resulting in:

$$\frac{\widetilde{F}_{rec}(v)}{MTF(v)}\xi(v) = F_{inc}(v)\xi(v) - \frac{N(v)}{MTF(v)}\xi(v) \cong F_{inc}(v) \tag{5.8}$$

Then, by inversely transforming $\widetilde{F}_{rec}\xi / MTF$, an estimate of the real image can be obtained. Such an estimate will be a good approximation of $I_{inc}(x,y)$ only if the choice of the filter is appropriate.

In order to test the effect of the deconvolution procedure in our images, I decided to proceed in a very simply way by smoothing the decrease of the *MTF* curve. Starting from a certain frequency (which value has been empirically derived), I have raised the *MTF* values at a fixed value. The result of this procedure is shown in Figure 5.8 (dashed blue line).

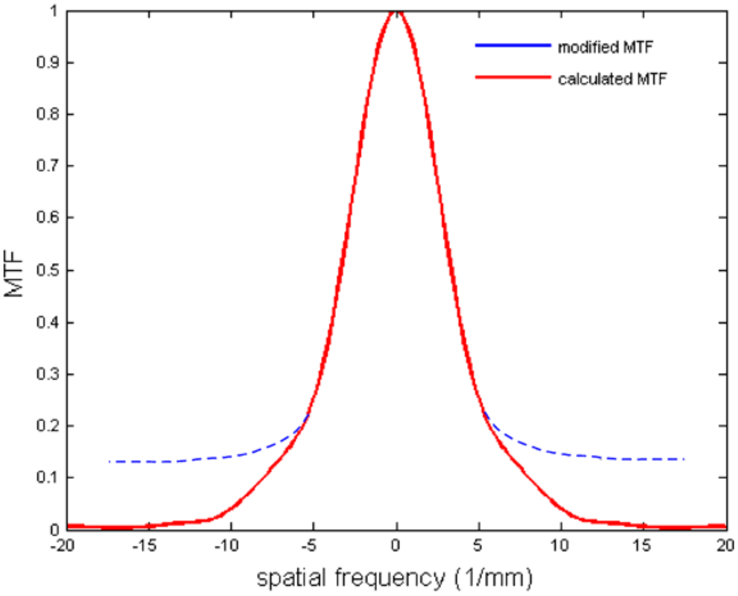

Figure 5.8. Filtered *MTF*.

In Figure 5.9 the deconvoluted images obtained by using this filtered *MTF* are presented. The starting images are the same use as example in Figure 5.7.

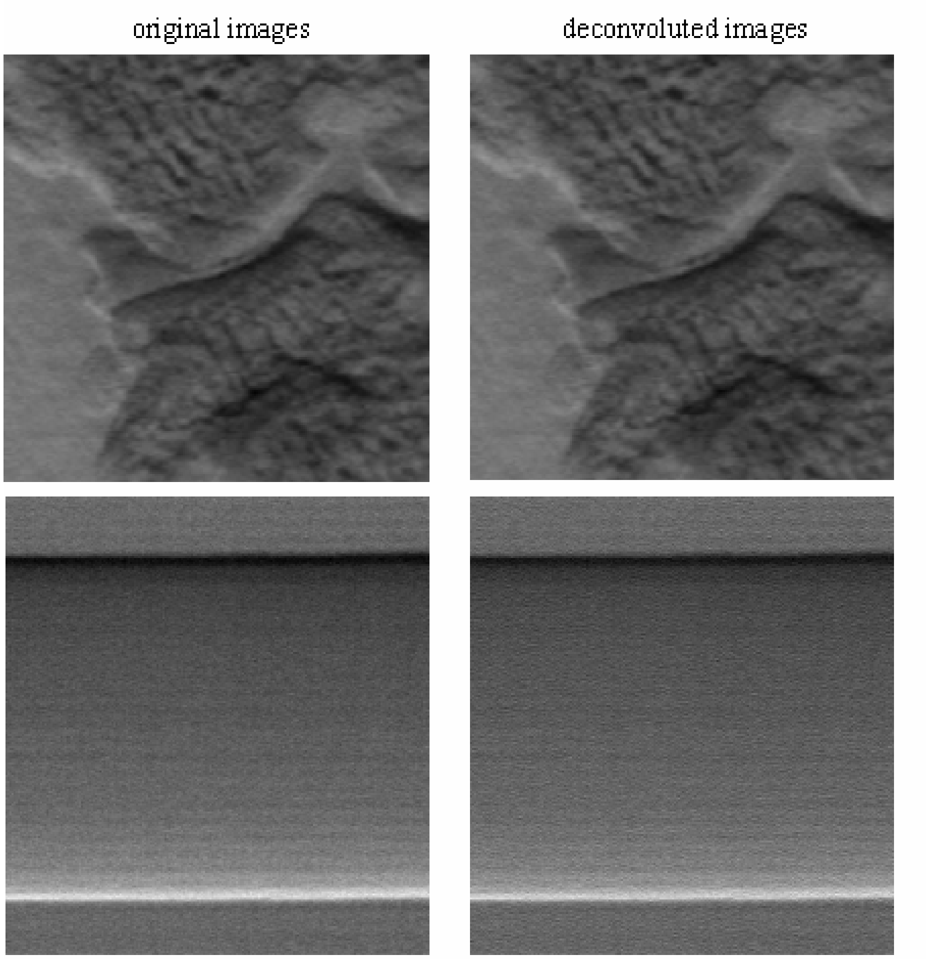

Figure 5.9. Results of the deconvolution algorithm by using filtered *MTF*.

Corrected images are much less noisy than ones obtained with the unfiltered *MTF*. The quality of the deconvoluted images is good but, on the other hand, the image resolution has not significantly increased.

In the light of these results and of other studied examples not presented here, I preferred not to deconvolute images with the detector since the gain in image quality is not significant while the risk of introducing additional noise into the image is not negligible.

5.4.5 Color-coded ABI images

As an alternative to separately calculate absorption and refraction information in AB images derived from different angular positions of the analyzer crystal (by applying the DEI algorithm), physicians have expressed the need to summarize as much information as possible in one unique image.

From a medical point of view, in many cases, slope images and the top image themselves seem to carry most of the meaningful details. For this reason, an algorithm has been written (Marco Stoessel, Dept. of Orthopaedics at the Waldkrankenhaus Rudolf Elle) in order to obtain an image that is the mere overlap of a set of "minus", "top" and "plus" images. By differently colouring each of these images (Figure 5.10), a composite image is created: dominating features coming from one specific image (that is, a specific analyzer angular position) of the set will appear in the corresponding pure colour, whereas mixed features will appear in mixed colours. This new image will be called "Diffraction-colour image" in the rest of chapter. An example of the procedure is presented in Figure 5.10.

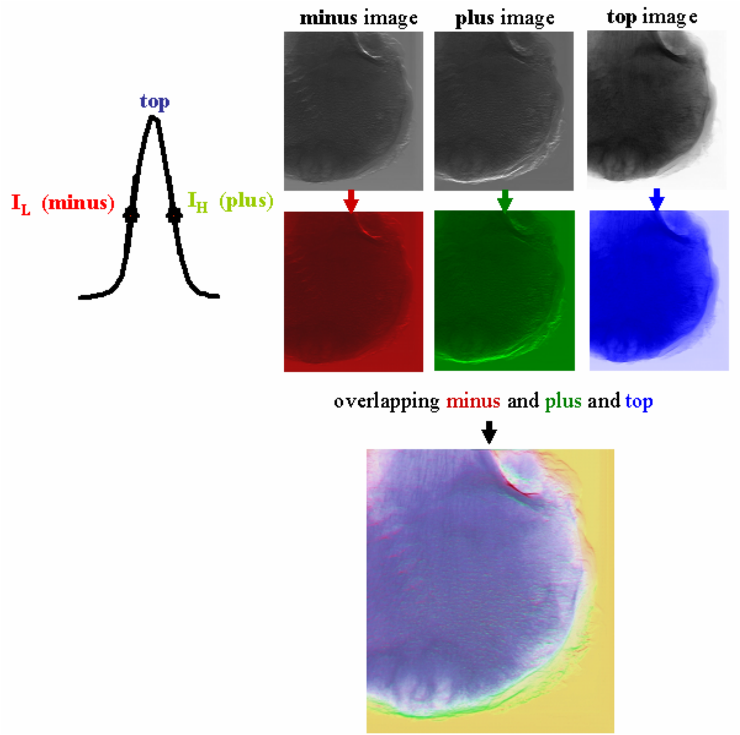

Figure 5.10. Example of a "Diffraction colour image" of a hip obtained by overlapping "minus", "plus" and "top" ABI images differently coloured. Note the dominating blue in the center of the hip bone where x-ray absorption is strongest, and the green and red stains at the edges within the cartilage, where diffraction generates the main image component.

5.5 Results of the *in-vitro* experiments

In Table 5.2, I have summarized the acquisition details for the different samples considered in this study. In particular, the energy, the imaging mode (planar projection and/or tomography), and the detector used are reported here.

In the following paragraphs, results obtained for each sample are presented. The most complete studies regard the femoral head and metal implants since they include both projection and tomography analysis and a full comparison with all the conventionally used clinical imaging techniques. This work, which is the fruit of the collaboration between the Department of Orthopaedics of the University of Jena with the ID17 at ESRF, the HASYLAB at DESY (Hamburg), ELETTRA (Trieste) and the Rush Medical College (Chicago), has resulted in two papers:

- A. Wagner, *et al.* "*Chance and limit of imaging of articular cartilage in vitro in healthy arthritic joints - DEI (Diffraction Enhanced Imaging) in comparison with MRI, CT and ultrasound*", SPIE Proceeding, Vol. 5746, 542-549, 2005.
- A. Wagner, *et al.* "*Options and Limitations of Joint Cartilage Imaging: DEI in Comparison to MRI and Sonography*", Nuclear Instruments and Methods A, Vol. 548, 47-53, 2005.

Some of the results here presented on the application of the ABI technique on metal implants and their comparison with conventional radiography and histology have been published in:

- A. Wagner, *et al.* "*Quality evaluation of Titanium Implant Ingrowth into Bone by Diffraction Enhanced Imaging (DEI)*", Phys. Med. Biol.,Vol. 51, 1313-1324, 2006.

sample	**energy (keV)**	**acquisition mode**	**detector**
human hip	30	projection	46 µm FReLoN camera
	50	tomography	"
human ankle	50	projection	"
	50	tomography	"
human toe	30	projection	"
	30	tomography	"
metal implant	50	projection	"
	50	tomography	"

Table 5.2. Acquisition details.

5.5.1 The femoral head (hip)

The hip is a ball-and-socket joint where the head of the femur articulates with the cup-like acetabulum of the pelvic bone (Figure 5.11 (a)).

Human femoral heads from patients with hip osteoarthritis (OA) or necrosis of the femoral head obtained through joint replacement surgery were **investigated by macroscopic inspection, conventional X-ray examination and conventional tomography (CT), analyzer-based imaging (ABI), magnetic resonance imaging (MRI), ultrasound (UI) and histology.**

In Figure 5.11 (b-c), the cases of a healthy and an arthritic hip joint are schematized. As explained in Chapter 1, OA is a disease that involves the breakdown of the cartilage tissue that normally allows the joint to move smoothly. When the gliding surface of the cartilage is damaged or has disappeared, the bones grind against each other, creating pain and loss of normal joint movement. Clinically overt OA is conventionally diagnosed by planar x-ray radiology measuring the joint space narrowing. Unfortunately, until now OA is detectable only at advanced disease stages. Therefore, detection of early signs of degeneration has been one objective of this study.

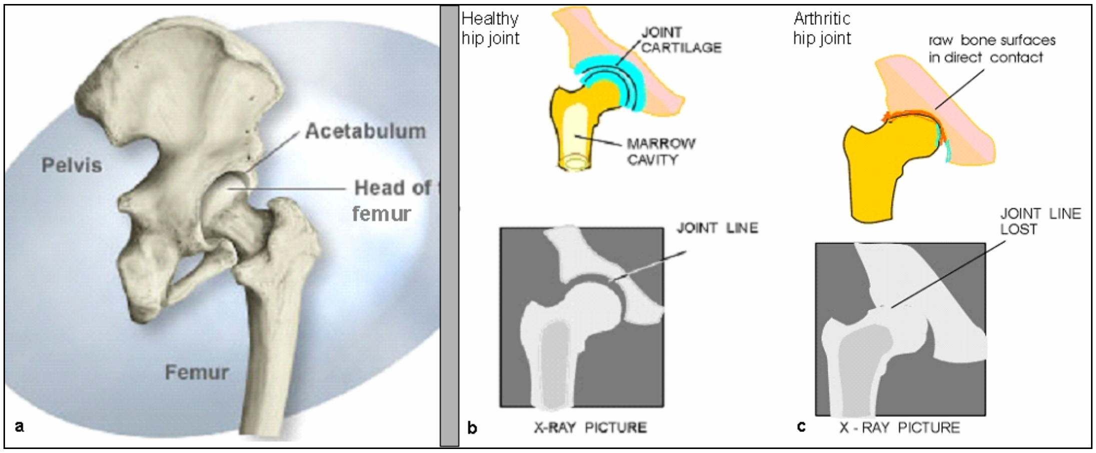

Figure 5.11. a) Anatomy of the hip joint. b) and c) schemes of a healthy and arthritic hip joint.

Figure 5.12 shows the morphology of a femoral head used for images afterwards presented: (a) and (b) are the 'frontal and above' view and the 'frontal' view, respectively, of the sample. Some details are indicated: 1- the ligament base (removed after ABI examination), 2- a defect, and 3- an artificial damage (knife cut).

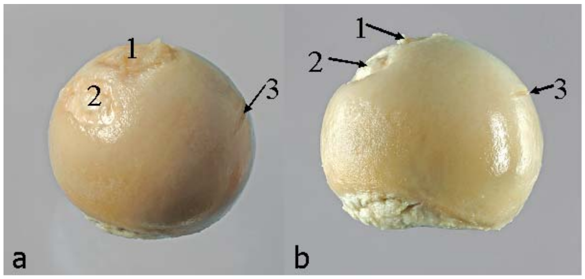

Figure 5.12. Pictures of the hip used in this study.

– **ABI** images have been acquired at different angular positions of the crystal analyzer. These positions are referred to by the fraction of intensity with respect the maximum (*top*) of the rocking curve of the analyzer (see figure on the right).

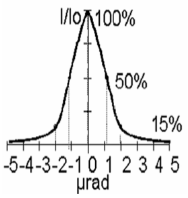

– **Conventional X-ray** images were obtained by a General Electric GE mammography unit.

– **UI** was performed applying a high resolution commercially available device used in dermatology at 20 MHz and conventional 7,5 and 10 MHz devices (Siemens).

– **MRI** were performed on a T5NT (Philips) with surface coil, using two kinds of sequences: the T1 SPIR TFE TE 22, TR 95, Flip 50 and the T1 FFE MTL TE 22, TR 80, Flip 50 (slice thickness 1.2 mm).

– **Conventional CT** was performed using a Siemens Somatom Balance at 120 kV (1 mm slices).

– **Histology** was performed on 5 µm sections from decalcified and paraffin embedded select segments from the femoral head. The sections were stained by either the azan-based Masson-Goldner procedure[4] to discriminate bone and soft tissue, or by safranin O/fast green to visualize the composition of articular cartilage.

Examinations by using conventional diagnostic techniques have been performed by at the Department of Orthopaedics (Univ. of Jena).

- **PROJECTIONS**

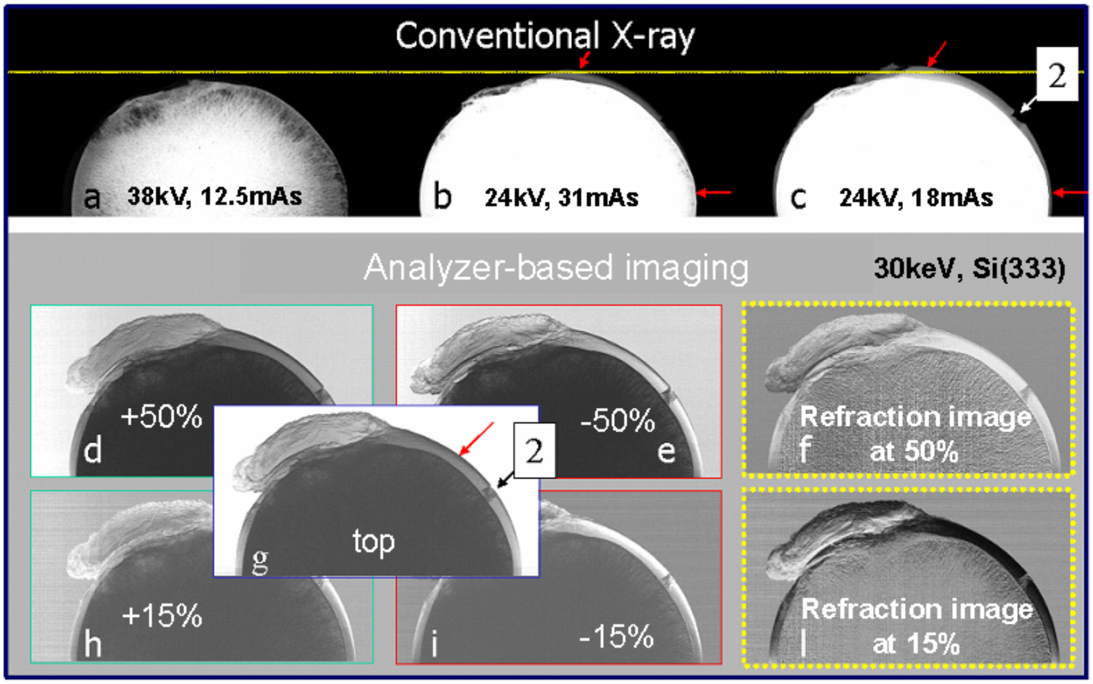

Figure. 5.13. Conventional radiographs and ABI projection of a hip acquired at different experimental conditions (detailed description in the text).

Figure 5.13. Conventional absorptive X-ray examination of the femoral head is shown in (a-c). The experimental parameters are respectively: (a) 38 kV, 12.5 mAs, (b) 24 kV, 31 mAs, (c) 24 kV, 18 mAs. In Figure (a) Conventional absorptive X-ray examination, cartilage is invisible. Only conditions with selected experimental voltage and currents allow for visualizing cartilage

---

[4] http://www-medlib.med.utah.edu/WebPath/HISTHTML/MANUALS/MANUALS.html
or http://www.protocol-online.org/prot/Histology/

but the surface, the cartilage height, and eventual internal features are still not clearly defined (see red arrows).

In (d-l) ABI projection images from the same femoral head are presented: (d) + 50%, (e) –50%, (f) Refraction-Image at 50%, (g) Top-Image, (h) + 15%, (i) –15%, (l) Refraction-Image at 15%. Images are optimized to detect cartilage and ligament. On contrary to conventional radiographs, in ABI images cartilage height is clearly defined in all images (red arrow). The arrow with the number "2" points out the artificial detail on the cartilage tissue.

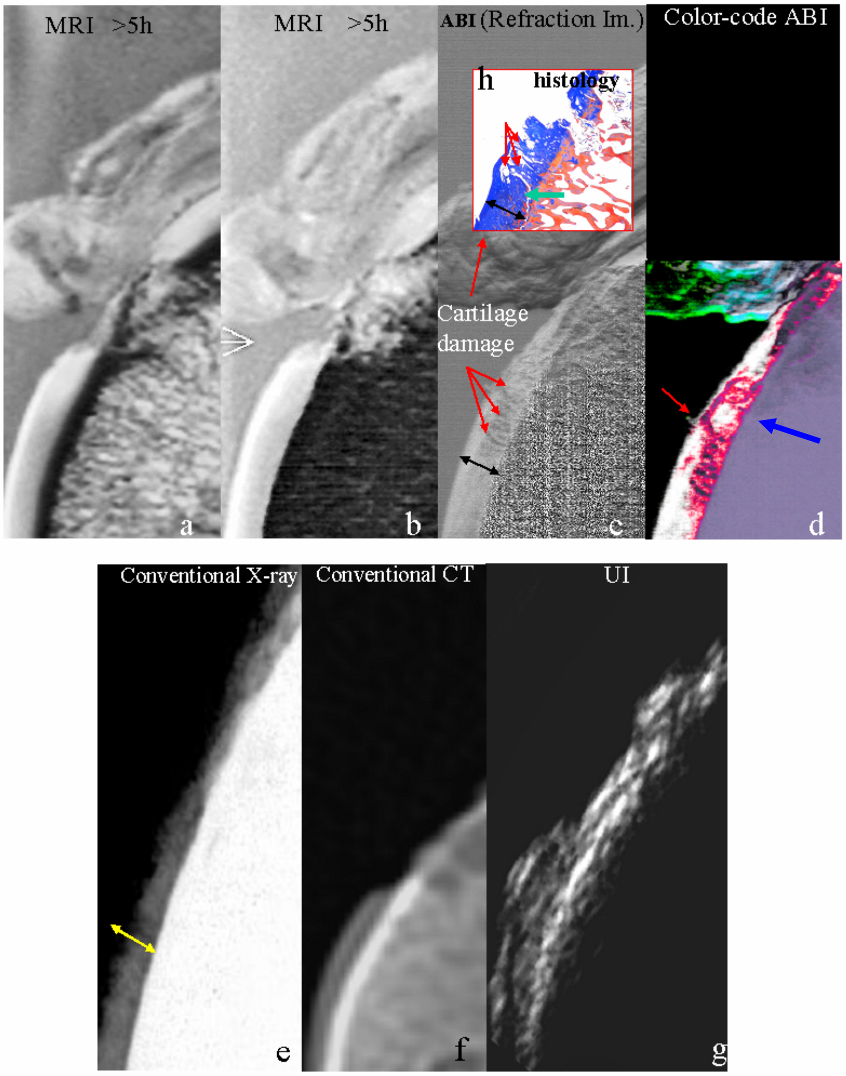

Figure 5.14. Comparison of ABI projections of the hip with images obtained with conventional techniques (detailed description in the text).

Figure 5.14 (a-g) shows the comparison of <u>projection images</u> (**(e)** conventional X-ray: 24 kV, 18 mAs; **(c)** ABI: refraction image at 50%) and <u>tomographies</u> (**(f)** Conventional CT [130 kV, 60 mA, window 1500, level 400]) and <u>MRI</u> **(a, b)** (exposure time longer than 5 hours) from an arthritic lesion of the femoral head shown in Figure 5.12. The yellow double-headed arrow indicates the real thickness of cartilage. Despite (c) is a projection image, structural damage of cartilage, invisible even in CT and MRI images, is displayed. Conventional X-ray shows only deep zone of cartilage but is not able to visualize structural irregularities seen in ABI. The image in (d) is a colour-coded ABI diffraction image (minus 50% - red; plus 50% - green; top – blue). The image in (h) presents the histological correlate ([Masson-Goldner 1.25x]). Refraction ABI image and colour-coded ABI unmask internal structures in cartilage (red arrows) which are signs of cartilage tissue damages. The blue arrow points out a nascent osteophyte (a growing cartilage/bone spur).

▪ TOMOGRAPHY

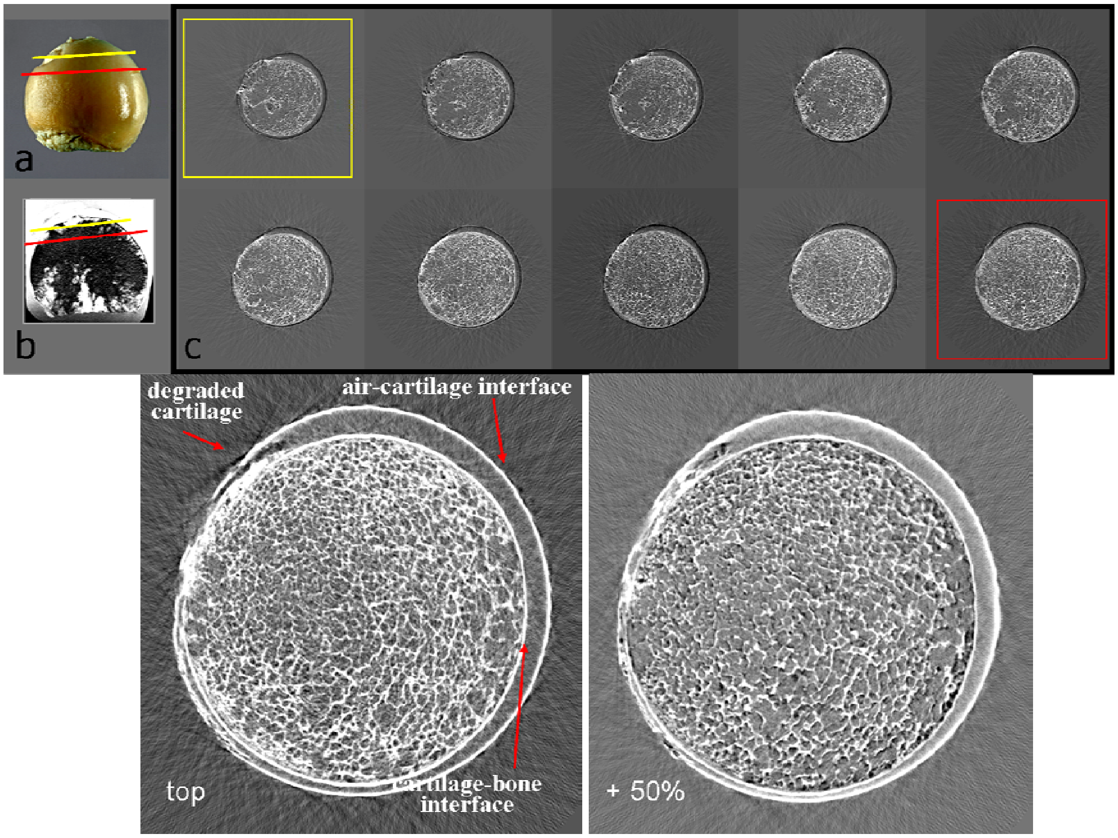

Figure 5.15. ABI tomographic images of the hip (detailed description in the text).

In **Figure 5.15**, ABI tomographies acquired at 50 keV (Si (333)) of the same hip are presented. In (a, b) the section where ABI-CT have been performed is indicated by yellow and red lines. In (c) ABI-CT slices at "minus 50%" are shown. The two ABI slices at the bottom of the figure are a "top" and a "plus 50%" ABI CT. Cartilage-bone and cartilage-air interfaces are highlighted and defined. Cartilage thinning and degradation on the left of the sample are perfectly detected as well. The meshwork of the trabecular bone tissue is clearly defined both in the "top" and in the "plus 50%" ABI CT.

Figure 5.16 shows the comparison of MRI, UI, conventional CT, and ABI-CT: (a-c) experimental MRI with 5.5 hours of exposure; (d) circumferential reconstruction of segmental UI with 13.5 mHz; (e) conventional CT with false colour contrast for better optical visualization of cartilage (130 kV, 60 mA, window 1500, level 400); (f) colour-coded ABI-CT.
All images show the approximately same slice of the femoral head segment as illustrated by red line in the inset (c). The yellow arrows point to damaged cartilage and the asterisks indicate the artificial artefact made with a knife.
In the right part of the figure, the pixel intensity profiles of the tissues borders are presented. The curves show no defined transitions in MRI and conventional CT. Only the ABI curve displays clear intensity jumps at the interfaces between tissues clearly delineate the borders of cartilage.

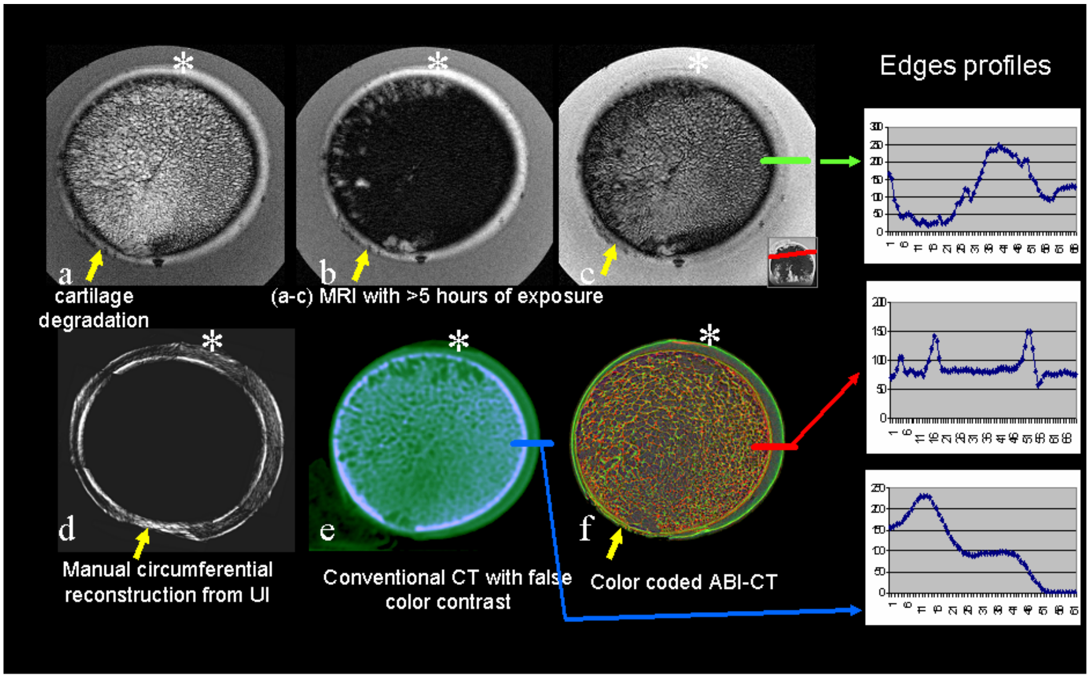

Figure 5.16. Comparison of ABI tomography of the hip with slices obtained with conventional techniques (detailed description in the text).

Figure 5.17 A comparison of structural details obtained from ABI-CT and from histology of a healthy segment from the femoral head. (a) ABI-CT slice, refraction image. The blue box indicates the magnified region in (b), the dashed-white box the safranin O/ light fast green - stained histological section in (c). Safranin O (red) stains for regions with high proteoglycan content, light green (blue) contrasts regions with low proteoglycan content. Note that ABI is capable to separate the intensely red stained mineralized cartilage from the unmineralized cartilage. In addition, the superficial layer cartilage of the joint surface, stained in blue, is also discriminated.

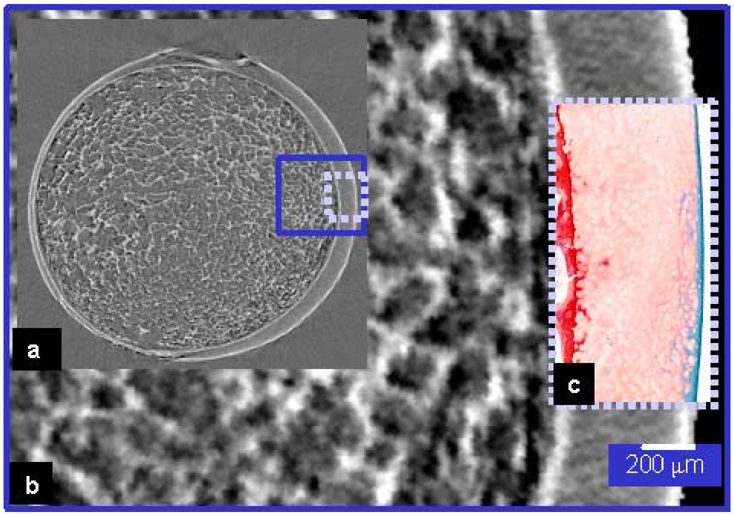

Figure 5.17. ABI tomographic slice of the hip compared with histology (detailed description in the text).

Figure 5.18. Colour-coded ABI-CT segment (0.25 mm slice) compared to 5 µm thick microscopic histology sections. The picture shows a comparison of normal-looking cartilage from two selected sites. Note that the damaged trabecular meshwork of the bone to the left and the fine trabecular meshwork to the right are equally well imaged in ABI as in microscopy. Also, the thickness of the cartilage in histology matches the imaged geometry from ABI.

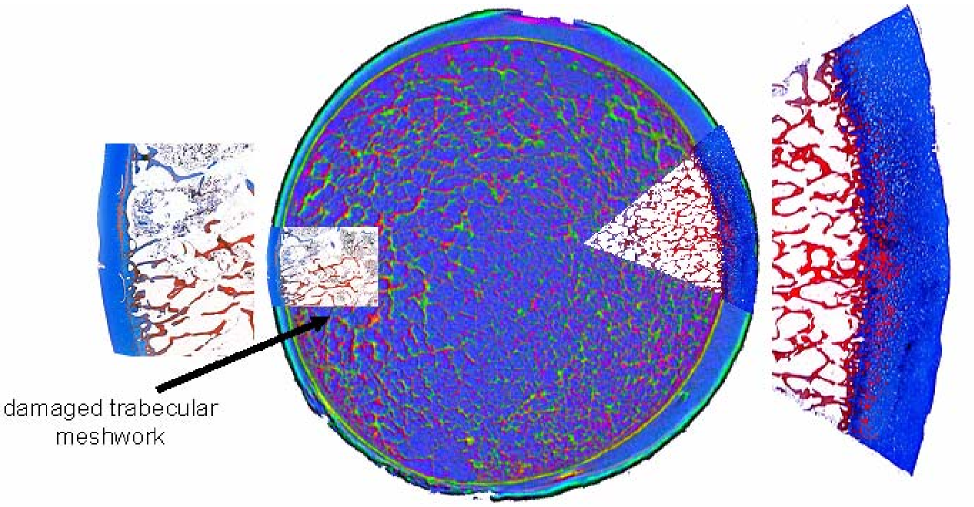

Figure 5.18. Color-coded ABI tomographic image of the hip compared with histologic sections (detailed description in the text).

Of all techniques, ABI provided highest image contrast and resolution revealing the structural tissue architecture with the least amount of false signals. MRI needs a very long exposure time to achieve comparable quality. Application of ultrasound is limited because of joint geometry and, at high sound frequency, the necessity of close contact between cartilage and transducer.

The clear presentation of the cartilage surface is imperative for unequivocal diagnosis of the state of disease of the joint. As proven by Figures 5.12 and 5.13, this interface is clearly defined in ABI images only. Cartilage changes its absorptive properties (due to water and fat content) gradually towards the joint space, with density coming close to that of the joint gap fluid, resulting in ambiguous visualization of cartilage borders in conventional X-ray, CT and MR imaging. CT and conventional X-ray imaging produce no clear borders of cartilage, when using the typical physical parameters of orthopaedic radiology, since the density of cartilage is too low. In MRI, either by generating fat or water-weighed images, the layered structure of cartilage forces a compromise that either obscures the border to the bone or the border to the joint space. The MRI-imaging of cartilage will only generate good results after excessively long exposure times and optimal arrangement of the presented image layer (Figure 5.15). If the layer is not in the median cross section, the cartilage border will be at an oblique angle producing very blunt signals (partial volume effect).

ABI, in contrast, is specifically based on the refraction properties of the tissues and it is able to enhance material edges. The ABI technique generates images that most closely resemble the appearance of anatomical and histological tissue structures (Majumdar, Sema-Issever *et al.*, 2004). Even though the physical basis for the generation of the images differs drastically from the otherwise commonly used techniques, image interpretation is therefore, in the end, facilitated for physicians.

5.5.2 The ankle

The ankle joint is made up of three bones: the lower end of the tibia (shinbone), the fibula (the small bone of the lower leg) and the talus, the bone that fits into the socket formed by the tibia and the fibula (Figure 5.19 (a)). Inside the joint, the bones are covered with articular cartilage.

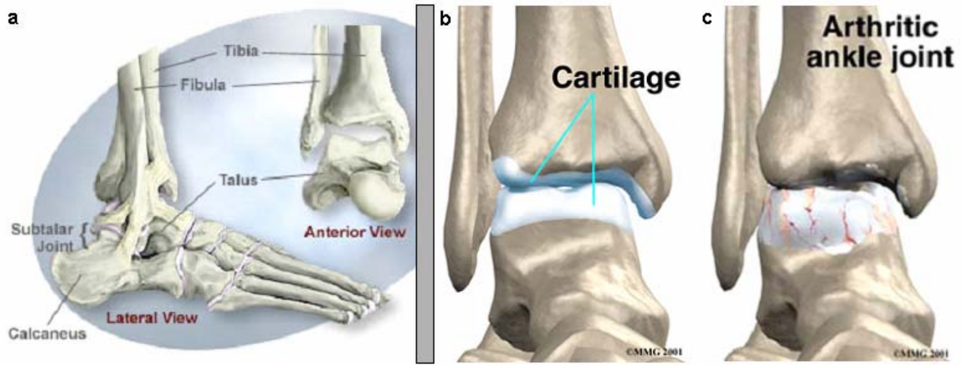

Figure 5.19. a) Anatomy of the ankle. b) Healthy ankle joint; b) arthritic ankle with degeneration and loss of cartilage

The ankle is one of the most crucial joints in our body. Since the ankle is a weight-bearing joint that absorbs the body's full impact, pain from an injured or diseased ankle is especially severe and debilitating. Because the ankle is so integral to an active lifestyle, it is an injury-prone part of the body for young and older people alike. Even moderate sprains and fractures can lead to problems, sometimes years later.

In OA conditions that affect only a small part of the joint, surgery may be used to replace a damaged cartilage using cartilage from another part of the body. When OA is advanced, ankle replacement with an artificial joint or ankle *arthrodesis* (fusion) may be used (see figure on the left). Arthrodesis is successful and durable but makes the joint permanently fixed. Early detection of cartilage degeneration for the ankle joint is therefore a crucial issue for orthopaedics.

- **PROJECTIONS**

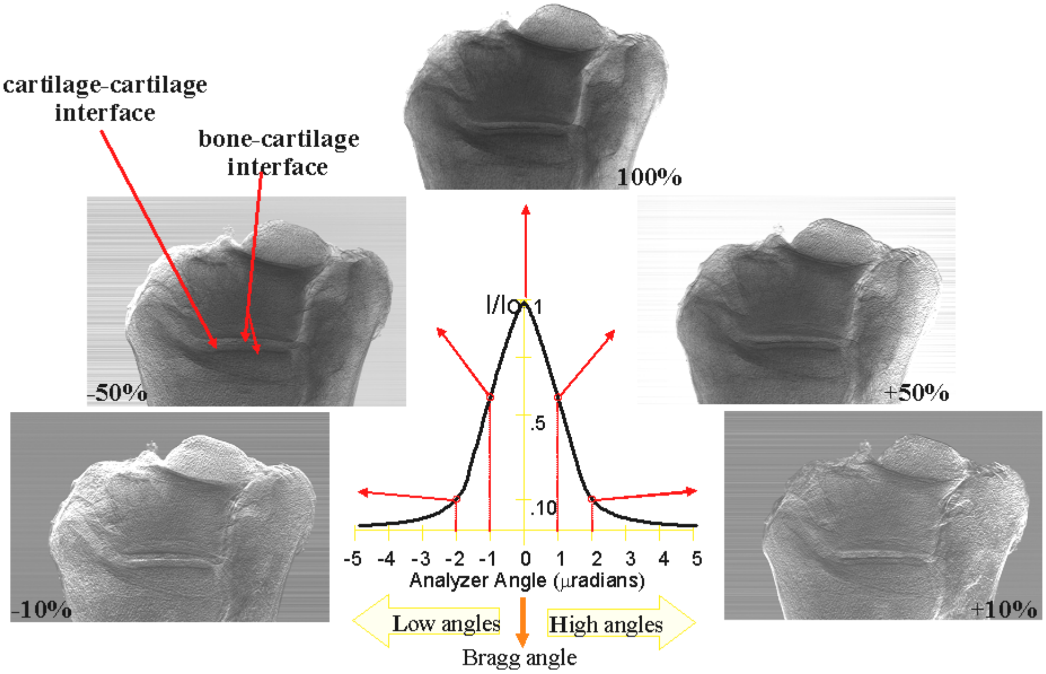

Figure 5.20. ABI projection at of a human ankle different angular position of the analyzer crystal along its rocking curve (detailed description in the text).

Figure 5.20 shows ABI projection images of an ankle joint for five different positions along the Si (333) analyzer crystal rocking curve. Images have been acquired at an energy of 50 keV. The calculated "apparent absorption" and "refraction" images, obtained combining ABI radiographs at 50 % and 10 %, are presented in **Figure 5.21**. In "slope" and "refraction" images, interfaces between bone and cartilage tissue and between the cartilages surrounding the two bones of the articulation are clearly visible but no inhomogeneities inside the cartilage tissue are detected for the studied joint. "Refraction" images, in particular, enhance the trabecular meshwork of the bone.

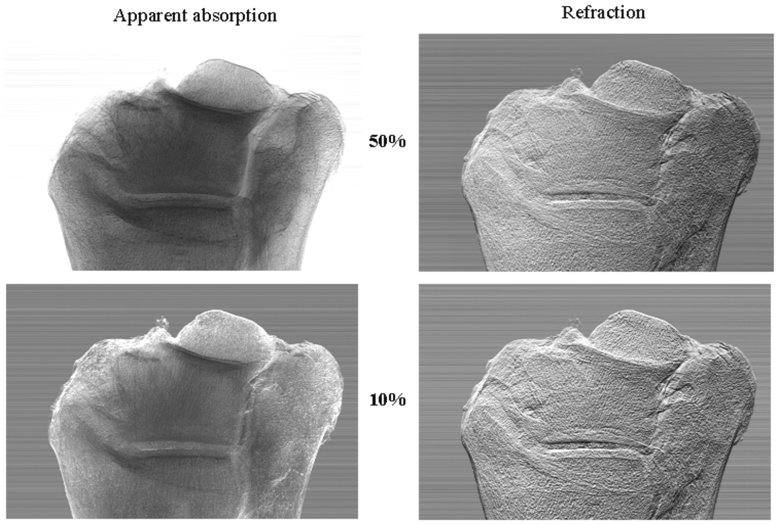

Figure 5.21. "Apparent absorption" and "refraction" images of the ankle (detailed desciption in the text).

- **TOMOGRAPHY**

ABI tomography slices at three different heights inside the ankle joint are presented in **Figure 5.22**. Images have been acquired at 50 keV with the Si (333) analyzer crystal set at the "top" (left column) and 50 % (right column) positions. In both slices "1" the three bones forming the articulation (tibia, fibula and talus) and the borders of the cartilage tissues covering the bones are visible. By moving up along the articulation, the talus (bone in the central part) gradually disappears and we enter into the joint space (slices "3") taken up by the cartilage tissue covering the tibia and talus extremities.

After having piled up the acquired *xy*-slices, suitable software (in this case ImageJ 1.33u[5]) can be used to virtually re-slice the volume and obtain frontal (*yz*-) and sagittal (*xz*-) slices of the sample (see figure on the left).

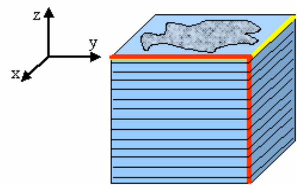

In **Figure 5.23** an example of frontal and sagittal slices of the ankle under investigation is shown. Thanks to the high edge-detection capability of the ABI technique, the lateral views of the sample allow to analyze the status and the thickness of the cartilage tissue as function of the depth inside the articulation in a much easier way than axial (*xy*-) tomographs. This kind of evaluation is not possible on simple projections since they are an integral of the signals produced all along the X-rays path inside the object.

---

[5] ImageJ 1.33u, Wayne Rasband - National Institutes of Health, USA (http://rsb.info.nih.gov/ij)

The study of lateral sections of the examined ankle has revealed some irregularities (yellow arrow) in the cartilage tissue that need to be histologically verified in order to establish if they are real damages or just image artefacts.

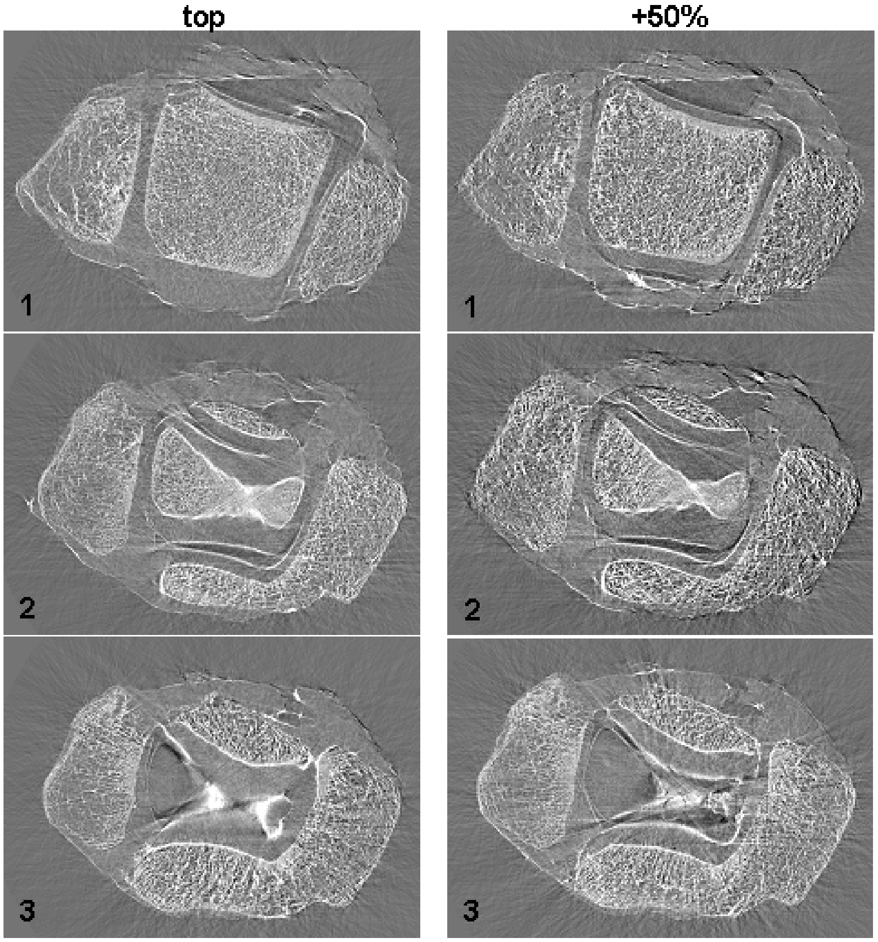

Figure 5.22. ABI tomographic images of the ankle (detailed description in the text).

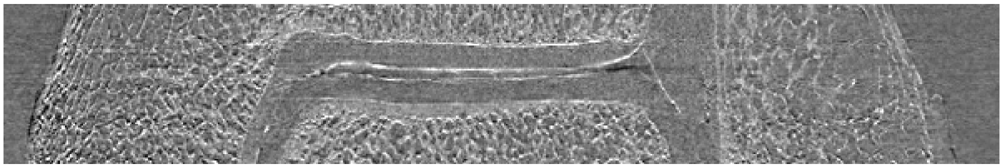

Frontal view

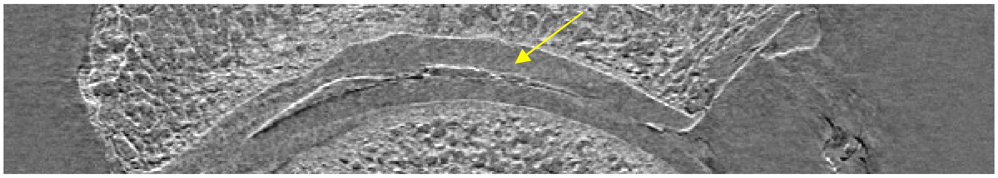

Sagittal view

Figure 5.23. Lateral slices of the ankle constructed by ABI tomography acquisitions (details in the text).

5.5.3 The big toe articulation

In this study, the cartilage tissue between the proximal and the distal phalanges (Figure 5.24) of a human big toe has been examined. Cartilage tissue around the extremities of the two phalanges is very thin and is usually undetectable by conventional imaging techniques.

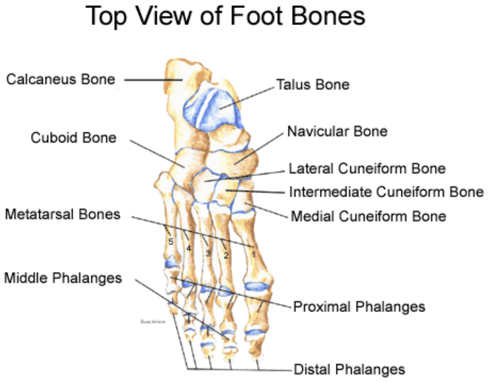

Figure 5.24. Anatomy of the foot.

Some ABI projection images of the big toe have been performed but the cartilage was not visible. This fact is largely due to the particular saddle-shape morphology of the bones which, whatever is the orientation of the toe, overlap the soft tissue in between.

An example of ABI projection image of the investigated sample is presented in **Figure 5.25** (50 % slope image at 30 keV and with Si (333)).

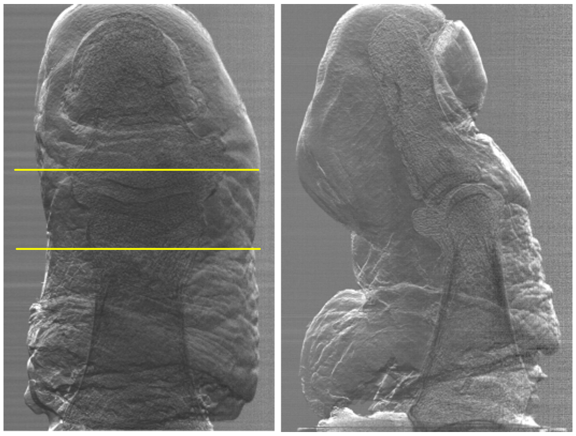

Figure 5.25. ABI projections of a human big toe (detailes in the text).

▪ **TOMOGRAPHY**

In order to overcome the intrinsic limitations due to the sample structure, ABI tomography at the joint site (region indicated by the two yellow lines in Figure 5.25) has been performed at an energy of 30 keV and with a Si (333) analyzer crystal.

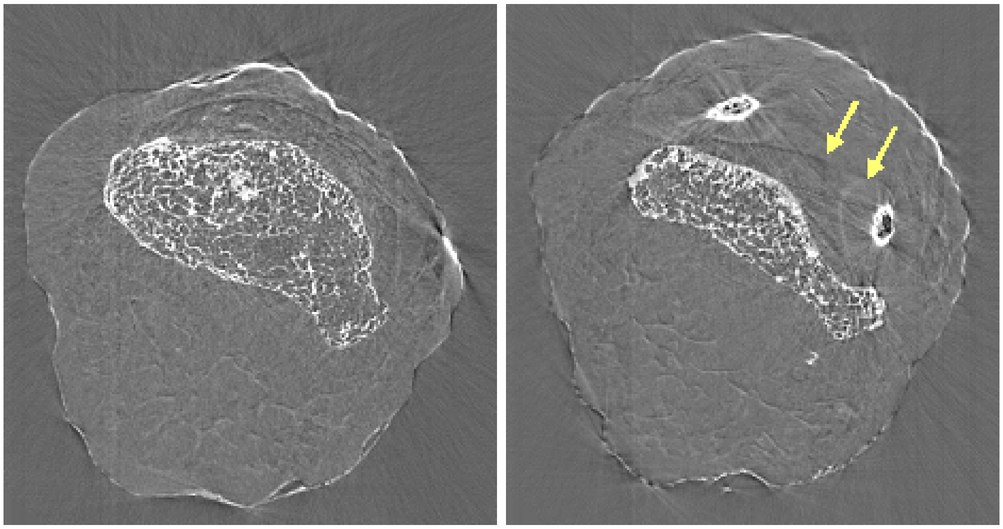

Figure 5.26. ABI tomographic slice of the human big toe (details in the text).

In **Figure 5.26**, a couple of ABI CT slices of the big toe acquired with the analyzer at the "top" position are shown as example. The image on the left is a slice inside the distal phalange, while the image on the right has been acquired in proximity of the joint space. In particular, in the latter, besides bone trabecles, some lines appear (indicated in the image by yellow arrows) and they precisely are the borders of the cartilage tissue surrounding the two phalanges. I would especially like to point out the elliptical lines around the two small bone spots, which are the tips of the proximal phalange, and the darker line in the middle, which is due to the contact between cartilages of the two bones.

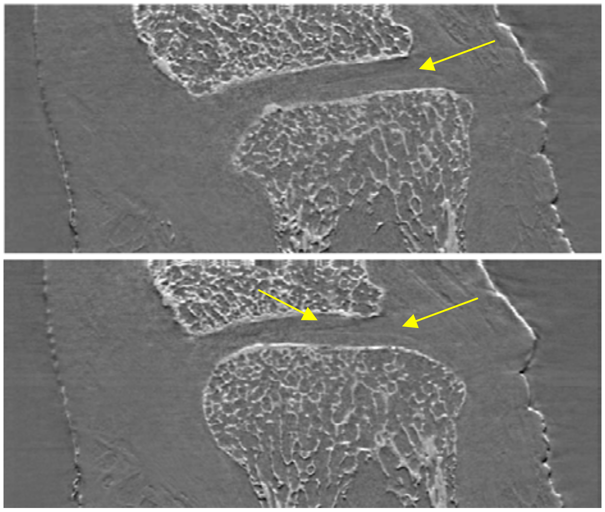

Figure 5.27. Lateral slices of the big toe constructed by ABI tomography acquisitions (details in the text).

Frontal and sagittal slices, virtually obtained and presented in **Figure 5.27**, allow the visualization of the cartilage covering the two phalanges of the big toe joint as well, proving the high potential of ABI tomography with respect to simple projection for this kind of investigation.

5.5.4 Metal implants

Implant properties have already been described in Paragraph 5.2. The alignment of the cylindrical implants allows a longitudinal view of the implant at X-ray imaging and thus a standardized evaluation of bone healing. Healing progress was assessed by conventional X-ray imaging in the living animal at week 1, week 6 and at week 9 from implantation. Each treatment group consisted of four animals. The animals were sacrificed at week 9. All the specimens were histologically examined after fixation with buffered 4% paraformaldehyde and sectioning, either with the implant in place as hard tissue sections or after cautious removal of the cylinders from demineralized specimens and paraffin embedding. This part of the work has been carried out at the Department of Orthopaedics (Univ. of Jena).

Prior to histology, bones were cut into $3 \times 3 \times 4$ cm^3 samples around the implant cylinder and then submitted to ABI investigation.

– **ABI** images have been acquired at different angular positions of the crystal analyzer at an energy of 50 keV and a Si (333) crystal analyzer.

– **Conventional X-ray** images were taken at 50 kV and 5 mAs at the X-ray tube and using a ‘Mammoray HDR PQ’ mammographic film (Agfa) and HDS Mammoray screens cassette (Agfa).

– **Histology**. After ABI, samples were demineralized. The specimens with the metal implant still in place were dehydrated via ascending alcohol concentrations, and then were impregnated with a 1:1 mixture of alcohol/Technovit 7200VLC, followed by infiltration with pure Technovit 7200VLC (Heraeus Kulzer, Germany) and embedding into methacrylate-based resin. Thin ground sections of 100–200 µm and with slices ground to a thickness of 5–10 µm were produced. Staining was performed with either Masson–Goldner or alizarin S[6] to follow calcification processes. Microscopy was performed on a Zeiss Axiovert 200M microscope equipped with the ‘Axiocam’ digital camera.

- **PROJECTIONS**

Figure 5.28 shows conventional radiographs of the sheep implants, without (a) and with (b) BMP-2 factor, which have been afterwards used for the ABI investigation.

---

[6] http://www-medlib.med.utah.edu/WebPath/HISTHTML/MANUALS/MANUALS.html

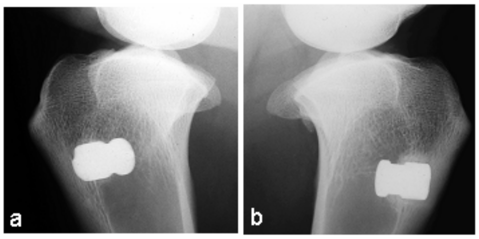

Figure 5.28. Conventional radiographs of sheep imlants (details in the text).

Because of the X-ray beam hardening, a typical artefact of implant imaging (Brooks and Di Chiro, 1976), the status of the healing of the implants into bone is not appreciable: edges between metal and tissue appear highly blurred.

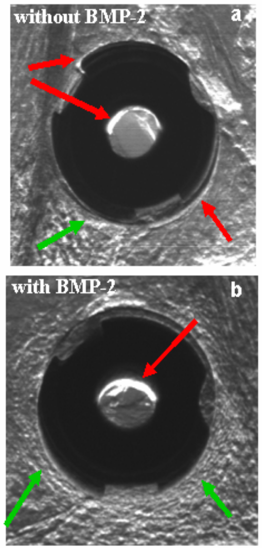

Figure 5.29. Axial ABI projections of sheep implants (details in the text).

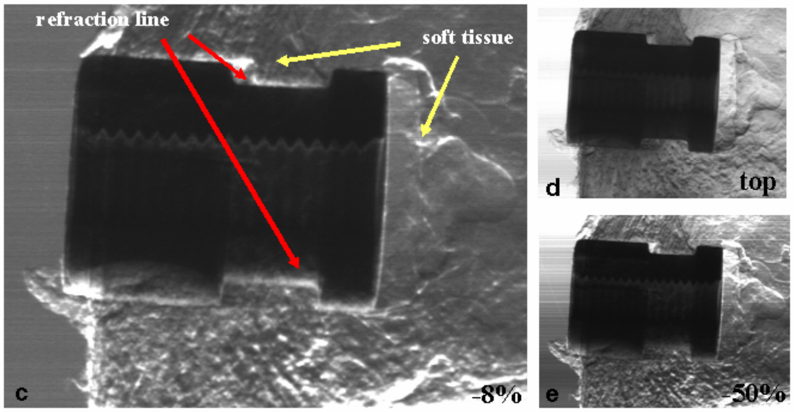

Figure 5.30. Lateral ABI projections of sheep implants (details in the text).

Figures 5.29 and 5.30 present ABI projection images of the same sheep implants viewed from the axial and lateral orientations respectively. Images have been acquired at the "top" position and at the ±50 %, ±15 % and ± 8 % "slope" positions of the crystal analyzer. The comparison between these images (Figure 5.30 (c-e)) has revealed, for this kind of sample, that the highest sensitivity of the ABI technique is achieved at the very far slope of the analyzer rocking curve (e.g. 8 % like shown in Figure 5.29 and 5.30 (c)).

Figure 5.31 presents the comparison between ABI images and histological sections. In particular: A and B are images of a specimen without BMP-2 (bone growth factor) while C and D are images of a specimen with BMP-2. A and C are the histological sections of the specimens presented in the ABI images (15 % analyzer position) in B and D, respectively. Note the black and white refraction lines around the BMP-free cylinder in B in the location where histology (A) indicates absence of new bone. The intricate trabecular network in both specimens strongly suggests almost completed healing for both but, as histology demonstrates, only the BMP-2 treated cylinder (C, D) is surrounded by re-oriented trabecular elements.

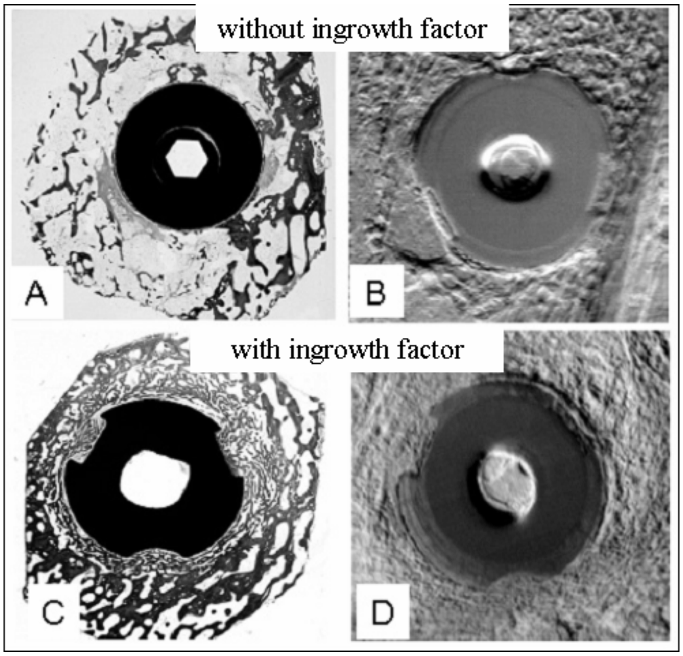

Figure 5.31. Comparison between ABI projections and histology of sheep implants (detailed description in the text).

The analysis of the images in Figure 5.29, 5.30 and 5.31 proves that the ABI technique is able to reveal two significant features of the implant healing process: the intense inter-digitations of the bone with hydroxyapatite and the formation of oriented trabecular structures around the implant. First, ABI images taken at the slopes of the rocking curve of early stages of bone growth always display the edges of the implant as highly refractive elements. While, upon completed integration into the host tissue, inter-digitations of the tissue with the implant modulate the refractive signal, thereby demonstrating completed integration. Defined implant borders disappear and implants seem to 'melt' into the background of the bone (Figure 5.31 (D)). Secondly, the application of the growth factor BMP-2 has additional consequences. In the sheep, the new trabecular network orients itself towards the circular geometry of the cylindrical implants, as seen in the histological images (Figure 5.31 (E)). ABI is able to pick up these regular patterns, visible in particular at high magnification of the images within the adjacent 200 μm around the implant (Figure 5.31 (E)).

The process of guided bone growth did not take place to the same extent in the samples without BMP-2 (Figure 5.31 (A)), and consequently concentric signals in the region immediately surrounding the implant are absent (Figure 5.31 (B)).

These results demonstrate that **the ABI technique provides an indirect measure of implant healing** because of its inherent property to generate particular signals from edges. The results suggest that the images from very far slope of the rocking curve provide the greatest level of information concerning bone ingrowth due to their ability to detect interfaces between different tissues (or matter). Since implants have elaborate edges, in particular when coated with minerals such as hydroxyapatite, the X-ray refraction signal from those edges is particularly intense when healing does not occur. Any ingrowth of bone into these three-dimensional superficial structures weakens the signal, thus providing an indirect measure for implant integration, independent of the angle of sight or thickness of the sample.

- **TOMOGRAPHY**

Pilot ABI tomography imaging of implants have also been performed in the framework of my thesis. **In Figure 5.32**, some slices of a sheep implant (7 days post surgery) acquired at 51.5 keV with a Si (333) analyzer crystal set at the "top" position are presented. In these images, the implant appears as a white perforated disk in the center of the bone in which it is embedded. The seemingly “empty” space within the specimen is occupied by fat tissue typical for the bone marrow in old animals (see also histology in Figure 5.31). The cortical bone (the hardest form of tissue) with its trabecles is the bright part of the specimen. In both slice "2"and slice "3" it is possible to see the starting of growth towards the metal surface, while the slice "1" does not show any trabecular formation around the metal implants. Slice "4" shows instead the hole formed in the implantation operation.

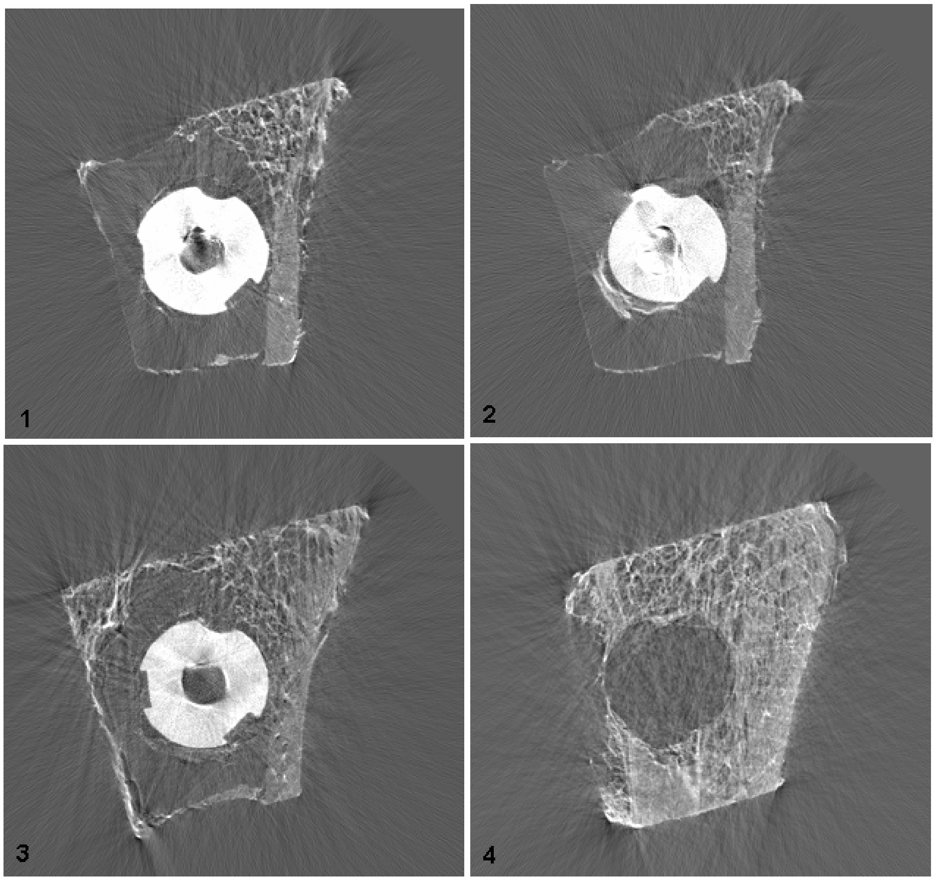

Figure 5.32. ABI tomographic slices of a sheep metal implant (detailed description in the text).

In **Figure 5.33**, an example of the virtual frontal and sagittal slices of the sheep implant is presented. These images are quite noisy since the energy used was not the optimal one for this kind of sample (excess absorption due to low energy). However, some interesting details are visible. The yellow arrow indicates a line which is very probably the interface between the bone tissue and a soft tissue formed between the bone and the implant, possibly inflammatory granulation tissue, while the red arrows points out the beginning of cortical bone formation at the indentation of the implants, maybe due to BMP accumulation.

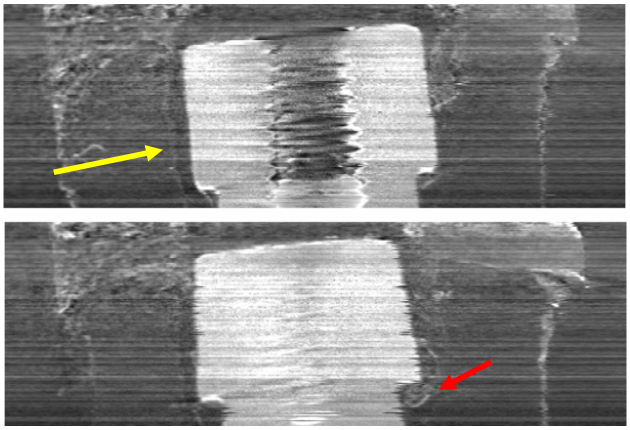

Figure 5.33. Lateral slices of the metal implant constructed by ABI tomography acquisitions (details in the text).

These results presented in this section demonstrate that by using the ABI technique, a destruction-free evaluation of the quality of ingrowth of bone into metal implants is not only possible but also much more sensitive with respect to conventional radiography. In addition, the feasibility of ABI CT of metal implants has been proven by producing ABI slices, which could be able to become in the future an important non-invasive alternative to the histological examination.

5.6 Three-dimensional rendering of articulations and implants

The application of the ABI tomography to the cartilage study and implants healing evaluation presented in this Thesis is one of the most original points for this kind of investigation. Results shown up to here are diagnostically relevant since they offer a means for better examining and understanding OA progression and the bone growth in implant surgery.

Starting from ABI CT images, it was possible to achieve something even better, that is to perform a three-dimensional reconstruction of the sample under investigation.

The specimens considered in this particular work are the big toe articulation and a sheep implant.

- **The human big toe joint**

A slice by slice manual segmentation of the two cartilages of the toe articulation using a specific script developed on Adobe® Photoshop 5.5 has been performed.

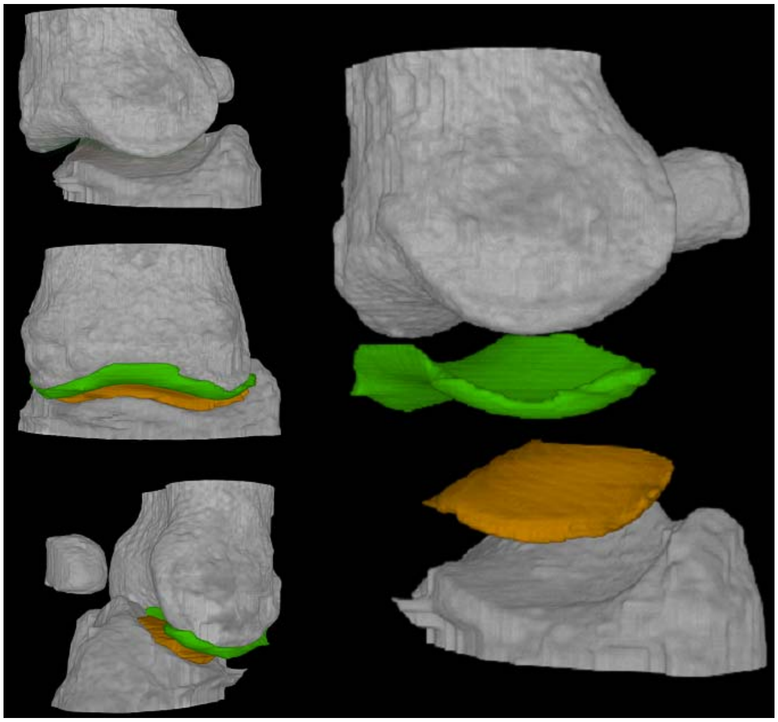

Figure 5.34. Three dimensional rendering of the human big toe (details in the text).

The segmentation consisted in delineating the cartilages by following the interfaces revealed by the ABI contrast. The resulting volumes of cartilage were then reconstructed in 3D using the software VGStudioMax 1.2 (Volume graphics, Heidelberg, Germany). Segmentation of the different bones was performed by region growing using the "3D magic wand tool" of VGStudio Max. The final rendering consisted in displaying all the segmented volumes (bones and cartilages) in a common 3D virtual space with different colours. The result is shown in **Figure 5.34**.

- **The sheep implant**

In **Figure 5.35** the three-dimensional rendering of a metal implant is presented. The volume has been reconstructed using the software VGStudioMax 1.2 like for the big toe but, in this case, the segmentation has been performed by operating on the grey levels histogram. Thresholds have been chosen in such a way to enhance the visualization of the metal implant and the cortical bone. In the figure, different views of the reconstructed volume are shown. The emerging part of the implant is in reality embedded in bone tissue and sometimes is covered by a layer of soft tissue (e.g. fat), as demonstrated by the results previously presented on ABI projections and tomography. In the last image of figure 5.35, the hole in the cortical bone made during surgical implantation can be clearly discriminated.

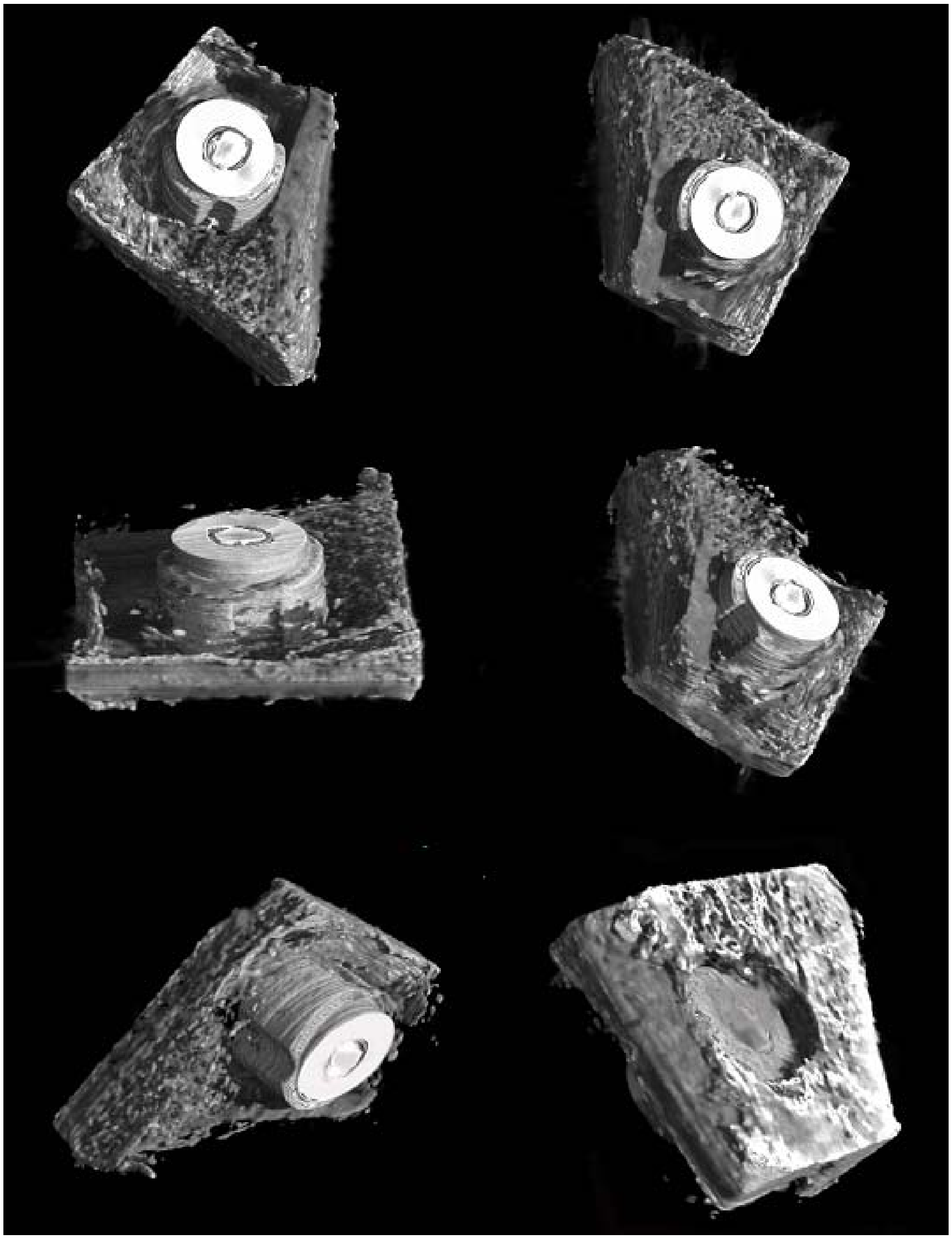

Figure 5.35. Three dimensional rendering of the sheep metal implant (details in the text).

5.7 *In-vivo* experiments results

The ability of the ABI technique of visualizing and monitoring joint tissue diseases has been largely proven both in projection and CT configurations. All the results until now presented have been obtained on excised specimens from the human or animal body. It remains to be determined now whether the technique can be extended to *in-vivo* study by using living animals. A preliminary test has been performed on guinea pigs because of their genetic constellation to develop arthritis. The energy used in this study was 51.5 keV with a Si (333) analyzer crystal. Acquisitions have been performed in projection mode and the targets to investigate were the hip and knee. All relevant experimental parameters are summarized in Table 5.3.

Animals have been anaesthetized by injection of Chloralhydrate (1 ml/100 gr) and the measured skin dose rate in air at the maximum photon flux was 0.3 mGy/s. That means a total delivered dose to the animal of about 0.9 mGy per set of ABI images. The scheme of the used experimental set-up and a picture of the animal fixation are shown in Figure 5.36.

sample	energy (keV)	analyzer	acquisition mode	detector
Guinea pigs	51.5	Si (333)	projection	46 µm FReLoN camera or 30 µm optics FReLoN camera

Table 5.3. Experimental parameters used for *in-vivo* acquisitions.

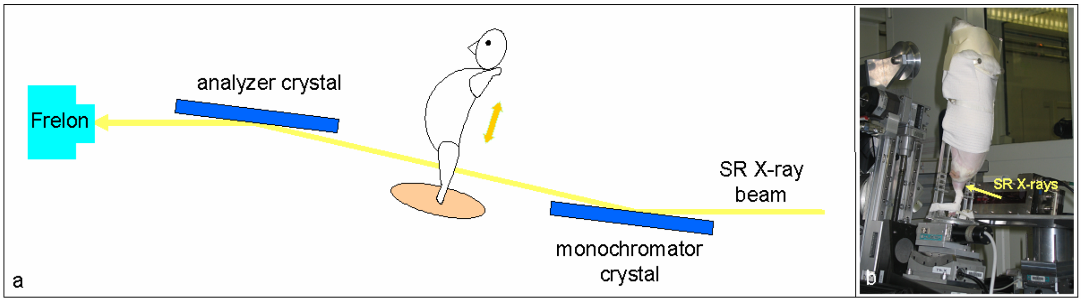

Figure 5.36. a) Scheme of the ABI set-up for *in-vivo* experiments; b) animal fixation.

Figures 5.37 and **5.38** present ABI images of a hip and a knee of a guinea pig, respectively, recorded at different angular positions of the analyzer crystal (top, ±50%, 15% and 8%). For both joints, the detector was a 2000 FReLoN camera coupled with a 30 µm optics. Because of the particular joint anatomy, the study of the hip appears to be more complicated than that of the knee because of the significant structural overlapping between acetabulum and femural head. Anyway, edges of the acetabulum and femur head are clearly defined and in many cases (see image of a hip on the left), the fibrous capsule enclosing the hip joint and most of the femur neck is visible. The hip joint capsule, which possesses a crucial role in the hip stability, functions to constrain translation between the femur and acetabulum while allowing rotational and planar movements.

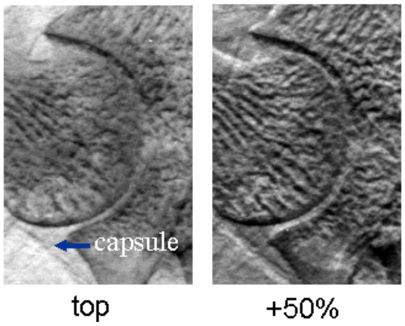

Other images of the knee of guinea pigs acquired with the ABI technique are shown in **Figure 5.39** ((a) -50% slope image, (b) -15% slope image) and **Figure 5.40** (top image). In those cases the 30 μm optics FReLoN camera was used, while for images presented in Figure 5.38 the 47 μm FReLoN camera was employed.

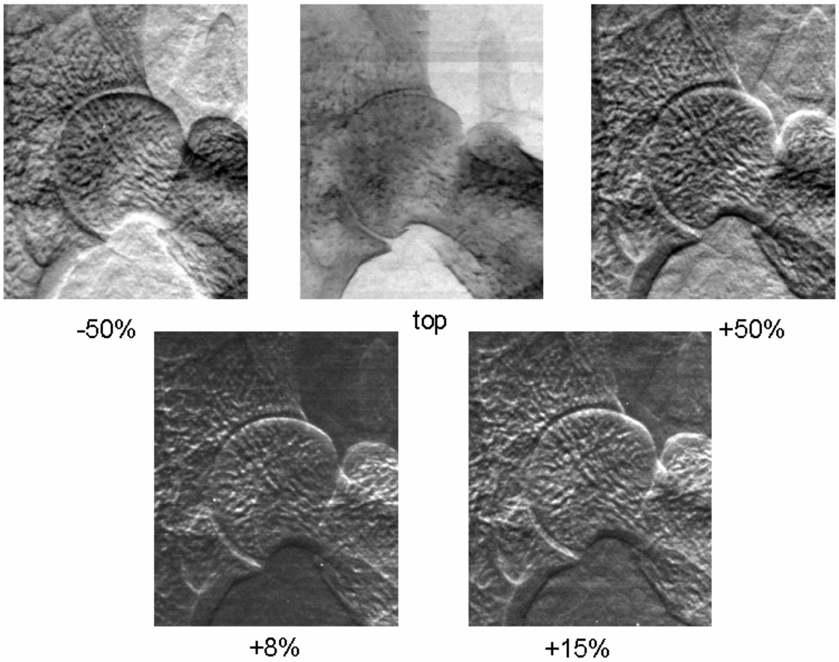

Figure 5.37. ABI projections of a hip of a guinea pig (details in the text).

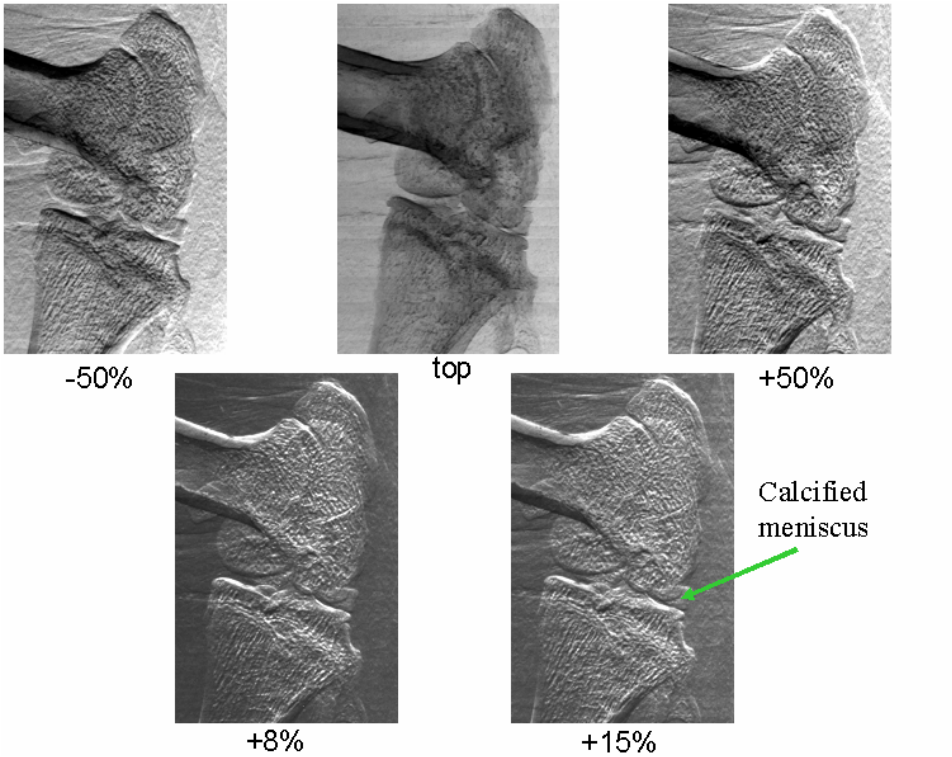

Figure 5.38. Lateral view-ABI projections of a knee of a guinea pig (details in the text).

In these images, the cartilage tissue is not clearly visible because of the overlapping of various soft tissues present around the joint (skin, fat tissues, synovial fluid etc.). Nevertheless, physicians have detected possible signs of osteoarthritis, as indicated by arrows in the figure. In particular, protrusions (yellow arrows) at the sides of the extremities of bones of the articulation are very likely osteophytes (bone spurs) while features in the joint gap in between may be due to ossification (red arrow) or calcification of the meniscus (green arrows).

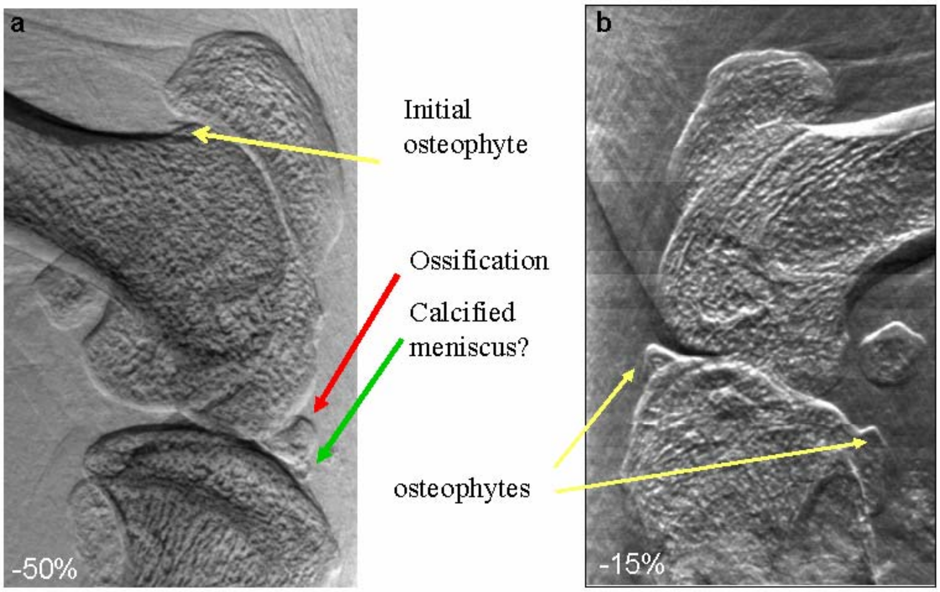

Figure 5.39. Lateral view-ABI projections of the knee of guinea pigs (details in the text).

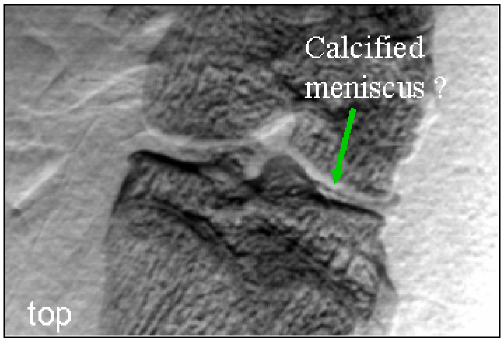

Figure 5.40. Frontal view-ABI projection of the knee of a guinea pig (details in the text). 47 mu

In **Figure 5.41** the "apparent absorption" and "refraction" images of the same hip shown in Figure 5.40 are presented. The quality of these images is not very good because of the slight animal movements between different acquisitions. Yellow and green arrows indicate signs of osteophytes and possible calcification of the meniscus or cartilage damages, respectively.

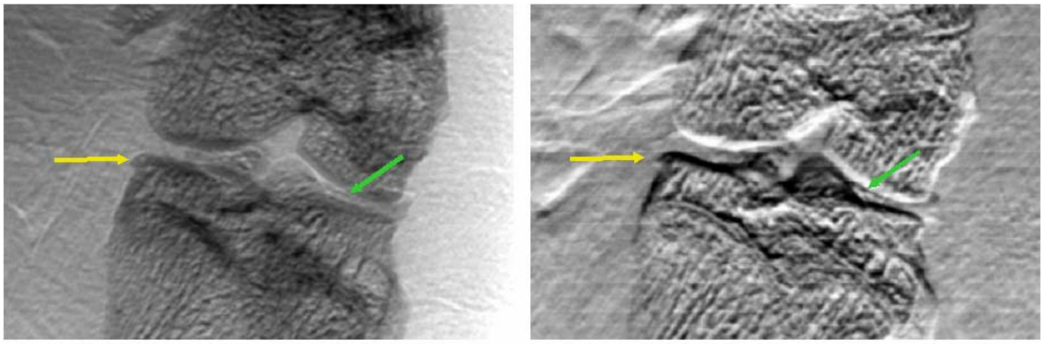

Apparent absorption image

Refraction image

Figure 5.41. "Apparent absorption" image and "refraction" image of the knee of a guinea pig (details in the text).

Images here presented represent the first results obtained on *in-vivo* ABI images for studies of articular diseases. These preliminary results encourage further investigations in this direction. Moreover, thanks to the significantly lower radiation dose delivered than in conventional X-ray imaging or micro-CT and to the enhanced sensitivity of the technique, *in-vivo* ABI could also allow to follow the bone/metal ingrowth in individual animals and, thus, to generate more precise insights into bone remodelling at implant sites in addition to follow up development of OA.

Nevertheless, some important considerations have to be pointed out.

- The lack of a deeper knowledge of the guinea pig anatomy made the image interpretation sometimes difficult. On the other hand, on these results it has to be said that none of the examined guinea pigs (5 in total) presented overt and irrefutable signs of OA, probably because animals were not old enough.
- The joint spatial orientation with respect to the incident laminar X-ray beam is a really crucial point. This is especially true for the knee imaging: in order to obtain as much information as possible on the status of the articular cartilage, the patella must face the beam directly and the head of the tibia must be exactly parallel to the beam. If the knee joint is not well oriented, images are inevitably jeopardized. To this end, the presence of the physician during image acquisition is fundamental for the image optimization.
- The duration and efficacy of anaesthesia were very animal dependent. Animals sometimes moved during image acquisition making, for instance, impossible the application of the DEI algorithm. For this reason, in the second campaign of experiments performed on guinea pigs, anaesthesia was given via inhalation allowing a control of its duration and depth.
- Another critical aspect is vertical positioning of the animal. The support has to be designed in such a way to avoid that animals bear their weight on their fore legs. For this purpose, a special stage has been produced in order to make the animal sit on its bottom and allow one of its legs to pass through a hole and be fixed at the ankle. This position, which initially

seemed comfortable for the animals, has revealed to be not adapted to the musculoskeletal structure of the guinea pig. This animal, in fact, does not possess a muscular configuration that allow it to stay in a vertical position (conversely to rats, for instance); the rib cage tends to collapse and suffocates the animal. Therefore, in all the experiments performed, the guinea pigs were always also fixed at the head and shoulder levels. Alternative positioning and supports are under examination.

5.8 Dose effect study: assessing the biological response of chondrocytes

The X-ray dose delivered to the sample imaged with the ABI technique is generally much lower compared to doses used during conventional radiography (Bravin, Fiedler *et al.*, 2002) with an actual benefit for the sample/patient.

Nevertheless, there is some literature presenting evidence of a hyper-radio sensitivity to low doses (0-0.5 Gy) of certain type of cell lines (in most of the cases tumour cell lines were investigated) (Marples, Wouters *et al.*, 2004; Short, Bourne *et al.*, 2005); in particular, an increased cell death after exposure to low doses has been observed.

Intrinsic cellular radiation sensitivity is largely determined by the efficiency and fidelity of dynamic processes that control and govern cell cycle arrest, DNA repair and apoptosis. Many radiation-induced lesions in DNA (e.g. base damage, single-strand breaks) are readily repaired by error-free mechanisms and therefore have little consequence for survival, mutagenesis or genomic instability in repair-competent cells. In contrast, radiation-induced DNA double-strand break (DSB) activation, and failure to repair (or the misrepair of) DSB is a prime cause of cell death even in the context of repair-proficient cells (Jeggo, 1998). In the past years, considerable progress has been made establishing the molecular associations between damage recognition, check-point arrest and damage repair that occur in the response of cells to high-dose radiation injury. However, the way in which these processes dictate and control the response of cells at low radiation doses remains poorly understood.

In the light of the experimental observations of cell hyper-radio sensitivity presented in literature, I wondered whether the low doses delivered to the cartilage tissue during AB imaging could somehow provoke any effect on chondrocytes, the main resident cells of the tissue.

With this aim, a campaign of radiobiological experiments has been performed in order to study the biological effects of the radiation (and therefore the possible toxicity of the AB imaging) in human chondrocytes.

The radio sensitivity of chondrocytes is not very well known and established, especially for primary cells (Takahashi, Mizobuchi *et al.*, 2003). Therefore, for this experiment, two human primary culture cell lines have been compared: chondrocytes (taken from human hip) and human skin fibroblasts (whose radio sensitivity was already well studied in the laboratory).

The phospho-histone H2Ax (γH2Ax) and the Heat Shock Protein 70 (HSP70) through immunofluorescence technique at different repair times have been studied.

- **γH2Ax** has the particularity to be phosphorylated and to make discrete foci when the DNA suffers DSB (Rothkamm and Lobrich, 2003; Foster and Downs, 2005). This marker allows us to visualize directly the DSB in the cell, and by this mean to investigate how the cells are tolerating the ABI-treatment.
- **HSP70** has been shown to be a stress biomarker (Welch and Suhan, 1986; Delmas, Trocheris *et al.*, 1996; Ryan and Hightower, 1996; Rajdev and Sharp, 2000), to be over-expressed after X-ray irradiation and to cause nucleoshuttling between cytoplasm and nucleus (Rénier, Gamo *et al.*, ; Velazquez and Lindquist, 1984).

In the following paragraphs the experimental radiobiological methodologies used in this study, first, and the obtained results, secondly, will be described.

5.8.1 Radiobiological and irradiation methods

- **Cell culture**

Cell lines used are:	- 1BR3 primary human skin fibroblasts (usually cultivated in the cell-laboratory at ID17);
	- human primary chondrocytes (taken from human hip) provided by Promocell GmbH (Heidelberg, Germany).

1BR3 were grown in Dulbecco’s modified Eagle’s minimum medium (DMEM) (Gibco-Invitrogen-France, Cergy-Pontoise, France) supplemented with 10% of foetal bovine serum and chondrocytes were grown in chondrocyte medium (provided by Promocell GmbH) supplemented with 10% of foetal bovine serum, and 1% of penicillin and streptomycin (Sigma-Aldrich, l’Isle d’Abeau-Chesne, France).

- **Immunofluorescence technique**

Cells were fixed in 4% paraformaldehyde 2% sucrose PBS for 10 min at room temperature and permeabilized in the lysis solution (20 mM HEPES, pH 7.4, 50 mM NaCl, 3 mM $MgCl_2$, 300 mM sucrose 0.5% Triton X-100 (Sigma-Aldrich, Poole, U.K.)) for 5 min at 4°C. Thereafter, cover slips were washed in PBS prior for immunostaining. Primary antibody incubations were performed for 40 min at 37°C at 1/100 dilutions (except γH2Ax (Upstate-Euromedex, Mundolsheim, France: monoclonal mouse): dilution 1/800) in PBS supplemented with 2% bovine serum fraction V albumin (BSA) (Sigma-Aldrich) and followed by PBS washing. Incubations with anti-mouse FITC or with anti-rabbit TRITC secondary antibodies (Sigma-Aldrich) were performed 37 °C at 1/100 in 2% BSA for 20 min. Nuclei were counterstained by 4, 6-Diamidino-2-phenylindole (DAPI) contained in the mounting solution Vectashield (Vector laboratories, Burlingame, CA, USA – Abcys, Paris, France) and then the cells were examined (and foci were counted if there were any) by a fluorescence microscope (Olympus). Anti-HSP70-1 (polyclonal rabbit IgG) was also provided by Upstate-Euromedex.
A scheme of the immunofluorescence procedure is shown in Figure 5.42.

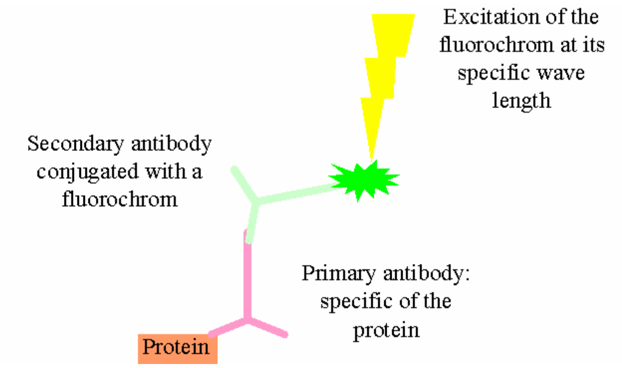

Figure 5.42. Scheme of the protein detection procedure of the immunofluorescence technique.

- **Irradiation**

In the case of the *in-vivo* experiments presented in Paragraph 5.7, the total dose for a set of ABI images was measured of 9 mGy per animal (at an energy of 51.5 keV). Therefore, cells used in this dose investigation have been irradiated with the same dose. Since the measured 9 mGy are a skin dose (kerma), they represent an overestimation of the dose delivered to the joint cartilage tissue. For this reason, cell lamellae were made adhere to the internal wall of a rectangular container filled by cell medium (about 1 cm width liquid volume) and then they were irradiated by scanning them through the laminar SR X-ray beam. The 1 cm thickness of the cell medium simulated, in first approximation, the tissue surrounding the animal knee joint cartilage.
In order to confirm results and increased statistics, the experiment has been made twice, both for chondrocyte and for skin fibroblasts.

5.8.2 Immunoflurescence results

➡ γH2AXx, cellular localization of DNA double strand breaks

In Figures 5.43 and 5.44 microscope pictures of human chondrocytes and skin fibroblasts, respectively, at different times after irradiation are presented. For this study, γH2Ax monoclonal mouse antibody and FITC conjugated secondary antibody were used. Pictures (1, 3, 5) are the fluorescence images of the γH2Ax protein, green dots represent DNA breaks (only the biggest and lightest dots are DNA-DSB); while images (2, 4, 6) are the DAPI-coloured cell nuclei (same cells of images 1, 3, 5). Other details are described in the figure captions.

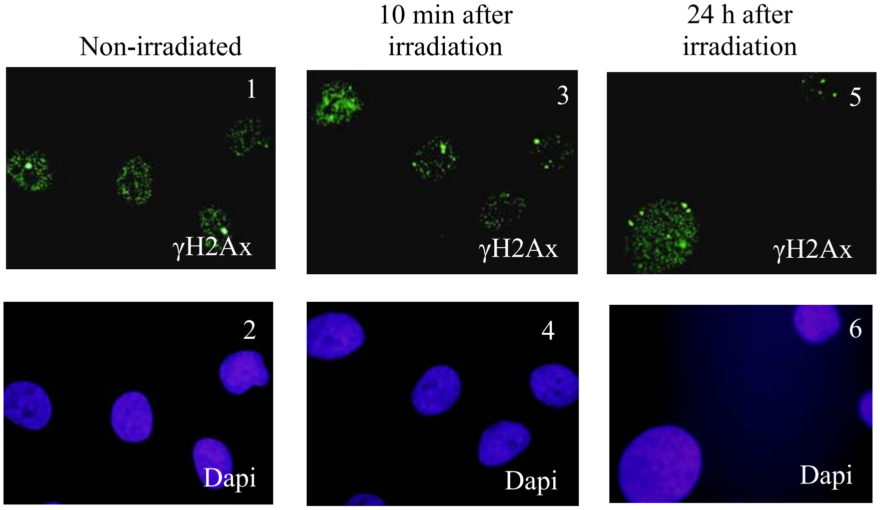

Figure 5.43. Pictures of chondrocytes after irradiation acquired with the fluorescence microscope and the focus of 100x. 1 - 2: chondrocytes non-irradiated; 3 - 4: chondrocytes directly after irradiation; 5 - 6: chondrocytes 24 hours after irradiation (cells were kept at 37ºC, 5%CO$_2$).

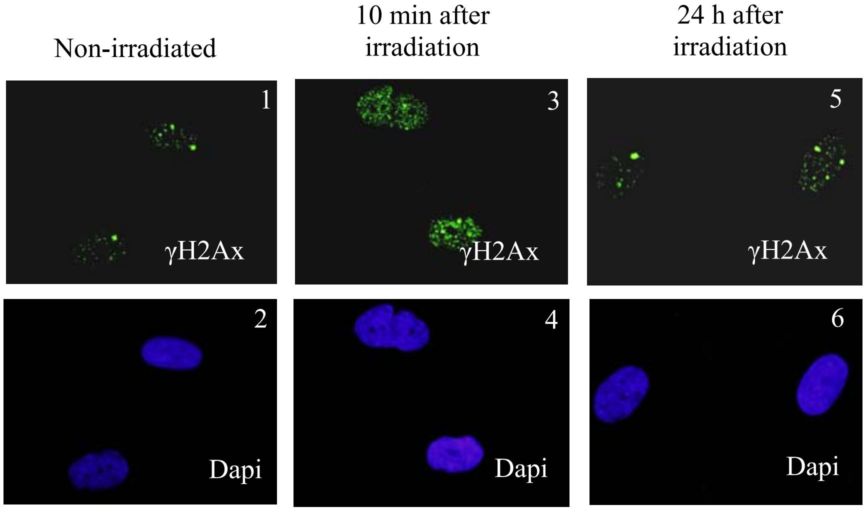

Figure 5.44. Pictures of skin fibroblasts after irradiation acquired with the fluorescence microscope and the focus of 100x. 1 - 2: fibroblasts non-irradiated; 3 - 4: fibroblasts directly after irradiation; 5 - 6: fibroblasts 24 hours after irradiation (cells were kept at 37ºC, 5%CO2).

In figures 5.45, 5.46 and 5.47, the number of γH2Ax foci per cell as function of the number of cells is reported for the three cases considered in the study: non-irradiated cells as control (NI), directly after irradiation (10 minutes) and for a repair time of twenty four hours (24 hours). Foci have been counted under the microscope (in this histogram 34 representative cells per condition have been considered). Violet bars represent non-irradiated chondrocytes, orange bars relate to chondrocytes directly after irradiation and green bars correspond to chondrocytes after 24 hours of repair time after irradiation (cells have been kept at 37 ºC, 5% CO_2). For chondrocytes, two histograms are reported corresponding to the two performed experiments.

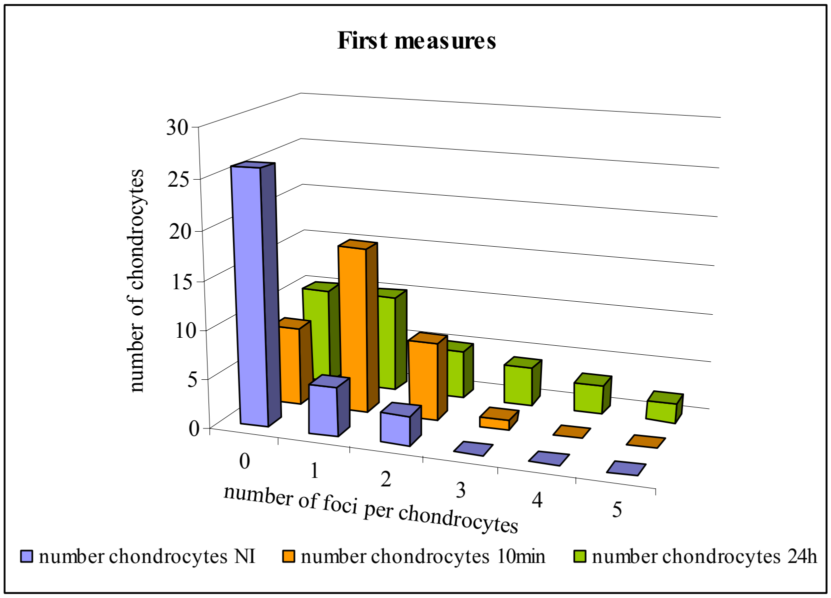

Figure 5.45. Histogram showing the number of γH2Ax foci per chondrocyte after irradiation (N=34 cells per condition) (1st test). Details in the text.

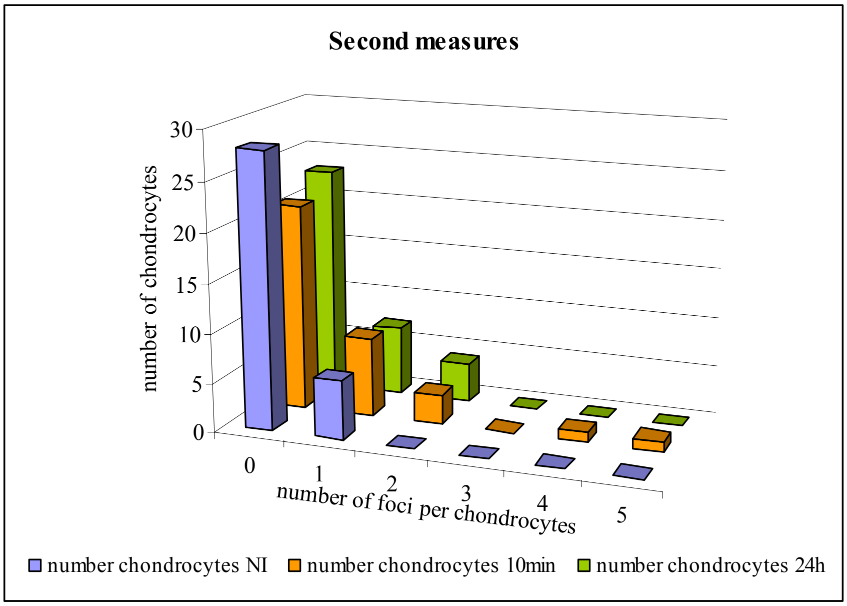

Figure 5.46. Histogram showing the number of γH2Ax foci per chondrocyte after irradiation (N=34 cells per condition) (2nd test). Details in the text.

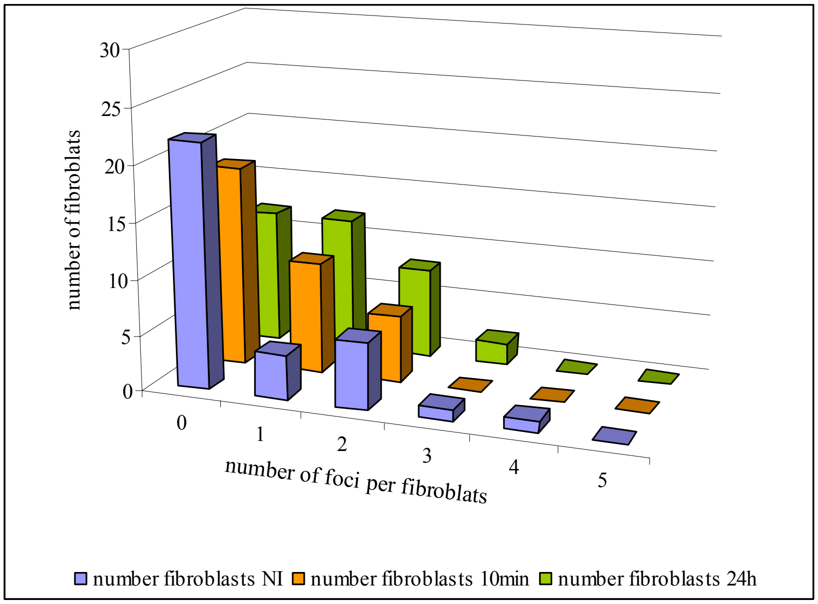

Figure 5.47. Histogram showing the number of γH2Ax foci per fibroblast after irradiation (N=34 cells per condition) (2nd test). Details in the text.

The mean of γH2Ax foci for both non-transformed chondrocytes and fibroblasts 1BR3 for the non-irradiated cells, directly after irradiation and 24 hours after irradiation, respectively, are reported in Tables 5.4 and 5.5.

	Chondrocytes	**Skin fibroblasts**
Non-irradiated	0.32 ± 0.11	1.00 ± 0.2
10 minutes	1.06 ± 0.13	2.00 ± 0.8
24 hours	1.60 ± 0.26	2.00 ± 0.8

Table 5.4. Mean of γH2Ax foci per cell (1st test).

	Chondrocytes	**Skin fibroblasts**
Non-irradiated	0.18 ± 0.07	0.68 ± 0.18
10 minutes	0.68 ± 0.20	0.65 ± 0.13
24 hours	0.44 ± 0.12	1.00 ± 0.16

Table 5.5. Mean of γH2Ax foci per cell (2nd test).

By looking at Figures 5.43 and 5.44 (1-2), it can be pointed out that the non-irradiated chondrocytes present the same behaviour in both experiments, that is an absence of foci.

The main difference between the two experiments on chondrocytes consists in the prevalence of the absence of foci after 10 minutes and 24 hours. When comparing with the fibroblasts, it can be stressed that there is no major difference between the non-irradiated and the irradiated samples.

Averaged values in Tables 5.4 and 5.5 highlight the fact that the mean number of foci per non-irradiated cell is always lower than the values from the irradiated cells, for both the tested cell types.

Concerning the first experiment results, it has been noticed that, after 24 hours of repair time, the mean of the foci per cell seems to slightly increase. This increase can be explained by the fact that the cells are primary cultures (not immortalized cells) so this proportion can be due to normal senescence (Guarente and Kenyon, 2000) or it can also be explained by a potential radiobiological effect. However, even though there might be a radiobiological impact of the radiation on these cells, it is not potentially endangering the cell survival in average. Conversely, in the second experiment, no increase has been observed. This suggests that the effect noticed before could be attributed more likely to the cells them-selves (senescence) rather than to the irradiation.

Moreover, after 24 hours of repair time, most of the cells are not presenting foci, whereas some of them are showing abnormal phenotypes like highly marked or multi-damaged cells. In Figures 5.48 and 5.49, examples of abnormal phenotypes presented by chondrocytes and skin fibroblasts respectively are shown.

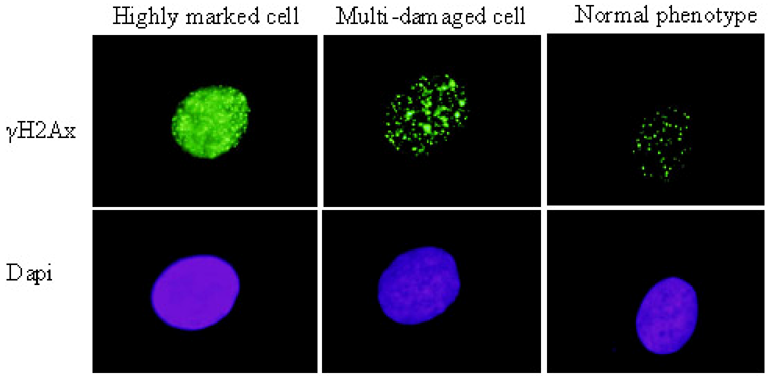

Figure 5.48. Abnormal phenotypes presented by chondrocyte cells after irradiation (repair time= 24 hours). Same experimental details of Figures 5.43 and 5.44.

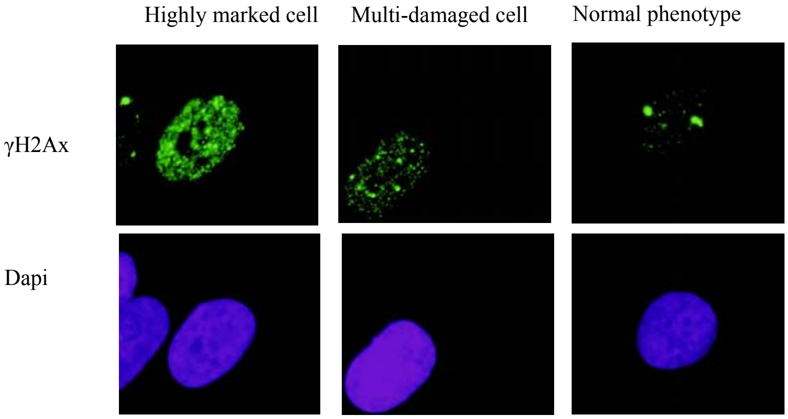

Figure 5.49. Abnormal phenotypes presented by fibroblasts after irradiation (repair time= 24 hours). Same experimental details of Figures 5.43 and 5.44.

- The highly γH2Ax marked phenotype, but with no discrete focus, might correspond to cells in division or to a huge amount of DNA single stand breaks (SSB) that causes a nucleus enlargement.
- The multi-damaged phenotype, instead, consists in low marked background with an increased number of discrete foci which are DNA double strand breaks (DSB).

The percentage for the highly marked phenotype is of 2,6 % for the chondrocytes and 3,8% for the fibroblasts, respectively; while for the multi-damaged phenotype, the percentage is 4,3% for the chondrocytes and 11,4% for the fibroblasts.

Therefore, in the light of these results, the radio-sensitivity of the fibroblasts seems to be slightly higher than the one of the chondrocyte cells.

In Figure 5.50, a 10x focused microscope image of chondrocytes and fibroblasts are shown. This image represent an overview of the irradiated cells before and 24 hours after irradiation for chondrocytes.

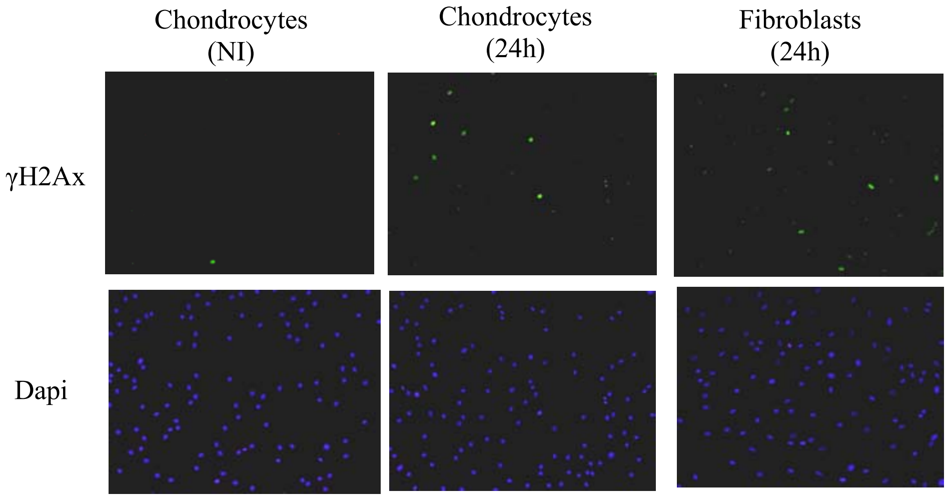

Figure 5.50. Cell observation using the 10X focus. Same experimental details as in Figures 5.43 and 5.44.

Results obtained in this study seem to be in accordance, at least in the proportion (number of observed γH2Ax foci) and in the cell types (non tumour cell in our case), with literature showing persistent γH2Ax foci per cell for long repair times (24 hours) and low doses (1,2 and 5 mGy) (Rothkamm K and Lobrich M, 2003).

➡ HSP70, cellular localisation of stress

The human protein HSP70 has recently been shown to be an efficient stress biomarker (Delmas, Trocheris *et al.*, 1996). Therefore, the HSP70 content in non-irradiated and irradiated human chondrocytes and fibroblasts has been investigated.

Results are presented in Figures 5.51 and 5.52 where microscope images of the two cell lines in exam before and 1 hour after irradiation are respectively reported. HSP70 polyclonal rabbit antibody and TRITC conjugated secondary antibody were used for this measure. Pictures (1, 3) are fluorescence image enhancing the HSP7- distribution in the cell, while images (2, 4) are the DAPI coloured cell nuclei (same cells of images 1, 3).

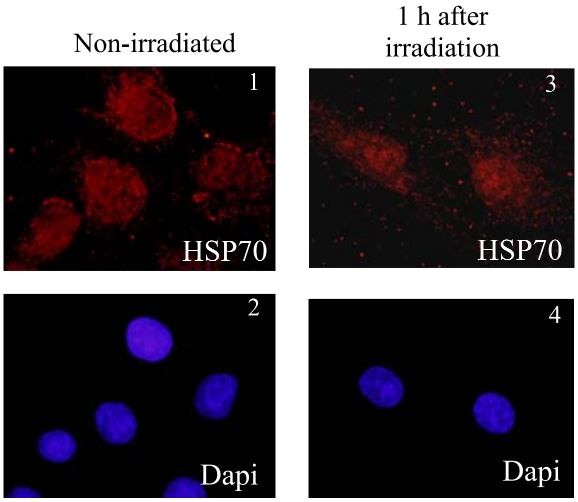

Figure 5.51. Fluorescence microscope images of human chondrocytes and the focus at 100fold magnification. 1 - 2: chondrocytes non-irradiated; 3 - 4: chondrocytes 1 hour after irradiation (cells were kept at 37ºC, 5%CO2).

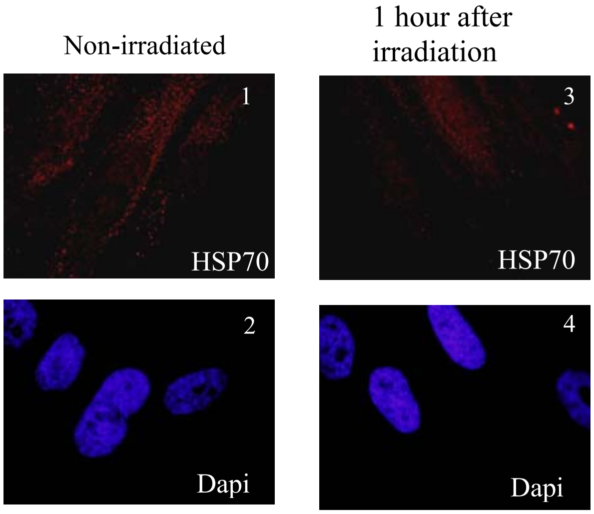

Figure 5.52. Fluorescence microscope images of human skin fibroblasts and the focus at 100fold magnification. 1 - 2: fibroblasts non-irradiated; 3 - 4: fibroblasts 1 hour after irradiation (cells were kept at 37ºC, 5%CO2).

At 1 hour after X-rays irradiation, when the effect for HSP70 (nucleo-shuttling and over-expression (Rénier, Gamo *et al.*)) should be at maximum, there is not any difference visible between non-irradiated and irradiated in both cell types.

This fact means that the stress occurring at doses delivered during AB imaging protocol is not significant in terms of HSP70 response, at least in the performed experiment.

5.8.3 Immunoflurescence conclusions

The results obtained by using the two model proteins γH2Ax and HSP70 here presented are destined to prove the risk-free application, from a radiobiological point of view, of the ABI technique for the sample/patient.

The experimental observations have demonstrated the low radio-sensitivity of chondrocytes even with respect to the fibroblasts´ radio-sensitivity (skin or pulmonary fibroblasts (Rothkamm and Lobrich, 2003)).

The visible persistence of nuclear γH2Ax foci can be noticed for long repair times (24 hours), even with conventional X-rays source (Rothkamm and Lobrich, 2003).

The radiation impact on cellular phenotypes, for the two tested cell types, does not seem to be relevant, since it is *less than 5%*; moreover, the observed effects may even be attributed to other phenomena like cellular senescence or DNA synthesis in which a nuclear inflation appears, for instance (Karp, 1998).

According to these data, it is possible to conclude that doses delivered during AB imaging, using synchrotron light, do not seem, a priori, toxic for the specific application concerning the joint cartilage diseases investigation.

REFERENCES

A. Bravin, S. Fiedler and W. C. Thomlinson (2002). Very low dose mammography: new perspectives in Diffraction Enhanced Imaging (DEI) mammography. SPIE Medical Imaging, S. Diego, CA, SPIE.

R. A. Brooks and G. Di Chiro (1976). "Beam hardening in X-ray reconstructive tomography." Phys Rev Lett **21**: 390-398.

J. Dainty and R. Shaw (1974). *Image science*. London, Academic Press.

F. Delmas, V. Trocheris, C. Miro, J. Murat and I. Villaescusa (1996). "Expression of stress proteins in cultured human cells as a sensitive indicator of metal toxicity." Anal Bioanal Chem **354**: 615-619.

E. R. Foster and J. A. Downs (2005). "Histone H2A phosphorylation in DNA double-strand break repair." FEBS Journal **272** (13): 3231-40.

L. Guarente and C. Kenyon (2000). "Genetic pathways that regulate ageing in model organisms." Nature **408** (6809): 255-262.

B. H. Hasegawa (1990). *The Physics of Medical X-ray Imaging*. Wisconsin, Medical Physics, Medison.

P. A. Jeggo (1998). "DNA breakage and repair." Adv. Genet. **38**: 185-218.

G. Karp (1998). *Cell & Molecular Biology - Concepts & Experiments* Tr - Second Edition, John Wiley & Sons Inc.

S. Majumdar, A. Sema-Issever, A. Burghardt, J. Lotz, F. Arfelli, L. Rigon, G. Heitner and R. H. Menk (2004). "Diffraction enhanced imaging of articular cartilage and comparison with micro computed tomography of the underlying bone structure." European Radiology **14**: 1440-1448.

B. Marples, B. G. Wouters, S. J. Collis, A. J. Chalmers and C. Joiner (2004). "Low-dose hyper-sensitivity: a consequence of ineffective cell cycle arrest of radiation-damaged G_2-phase cells." Radiation Research **161**: 247-255.

J. Mollenhauer, M. E. Aurich, Z. Zhong, C. Muehleman, A. A. Cole, M. Hasnah, O. Oltulu, K. E. Kuettner, A. Margulis and L. D. Chapman (2002). "Diffraction-enhanced X-ray imaging of articular cartilage." Osteoarthritis and cartilage **10**: 163-171.

A. Olivo, L. Rigon, F. Arfelli, G. Cantatore, R. Longo, R. Menk, S. Pani, M. Prest, P. Poropat, G. Tromba, E. Vallazza and E. Castelli (2000). "Experimental evaluation of a simple algorithm to enhance the spatial resolution in scanned radiographic systems." Med Phys **27** (11): 2609-16.

S. Rajdev and F. Sharp (2000). "Stress proteins as molecular markers of neurotoxicity." Toxicol Pathol **28**: 105-112.

W. Rénier, K. Gamo, A. Joubert, Z. Bencokova, J. Gastaldo, D. Marot, S. McSweeney and N. Foray "Human HSP70-1 is a phosphorylation substrate of ATM that is required for stress signaling and DNA double-strand breaks repair pathways in response to ionizing radiation." Submitted January 2006.

K. Rothkamm and M. Lobrich (2003). "Evidence for a lack of DNA double-strand break repair in human cells exposed to very low X-ray doses." Proc Natl Acad Sci USA **100** (9): 5057-5062.

J. A. Ryan and L. E. Hightower (1996). "Stress proteins as molecular biomarkers for environmental toxicology." Stress Inducible Cellular Responses, EXS **77**: 411-424.

S. C. Short, S. Bourne, C. Martindale, M. Woodcock and S. P. Jackson (2005). "DNA damage responses at low radiation doses." Radiation research **164**: 292-302.

T. Takahashi, H. Mizobuchi, M. Toda, A. Maeda, S. Mizuno, Y. Ogawa, S. Yoshida and H. Yamamoto H (2003). "Metabolic effects of X-ray irradiation on adult human articular chondrocytes." International Journal of Molecular Medicine **11** (5): 631-4.

J. M. Velazquez and S. Lindquist (1984). "hsp70: nuclear concentration during environmental stress and cytoplasmic storage during recovery." Cell **36** (3): 655-662.

A. Wagner, M. Aurich, N. Sieber, M. Stoessel, W. Wetzel, K. Schmuck , M. Lohmann, J. Metge, B. Reime, P. Coan, A. Bravin, F. Arvelli, G. Heitner, R. Menk, T. Irving, Z. Zhong, C. Muehleman and J. Mollenhauer (2005). "Options and Limitations of Joint Cartilage Imaging: DEI in Comparison to MRI and Sonography." Nucl. Instr. Meth. A **548**: 47-53.

A. Wagner, M. Aurich, M. Stoessel, N. Sieber, W. Wetzel, J. Mollenhauer, K. Schmuck, C. Muehleman, M. Lohmann, B. Reime, J. Metge, P. Coan, A. Bravin, F. Arfelli, L. Rigon and R. Menk (2005). Chance and limit of imaging of articular cartilage in vitro in healthy and arthritic joints - DEI (Diffraction Enhanced Imaging) in comparison with MRI, CT and ultrasound. SPIE Medical Imaging, SPIE.

A. Wagner, A. Sachse, M. Keller, O. Wagner, M. Aurich, W. D. Wetzel, R. A. Venbrocks, B. \Wiederanders, P. Hortschansky, J. Horn, K. Schmuck, M. Lohmann, B. Reime, J. Metge, F. Arfelli, R. Menk, L. Rigon, C. Muehleman, A. Bravin, P. Coan and J. Mollenhauer (2006). "Quality evaluation of Titanium Implant Ingrowth into Bone by Diffraction Enhanced Imaging (DEI)." Phys. Med. Biol. **51**: 1313-1324.

W. J. Welch and J. P. Suhan (1986). "Cellular and biochemical events in mammalian cells during and after recovery from physiological stress." J Cell Biol **103** (5): 2035-2052.

6

Analyzer-based imaging technique development

Contents

Les développements possibles de l'imagerie par contraste de phase avec un analyseur (ABI) sont discutés et vérifiés dans ce chapitre. Notamment, il est montré que l'association de l'ABI avec la technique par propagation de phase (PPI) conduit à des caractéristiques spécifiques qui peuvent être interprétées comme le mélange des signaux de contraste de phase issus des deux techniques considérées individuellement. Des résultats expérimentaux sont comparés à des simulations réalisées par un code écrit spécifiquement et qui inclut la solution des équations de Takagi-Taupin, ainsi que la propagation du front d'onde entre les éléments optiques. La dernière partie de ce chapitre présente une méthode alternative d'exploitation des effets de phases : des résultats expérimentaux préliminaires, avantages et limitations de la technique sont discutés.

In this chapter, possible developments of the analyzer-based imaging (ABI) technique are discussed and experimentally demonstrated. In particular, the combination with the X-ray 'Propagation-based' imaging (PBI) is qualitatevely and quantitatively investigated showing peculiar features that can be interpreted as the mixture of the two independent (ABI and PBI) phase contrast signals. Experimental results will be compared with simulations performed with a specifically written code based on an approach encompassing the solution of the Takagi-Taupin equations and the wavefront propagation between the optical elements.

In the last part of the chapter, an alternative modality for exploiting phase effects will be presented: preliminary experimental results and advantages and limitations of the technique will be discussed.

6.1 Introduction

As more extensively discussed in Chapter 2 and shown in Chapter 5, hard X-ray phase contrast imaging techniques present important advantages with respect conventional absorption radiography, above all when samples consisting of light elements (e.g. biological samples) have to be investigated (see Paragraph 2.2)

The propagation-based imaging (PBI) and the analyzer-based imaging (ABI) have become particularly popular using both synchrotron radiation and laboratory X-ray sources. Just as reminder, the principles of the image formation of these two imaging modes are:

- PBI: phase contrast is formed as a result of free-space propagation of an X-ray beam transmitted through a sample. The detector is placed at a sufficient distance from the object to allow the transformation of transverse phase-shift variations (occurred inside the sample) into intensity variations by means of Fresnel diffraction.
- ABI: the transformation of the phase shifts into intensity variations in the detector plane is obtained by analyzing the transmitted X-ray beam by a perfect crystal which plays the role of a one-dimensional Fourier filter (Davis, 1996).

Each of the two techniques has its relative advantages and disadvantages: PBI is simpler to be implemented and is sensitive to phase variations in any direction orthogonal to the optical axis; ABI can produce stronger image contrast and better scatter rejection but it is sensitive to phase shifts occurring only in the diffraction plane. A detailed comparison of the two phase contrast imaging modalities can be found in (Pagot, Fiedler *et al.*, 2005).

Despite their common origin (wave phase shifts), phase contrast imaging techniques have been theoretically and experimentally treated separately in the literature.

Recently, as part of this Thesis work, it has been experimentally shown that by using a coherent X-ray beam and choosing an appropriate set-up that combines propagation as well as diffraction by a crystal-analyzer, the resulting images show original features, which combine some advantages of the two methods. This technique has been introduced as 'Hybrid phase contrast imaging' (HI) and is the subject of a publication:

- P. Coan, E. Pagot, S. Fiedler, P. Cloetens, J. Baruchel, A. Bravin, “Phase-contrast X-ray imaging combining free space propagation and Bragg diffraction”, *Journal of Synchrotron Radiation*, Vol. 12, 241-245, 2005.

The theory of these studies has been presented by Pavlov *et al.* (Pavlov, Gureyev *et al.*, 2004; Pavlov, Gureyev *et al.*, 2005) and Nesterets (Nesterets, Gureyev *et al.*, 2006).

The theoretical model of the combined PBI-ABI technique can also be used for better understanding and for quantitatively analysing certain contrast features in conventional ABI.

In order to explore the full potential of the ABI technique itself and also taking into account the combined effect of the free-space propagation, **an advanced wave-optical approach for simulating a monochromator-analyzer set-up in Bragg geometry has been developed** (Bravin, Mocella *et al.*). Simulations produced by using this code will be here presented and compared with experimental results.

The last part of the chapter will be dedicated to the presentation of an alternative way for exploiting the phase shifts of the X-ray beam passed through a sample and some preliminary results obtained by imaging simple phase objects (showing negligible absorption). This method is characterized by a set-up very similar to that of PBI technique, where the principal element is the array-structured detector used like a slit system that is like a spatial filter of the radiation refracted and scattered inside the object.

6.2 Hybrid imaging (HI) compared to PBI and ABI

6.2.1 Material and methods

The experimental investigation of the combination of the propagation-based and analyzer-based imaging techniques has been performed at the ID19 beamline. Results of this hybrid imaging technique are also compared to images of the same samples produced by using the PBI and ABI techniques separately.

The experimental set-up included the fixed-exit double crystal silicon (111) monochromator operating in reflection geometry in the vertical plane, and the FRELON CCD based X-ray detector system with an effective pixel size of 7.5×7.5 μm^2, producing images with a spatial resolution of about 16 μm (Cloetens, 1999). A detailed description of the set-up is reported in Chapter 3.

Figure 6.1 shows schematically the different experimental configurations used in this work: (a) set-up used for PB images, the sample-to-detector distance varying from 0 to 7 meters; (b) set-up for AB, where the X-ray beam analyzer is a Si (111) crystal operating in Bragg geometry with a vertical diffraction plane; (c) set-up for the HI technique in which the wave transmitted by the sample is analyzed by the Si (111) crystal after propagation in air. The experimental data have been acquired using 25 keV X-rays; the measured analyzer rocking curve width (FWHM) is 14.5 μrad (curve shown in Figure 6.2).

The AB and HI images have been recorded at different angular positions (intervals of 2.8 μrad, corresponding to the sampling points of Figure 6.2) along the rocking curve that has been centered at the Bragg angle for the Si (111) reflection at 25 keV ($\Delta\theta = 0$). Every image has been normalized by acquiring a supplementary image after having removed the sample from the X-ray beam. The normalization procedure is the same as that described in Paragraph 5.4.

In order to visualize only the phase effects, thin cylindrical polymer fibers have been chosen as sample, because they can be considered as pure phase objects, showing almost negligible absorption contrast at this photon energy. The sample characteristics are summarized in Table 6.1.

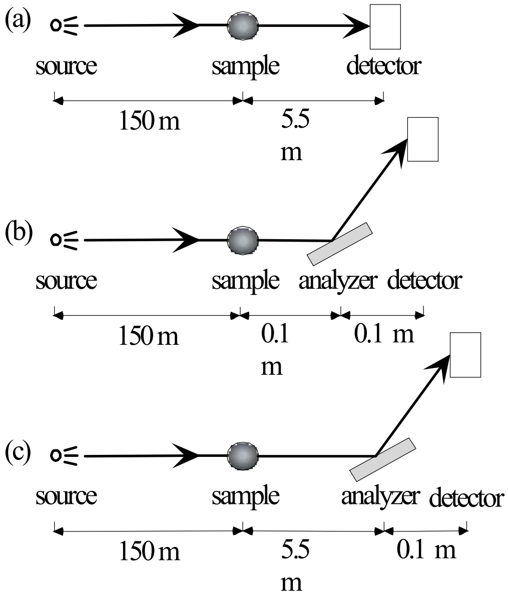

Figure 6.1. Schematic representation of the set-ups used for the image acquisition in the Propagation-based Imaging (a), Analyzer-based Imaging (b) and Hybrid Imaging (c) configurations, respectively.

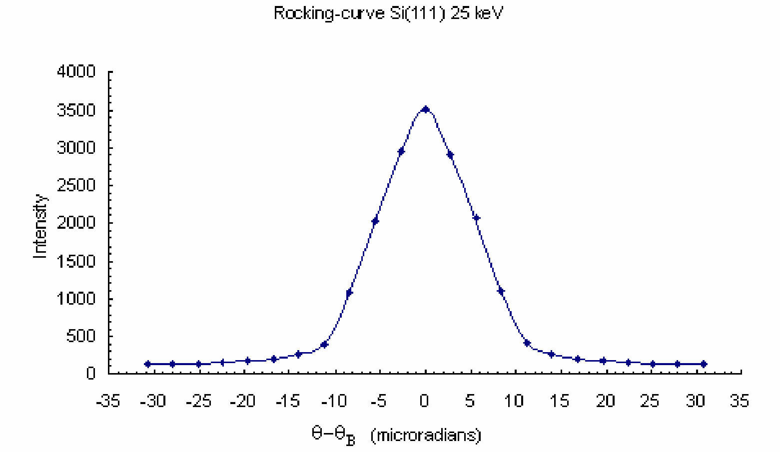

Figure 6.2. Experimental rocking curve of the Si(111) analyzer crystal. The measured curve width is of 14.5 µrad.

Sample	Diameter (µm)	Material	Density (gr/cm^3)	δ	Contrast
wire 1	350	Nylon	0.93	3.52×10^{-7}	1%
wire 2	100	Kevlar	1.44	5.45×10^{-7}	0.5%

Table 6.1. Some physical parameters of the two samples used for this study; in the last column, the calculated maximum absorption contrast is reported.

6.2.2 Data analysis and discussion

Figure 6.3 shows an example of the images and the extracted intensity profiles acquired using the PB, AB and HI techniques. In the case of the AB technique, each edge of the object gives rise to a peak that can be either positive or negative. The signal is evaluated by calculating the difference between the recorded peak and the background. Both edges of wires in PB images show symmetrical contrast, with contiguous positive and negative peaks. This occurs also in the HI images, due to the combination of the propagation and analyzer effects. In these cases, the signal is calculated as the differences between each maximum and minimum signal.

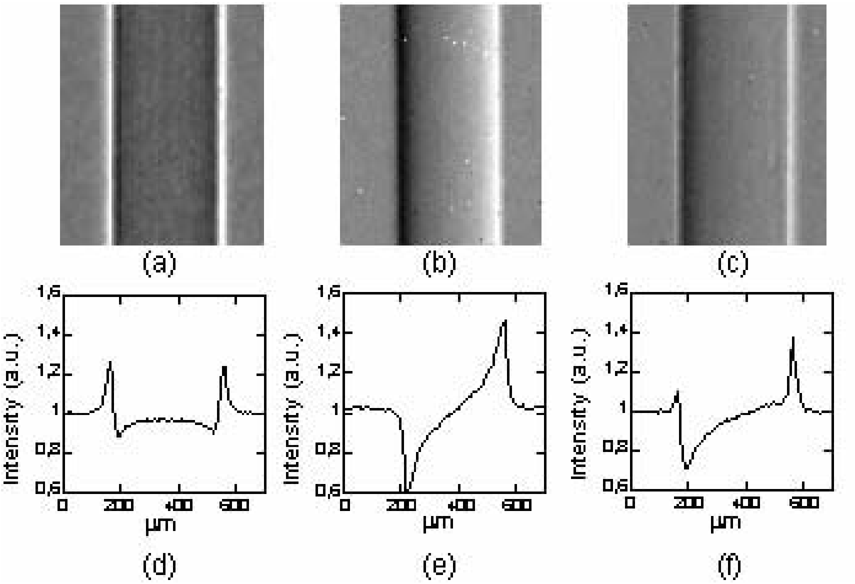

Figure 6.3. Images and vertical profiles of the nylon wire with the Propagation-based Imaging (a, d), the Analyzer-based Imaging at $\Delta\theta$ =5.6 µrad (b, e) and Hybrid Imaging at $\Delta\theta$ =5.6 µrad (c, f) techniques, respectively. The diffraction plane is horizontal in images a, b, and c.

The quantitative analysis has been carried out by evaluating the signal-to-noise ratio (SNR). The SNR has been calculated using the relation:

$$SNR = \sqrt{A}\left(I_{\max} - I_{\min}\right)/I_0\sigma_0 \tag{6.1}$$

where A is the area (in pixels) over which the signal has been evaluated as the mean of the pixel counts (Evans, 1981); I_0 is the average of several values of the background intensity, each one being the mean of the pixel counts over a different area A on the background, and σ_0 the related standard deviation; $I_{\max}$ and $I_{\min}$ represent the maximum and the minimum of the diffraction pattern produced by an edge with respect to the background. In particular, in the case of a single positive or negative peak, $I_{\min}$ and $I_{\max}$ correspond to the background values, respectively. The shown SNR values (Figure 6.6) have been obtained by averaging repeated evaluations of this parameter on the recorded images and the reported error bars are the calculated standard deviations.

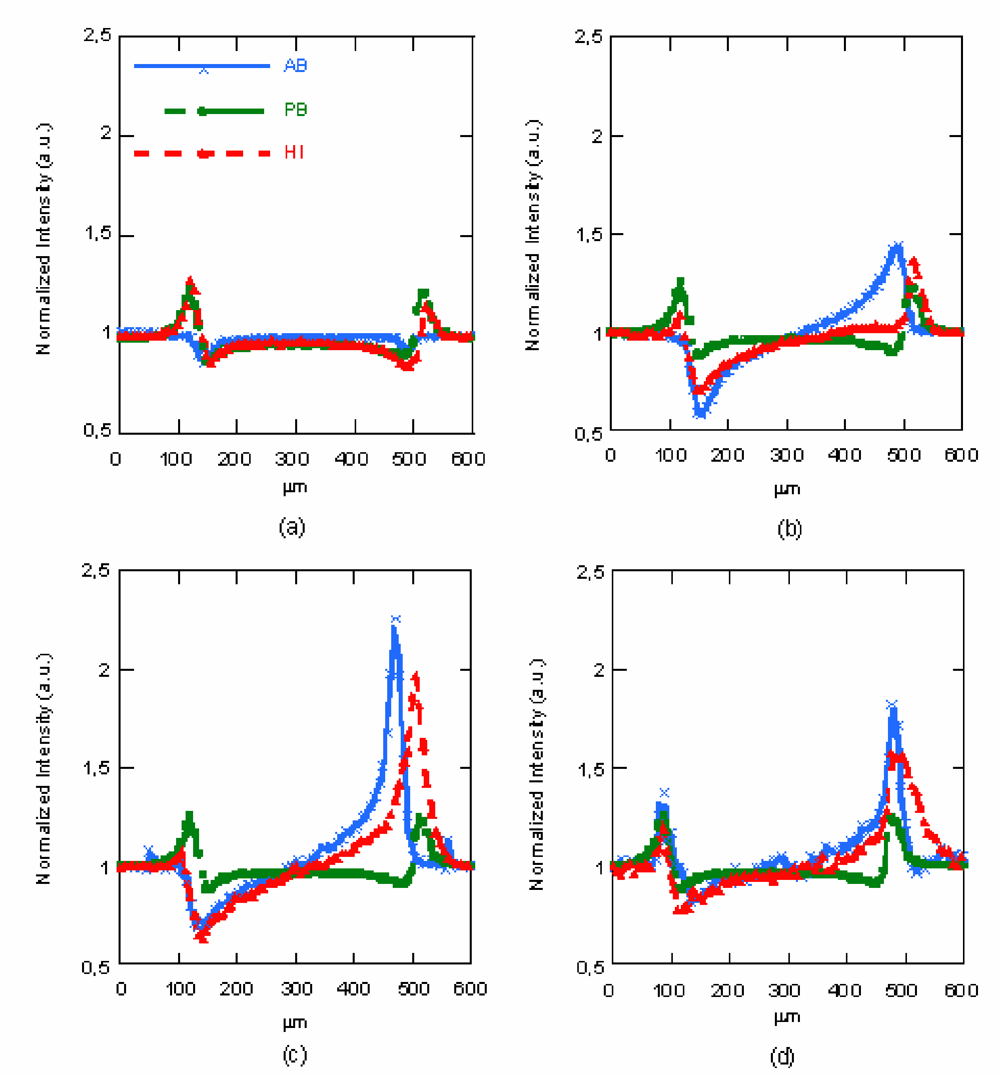

(a) (b) (c) (d)

Figure 6.4. Signal profiles (evaluated by averaging the signal over 30 pixels) of the nylon wire at four different angular positions along one flank of the rocking curve of the analyzer: $\Delta\theta$ =0 (a), $\Delta\theta$ =5.6 μrad (b), $\Delta\theta$ =11.2 μrad (c) and $\Delta\theta$ =16.8 μrad (d). The Propagation-based Imaging profile, related to a sample-to-detector distance of 5.5 m, appears in each plot for comparison with the signals obtained in the Analyzer-based Imaging and Hybrid Imaging configurations.

Figure 6.4 shows the experimental profiles for the nylon wire using the three imaging techniques. The PB image has been acquired at 5.5 m from the sample and the AB and HI profiles are shown at four different positions on the rocking curve. The PB signal contrast, evaluated as $\left(I_{signal} - I_0\right)/I_0$, is as high as 27%; AB signal increases from a minimum of 3 % at $\Delta\theta$ =0 up to a maximum of 55 % at $\Delta\theta$ =11.2 μrad, while at the same angular positions, the HI shows values of 26 % and 46 %, respectively.

In the PB images, the signal is determined in first approximation by the Laplacian of the phase introduced by the object and by the sample-detector distance, while in AB images the wave passes through the crystal acting like a band pass filter; thus only some frequencies can reach the detector. The HI signal combines the propagation and diffraction effects, and it has been compared with the sum of the PB and AB signals in Figure 6.5. As expected, the calculated profile fits only approximately with the experimental HI signal, indicating that the latter is also an interference phenomenon (Pavlov, Gureyev *et al.*, 2004).

Figure 6.6 shows the graph of the SNR versus the angular setting of the analyzer, for the two edges of the wires imaged with the AB and the HI techniques. The SNR values for the left and right edge in the PB configuration are respectively 178.5±29.8 and 164.5±12.3 for the nylon wire and 241.9±29.9 and 207.2±24.9 for the kevlar wire. The visibility of the two edges, expressed in terms of SNR, changes substantially by varying the angle of the crystal. The profiles for respectively the left and the right edge are approximately mirror of each other with respect to the center of the curve ($\Delta\theta$=0). The slight difference in the absolute values can be explained by imperfections in the sample shape.

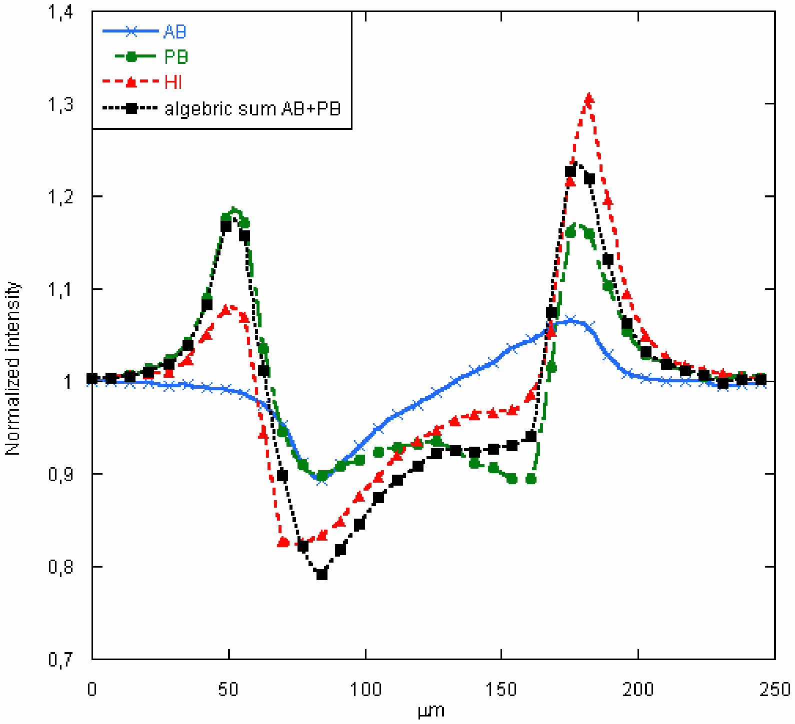

Figure 6.5. Propagation-based Imaging (PB), Analyzer-based Imaging (AB) and Hybrid Imaging (HI) signal profiles of the kevlar wire compared with the calculated profile obtained by algebraically summing the PB and AB signals at $\Delta\theta$=2.8 µrad.

In AB, this behaviour can be explained by considering the different origin of the signal for the various angular positions. In particular, while at $\Delta\theta$=0 the signal mainly derives from refraction and the reduction of the scattering component on the image (and, in thicker samples, from X-ray absorption), for the other angular positions, the signal is determined by the alignment of the analyzer with respect to a given direction of the refracted X-rays. Therefore, by rocking the crystal, it is possible to optimize the visibility of the details that, in the case of the studied wires, presents maximum values of the SNR for positions on the shoulders of the rocking curve. In other words, at around $\Delta\theta=0$ there is a minimum of the derivative of the rocking curve, and then the crystal is less sensitive to X-ray refracted inside the object, determining a low SNR. On the tails of the rocking curve, the low reflectivity increases the noise on images, also reducing the SNR.

In the case of the HI technique, the main difference with respect to AB concerns the SNR values around the exact Bragg angle. In fact, while the AB signal is maximum on the shoulders of the rocking curve and it decreases towards $\Delta\theta=0$, in HI the SNR is high even at this position where it also reaches its maximum values. Since the HI signal results from the combination of the PB and AB techniques, even if the contribution to the signal arising from AB decreases, the contribution coming from the PB is still present, retaining high SNR values.

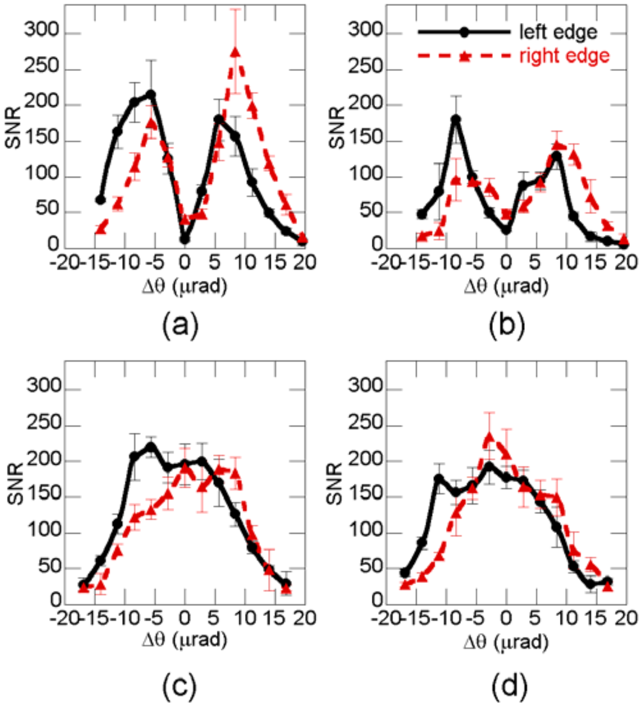

Figure 6.6. Signal-to noise ratio values of the signal produced by the edges of the two wires as function of the angular position along the rocking curve of the analyzer for the AB (nylon wire (a), kevlar wire (b)) and HI (nylon wire (c), kevlar wire (d)) configurations.

6.2.3 Conclusions of the HI investigation

It has been experimentally demonstrated that propagation-based and analyzer-based phase contrast imaging techniques can be combined, producing original features.

Images of simple polymer fibers obtained with this hybrid method have been analyzed in term of SNR and compared with the patterns produced independently by the two distinct techniques. Hybrid images present an almost constant value of the SNR over an angular range of the order of the FWHM of the rocking curve of the crystal-analyzer.

This weak dependence on the angular positioning of the analyzer reduces the constraints in terms of optical alignment and stability of the crystal, which is one of the critical issues of the AB imaging technique.

In order to fully described and understand the peculiar characteristics of the HI signal, studied in a preliminary way in this work, further theoretical and experimental investigations are required. This technique may find application in several fields already advanced by hard X-ray phase contrast imaging, producing as high SNR as PB, while bringing the advantages of the higher refraction sensitivity of the AB technique.

6.3 DEIWAVE: a wave-optical approach code

As already stated and proven in this Thesis, the analyzer-based imaging is a technique that has been successfully tested and widely used in life science imaging. The full potential of this method has, however, still to be explored and many experimental parameters (energy, analyzer angular position, analyzer reflection etc. for a given sample) can be optimized. In order to reach this goal, an advanced wave-optical approach for simulating a monochromator-analyzer set-up in Bragg geometry (Figure 6.7) has been developed in the framework of a collaboration between the ESRF SciSoft group and ID17. This code has been called DEIWAVE and is presented here.

Free-space propagation and crystal diffraction are taken into account, assuming that both crystals are perfect. Therefore, DEIWAVE can be used to investigate not only the conventional ABI but also the features of the HI signal.

The polychromaticity of the incident wave on the monochromator is accounted for by using a distribution of incoherent point sources along the surface of the crystal. The preliminary results of this new approach show an excellent agreement with experimental data as afterwards presented.

Until now the results of the ABI technique have been interpreted mainly in terms of geometrical optics (Keyriläinen, Fernández *et al.*, 2002). It is clear that this description fails in various occasions, in particular where the wave nature of the beam is highlighted. This is for instance the case in the vicinity of the borders of the object or when the details to be visualized are of the same order of magnitude as the point spread function of the analyzer crystal.

6.3.1 DEIWAVE code description

The simulated SR imaging set-up is schematized in Figure 6.7. The object being visualized is placed in the pseudo-planar beam produced by the mononochromator. The analyzer is fixed in Bragg position. In conformity to the ABI principles, the degree of contrast created by a refracting object depends on the relative intensities of the waves, corresponding to the object and its background, that are reflected by the analyzer. Changing the orientation of the analyzer alters this proportion and thereby the contrast.

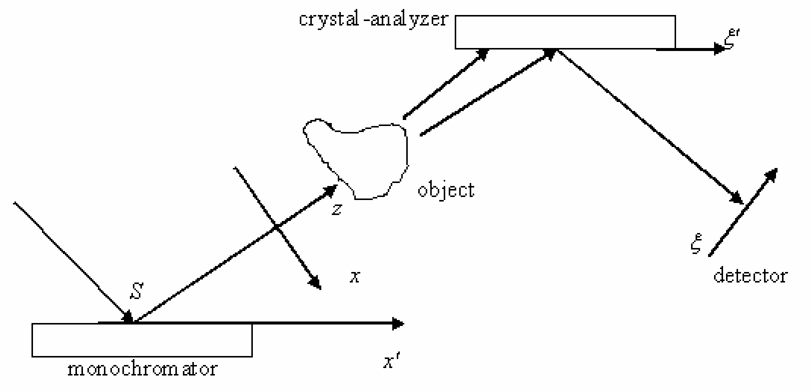

Figure 6.7. Scheme of the set-up and reference systems used for simulating the ABI and HI in the DEIWAVE code.

This set-up has been chosen in order to reproduce the experimental conditions used for the ABI and HI acquisitions presented in Paragraph 6.2. Briefly, the experimental set-up used included a pre-monochromator (fixed-exit double crystal Si (111) in Bragg geometry) reducing the incoming continuous energy spectrum to $\Delta E/E \cong 5\times10^{-4}$, a symmetrically cut Si (111) Bragg monochromator and an identical analyzer (non dispersive setting).

The polychromaticity on the monochromator is considered and described using a distribution of incoherent point sources along the surface of the crystal. It should be underlined that this is not an approximation: when the polychromaticity of the incident beam is much larger than the wavelength acceptance of the diffracting crystal, the illumination on the entrance surface is completely incoherent (Carvalho and Epelboin, 1993; Epelboin, Mocella *et al.*, 1999; Mocella, Epelboin *et al.*, 2000).

In order to correctly describe the experimental set-up, simulations have been performed using a wave-optical approach that takes into account both free space propagation and crystal diffraction. Both crystals, monochromator and analyzer, are assumed to be perfect. The incoherence assumption implies that calculations can be performed independently for each point source along the surface of the monochromator.

The wave amplitude diffracted by the monochromator is given by the Kato spherical wave solution of the Takagi-Taupin (T-T) equations for a perfect crystal (Uragami, 1969; Afanas'ev and Kohn, 1971), which corresponds to the Green-Riemann function of the T-T equations (Takagi, 1969). More recent theoretical studies showed the same conclusions with a straightforward derivation from the multiple scattering expansion of the T-T equations (Guigay, 1999).

In our case, for an infinitely thick, symmetrically cut crystal in Bragg geometry, the expression of the diffracted Kato spherical wave as a function of the x' coordinate along the entrance surface is (Authier, 2001):

$$R_h\left(x',S\right)=-i\pi Ck\chi_h\left[J_0\left(\left(x'-S\right)\frac{\pi kC}{\sin\theta_B}\sqrt{\chi_{\bar{h}}\chi_h}\right)+J_2\left(\left(x'-S\right)\frac{\pi kC}{\sin\theta_B}\sqrt{\chi_{\bar{h}}\chi_h}\right)\right] \tag{6.2}$$

where $\chi_{\bar{h}}$ and χ_h are the Fourier components of the dielectric susceptibility for a given reflection *h*, *C* is the polarization factor, $k=1/\lambda$ (λ is the x-ray wavelength) and J_0 and J_2 are the zero-th and second order Bessel functions, respectively. The point *S* is referred to in Figure 6.7.

By reminding some notions already introduced in Chapter 2, indicating the deviation from unity of the complex refractive index *n* of the object as:

$$n\left(x,z\right)-1=\delta\left(x,z\right)+i\beta\left(x,z\right) \tag{6.3}$$

the complex phase modulation introduced by the object is:

$$\Phi\left(x\right)=\frac{2\pi}{\lambda}\int\left[\delta\left(x,z\right)+i\beta\left(x,z\right)\right]dz \tag{6.4}$$

Its transmission function *A* can be expressed as:

$$A\left(x\right)=e^{i\Phi\left(x\right)}=A_0\left(x\right)e^{i\varphi\left(x\right)} \tag{6.5}$$

where $A_0\left(x\right)$ describes the absorption and $\varphi\left(x\right)$ the phase modulation introduced by the object. Using (6.4) we can write:

$$A_0\left(x\right)=\mathrm{e}^{-\frac{2\pi}{\lambda}\int\beta\left(x,z\right)dz} \tag{6.6}$$

$$\varphi\left(x\right)=\frac{2\pi}{\lambda}\int\delta\left(x,z\right)dz \tag{6.7}$$

In a scalar approximation (Born and Wolf, 1999) the spherical wave emitted by the first crystal is modified by the sample object. Downstream of it, the wave complex amplitude along the transverse direction *x* is given by:

$$\psi\left(x,S\right)=R_h(x,S)A\left(x\right) \tag{6.8}$$

This is the incident wave impinging on the analyzer (see Figure 6.7).

The diffraction mechanism of this wave on the analyzer is described by its convolution with the Green-Riemann function (6.2) of the analyzer R_h, (Authier and Simon, 1968; Takagi, 1969):

$$\Upsilon(\xi',S)=\int \psi(\tau,S)R_h(\xi'-\tau,S)\,d\tau \qquad (6.9)$$

where ξ' is the coordinate along the analyzer surface (Figure 6.7). In our case *h* and *h'* are the same because the monochromator and the analyzer are identical. In paraxial approximation, the free space propagation after the analyzer is described by a Fresnel-Kirchhoff convolution integral. In particular, the amplitude at the detector position due to an individual point source *S* along the monochromator is given by:

$$\Psi(\xi,S)=\int \Upsilon(\tau,S)e^{-\frac{i\pi k(\xi-\tau)^2}{d}}\,d\tau \qquad (6.10)$$

where ξ is the coordinate along the detector surface. In Eq. (6.10), phase terms inessential for the calculation of the intensity have been omitted.

By using the commutative properties of convolution integrals, it is easy to verify in Fourier space that the only relevant length is the distance *d* between the object and the detector. Finally, the total intensity recorded by the detector is the incoherent sum over *S* of individual point-source contributions:

$$I(\xi)=\int \left|\Psi(\xi,S)\right|^2 dS \qquad (6.11)$$

Equations (6.2)-(6.11) have been used in numerical simulations, the results of which have been compared with experimental data. The dependence of the contrast on the size of the objects and the divergence of the incident radiation has been investigated.

6.3.2 Experimental data and signal simulation details

The parameters used for the experimental data acquisitions and simulations are those reported in Paragraph 6.2. Summarizing:

- X-ray energy: 25 keV;
- Detector: FReLoN CCD camera with an effective pixel size of 7.5×7.5 μm^2, producing images with a spatial resolution of about 16 μm;
- Samples: plastic wires of different radii (*R*) (see Table 6.1);
- Two values of the sample-to-detector-distance *d* were: 0.5 m and 5.5 m.

The angular offset θ_a ($\Delta\theta$, that is the angular misalignment of the crystal analyzer with respect to the Bragg angle for the used energy) of the analyzer was also varied during the measurements. The point-spread function (*PSF*) of the detector has been taken into account.

Operationally, a series of **input files** containing all the experimental parameters to be used for the simulation have been written and can individually be selected in the "main" macro of the DEIWAVE code. An example of these input files with all the different parameters that can be changed in the code is given and explained hereafter (numbers correspond to a given simulated case):

INPUT PARAMETERS FILE (example)

E=25;	X-ray beam energy (in keV)
hkl=1;	Order of reflection for diffraction vector calculation
phid=0;	Crystal analyzer asymmetry angle (
chi0=0.1548e-5+i*0.3695e-8;	0-Fourier component of the susceptibility of the analyzer
chih=0.58405e-6-i*0.5803e-6;	h-Fourier component of the susceptibility of the analyzer
chib=0.5803e-6+i*0.58405e-6;	-h-Fourier component of the susceptibility of the analyzer
deltatheta=0;	analyzer crystal angular position
ob_name='fiber'	sample definition: recall of the macro defining the object
R=175;	fiber radius (in μm)
delta=-3.52e-7;	real part of the sample refractive index
beta=3.0e-11;	imaginary part of the sample refractive index
d=0.5;	sample-to-detector distance (in meters)
answd_psf='y';	for enabling and disabling the convolution with detector *PSF*
FWHM=20;	*PSF* value used in the convolution (result of Eq. (6.12))
answd_sc='n';	for enabling and disabling an angular scan of the crystal analyzer (at every position a simulation is calculated)

- **X-ray source size and magnification**

The finite source size of the X-ray beam is taken into account in the code by convolving the source spatial distribution, which is assumed to be a Gaussian with a given FWHM (see Paragraph 3.5), with the detector *PSF*. Practically, the value of the detector point-spread function that is given in the input file already includes the convolution with the source size rescaled by the magnification factor $M = d/L$, where L is the source-to-sample distance. Therefore the effective *PSF* value is calculated as

$$FHWM_{tot} = \sqrt{FWHM_{\det}^{2} + \left(M \cdot FWHM_{source}\right)^{2}} \tag{6.12}$$

where the $FWHM_{source}$ values are 24 μm and 150 μm in the vertical and horizontal directions respectively (Cloetens, 1999) (only the vertical direction, corresponding to the diffraction plane, is used).

- **Object edge discontinuity**

In order to avoid artefacts in the proximity of the borders of the object, due to the abrupt variations of the phase, a smoothing of the sample edges has been necessary. For this reason, the connection between the object and the background (zero-phase) has been realized by means of an arc-tangent function with an adjustable slope. How the profile of the object is modified is shown in Figure 6.8.

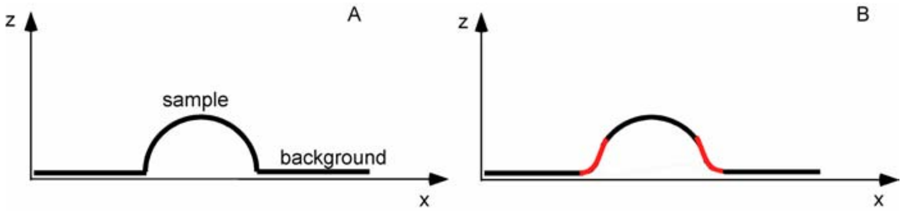

Figure 6.8. Profile of a circular wire before (A) and after (B) edges smoothing by using an arc-tangent function.

6.3.3 Results and discussion

In Figure 6.9-6.12, experimental results and theoretical predictions of the intensity patterns as reflected from the analyzer for selected angular positions and recorded on the detector are displayed for both studied samples. Each experimental profile has been calculated as the average over thirty profiles, and error bars correspond to standard deviations.

In particular the presented cases are summarized in Table 6.2.

Sample	R (μm)	*d* (m)	Δθ (μrad)
wire 1	175	0.5	0 and -11.2
		5.5	0 and -11.2
wire 2	50	0.5	0 and -11.2
		5.5	0 and -11.2

Table 6.2. Studied cases presented in this Thesis.

⇨ **Sample-to-detector distance (*d*) = 0.5 meters**

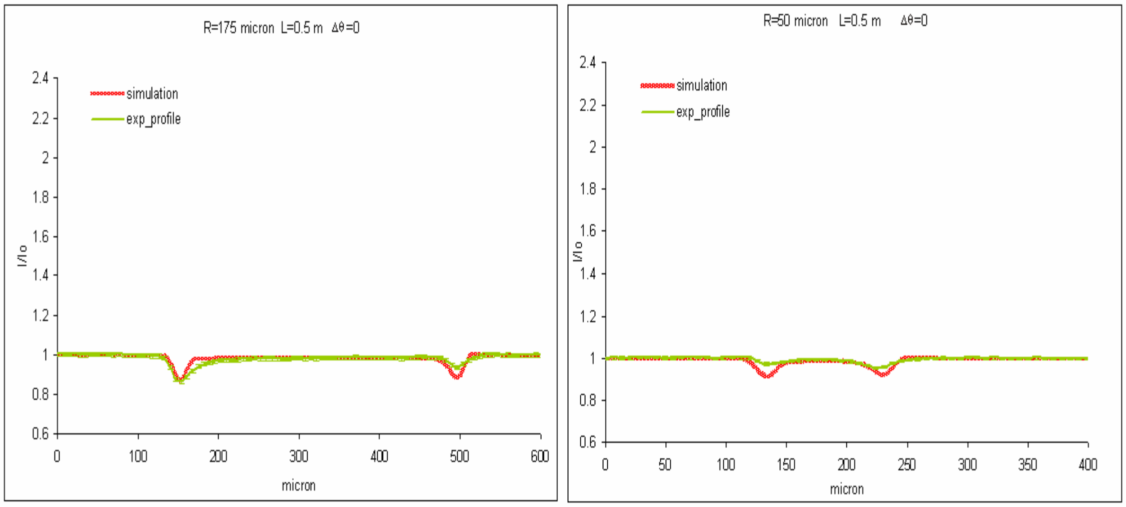

Figure 6.9. Intensity pattern (a.u.) for the two studied wires (nylon wire with R=175 μm on the left and kevlar wire with R=50 μm on the right): experimental (green curve) and theoretical (red curve). Si (111) reflection, d = 0.5 m, $\theta_a = \Delta\theta = 0$ μrad.

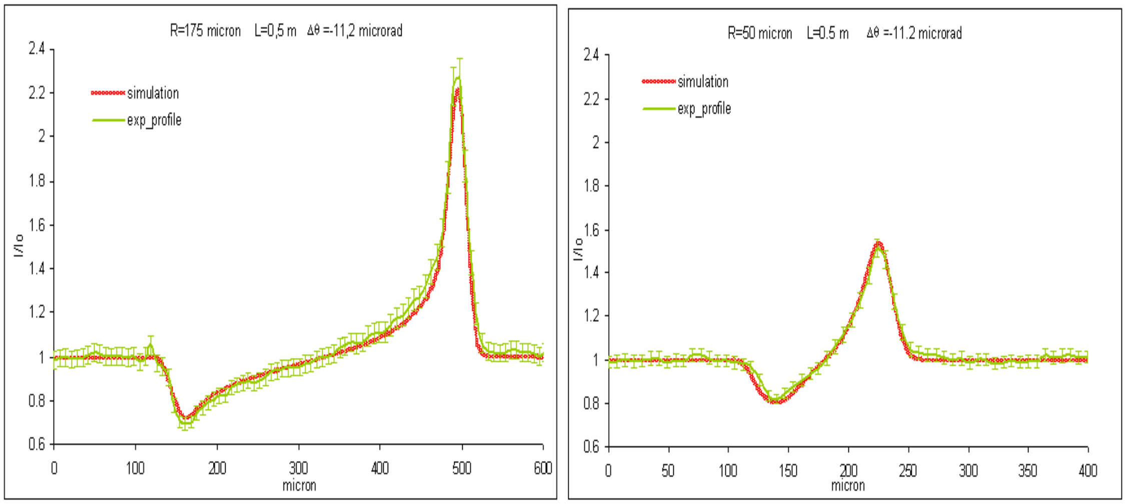

Figure 6.10. Intensity pattern (a.u.) for the two studied wires (nylon wire with R=175 µm on the left and kevlar wire with R=50 µm on the right): experimental (green curve) and theoretical (red curve). Si (111) reflection, d = 0.5 m, $\theta_a = \Delta\theta =$ -11.2 µrad.

⇨ Sample-to-detector distance (*d*) = 5.5 meters

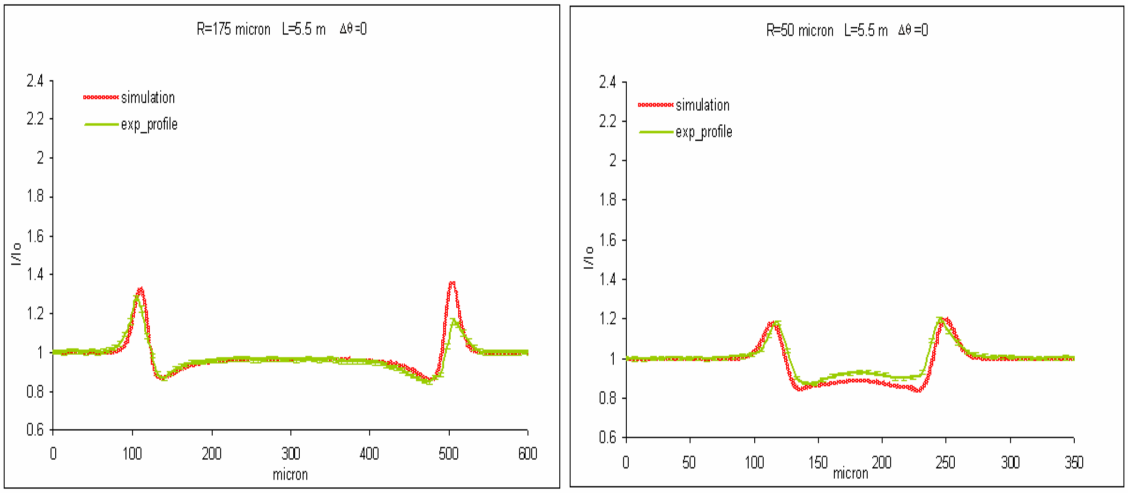

Figure 6.11. Intensity pattern (a.u.) for the two studied wires (nylon wire with R=175 µm on the left and kevlar wire with R=50 µm on the right): experimental (green curve) and theoretical (red curve). Si (111) reflection, d = 5.5 m, $\theta_a = \Delta\theta = 0$ µrad.

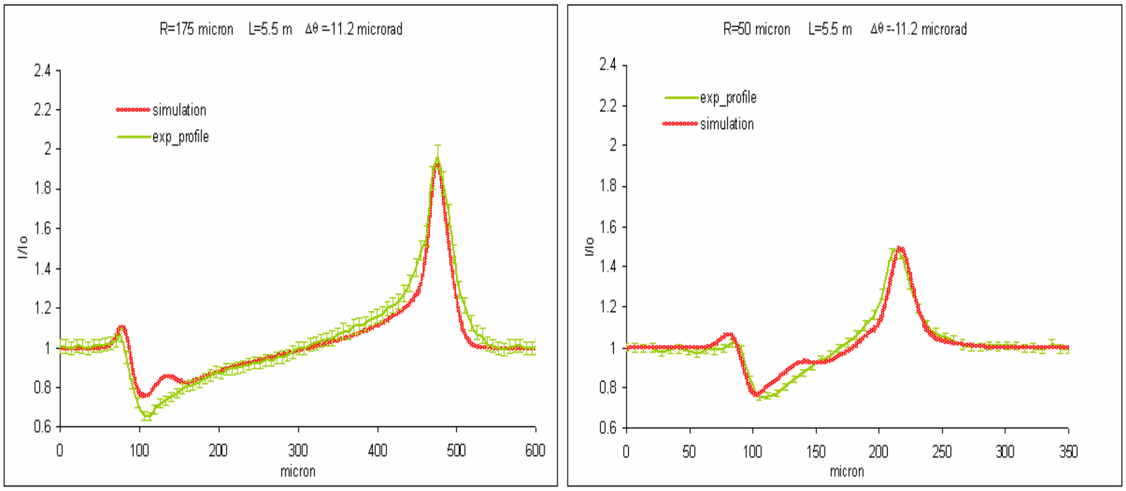

Figure 6.12. Intensity pattern (a.u.) for the two studied wires (nylon wire with R=175 μm on the left and kevlar wire with R=50 μm on the right): experimental (green curve) and theoretical (red curve). Si (111) reflection, d = 5.5 m, $\theta_a = \Delta\theta =$ -11.2 μrad.

In all the presented cases, there is an excellent agreement between simulation and experimental data. This fact gives a high level of confidence in this comprehensive wave-optical approach, which will be used, prospectively for other samples with more complex shapes and for higher order reflections. Nevertheless some important considerations have to be pointed out:

- In the studied cases, the main discrepancies regard the $\theta_a = \Delta\theta = 0$ μrad cases since simulations are not able to reproduce the slightly asymmetric profile of the experimental data. In order to investigate if this fact was due to an inaccuracy of the analyzer angular position, I performed several simulations around the nominal experimental analyzer angles. The obtained results did not show any significant improvement. The difference between simulation and experimental data has to be probably attributed to the paraxial approximation assumed for the propagation-based contribution.
- Similar reasons could explain the strange behaviour of simulations in the cases corresponding to *d*=5.5 m and $\theta_a = \Delta\theta =$ -11.2 μrad. The simulated profiles follow quite well the experimental ones, expect for some features near the object edges.

Despite the above described discrepancies, the capability of the DEIWAVE code of simulating the ABI signal, also taking into account the propagation effect, is largely demonstrated by the results so far obtained.

The potential of the code could be particularly important for the optimization of the parameters of the analyzing system (crystal reflection and alignment versus the main monochromator) for given sample properties (shape, chemical composition, homogeneity….) and for understanding the contribution of the free-propagation to the signal produce by the analyzer-based imaging technique (HI investigation).

Therefore, upon entire validation, the DEIWAVE method might be integrated eventually into parametric studies for optical design optimization.

For sake of completion, it is worth to note that a new theoretical method combining analyser-based and propagation-based hard X-ray phase-contrast imaging has been recently published by Nesterets *et al.* (Nesterets, Gureyev *et al.*, 2006). In this work the assumption of a weak scatterer is considered. Consequently, the results are not limited to the case of short propagation distances or low-resolution imaging. An explicit expression for the combined transfer function is derived and analytical and numerical examples solving related inverse imaging problems are presented.

6.4 How to simplify the ABI technique?

In this paragraph, a new application is presented to investigate and analyse the X-ray beam scattered and refracted by a sample. The **idea** is based on the fact that the **analyzer crystal**, being a spatial filter of the radiation incident on its surface, **can be thought as a slit system with an extremely narrow angular acceptance (~µrad).** (Figure 6.13). Therefore, by replacing the crystal with a slit system of suitable aperture and positioned at a suitable distance from the sample, it is possible to discriminate X-rays deviated at different angles inside the specimen. In practice, to register the X-rays deviated at a certain angle with respect to the incident beam, the slit is kept fixed and the sample is scanned through the beam. Then the slit is displaced vertically and a different angular deviation of X-rays can be recorded.

A proof of this is presented in Figure 6.14, where an example of the profiles of the signal produced by a nylon wire is reported. They were obtained by using a slit system with an aperture of 80 µm and positioned at 10.5 m after the sample (further details in the figure caption). As it can be qualitatively pointed out, the shown experimental profiles in (A) and (B) are very similar to those obtained with the ABI and the PBI techniques, respectively (refer to Figure 6.3). These two profiles correspond to the situations in which the slit system is not centered or is centered with respect to the incident beam on the sample, respectively. In the first case the X-rays deviated inside the sample at certain angles can reach the detector, while in the second case only the non-deflected (or deviated at (small) angles within the angular acceptance of the slits) photons are detected.

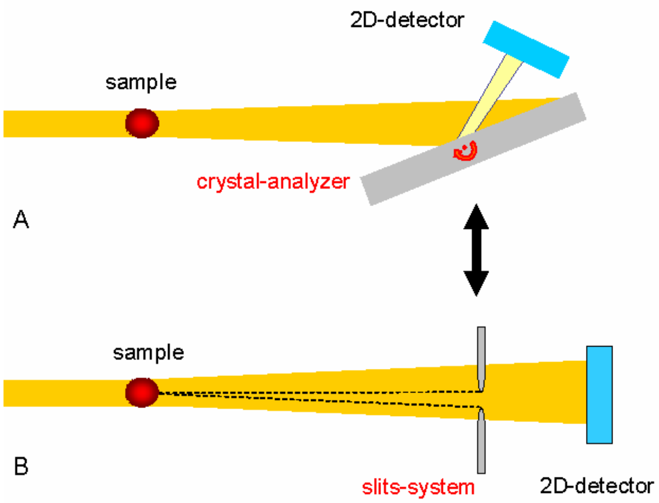

Figure 6.13. The crystal analyzer present in the conventional ABI set-up (A) can be in principle assimilated to (and replaced by) a slit system (B) set a given distance from the sample and with a suitable aperture.

The signal produced and the sensitivity and resolution obtained with this modality depends on the slit aperture with respect to the vertical beam size and, of course, on the used detector.

If the suitable distance from the sample and aperture of the slit system are used, in principle results similar to the ABI ones should be produced. In addition, this modality has some advantages with respect to the conventional ABI technique mainly from the set-up point of view. In fact, once aligned, the slit system presents less stringent stability requirements than a crystal, even if some problems could derive from the necessity of scanning the system through the refracted radiation.

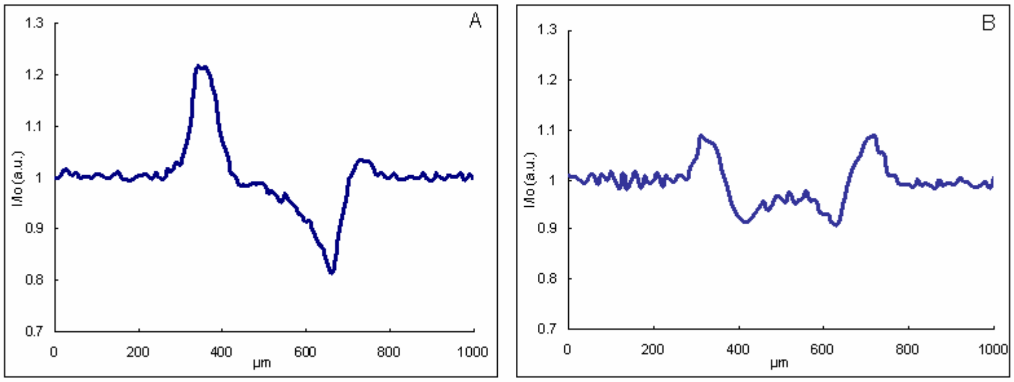

Figure 6.14. Profiles of a nylon wire obtained by using a slit system instead of a crystal analyzer. Experimental details: energy=25 keV, slit aperture=80 μm, wire radius=350 μm.

Starting from this observation, a further simplification of the experimental set-up has been introduced and experimentally verified.

The **basic idea** is now linked to the **array structure of the CCD FReLoN camera** detector and its versatile **acquisition/readout mode** system (refer to Chapter 4 for a full description). In particular, the so-called **"concatenate" mode**, consisting in the **read out of a ROI** (of pixels) between two movements of the sample, allows to use the camera like a slit system.

Precisely, each line of pixels of the CCD array, which can be read and stored indipendentely, acts as a slit system whose angular acceptance is given by the vertical pixel size of the camera (see Figure 6.15). Since this imaging modality is intrinsically linked to the detector, in the following paragraphs it will be refered to as "**detector-based analyzer imaging**" **(DBA)**.

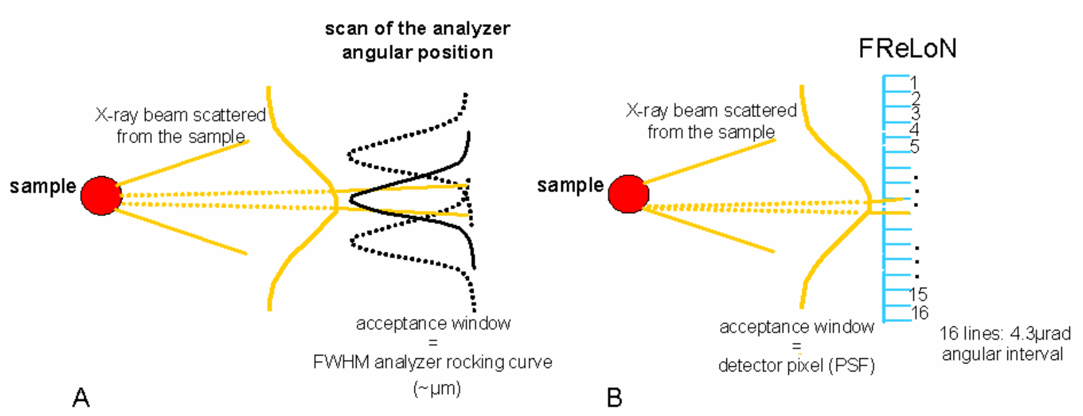

Figure 6.15. (A) Principle of the ABI technique: the radiation emerging from the sample is analyzed by the crystal analyzer with a resolution determined by the FWHM of its rocking curve. By changing the angular position of the crystal, different portion of the wavefront are diffracted towards the detector. (B) A CCD array detector may be used for analyzing the radiation: each line of pixels of the CCD array can be independently read out functioning like a slit system. The resolution is defined by the detector vertical pixel size (schemes not in scale).

6.4.1 Exploiting the detector-based analyzer imaging

Instead of analyzing the radiation refracted and scattered inside the sample by means of a crystal whose sensitivity is given by the FWHM of its rocking curve, detector pixel lines can be independently read out and used like a slit system (see Figure 6.15 (B)). The basic requirement is that the X beam is as high as the vertical pixel size of the array detector (see point 5 hereafter).

The **principles** at the basis of the **DBA technique** can be summarized in the following points (Figure 6.16):

1. A **ROI** containing **all the** detector **pixel lines illuminated** by the radiation emerging from the sample is selected. Let be n_l the number of pixel lines, each of them indicated with a number ('1', '2' ...);
2. Each of the n_l pixel lines are **independently read out and stored**;
3. In order to obtain **two dimensional images** of the **sample**, the latter is **scanned** through the incoming laminar X-ray beam with a vertical scanning step equal to the vertical pixel size. At each position of the sample, a ROI of n_l is acquired.

4. At the end, n_l **images** are built up: any $(n_l)_j$ image will results from the combining of acquisitions made with the $(n_l)_j$ pixel line of the detector.
5. If the **X-ray beam** incident on the sample has a **vertical size equal to the vertical pixel size** then:

   – the **pixel line aligned with the incoming X-ray beam** will detect the direct **X-ray that have not interacted** with the matter (neither absorbed nor deflected) (e.g. line # 1 in Figure 6.16);

   – the other **pixel lines** (e.g. lines # 2-5) **by the side of the central line will record the X-rays that have been deviated** from their path because of the refraction and scattering inside the object at angles as higher as farer the line is from the central one.

Therefore, referring to the example of Figure 6.16**:**

➡ **Image '1'** (acquired with the pixel line # 1) will give information on the **absorption** properties of the sample;

➡ **Images '2-5'** (acquired with the pixel lines # 2-5) will contain information on the **refraction properties** of the sample.

The different images obtained by combining the pixel lines of the selected ROI on the detector somehow correspond to the images acquired with the ABI technique at different angular position of the crystal analyzer: image '1' ~ 'top' image and images '2-5' ~ 'slope' images.

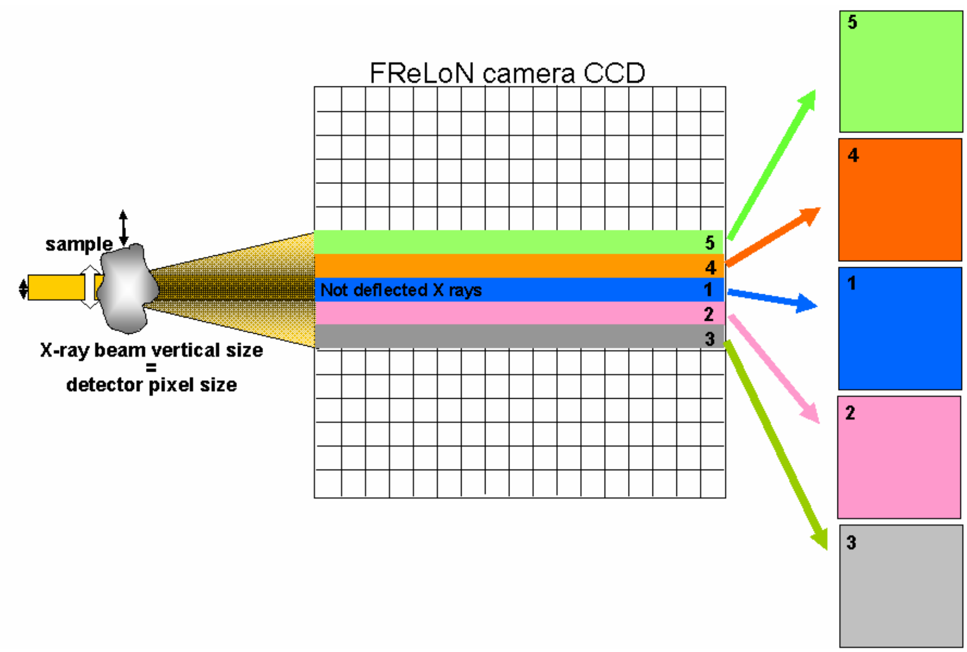

Figure 6.16. Scheme of the detector-based analyzer imaging modality (details in the text).

- **The DBA set-up**

The experimental set-up for implementing the detector-based analyzer imaging technique is relatively simple. A scheme is shown in Figure 6.17.

A slit system positioned upstream the sample defines the size of the X-ray beam from the monochromator in such a way to have a photon beam height equal to the detector pixel size. The beam after passing through the sample is let freely propagate over a distance of some meters and then it is recorded by the two dimensional array detector (FReLoN camera) according to the modality above described.

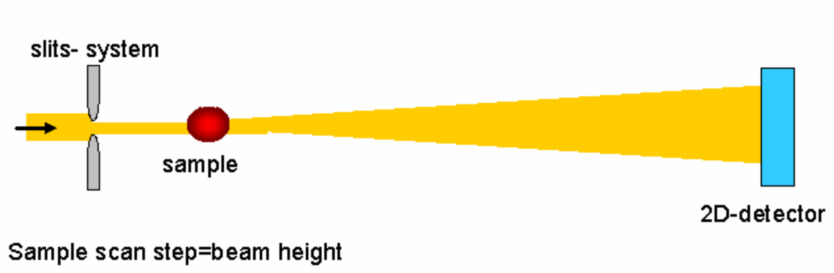

Figure 6.17. Scheme of the experimental set-up used for acquisition with the detector-based analyzer imaging technique.

- **Important remarks**

– Optically, there are some important requirements that have to be fulfilled:

- the slit system has to be perfectly polished since the needed aperture is of the order of few tens of micrometers (~50 μm in the case of the ID17 taper optics FReLoN camera);
- the slit system and the array detector have to be perfectly aligned: the laminar beam has to be parallel to the detector pixel lines to avoid phase mixing (a given pixel line has to detect X-rays deviated within the same angular band);
- long sample-to-detector distances are needed in order to profit by the wavefront free propagation and to be able to separate the X-rays refracted at different angles;
- high brilliant X-ray beam (high X-ray flux over the beam height) is needed for short exposure time.

– If small detector pixel size is used (for achieving higher angular sensitivity), the definition of the X-ray beam by means of the upstream slit system can encounter some problems since the diffraction pattern of the slit itself could limit the beam size on the detector, and jeopardize the technique resolution and sensitivity.

– In a single acquired ROI, the refracted and scattered X-ray beam emerging from the irradiated portion of the sample is completely analyzed: the whole set of ABI images acquired at the different angular positions of the crystal analyzer are acquired in a single scan of the sample.

– With the DBA technique, the propagation and analyzing effects are combined similarly to what happens in the Hybrid phase contrast imaging.

- **Achievable angular resolution: some numbers**

As already discussed, in the ABI technique the angular resolution is determined the FWHM of the analyzer rocking curve. Some values are reported in Table 6.3 for Si (111) and Si (333) at two different energies.

	Si (111))	Si (333)
25 keV	10.50 µrad	1.96 µrad
51.5 keV	5.14 µrad	0.94 µrad

Table 6.3. Theoretical FWHM of reflectivity curves of a Si (111) and Si (333) crystal at 25 and 51.5 keV.

In the case of the DBA technique, the angular resolution is instead linked to the vertical pixel size of the detector and to the sample-to-detector distance.

Referring to Figure 6.18, the angular resolution with which the X-ray beam emerging from the specimen is sampled (and so analyzed) can be easily geometrically calculated.

Let's consider the following two experimental configurations (the first one is that used for the experimental data presented afterwards):

	case 1	case 2
sample-to-detector distance (m)	11	11
detector pixel size (µm)	46	7
angular resolution (µrad)	4.3	0.6

The obtained values for the angular resolution are of the same order of magnitude of the FWHM of Si crystals (refer to values reported in Table 6.3).

In particular, if a 7 µm pixel size array detector is used, the beam refracted and scattered inside the sample and incident on the detector can be sampled with an angular step (0.6 µrad) which is, for instance, ~17.5 times smaller than the FWHM of the Si (111) at 25 keV.

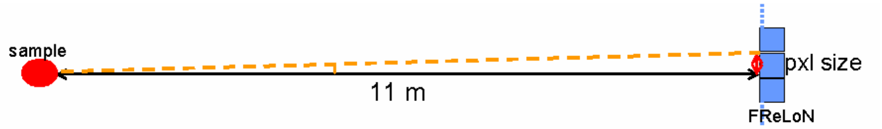

Figure 6.18. Geometrical scheme for calculating the angular resolution depending on the detector pixel size and sample-to-detector distance.

6.4.2 Detector-based analyzer imaging (DBA) experimental results and discussion

Pilot experiments on simple phase objects (plastic wire and edges patterns) have been performed for verifying the feasibility of the so-called detector-based analyzer imaging technique.

In the following, I will report the results of the study realized on fibers, which have the same characteristics of those used for the HI technique experiments (Paragraph 6.2, Table 6.1). Results are compared with those obtained by using the ABI technique on the same samples.

The experimental parameters used for the ABI and DBA acquisitions have been respectively:

ABI – monochromator and analyzer: Si (111)

– energies: 25 and 51.5 keV

– detector: FReLoN camera with a pixel size of 46 μm x 46 μm

DBA – slit system aperture ~ 50 μm

– slit system aperture ~ 50 μm

– sample-to-detector distance = 11 m

– energies: 25 and 51.5 keV

– detector: FReLoN camera with a pixel size of 46 μm x 46 μm

– ROI on the detector: 16 pixel lines

In Figure 6.19 and 6.20, images of the nylon wire of 350 μm diameter obtained with the analyzer-based imaging and the detector-based analyzer imaging technique respectively are presented. In the same figures, the related signal profiles for each image are reported.

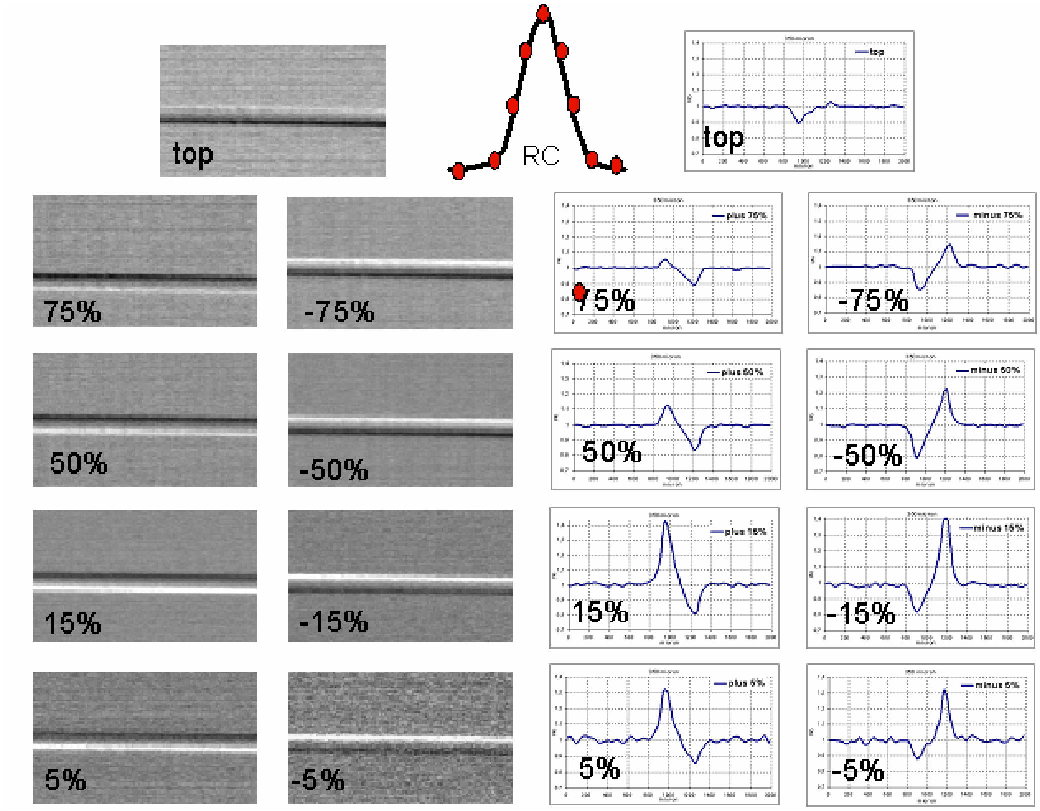

Figure 6.19. ABI images and signal profiles of a nylon fiber of 350 μm diameter acquired at 25 keV and at different angular positions of the crystal analyzer (positions indicated as percentage of the peak intensity of the crystal rocking curve).

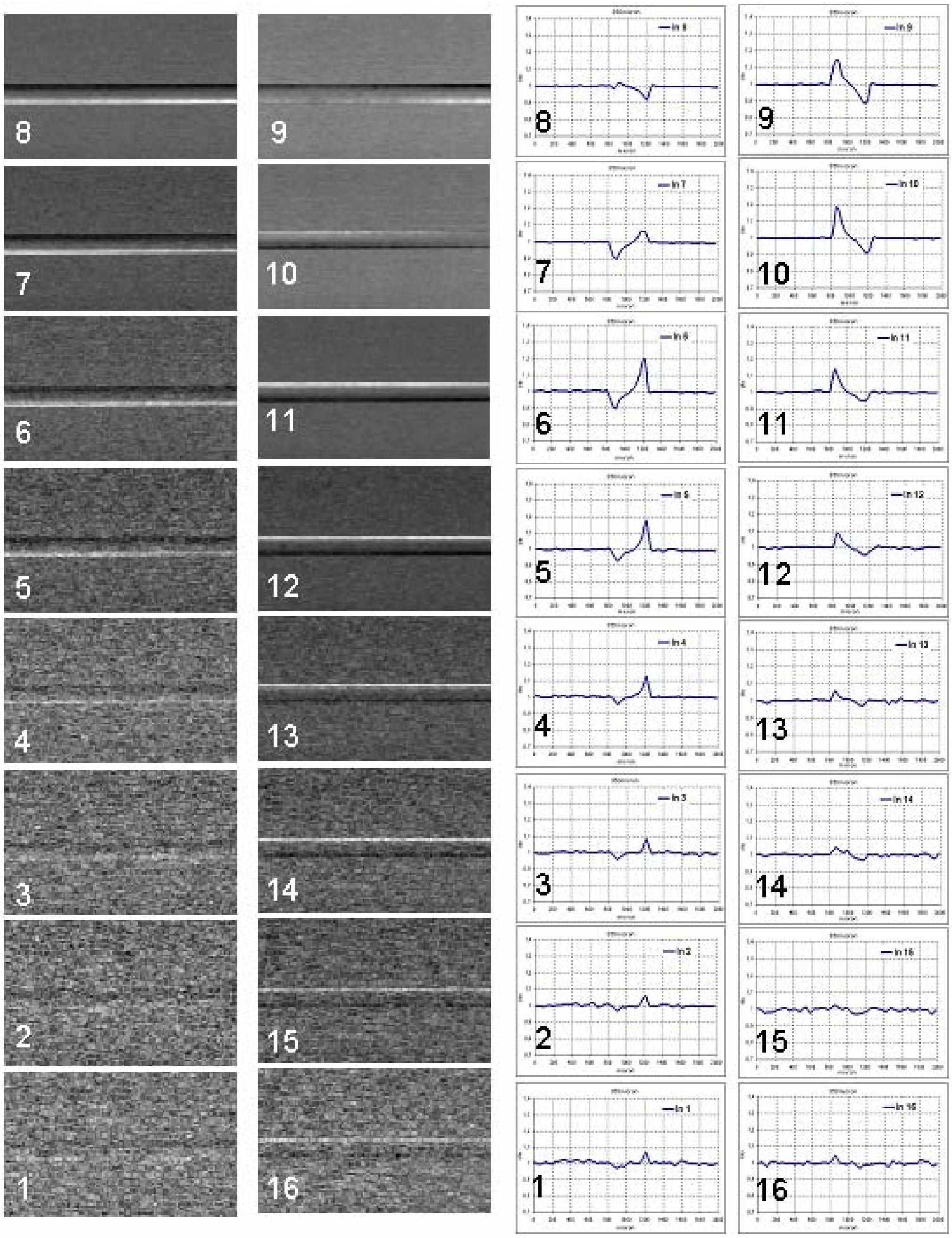

Figure 6.20. DBA images and signal profiles of a nylon fiber of 350 μm diameter acquired at 25 keV acquired in the 16 pixel lines of the acquired ROI respectively.

The quantitative analysis has been carried out by evaluating the signal-to-noise ratio (SNR) through the Eq. (6.1) with the same procedure described in Paragraph 6.2.2.

Figure 6.21 and 6.22 shows the graph of the SNR versus the angular setting of the analyzer and versus the pixel lines (expressed in angular distance from the central line set as '0' angle) respectively, for one edge of the two wires imaged with the ABI and the DBA techniques at 25 and 51.5 keV.

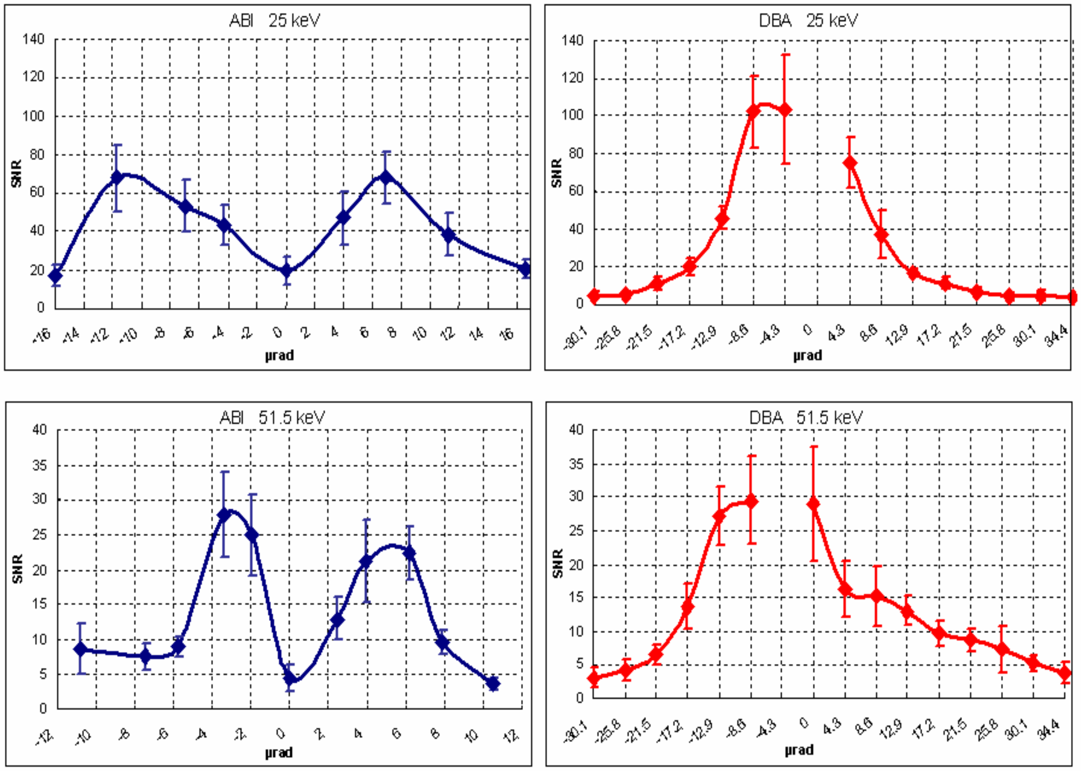

Figure 6.21. Signal-to-noise ratio values produced by an edge of the kevlar fiber (200 µm diameter) as function of the analyzer angular position for the ABI configuration (graphs on the left) and as function of the pixel line (expressed in angle from the central line) for the DBA configuration (graphs on the right). Energies: 25 and 51.5 keV.

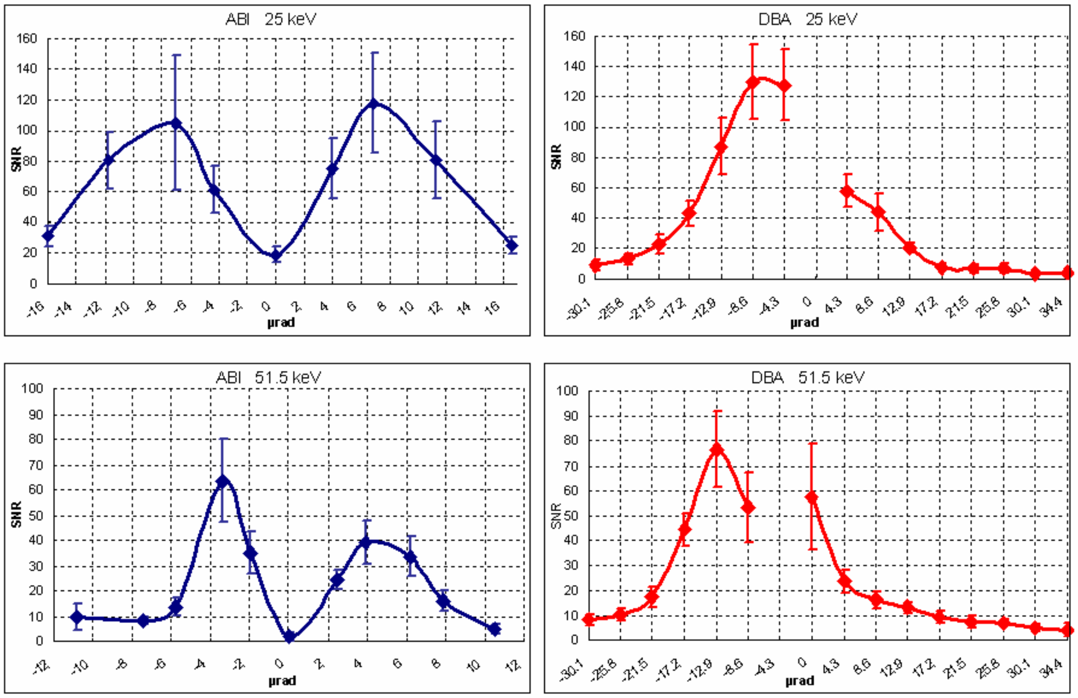

Figure 6.22. Signal-to-noise ratio values produced by an edge of the nylon fiber (350 µm diameter) as function of the analyzer angular position for the ABI configuration (graphs on the left) and as function of the pixel line (expressed in angle from the central line) for the DBA configuration (graphs on the right). Energies: 25 and 51.5 keV.

- By comparing images in Figure 6.19 and 6.20, it is clear that **the appearance of DBA images of the used wire is really similar to that one of ABI images**. By passing from one side to the other with respect to the central pixel line (aligned with the incoming beam on the sample) within the selected ROI, the **inversion of image contrast** at edges of the sample occurs as in the ABI case. The fiber profile of the DBA signal is characterized by the usual asymmetric double-peaked curve for images acquired with non-centered pixel lines similarly to profiles of the signal in the ABI slope images. In fact, as elsewhere already discussed, the highest X-ray deflections occurs at the sample edges so that the pixel lines at one side of the ROI will angularly accept X-rays refracted by one fiber edges and reject those of the other edge. This fact explains the signal increase and depletion, respectively, at the border of the sample in DBA images.
- A point to be stressed is the behaviour of the signal acquired by the **central lines** (# 9-10, corresponding to images '9' and '10' in Figure 6.20) probably due to a **mixing of the slightly different phases** of the X-rays emerging from the central part of the sample: different parts of the wire image present different contrast (black/white). This fact can be attributed either to a non perfect alignment of the detector with respect to the incoming beam or/and a non-sufficient angular resolution. For this reason, I made the choice of not reporting any value of SNR for these positions since the high variability of the signal depending on the considered part of the border of the sample.
- With reference to Figure 6.21 and 6.22, it can be highlighted the fact that, by using the DBA imaging technique, the achievable SNR values are at least as high as those obtained with the ABI technique. Even if the central point is missing, it can be inferred that, contrary to the ABI case but similarly to the HI case, the SNR remains high even around the central positions thanks, once more, to the propagation contribution (see Paragraph 6.2.2)
- The size of the ROI on the detector is in principle limited by the number of pixels of the CCD camera itself (2048 x 2048 pixels^2 in the presented case). Practically, for speeding up the acquisition/readout process, it is convenient to consider only the pixel lines illuminated on the detector by the radiation coming from the sample. This freedom in the selection of the ROI makes it possible to analyze an angular window width at will. For instance, by choosing 16 lines in the considered experimental conditions, an angular window of 60.5 μrad (from -30.1 μrad up to 34.4 μrad) cab be used (Figure 6.21 and 6.22 for the DBA case).
- Thanks to this fact, scattering at wide angles can be investigated (see images in Figure 6.20 acquired with the first and last pixel lines).

- **Limitations of the technique**

When imaging in tomographic (CT) mode, just one line per time can be acquired if the DBA technique is employed. Presently, in ABI configuration, for a given angular position of the crystal analyzer, a certain number of pixel lines are independently acquired obtaining an equal number of sinograms and therefore image slices. This procedure allows for speeding up the CT acquisition. This fact is balanced by the simultaneous recording of different scattering angles with a single image acquistion.

- **Preliminary tests of the DBA on biological samples**

In conclusion, I would like to show an example of some preliminary results obtained on a biological sample, precisely on the same big toe used for the ABI cartilage investigations presented in Chapter 5.

In Figure 6.23, a DBA radiograph of the big toe is shown and the ROI zoomed out in Figure 6.24 is indicated. The experimental parameters for these DBA acquisitions are the same of those reported at the beginning of this paragraph for the previously presented results. The only changed parameters are the energy, which is now 33 keV, and the size of the ROI of the detector, which consists here of 32 pixel lines corresponding to an angular window of ~133 μrad.

In Figure 6.24, some of the thirty two DBA images of a portion of the big toe are presented. The first and last images corresponds to angle of -68.8 μrad and 64.5 μrad respectively, therefore their contrast is given by the wide scattering produced by the sample. Because of this fact, these images are rather blurred while, moving towards images acquired with the central pixel lines, features (in particular bone trabeculae) become more and more sharp. The cartilage tissue is not visible exactly as in the ABI images. This is probably due to a non-sufficient spatial resolution and to the overlap with the thick layer of soft tissue surrounding the joint space.

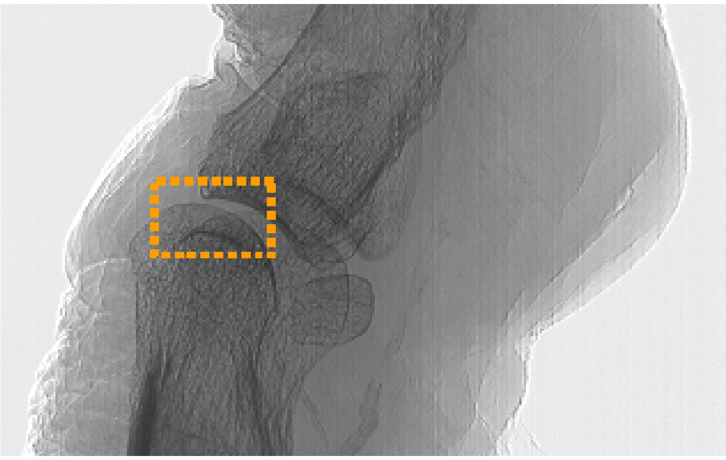

Figure 6.23. DBA radiograph of a big toe. The ROI defined by the orange box is zoomed out in Figure 6.24.

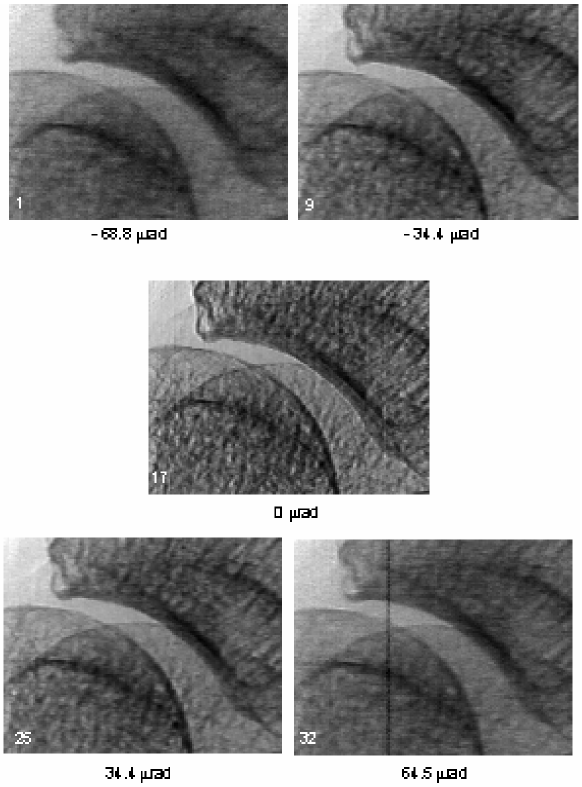

-68.8 µrad -34.4 µrad

0 µrad

34.4 µrad 64.5 µrad

Figure 6.24. DBA images of the ROI of the big toe indicated in Figure 6.23.

6.4.3 Conclusions

The results presented in this paragraph are the experimental proof of the feasibility of the so-called detector-based analyzer imaging technique here introduced. Further experimental and theoretical investigations are anyway needed for better understanding the signal and image contrast formation. The advantages in terms of less stringent optical stability requirements make this technique an interesting tool for exploiting the phase effects above all for applications where a very high resolution is not needed.

REFERENCES

A. M. Afanas'ev and V. G. Kohn (1971). "Dynamical theory of X-ray diffraction in crystals with defects." Acta Cryst. **A27**: 421-430.

A. Authier (2001). *Dynamical theory of X -ray diffraction*. New York, Oxford Press.

A. Authier and D. Simon (1968). "Application de la théorie dynamique de S. Takagi au contraste d'un défaut plan en topographie par rayons X. I. Faute d'empilement." Acta Cryst. **A 24**: 517-526.

M. Born and E. Wolf (1999). *Principles of optics: electromagnetic theory of propagation, interference and diffraction of light*. C. U. Press. Cambridge.

A. Bravin, V. Mocella, C. Ferrero, P. Coan, S. Fiedler and W. Thomlison "A wavefront propagation approach to Diffraction Imaging." In preparation.

C. A. M. Carvalho and Y. Epelboin (1993). "Simulation of X-ray traverse topographs and synchrotron Laue topographs: application of the reciprocity theorem." Acta Cryst. **A49**: 467-473.

P. Cloetens (1999). Contribution to Phase Contrast Imaging, Reconstruction and Tomography with hard Synchrotron Radiation. Principles, Implementation and Applications. Vrije Universiteit. Brussel.

P. Coan, E. Pagot, S. Fiedler, P. Cloetens, J. Baruchel and A. Bravin (2005). "Phase-contrast X-ray imaging combining free space propagation and Bragg diffraction." Journal of Synchrotron Radiation **12**: 241-245.

T. Davis (1996). "X-ray diffraction imaging using perfect crystals." Journal of X-ray Science and Technology **6**: 317-342.

Y. Epelboin, V. Mocella and A. Soyer (1999). "Optical characteristics of synchrotron sources and their influence in the simulation of X-ray topographs." Phil. Trans. R. Soc. Lond. **357**: 2731-2739.

A. L. Evans (1981). T*he evaluation of medical images*. A. H. Ltd. Bristol, Adam Hilger Ltd.

J. P. Guigay (1999). "A simple view of the spherical wave in dynamical theory." Acta Cryst. **A55**: 561-563.

J. Keyriläinen, M. Fernández and P. Suortti (2002). "Refraction contrast X-ray imaging." Nucl Instr Meth A **488**: 419-427.

V. Mocella, Y. Epelboin and J. P. Guigay (2000). "X-ray dynamical diffraction: the concept of a locally plane wave." Acta Cryst. **A56**: 308-316.

Y. I. Nesterets, T. E. Gureyev, K. M. Pavlov, D. M. Paganin and S. W. Wilkins (2006). "Combined analyser-based and propagation-based phase-contrast imaging of weak objects." Optics Communications **259**: 19-31.

E. Pagot, S. Fiedler, P. Cloetens, A. Bravin, P. Coan, K. Fezzaa, J. Baruchel and J. Härtwig (2005). "Quantitative comparison between two-phase contrast techniques: Diffraction Enhanced Imaging and Phase Propagation Imaging." Phys Med. Biol. **50**: 709-724.

K. M. Pavlov, T. E. Gureyev, D. Paganin, Y. I. Nesterets, M. J. Kitchen, K. K. W. Siu, J. E. Gillam, K. Uesugi, Y. Yagi, M. J. Morgan and R. A. Lewis (2005). "Unification of analyser-based and propagation-based X-ray phase-contrast imaging." Nucl. Instr. Meth. A **548**: 163-168.

K. M. Pavlov, T. E. Gureyev, D. Paganin, Y. I. Nesterets, M. J. Morgan and R. A. Lewis (2004). "Linear systems with slowly varying transfer functions and their application to X-ray phase-contrast imaging." J. Phys. D: Appl. Phys. **37**: 2746–2750.

S. Takagi (1969). "A Dinamical Theory of Diffraction for a Distorted Crystal." Journal of the Physical Society of Japan **26** (5).

T. Uragami (1969). "Pendellösung Fringes of X-Rays in Bragg Case." J. Phys. Soc. Jpn. **27**: 147-154.

Conclusions en français

Ce travail de Thèse a eu un double objectif: d'une part l'analyse des performances de l'imagerie en contraste de phase dans le diagnostique de l'ostéoarthrite (OA), et d'autre part, le développement théorique et expérimental des techniques de contraste de phase.
Des résultats originaux ont été obtenus dans les deux cas, permettant de répondre à certaines des questions scientifiques qui avaient motivé ce travail de recherche. Certains résultats ont déjà fait l'objet de publications dans des revues internationales.
D'autre part, les résultats présentés ici soulèvent de nouvelles questions scientifiques, qui pourraient être le point de départ pour d'autres investigations et développements.
De par l'architecture de ce travail, les conclusions de la Thèse seront présentées en deux parties distinctes.

▪ Technique d'imagerie basée sur un cristal analyseur: application à l'étude de l'ostéoarthrite et des implants osseux.

La qualité d'image offerte par quasiment toutes les techniques conventionnelles d'imagerie médicale pour l'étude des cartilages osseux est relativement médiocre. Le développement de nouvelles techniques, qui permettraient de visualiser les modifications du cartilage avant d'atteindre des dommages irréversibles, est ainsi particulièrement souhaitable.
La nécessité de développer une technique d'imagerie à visée diagnostique et de suivi, qui permettrait la détection précoce de l'ostéoarthrite et l'évaluation de l'intégration osseuse des implants est discutée dans le Chapitre 1, et ensuite démontrée par une étude comparative dans le Chapitre 5.

La radiographie X reste la technique, utilisée en clinique, qui présente la meilleure résolution spatiale et qui est la plus utilisée pour détecter des anomalies articulaires. Cette technique n'est cependant pas suffisamment sensible dans certains cas, de par ses limitations intrinsèques. Ce problème est abordé dans le Chapitre 1 et présenté dans le Paragraphe 5.5. En effet, le tissu cartilagineux lui même, ses défauts ou anomalies structurelles au premier stade de développement de la maladie sont invisibles sur des radiographies ou tomographies X conventionnelles.

Dans ce travail, la faisabilité et les performances potentielles de l'imagerie basée sur un cristal analyseur (ABI) ont été démontrées dans le cadre d'une étude comparative avec des techniques conventionnelles; ces résultats corroborent les résultats préliminaires obtenus par Mollenhauer *et al.* (Mollenhauer, Aurich *et al.*, 2002; Muehleman, Chapman *et al.*, 2003).

Nous avons étudié un assortiment varié d'échantillons en utilisant différentes méthodes d'acquisition de données et de rendus visuels. En particulier, nous avons réalisé :

1. Des **études *in-vitro*** utilisant la technique **ABI en mode radiographique ou tomographique** de différents échantillons d'origine humaine (hanche, articulations du gros orteil et de la cheville) et des implants de brebis.
2. Un **rendu tri-dimensionnel** (réalisé par segmentation manuelle et empilage des coupes tomographiques ABI.) d'une articulation et d'un implant de brebis.
3. **La comparaison de la technique ABI avec les techniques conventionnelles d'imagerie** (radiographie, tomographie (CT), ultrason (UI), imagerie par résonance magnétique (IRM) et histologie).
4. Des **tests préliminaires *in-vivo*** sur des cochons d'Inde (un modèle animal d'ostéoarthrite bien établi).
5. Des **investigations radio-biologiques des effets de la dose** de rayonnement sur les cellules du cartilage.

¬ Les résultats présentés dans le Chapitre 5 démontrent clairement le grand potentiel de la technique ABI pour ce type d'applications et sa capacité à **détecter les anormalités cartilagineuses d'une façon non invasive**, tout particulièrement lors des **stades initiaux des maladies dégénératives des articulations** (OA) ou tôt dans leur développement.

De toutes les techniques comparées, l'ABI procure les meilleurs contraste et résolution d'image permettant de voir l'architecture du tissu structural avec le moins d'artefacts possible. La CT conventionnelle ne permet pas de visualiser les couches externes des cartilages (les plus à même d'être endommagés) et de ce fait sous estime systématiquement l'épaisseur des cartilages (mesurée à l'histologie, pris comme standard de référence); l'IRM nécessite un temps d'exposition très long pour obtenir des images de qualité comparable à celles obtenue avec l'ABI. Il a été démontré que l'utilisation des ultrasons est limitée, en particulier à cause de la géométrie complexe des articulations. Le cartilage voit ses propriétés d'absorption changer (du fait de sa contenance en eau et en graisse) au fur et à mesure de l'approche de l'articulation, avec une densité qui devient proche de celle du liquide des cavités articulaires. Ceci entraîne une visualisation ambiguë des limites des cartilages en imagerie X, CT et IRM conventionnelles. L'ABI, au contraire, est plus sensitif pour les propriétés de réfraction des tissus et il est capable de mettre en évidence l'interface entre deux matériaux. En d'autre mots, la technique ABI génère les images les plus poches de la réalité tant anatomique que de la structure histologique des tissus (Majumdar, Sema-Issever *et al.*, 2004).

Même si les bases physiques pour la formation de l'image présentent de grandes différences avec les autres techniques utilisées couramment, l'interprétation des images et le diagnostic restent généralement aisés. En fait, les paramètres structurels et anatomiques diffèrent très peu dans la population et le diagnostic est principalement basé sur l'analyse des bords externes du cartilage et des interfaces cartilage-os ou cartilage-liquide synovial. Toutes ces structures sont visualisées correctement grâce à la technique ABI. C'est aussi un aspect important de l'ABI appliqué à l'étude des cartilages, car l'interprétation radiologique des images ABI n'est pas toujours simple dans les autres applications (Keyriläinen, Fernández *et al.*, 2005).

Cette analyse comparative est l'un des aspects le plus original de ce travail qui a été rendu possible grâce à la synergie des compétences spécifiques complémentaires des deux équipes impliquées: celle de ID17 (ESRF) et l'équipe de recherche du Département d'Orthopédie de l'Université de Jena (Allemagne).

¬ Dans cette thèse, il a aussi été démontré que **la technique d'imagerie ABI peut être utilisée comme méthode non destructive pour évaluer la qualité de la repousse osseuse en présence d'implant** et ceci avec davantage de sensibilité que la radiographie classique. **De plus, des coupes CT ABI d'un implant en métal ont été faites afin de valider la faisabilité de cette technique qui pourrait devenir une importante alternative non invasive à l'examen histologique.**

L'ABI permet la visualisation de deux caractéristiques majeures de la bonne incorporation de l'implant dans le tissu osseux: la réorientation des structures trabeculaires ainsi que la jonction de l'os sur la surface de l'implant. Des avancées expérimentales en imagerie X des microstructures osseuses ont récemment été publiées. Elles incluent la micro focalisation et la technologie synchrotron (Bernhardt, Scharnweber *et al.*, 2004). La plupart de ces techniques dépendent des propriétés optiques des faisceaux polychromatiques microfocalisés, prévu à la fois pour la haute résolution et le grossissement de caractéristiques de l'objet. Cependant, chacune de ces méthodes est basée sur l'absorption des rayons X comme principal mode de détection. Les tissus peu absorbants ne sont pas, ou insuffisamment, visibles. De plus, des artefacts typiques, tels que le durcissement de faisceau ou le flou des images dû à la diffusion des rayons X (Brooks and Di Chiro, 1976; Joseph and Spital, 1982), perturbent les systèmes polychromatiques microfocalisés.

Une des questions clé concernant la correcte intégration implant/os, ne peut cependant pas être résolue par une géométrie microfocalisée puisqu'elle nécessite la visualisation de la structure de la surface de contact, caractéristique non observable par radiographie “conventionnelle”. Ici, l’ABI permet une mesure indirecte grâce à cette propriété inhérente de générer du signal par les bords. Il a été montré que les images par réfraction sont celles qui apportent le plus d’informations sur la repousse osseuse grâce à leur capacité de détecter les interfaces tissus-implants. Comme les implants ont des surfaces de contact élaborés, en particulier lorsqu’ils sont recouverts de minéraux comme l’hydroxyapatite, le signal initial de réfraction sur ces bords est particulièrement intense. (Paragraphe 5.5). Toute interaction de l’os avec ces structures surfaciques 3D atténuera le signal, et permettra ainsi une mesure indirecte de l’intégration de l’implant. Une comparaison entre histologie et images ABI, comme celle présentée dans cette étude, suggère que les structures minéralisées influencent davantage le signal réfracté que les tissus mous.

¬ **Les reconstructions 3D de l’articulation de gros orteil et d’un implant de brebis** présentées dans le Paragraphe 5.6 sont également originales et pertinentes d’un point de vu diagnostic.
Par segmentation manuelle, il a été possible de séparer le cartilage de toute la structure articulaire, permettant l’évaluation de son état. Dans le cas de l’implant métallique, le rendu 3D est particulièrement intéressant car il permet de visualiser la repousse osseuse intégrée avec l’implant et de séparer l’os cortical des tissus mous. Ce résultat pourrait être utile par exemple, pour évaluer prochainement *in vivo* l’efficacité des facteurs de repousse osseuse.

¬ **Les toute premières expériences *in vivo* réalisées sur modèle animal** (aucun exemple décrit à ce jour dans la littérature) ont donné des résultats encourageants. Les images ABI de hanche et genou acquises chez des cobayes montrent l’existence d’OA (par exemple des ostéophytes) précoces. Certaines questions techniques, concernant notamment le positionnement ou l’anesthésie de l’animal, ont besoin d’être résolues; cependant les résultats préliminaires sont prometteurs et encouragent d’autres investigations. De plus, grâce à la dose de radiation délivrée qui est significativement plus faible qu’en imagerie X conventionnelle ou en micro CT, l’ABI *in vivo* pourrait aussi permettre, chez l’animal, de suivre longitudinalement le bon contact os/métal lors de la repousse osseuse. Cela permettrait de mieux comprendre le remodelage de l’os au niveau de l’implant en plus de pouvoir suivre le développement de l'ostéarthrite.

¬ Une série d’**expériences en radiobiologie** a été réalisée afin d’étudier les effets biologiques des radiations (et par conséquent la possible toxicité de la technique ABI) dans les chondrocytes humains (principales cellules des tissus cartilagineux).

Les observations expérimentales ont prouvé une plus faible radiosensibilité des chondrocytes en ce qui concerne les fibroblastes. L'impact des radiations sur le phénotype cellulaire, pour les deux lignées cellulaires testées, ne semble pas pertinent, puisqu'il reste *inférieur à 5%*; de plus, les effets observés peuvent être attribués à d'autres phénomènes comme par exemple la sénescence cellulaire ou la synthèse de l'ADN avec apparition du gonflement du noyau (Arp, 1998). Etant donné les résultats obtenus, il est possible de conclure que les doses délivrées, pendant l'imagerie AB en utilisant la lumière synchrotron, ne sont a priori pas toxiques pour l'application spécifique qui consiste à étudier, sur modèle animal, les maladies des cartilages.

▪ Développement d'une technique d'imagerie utilisant un cristal analyseur

Les deux objectifs suivants, visant à développer les techniques de contraste de phase, ont été atteints (Chapitre 6):

1. il a été démontré de façon expérimentale, et ce pour la première fois, que les techniques sensibles au contraste de phase, en utilisant un cristal analyseur (ABI) et la propagation du signal ("Propagation-based imaging", PBI), peuvent être combinées en vue d'obtention d'images apportant de nouvelles informations ("**Hybrid imaging**" (HI));
2. un **nouveau dispositif expérimental simplifié** a été et testé, afin de produire des images dont les propriétés sont similaires à celles obtenues par les techniques ABI ou HI

Finalement, la théorie relative aux deux techniques ABI et HI a été étudiée **en utilisant un programme de simulation innovant, basée sur l'utilisation de la théorie ondulatoire.** Ce programme a permis de reproduire de façon fiable les résultats expérimentaux.

¬ Les images de propagation (PBI) et les images obtenues en utilisant un cristal analyseur (ABI), à partir d'un rayonnement synchrotron ou d'une source de rayons X de laboratoire, sont très utilisées aujourd'hui.

Chacune des deux techniques présente des avantages et inconvénients relatifs: la technique PBI peut être mise en œuvre de façon simple, et cette technique est sensible aux variations de phase dans toutes les directions perpendiculaires à l'axe optique; la technique ABI permet d'obtenir un meilleur contraste et une meilleure élimination du rayonnement diffusé mais cette technique n'est sensible qu'au déphasage apparaissant dans le plan de diffraction. Une comparaison détaillée de ces deux techniques a été publiée (Pagot, Fiedler *et al.*, 2005).

Ces deux techniques d'imagerie par contraste de phase ont été traitées (de façon théorique et expérimentale) séparément dans la littérature, bien qu'issues d'une origine commune, basée sur le déphasage de l'onde qui passe à travers la matière.

Ce travail de Thèse (Chapitre 6) montre, de façon expérimentale, que l'utilisation d'une source de rayons X cohérente couplée à un dispositif expérimental combinant propagation et diffraction (par l'utilisation d'un cristal analyseur), permet d'obtenir un nouveau type d'image, combinant les avantages des deux méthodes.

Des images de fibres de polymères simples obtenues en utilisant cette technique hybride ont été analysées en terme de rapport signal sur bruit et comparées à celles obtenues en utilisant séparément les deux techniques. Les images hybrides présentent une valeur constante de rapport signal sur bruit sur une fourchette angulaire de l'ordre de la FWHM du balayage en angle du cristal analyseur (courbe de diffraction, ou "rocking curve").

Cette faible dépendance de la position angulaire du cristal analyseur réduit les contraintes en terme d'alignement optique et de stabilité du cristal, ce qui représente l'un des points les plus critiques de la technique ABI (Coan, Pagot *et al.*, 2005).

¬ Une méthode simple et innovante pour analyser les radiations réfractées et diffusées a été proposée au Chapitre 6. Au lieu d'utiliser un cristal parfait dont la sensibilité est donnée par la largeur à mi-hauteur de sa courbe de diffraction, la rangée de pixels du détecteur a été utilisé comme un système de fentes. Pour que cette technique marche (qui a été appelée "Detector-Based Analyser imaging", DBA), il faut que le faisceau de rayon X soit aussi haut que la taille verticale d'un pixel. Plus précisément, chaque rangée de pixels sur la caméra CCD, qui peut être lue et stockée de manière indépendante, agit comme une fente verticale dont l'acceptance angulaire correspond à la taille du pixel.

Dans le cadre de cette technique DBA, la résolution angulaire est liée à la taille verticale du pixel du détecteur et à la distance échantillon-détecteur.

Des expériences pilotes sur des objets de phase simples (fil en plastique, coins) ont été réalisées et les données ont été analysées de manière quantitative en terme de rapport signal sur bruit.

D'après les derniers résultats, il semble que les images DBA montrent de fortes ressemblances avec les images acquises avec la technique ABI. De plus, le rapport signal sur bruit obtenu en DBA est au moins aussi bon que celui obtenu en ABI.

Cette technique, qui demande plus de développements expérimentaux ainsi qu'une formulation théorique, pourrait permettre de contourner les fortes limitations en termes de stabilité optique que l'on a avec les dispositifs ABI.

¬ Pour étudier et optimiser la technique ABI, une approche d'optique ondulatoire, qui simule le dispositif monochromateur-analyseur, a été développée en géométrie Bragg. Ce travail est le fruit d'une collaboration entre le groupe SciSoft de l'ESRF et ID17. Le code appelé DEIWAVE prend en compte aussi bien la propagation dans l'espace libre que la diffraction par le cristal analyseur, ce qui permet de comprendre non seulement la technique ABI conventionnelle mais aussi les caractéristiques du signal HI. La polychromaticité de l'onde incidente sur le monochromateur est prise en compte en considérant un ensemble de points source incohérents le long de la surface du cristal.

Les résultats préliminaires de cette nouvelle approche sont en parfait accord avec les données expérimentales déjà acquises. Les prochains objectifs qui peuvent être atteints avec ce code sont l'optimisation des paramètres du système analyseur (réflexion du cristal et alignement par rapport à le monochromateur principal) pour des caractéristiques données de l'échantillon (forme, composition chimique, homogénéité,…) et la parfaite compréhension des paramètres gouvernant la formation des images en technique HI.

¬ L'évaluation détaillée des performances de la caméra FReLoN munie de son optique à guide de lumière a été une part essentielle et complémentaire de ce travail. Les résultats sont présentés et commentés au Chapitre 4. La caméra spécialement développée à l'ESRF pour les applications médicales a été principalement utilisée pendant ce travail de Thèse. Les propriétés du détecteur (linéarité, résolution spatiale, bruit spectral et efficacité) jouent un rôle clé dans la qualité des images et sont donc une base d'informations pour interpréter les résultats présentés aux Chapitres 5 et 6. De plus, ces paramètres mis avec les possibilités particulières de lecture des signaux de la caméra FReLoN sont à la base des développements de la technique d'images DBA présentée au Chapitre 6. Pour évaluer la qualité des images, des protocoles d'analyse innovants ont été proposés pour adapter les protocoles standards de rayons X à un flux laminaire de lumière synchrotron (Coan, Peterzol et al., 2006).

Les performances de la caméra FReLoN ont aussi été comparées à celles des détecteurs similaires que l'on trouve dans la littérature. Cette comparaison montre que la caméra est très bien positionnée dans le monde de l'imagerie rayon X. Aucun des détecteurs ne dépasse la FReLoN dans toutes ses propriétés simultanément. Ceci est dû au compromis effectué sur le dispositif pour s'ajuster aux besoins de l'imagerie médicale auprès d'un synchrotron. De plus la caméra offre une acquisition de données adaptée à un faisceau laminaire. Très vraisemblablement ses performances en termes d'efficacité vont être améliorées pour les nouvelles versions actuellement en développement.

Conclusions

A twofold objective has guided this Thesis work: on the one hand the assessment of the performances offered by the analyser-based X-ray phase contrast imaging in osteoarthritis (OA) diagnostics and, on the other one, the theoretical and experimental development of the phase contrast techniques.

Original results have been obtained in both these two subjects (a part of them already published in international journals) allowing addressing some of the scientific questions motivating this Thesis work. Besides, results here presented, also open new stimulating scientific questions that could be the starting point of further investigations and future developments.

Given the dual nature of this work, the conclusions of this Thesis will be addressed in two separate paragraphs.

▪ Analyzer-based imaging technique applied to osteoarthritis and implant investigations

Poor imaging quality in practically all conventional medical imaging technologies with respect to articular cartilage calls for the development of new techniques that are sensitive to stages preceding the point of irreversible damage of the cartilage tissue.

As discussed in Chapter 1 and also proven by the comparative study presented in Chapter 5, there is an important need of a high resolution, non-invasive diagnostic and monitoring technique allowing for **the early detection and follow-up of OA** and **the implant/bone healing assessment.**

Plain X-ray radiography is still the clinical technique having the highest resolution and currently the most widely used to detect joint abnormalities. But, as discussed in the Chapter 1 and presented in the Paragraph 5.5, in some cases it is not sufficiently sensitive because of its intrinsic limitations. Indeed the cartilage tissue itself and focal cartilage defects or structural abnormalities of early stages of the degenerative joint disease are invisible on conventional radiographs or X-ray computed tomography.

In this work, the feasibility and the potential of the analyzer-based imaging (ABI) has been demonstrated in a comparative study with the conventional techniques; these results reinforce preliminary evidences shown in literature by Mollenhauer *et al* (Mollenhauer, Aurich *et al.*, 2002; Muehleman, Chapman *et al.*, 2003).

Efforts have been addressed to investigate a certain assortment of samples by using a variety of data acquisition/rendering modalities. In particular, examinations included:

1. ***In-vitro* studies** using the ABI technique **in projection** and **computed tomography** modes of several human samples (hip, big toe and ankle articular joints) and sheep implants.
2. **Three dimensional rendering (**performed by a manual segmentation and combination of tomographic ABI slices) of a joint and sheep implant.
3. **Comparison of the ABI with conventional imaging techniques** (radiography, computed tomography (CT), ultrasound (UI), magnetic resonance (MRI) and histology).
4. **Pilot *in-vivo* ABI** tests on the guinea pigs (a widely accepted animal model for OA).
5. **Radiobiological investigation of dose effects** on cartilage cells.

¬ The results presented in the Chapter 5 clearly demonstrate the high potential of the ABI technique for this kind of application and its ability of **non-invasively detecting cartilage abnormalities**, especially **in the initial stages of degenerative joint disease** (OA) or early in its progression.

Of all compared techniques, ABI provided highest image contrast and resolution revealing the structural tissue architecture with the least amount of false signals. Conventional CT is unable to visualize the outer cartilage layers (the most prone to be damaged) and therefore systematically underestimates the cartilage thickness (measured on the histology, taken as gold standard); MRI needs a very long exposure time to achieve images of quality comparable to ABI. The application of ultrasound has been shown to be limited in particular by the complex joint geometry. Cartilage changes its absorptive properties (due to water and fat content) gradually towards the joint space, with density coming close to that of the joint gap fluid, resulting in ambiguous visualization of cartilage borders in conventional X-ray, CT and MR imaging. ABI, in contrast, is specifically sensitive on the refraction properties of the tissues and it is able to enhance material edges. In other words, the ABI technique generates images that most closely resemble the appearance of anatomical and histological tissue structures (Majumdar, Sema-Issever *et al.*, 2004).

Even though the physical basis for the image formation differs drastically from the otherwise commonly used techniques, image interpretation and diagnosis remains generally easy. In fact, structural and anatomical parameters do not substantially differ in the population and diagnosis is mainly based on analysis of cartilage outer borders and interfaces cartilage-bone or cartilage-synovial fluids. All these features are well visualized by the ABI technique. This is also an important aspect of ABI applied to cartilage studies, because the radiological interpretation of the ABI images is not always straightforward in other applications (Keyriläinen, Fernández *et al.*, 2005).

This comparative analysis is one the most peculiar and original aspects of this work, which has been made possible thanks to the synergy of complementary competences specific of the two involved teams, the one from ID17 (ESRF) and the research team of the Department of Orthopaedics of the University of Jena (Germany).

¬ In this Thesis, it has been also demonstrated that ABI can be used as **a destruction-free modality for evaluating the quality of ingrowth of bone into metal implants** with a higher sensitivity than that of conventional radiography. **In addition, the feasibility of ABI CT of metal implant has been proven by producing ABI slices, which could be able to become in the future an important non-invasive alternative to the histological examination.**

ABI allowed the visualization of two major signatures of proper implant ingrowth in the undestructed sample: the re-orientation of trabecular structures and thereafter the integration of bone onto the implant surface. Advanced experimental X-ray imaging for bone microstructures has been recently published. They include microfocus and synchrotron technology (Bernhardt, Scharnweber *et al.*, 2004). Most of these studies relied on the optical properties of polychromatic microfocus beams, allowing for both high resolution and magnification of features in the objects. However, each of these methods depends on X-ray absorption as the principle mode of detection. Weakly absorbing tissue is not, or is only insufficiently, visible. In addition, typical artefacts such as beam hardening or image blurs due to X-ray scattering (Brooks and Di Chiro, 1976; Joseph and Spital, 1982) also plague polychromatic microfocus set-ups.

One of the key questions concerning the extent of bone/implant integration, however, cannot be answered by microfocus geometry since it requires visualization of the integrated surface structure, a feat not achievable by ‘conventional’ radiography. Here ABI provides an indirect measure because of its inherent property to generate particular signals from edges. It has been found that the refraction images provided the greatest level of information concerning bone ingrowth due to their ability to detect edges (tissue-implant interfaces). Since implants have elaborate edges, in particular when coated with minerals such as hydroxyapatite, the initial X-ray refraction signal from those edges is particularly intense (Paragraph 5.5). Any ingrowth of bone into these three-dimensional edge structures will weaken the signal, thus providing an indirect measure of implant integration. A comparison of the histology with ABI images, as shown in the present study, suggests that the refraction signal is more likely determined by mineralized rather than soft tissue structures.

¬ **The three dimensional reconstruction of the big toe articulation and of a sheep implant** presented in the Paragraph 5.6 is also original and diagnostically relevant.

By manual segmentation, it was possible to separate the cartilage from the entire structure of the articular joint allowing the evaluation of it status. In the case of the metal implant, 3D rendering is particularly interesting since it permitted to visualize the bone ingrowth into the implant and to discriminate between cortical bone and softer tissue. This result could be useful, for instance, for future in-vivo evaluation of the effectiveness of ingrowth factors.

¬ The pilot ***in-vivo* experiments on a animal model** (never reported before in the literature) has produced encouraging results. ABI projection images of the hip and knee of guinea pigs have been acquired showing signs of early OA (e.g. osteophytes). Despite some technical questions to be solved concerning the animal positioning and anaesthesia, the preliminary outcomes are promising and promote further investigations. Moreover, thanks to the significantly lower delivered radiation dose than for conventional X-ray imaging or micro-CT, *in-vivo* ABI could also allow to longitudinally follow the bone/metal ingrowth in individual animals and, thus, to generate more precise insights into bone remodelling at implant sites besides following up the osteoarthritis development.

¬ A campaign of **radiobiological experiments** has been performed **in order to study the biological effects of the radiation** (and therefore the possible toxicity of the AB imaging) in human chondrocytes (principle cells of the cartilage tissue).

The experimental observations have also demonstrated a lower radiosensitivity of the chondrocytes with respect to the fibroblasts. The radiation impact on cellular phenotype, for the two tested cell lines, does not seem to be relevant, since it is *less than 5%*; moreover, the observed effects may even be attributed to other phenomena like cell senescence or DNA synthesis in which a nuclear inflation appears, for instance (Karp, 1998). According to the obtained data, it is possible to conclude that doses delivered during AB imaging, using synchrotron light, do not seem, a priori, toxic for the specific application concerning the joint cartilage diseases investigation in animal models.

- **Development of the analyzer-based imaging technique**

As part of the development of the phase contrast techniques, two objectives have been reached (Chapter 6):

1. it was experimentally demonstrated for the first time that the ABI and the propagation based imaging (PBI) can be combined to create images with original features (**Hybrid imaging**, HI);
2. a **new simplified set-up** has been proposed and experimentally tested being capable to produce images with properties similar to those obtained with the ABI technique or HI.

Finally, both the ABI and the HI have been theoretical studied with an innovative, **wave-based simulation program (DEIWAVE)**, which was able to correctly reproduce the experimental results.

¬ The propagation-based imaging (PBI) and the analyzer-based imaging (ABI) have become particularly popular using both synchrotron radiation and laboratory X-ray sources.

Each of the two techniques has its relative advantages and disadvantages: PBI is simpler to be implemented and is sensitive to phase variations in any direction orthogonal to the optical axis; ABI can produce stronger image contrast and better scatter rejection but it is sensitive to phase shifts occurring only in the diffraction plane. A detailed comparison of the two phase contrast imaging modalities can be found in (Pagot, Fiedler *et al.*, 2005).

Despite their common origin (wave phase shifts), phase contrast imaging techniques have been theoretically and experimentally treated separately in the literature.

As part of this Thesis work (Chapter 6), **it has been experimentally shown that by using a coherent X-ray beam and choosing an appropriate set-up that combines propagation and diffraction by a crystal-analyzer, the resulting images exhibit original features, which combine some advantages of the two methods.**

Images of simple polymer fibers obtained with this hybrid method have been analyzed in terms of SNR and compared with the patterns produced independently by the two distinct techniques. Hybrid images present an almost constant value of the SNR over an angular range of the order of the FWHM of the rocking curve of the crystal analyzer.

This **weak dependence on the angular positioning of the analyzer reduces the constraints in terms of optical alignment and stability of the crystal**, which is one of the critical issues of the AB imaging technique (Coan, Pagot *et al.*, 2005).

¬ In the Chapter 6 it has been proposed an innovative and simplified method to analyze the radiation refracted and scattered inside the sample. Instead of using a perfect crystal whose sensitivity is given by the FWHM of its rocking curve, detector pixel lines have been used like a slit system. The basic requirement for this technique, which has been called Detector based analyser imaging (DBA), is that the X-ray beam is as high as the vertical pixel size of the array detector. Precisely, each line of pixels of the CCD array, which can be read and stored independentely, acts as a slit system whose angular acceptance is given by the vertical pixel size of the camera.

In the case of the DBA technique, the angular resolution is linked to the vertical pixel size of the detector and to the sample-to-detector distance.

Pioneering experiments on simple phase objects (plastic wire and edges patterns) have been performed and results have been quantitatively analysed in terms of the signal-to-noise ratio.

In the results achieved so far, it appears that DBA images show strong similarities with the images acquired with the ABI technique. In addition, in DBA, the achieved SNR values are at least as high as those obtained with the ABI technique.

This technique, which needs further experimental development together with a detailed theoretical formulation, could overcome the severe limitations in terms of optics stability presently encountered with the ABI set-ups.

¬ In order to study and optimize the ABI technique, an advanced wave-optical approach for simulating a monochromator-analyzer set-up in Bragg geometry has been developed. This work is the fruit of a collaboration between the ESRF SciSoft group and ID17.

The code, named DEIWAVE, takes into account both the free-space propagation and the diffraction from an analyzer crystal allowing investigating not only the conventional ABI but also the features of the HI signal. The polychromaticity of the incident wave on the monochromator is accounted by considering a distribution of incoherent point sources along the surface of the crystal.

The preliminary results of this new approach show an excellent agreement with the experimental data compared so far. Next objectives, which can be reached with this powerful code, include: the optimization of the parameters of the analyzing system (crystal reflection and alignment versus the main monochromator) for given sample properties (shape, chemical composition, homogeneity….); the full understanding of the parameters governing the image formation in the HI technique.

- As a complementary but essential part of this work, the detailed evaluation of the image performances of the taper optics FReLoN camera has been assessed. Results are presented and discussed in Chapter 4. The camera, developed at the ESRF specifically for medical applications, represents the principal detector used for the data acquisition in this Thesis work. The detector parameters (like the linearity, the spatial resolution, the noise spectrum and the efficiency) play a key role in the image quality and therefore constitute important background information to fully interpret the results shown in the Chapters 5 and 6. In addition, these parameters, together with the peculiar possibilities offered by the signal readout of the FReLoN camera, are at the basis of the developments of the DBA imaging technique presented in the Chapter 6. For the assessment of the image performances, innovative analysis protocols have been proposed to adapt to a laminar beam (synchrotron light) the standard protocols used for area X-ray beams (Coan, Peterzol et al., 2006).

The performances of the FReLoN camera have been also compared to those of a selected number of detectors presented in the literature. This comparison reveals that the camera is very well positioned in the X-ray imaging detector world: no one of the compared detectors exceeds the FReLoN camera in all parameters simultaneously. This fact is the outcome of the compromise made in the detector layout to fit with the SR medical imaging needs. In addition, the camera offers the advantage of data acquisition modes specifically tailored to a SR laminar beam. Very likely, its performances will be improved even further, in terms of efficiency, in the newest version currently under development.

REFERENCES

R. Bernhardt, D. Scharnweber, B. Müller, P. Thurner, H. Schliephake, P. Wyss, F. Beckmann, J. Goebbels and H. Worch (2004). "Comparison of microfus- and synchrotron X-ray tomography for the analysis of osteointegration around Ti6Al4V-implants." Eur. Cell Mater. **7**: 42–51.

R. A. Brooks and G. Di Chiro (1976). "Beam hardening in X-ray reconstructive tomography." Phys Rev Lett **21**: 390-398.

P. Coan, E. Pagot, S. Fiedler, P. Cloetens, J. Baruchel and A. Bravin (2005). "Phase-contrast X-ray imaging combining free space propagation and Bragg diffraction." Journal of Synchrotron Radiation **12**: 241-245.

P. Coan, A. Peterzol, S. Fiedler, C. Ponchut, J. C. Labiche and A. Bravin (2006). "Evaluation of imaging performance of a taper optics CCD ;FReLoN' camera designed for medical imaging." J Synchrotron Radiat **13**: 260-270.

P. M. Joseph and R. D. Spital (1982). "The effects of scatter in X-ray computed tomography." Med. Phys. **9**: 464–72.

G. Karp (1998). *Cell & Molecular Biology - Concepts & Experiments* Tr - Second Edition, John Wiley & Sons Inc.

J. Keyriläinen, M. Fernández, S. Fiedler, A. Bravin, M. L. Karjalainen-Lindsberg, P. Virkkunen, E. M. Elo, M. Tenhunen, P. Suortti and W. Thomlinson (2005). "Visualisation of calcifications and thin collagen strands in human breast tumour specimens by the diffraction-enhanced imaging technique: a comparison with conventional mammography and histology." European Journal of Radiology **53**: 226-237.

S. Majumdar, A. Sema-Issever, A. Burghardt, J. Lotz, F. Arfelli, L. Rigon, G. Heitner and R. H. Menk (2004). "Diffraction enhanced imaging of articular cartilage and comparison with micro computed tomography of the underlying bone structure." European Radiology **14**: 1440-1448.

J. Mollenhauer, M. E. Aurich, Z. Zhong, C. Muehleman, A. A. Cole, M. Hasnah, O. Oltulu, K. E. Kuettner, A. Margulis and L. D. Chapman (2002). "Diffraction-enhanced X-ray imaging of articular cartilage." Osteoarthritis and cartilage **10**: 163-171.

C. Muehleman, L. D. Chapman, K. E. Kuettner, J. Rieff, J. A. Mollenhauer, K. Masuda and Z. Zhong (2003). "Radiography of rabbit articular cartilage with diffraction-enhanced imaging." The Anatomical record **272A**: 392-397.

E. Pagot, S. Fiedler, P. Cloetens, A. Bravin, P. Coan, K. Fezzaa, J. Baruchel and J. Härtwig (2005). "Quantitative comparison between two-phase contrast techniques: Diffraction Enhanced Imaging and Phase Propagation Imaging." Phys Med. Biol. **50**: 709-724.

Appendix 1

Basics of the dynamical diffraction theory of crystals

Contents

Diffraction from crystals is one of the primary means for controlling the divergence, spectral content and size of X-ray beams. In phase sensitive imaging techniques, crystals have an essential role as monochromators representing, for instance, the principal component of both propagation-based imaging (PBI) and analyzer-based imaging (ABI) set-ups.

Moreover, in the ABI case, a perfect crystal, acting as analyzer, is used to form the X-ray image (see Chapter 2).

It is clear, therefore, that the optical properties of the diffracting crystals have a dramatic effect on the image contrast and are crucial for coherent imaging.

Some basic results of the X-ray diffraction dynamical theory from perfect crystals are here presented. For more details, the reader can refer to (von Laue, 1931; Zachariasen, 1945; James, 1965; Authier, 2001).

A1.1 Diffraction of X-rays by single crystals

A1.1.1 General remarks

The X-ray diffraction from the different types of crystals which can be used for monochromatizing and/or analyzing an X-ray beam (perfect crystals, mosaic crystals and multilayers (Freund, 1996) is basically described by the Bragg's law: $2d\sin\theta = n\lambda$, where d is the spacing of crystal lattice planes, λ is the X-ray wavelength, θ is the angle which the incident ray makes to the reflecting plane and n is a positive integer number determining the reflection order ($n = 1$ fundamental energy, $n > 1$ harmonics).

From a continuous spectrum is therefore possible to select only those X-rays whose wavelength is such that $n\lambda \leq 2d$; this means that, depending on the wavelength to be selected, a crystal with the suitable lattice spacing *d* has to be chosen.

The Bragg's law is based on the assumption that the atoms of the crystal may be described as point-like scattering centers which are perfectly identical and lying on parallel planes. In this hypothesis, either the absorption process of the X-rays by the crystal and the different diffraction probability between the fundamental energy and the harmonics are not explained. Given the intrinsic limitation of this description, in order to depicting the behaviour of real crystals, two theories have been developed: the **geometrical or kinematical theory** and the **dynamical theory**.

– The **geometrical or kinematical theory** assumes that the incident wave amplitude stays constant at every diffracting center in the crystal, with only the phase changing from point to point. Each photon is therefore scattered only once and the interaction of an atom with the wave scattered by all the surrounding atoms is neglected at the cost of disregarding the conservation of energy. The effects of absorption are treated separately. The total diffracted wave amplitude is then the sum of individual amplitudes of the waves diffracted by each diffracting center.

The kinematical approximation is valid for very thin crystals (i.e. for thicknesses *t*, inferior to the extinction length Λ, see paragraph A1.2.2), for mosaic crystals or more generally, for highly imperfect crystals.

– The **dynamical theory** is applied when dealing with thick ($t > \Lambda$), perfect or deformed crystals. It considers the scattering by electrons of the crystal as coming from the incident wave as well as the scattered wave, and the scattering can occur many times (multiple scattering).

The propagation of X-rays in a crystal is described in terms of wavefields satisfying the Maxwell equations inside the crystal. In particular, the locus of the characteristic points in the reciprocal space (called *tie-points*) of the wavefields that can propagate through the crystal at a given energy is defined as the **dispersion surface** of the crystal (Figure A1.1).

The dispersion surface is asymptotic to two connected spheres of radius $1/\lambda$ and centred at O (origin of the reciprocal space) and H (point *hkl*) with OH=**h**. Strong diffraction will occur for wavevectors with tie-points very close to the intersection of the spheres; this surface corresponds to the Bragg condition. In this case, two wavefields are excited simultaneously.

Far from the intersection, only one wave field (the transmitted wave) propagates in the crystal. For crystals of finite dimensions, the boundary conditions impose the continuity of the tangential component of the wave vectors. The points of the wavefields excited in the crystal by an incident wave lie at the intersections of a normal n to the surface with the dispersion surface.

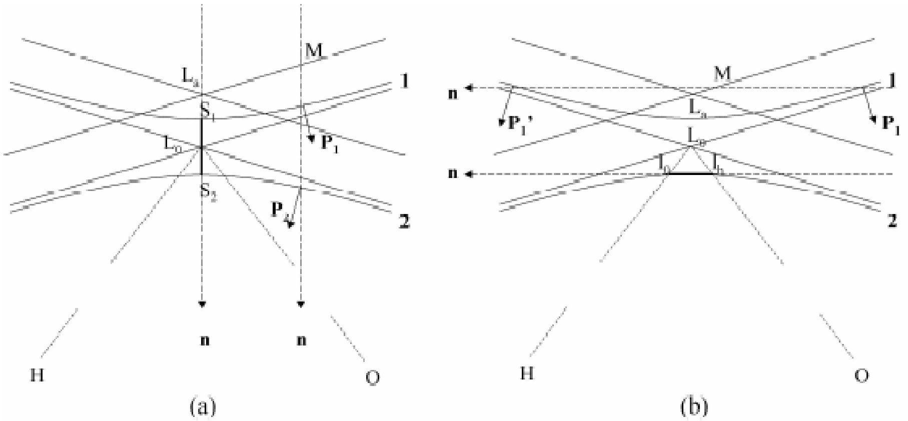

Figure A1.1. Representation in reciprocal space of the Laue (a) and Bragg (b) geometry, with propagation of the wavefields.

A1.1.2 Crystal geometries

The diffraction from a crystal can occur by using two different geometries, as shown in Figure A1.2:

- The **transmission geometry** (or **Laue geometry)**.

  In the symmetric case, the diffraction planes are perpendicular to the crystal entrance surface.

- The **reflection geometry** (or **Bragg geometry)**.

  In the symmetric case, the diffraction planes are parallel to the entrance surface of the crystal.

The symmetric case means that the angle formed between the vector ***n*** (perpendicular to the entrance surface of the crystal) and the planes of diffraction is zero or equals to 90°.

– In the Laue case, the incident wave with direction MO in the vacuum generates two wave fields represented by the intersection of **n**, passing through M with the dispersion surface. The two wave fields follow separate paths within the crystal, indicated by the pointing vectors $\mathbf{P}_1$ and $\boldsymbol{P}_2$, perpendicular to the dispersion surface, and different from the direction of the wave vectors $\mathbf{k}_0$, $\mathbf{K}_0$ and $\mathbf{k}_h$, $\mathbf{K}_h$. Their directions are contained in the **Borrmann triangle** (ABC in Figure A1.2 (a)) defined by the direction of the transmitted and diffracted beams. At the exit surface of the crystal each wave field is divided in two independent plane waves parallel to the transmitted (forward diffracted, refracted) $\mathbf{K}_0$ and diffracted (reflected) $\mathbf{K}_h$ directions, respectively.

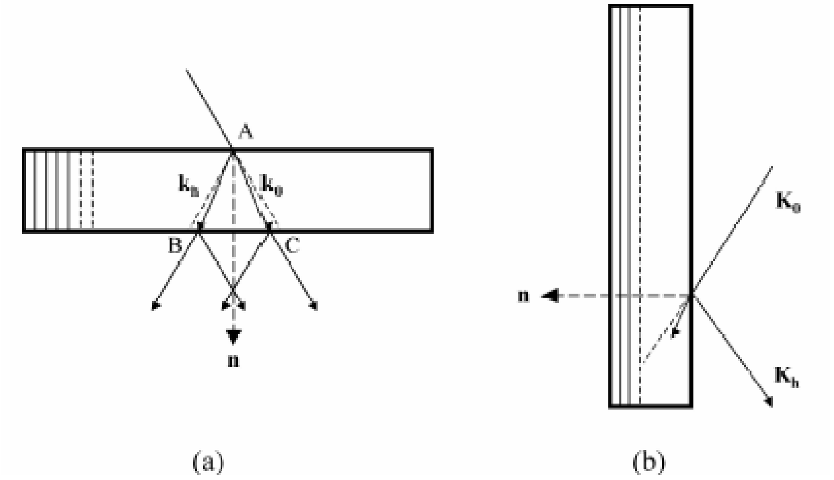

Figure A1.2. Laue (a) and Bragg (b) geometries represented in the direct space. $\mathbf{k}_0$, $\mathbf{k}_h$ are respectively the incident and diffracted wave vectors, in the crystal, $\mathbf{K}_0$, $\mathbf{K}_h$ are respectively the incident and diffracted wave vectors, outside the crystal.

If the incident beam has a significant divergence and can be considered as a spherical wave, all points of both branches of the dispersion surface are excited and the propagation directions of the wave fields fill up the Borrmann triangle.

– In the Bragg case, the intersection of the normal to the entrance surface of the crystal generates two wave fields that belong to the same branch, either the branch 1 or the branch 2 (Figure A1.1 (b)). One direction of propagation lies towards the inside of the crystal penetrating it, and the other outside the crystal corresponds to reflection at the surface of the crystal.

A particular situation is observed when **n** lies between the two branches of the dispersion surface, this corresponds to the *interference total reflection* of the incident wave. This situation occurs in an angular interval given by the Darwin width (Equation. (4.1)).

A1.2 Basics parameters of the dynamical diffraction theory

Two important properties of a crystal are its **energy resolution** and the **intensity of the reflection**.

- If one considers the differential form of the Bragg equation, $\Delta\lambda/\lambda = \Delta E/E = \Delta\theta \cot\theta_B$, the energy resolution is determined by the angular spread $\Delta\theta$ and the Bragg angle θ_B. Two factors contribute to $\Delta\theta$: the angular spread of the incident beam and the intrinsic reflection width of the crystal. The former depends on the geometry of the experiment and is determined by the angular opening of the source and/or by the preceding optics and by the source-crystal distance. About the latter, for a given wavelength, the reflection width of nearly perfect crystals depends on such parameters as crystal structure factor, Bragg angle, and angle between the Bragg plane and the crystal surface.
- The reflectivity power diffracted by a monochromatic plane wave through a crystal is a function of the rotation angle of the crystal around its Bragg position. This function is referred to as the "**reflectivity curve**". With this regard, two relevant quantities must be distinguished: the peak reflectivity that is the height of the reflectivity curve, and the integral reflecting power, that is the area under the curve.

  The intensity of the reflected beam is determined by the latter when the angular spread of the incident beam is much larger than the reflectivity curve. Both the quantities are affected by crystal perfection. Perfect crystals exhibit high reflectivity reaching 100% and low integral reflecting powers of the order of 10^{-4}-10^{-5} at crystallographic wavelength. In contrast, mosaic crystals are usually low in reflectivity while high in integral reflecting power (Matsushita and Hashizume, 1983).

A1.2.1 Darwin width

The width of the reflectivity curve of a crystal is characterized by the **Darwin width**, given by:

$$\omega_D = 2|C|\frac{r_e\lambda^2}{\pi V}\frac{\sqrt{|\gamma|F_h F_{\bar{h}}||}}{\sin 2\theta_B} = 2|C|\frac{\sqrt{|\gamma|\chi_h\chi_{\bar{h}}||}}{\sin 2\theta_B} \tag{1}$$

where C is the polarization factor: $C=1$ for σ polarization (electric field E perpendicular to the diffraction plane) and $C=\cos 2\theta_B$ for π polarization (E parallel to the diffraction plane), with θ_B the Bragg angle. r_e is the electron radius, λ the wavelength, V the volume of the unit cell, $\gamma=\gamma_h/\gamma_0$ is the asymmetry factor. $\gamma_0=(\mathbf{K}_0\cdot\mathbf{n})/k$ and $\gamma_h=(\mathbf{K}_h\cdot\mathbf{n})/k$, with $k=1/\lambda$, are respectively the direction cosines of the incident and diffracted beams. F_h and $F_{\bar{h}}$ are the structure factors for the hkl and $\bar{h}\bar{k}\bar{l}$ reflections respectively. χ_h and $\chi_{\bar{h}}$ are the Fourier components of the crystal susceptibility.

In Table A1.1 numerical examples of the Darwin width, in the case of a symmetric silicon crystal in the 111 and 333 reflections, respectively, are reported for different energies.

	Si (111)		**Si (333)**	
Energy (keV)	θ_B (rad)	ω_D (μrad)	θ_B (rad)	ω_D (μrad)
25	0.079	10.44	0.24	2.19
33	0.060	7.89	0.18	1.64
50	0.039	5.20	0.12	1.07
60	0.033	4.33	0.10	0.89

Table A1.1. Bragg angles and Darwin width values for Si (111) and Si (333) crystals in symmetrical Bragg geometry for four different energies.

A1.2.2 Extinction depth

The extinction length is defined as:

$$\Lambda = \frac{2\lambda}{|C|}\sqrt{\frac{\gamma_0\gamma_h}{\chi_h\chi_{\bar{h}}}} = \frac{2\lambda|\gamma_h|}{\omega_D \sin 2\theta_B} \tag{2}$$

In the symmetrical Laue and Bragg cases, the extinction depth is indicated and expressed respectively as:

$$\Lambda_L = \frac{\pi V \cos\theta_B}{r_e\lambda|C||F_h|} \quad \text{and} \quad \Lambda_B = \frac{\pi V \sin\theta_B}{r_e\lambda|C||F_h|} \tag{3}$$

- In Laue geometry, Λ_L gives the period of the interference between the two excited wavefields propagating in the crystal. It is called the **Pendellösung depth** (Λ_L) or *beat period* that corresponds to the depth at which the incident beam has been completely diffracted in the crystal. The beam will be completely re-diffracted at $2\Lambda_L$ and so on.
- In symmetrical Bragg geometry, Λ_B is proportional to the penetration depth of the wavefields in the crystal. It is called the **extinction depth**.

Table A1.2 gives numerical examples of the extinction length value in the symmetrical Bragg and Laue cases for different configurations.

	Si (111)		**Si (333)**	
Energy (keV)	Λ_B (μm)	Λ_L (μm)	Λ_B (μm)	Λ_L (μm)
25	1.53	60.78	8.40	108.06
33	1.54	80.47	8.42	144.83

Table A1.2. Extinction length values for Si (111) and Si (333) in Bragg and Laue symmetrical configurations for 25 and 33 keV.

▪ Penetration depth

The penetration depth p is the distance from the crystal surface at which the attenuation intensity factor drops by a factor of 1/*e* in a perfect crystal. Within the reflection domain ($|\eta|<1$), p can be expressed as:

$$p=\frac{\gamma_0}{\mu_e}=\frac{\Lambda_B}{2\pi\sqrt{1-\eta^2}} \tag{4}$$

where μ_e is the **effective absorption coefficient** of the waves penetrating the crystal and it is given by $\mu_e=-4\pi\,\mathrm{Im}(K_0)/\gamma_0$ with $\mathrm{Im}(K_0)$ imaginary part of the incident wave vector. η is the **deviation parameter** defined as:

$$\eta=\frac{\delta\theta-\delta\theta_0}{\omega_D/2} \tag{5}$$

where $\delta\theta$ and $\delta\theta_0$ are the misalignment from the Bragg angle and the deviation from Bragg's angle due to the refraction effect in the crystal (and that is neglected in the geometrical theory), respectively.

▪ Anomalous transmission and Borrmann effect

Borrmann (Borrmann, 1950) showed that the effective absorption coefficient is smaller than the normal absorption coefficient μ_0 for wavefields whose tie points lie on branch 1 of the dispersion surface (see Figure A1.1). This fact results in anomalously low absorption. Conversely, in the case of wavefields whose tie points lie on branch 2 of the dispersion surface, one has $\mu_e>\mu_0$ and anomalously large absorption occurs. The anomalous transmission of X-rays through the crystal, in the case of high absorption ($\mu_0 t>>1$) has therefore been called the **Borrmann effect**.

Physically, the anomalous absorption can be interpreted in terms of the positioning of the standing waves generated by the interference of the wavefield components. The nodes (minima) of the standing waves from branch 1 of the dispersion surface lie on the atomic planes, therefore the photoelectric absorption is minimal and the wavefields undergo low absorption. The antinodes (maxima) of the standing wavefields from branch 2 lie on the atomic planes, and the wavefields undergo, in this case, high absorption.

A1.2.3 Width of the Point Spread Function of a crystal

The spatial distribution of X-rays from a point source can be described by a Point Spread Function (PSF, generally defined as the response of a system to an input delta function).

Similarly, a PSF can be associated to a crystal: in fact, a point like illumination at the entrance surface of a crystal gives an intensity distribution over a finite width at the exit surface. This width is the Full Width at Half Maximum (FWHM) of the PSF, which general expression is given by $\left|\Im^{-1}\left(R_h\right)\right|^2$, where $\Im^{-1}$ denotes the inverse Fourier transformation and R_h is the crystal reflectivity curve (see Paragraph A1.2.4) (Davis, 1996). Moreover, because the X-ray diffraction occurs in a plane, the PSF is one dimensional.

In the rest of the paragraph, the width of the PSF for crystal in both Laue and Bragg geometries is derived.

- In <u>Laue geometry</u>, the intensity distribution at the exit surface occurs over a width l_L which corresponds to the base of the Borrmann triangle ([BC] in Figure A1.2 (a), if refraction effects are negligible). In the symmetric case, l_L depends on the incident angle θ and the thickness of the crystal *t*:

$$l_L = 2t\tan\theta \tag{6}$$

At the level of the detector, assumed to be perpendicularly to the diffracted beam, the width of the PSF is given by:

$$PSF_{Laue} = l_L\cos\theta = 2t\sin\theta \tag{7}$$

- In <u>Bragg geometry</u>, the situation is different in the sense that diffraction occurs at the entrance surface of the crystal and therefore a point like illumination at the entrance surface gives an intensity distribution over a width l_B at the same surface, and corresponds to the base [AC] of the triangle (if refraction effects are negligible) in Figure A1.3.

In the symmetric case, l_B depends on the incident angle θ and the penetration depth in the crystal *p*:

$$l_B = 2p\cot\theta \tag{8}$$

and the width of the PSF on the detector plane is given by:

$$PSF_{Bragg} = l_B\sin\theta = 2p\cos\theta \tag{9}$$

If the detector is positioned perpendicularly to the incident beam, a magnification of the image in the vertical direction of a quantity $1/\cos 2\theta$ occurs. The width of the crystal PSF in this configuration is therefore $PSF_{Bragg} = l_B \sin\theta / \cos 2\theta$.

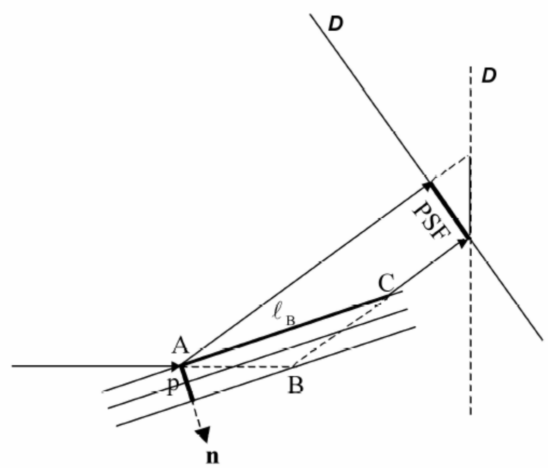

Figure A1.3. The image of a point in Bragg geometry is the segment l_B on the surface of the crystal whose length depends on the penetration depth *p*. The projection of l_B onto the detector plane is the width of the PSF of the crystal.

A1.2.4 Reflectivity

The ratio of the amplitudes of the diffracted and incident wave, assuming a monochromatic plane wave illumination, is given by:

$$\frac{D_h}{D_0} = \frac{\operatorname{sgn}(\gamma_h)}{\sqrt{|\gamma|}} \frac{\sqrt{\chi_h \chi_{\bar{h}}}}{\chi_{\bar{h}}} \left[\eta \pm \sqrt{\eta^2 + \operatorname{sgn}(\gamma_h)} \right] \tag{10}$$

where $\operatorname{sgn}(\gamma_h)$ is +1 in transmission geometry and -1 in reflection geometry.

The reflectivity in Bragg geometry (see Figure A1.4) for a thick crystal, assuming a monochromatic plane wave is given by:

$$R_h = \gamma \frac{|D_h|^2}{|D_0|^2} = \left| \frac{\chi_h}{\chi_{\bar{h}}} \right| \left[\eta \pm \sqrt{\eta^2 - 1} \right]^2 \tag{11}$$

An example of the shape of the reflectivity curve for a crystal set in Laue geometry is shown in Figure A1.5.

The expressions of the diffracted and reflected wave amplitudes, for a spherical wave illumination, are:

- in transmission geometry:

$$D_0\left(s_0,s_h\right)=\delta\left(s_h\right)-2\frac{s_0}{L^2}\frac{J_1\left(X\right)}{X} \tag{12}$$

$$D_h\left(s_0,s_h\right)=i\frac{\pi}{\lambda}\chi_h J_0\left(X\right) \tag{13}$$

- in reflection geometry:

$$D_0\left(s_0,s_h\right)=\delta\left(s_h\right)-2\frac{s_0-\gamma s_h}{L^2}\frac{J_1\left(X\right)}{X} \tag{14}$$

$$D_h\left(s_0,s_h\right)=i\frac{\pi}{\lambda}\chi_h\left[J_0\left(X\right)+\gamma\frac{s_h}{s_0}J_2\left(X\right)\right] \tag{15}$$

where s_0 and s_h are the coordinates along the incident and diffracted beam directions, $L=\pi\left(\chi_h\chi_{\bar{h}}\right)^{-1/2}/\lambda$, $X=2\left(s_0 s_h\right)^{1/2}/L$ and J_0,J_1,J_2 are the zero$^{\text{th}}$, first and second order Bessel functions respectively. Equations (12) to (15) can be obtained using a method based on multiple-scattering expansion (Guigay, 1999).

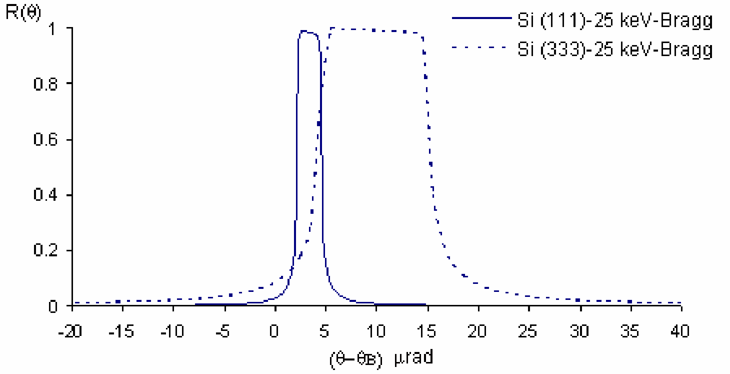

Figure A1.4. Reflectivity curves of a Si (111) and a Si (333) crystal in symmetrical Bragg geometry for an energy of 25 keV. The width of the curve is the so called Darwin width.

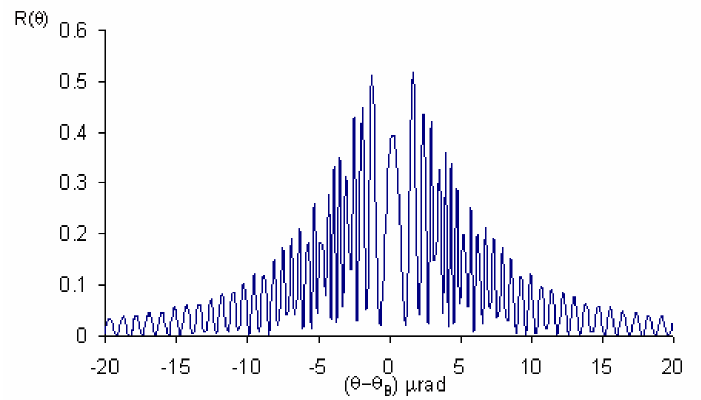

Figure A1.5. Reflectivity curve of a Si (111) crystal (with an asymmetry of 15 degrees) in Laue geometry. The crystal thickness is 1.2 mm.

A1.2.5 Integrated intensity

The integrated intensity is the integral of the reflectivity curve over all the angles. In the absence of absorption, the integrated intensity in the Bragg case is a constant proportional to the Darwin width and does not depend on the crystal thickness, if this one is thick enough. Actually, the wavefields penetrate up to a certain depth, proportional to the extinction length and the integrated intensity depends on the crystal thickness through the relation (Authier, 2001):

$$I_{h_{\text{int}}} = \frac{\omega_D}{2}\pi \tanh\left(\frac{\pi t}{\Lambda_B}\right) \tag{16}$$

For large thicknesses, the intensity tends towards $\pi\omega_D/2$.

The integrated intensity of the diffracted beam in the Laue case depends strongly on the crystal thickness. In the absence of absorption, it is given by (Authier, 2001):

$$I_{h_{\text{int}}} = \frac{\omega_D}{2}\frac{\pi}{2}\int_0^{2\pi t/\Lambda_L} J_0(z)\,dz \tag{17}$$

where $J_0(z)$ is the zero$^{\text{th}}$-order Bessel function.

The integrated intensity is an important parameter since the flux of the monochromatic X-ray beam after the crystal is proportional to it.

Figure A1.5 shows the integrated intensities of the diffracted beams (normalized by $\omega_D/2$) as a function of $\pi t/\Lambda$ for the Bragg and Laue case. One can observe that the integrated intensity in the Laue case is always lower (about one half) than the one corresponding to the Bragg case. The reason is that two wavefields are excited in the Laue case instead of one for the Bragg case. When t tends towards infinity, the oscillations attenuate and the integrated intensity tends to $\pi\omega_D/4$. The limit to the kinematical theory, for the Laue and Bragg geometries, is attained for thicknesses very small compared to Λ. It is represented using the dotted line in Figure A1.6.

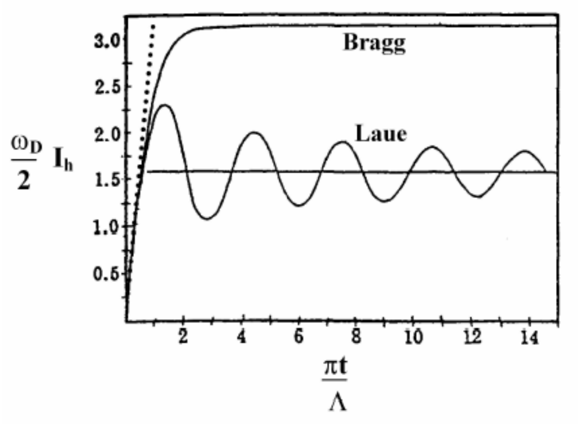

Figure A1.6. Integrated intensity normalized by $\omega_D/2$ as function of $\pi t/\Lambda$ in the Laue and Bragg geometry, in the case of no absorption. The dotted line represents the kinematical limit.

A1.3 Double crystal systems

The use of a single crystal for diffracting an X-ray beam determines a change in the direction of the rays equal to $2\theta_B$ both in the Bragg and Laue case. This fact is experimentally inconvenient since the position of the beam with respect to the sample varies depending on the selected energy. In order to overcome this limitation, double crystal systems are often used since they deliver a diffracted beam that is parallel to the incident one. Such systems can be employed for both monochromatizing and analyzing the radiation.

In the case of a single crystal, set in Bragg geometry, the integrated intensity $I_{h_{\text{int}}}$ for a linear polarization can generically be written as:

$$I_{h_{\text{int}}} = \int_{-\infty}^{+\infty} R(\theta)\,d\theta \tag{18}$$

If a double crystal system is considered, then the integrated intensity is obtained integrating the product of the reflectivity curve of the two crystals. That is:

$$I_{h_{\text{int}}}^{double} = \int_{-\infty}^{+\infty} R_I(\theta)R_{II}(\theta)\,d\theta \tag{19}$$

In the case the two crystals a tuned one to respect to the other (the resulted reflectivity curve is named in this case **rocking curve**), the integrated intensity is given by the autocorrelation of the two crystal reflectivities:

$$I_{h_{\text{int}}}^{double}\left(\theta'\right) = \int_{-\infty}^{+\infty} R_I(\theta)R_{II}\left(\theta-\theta'\right)d\theta \tag{20}$$

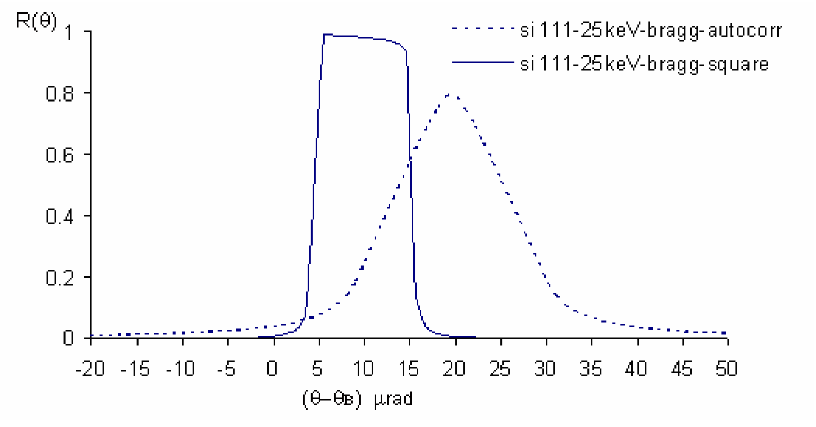

Figure A1.7. Reflectivity curve (square) of a double crystal system, with both crystals in Bragg geometry, compared with the rocking curve for the same configuration.

The most common combinations use crystals set in the same geometry (both in Laue or Bragg geometry) but mixed configurations are possible.

The fundamental requirement is that the individual reflectivity curves coincide over the whole X-ray profile; if this condition is not satisfied, losses or inhomogeneities in the intensity and in the width of the diffracted beam may occur.

A1.4 Laue and Bragg geometry comparison

The Bragg geometry is preferred with respect to the Laue one when a high angular (energetic) resolution is experimentally required. In fact, the reflectivity curve of a crystal in Bragg configuration is always narrower than that one obtained, for the same reflection, in Laue geometry.

The Laue geometry has anyway important advantages in specific experimental cases that are for instance:

- When a high power incident (polychromatic) beam impinging on the crystal (e.g. ~ kW). In this case distortions of the crystal structure may occur.

  The Laue geometry is preferably used since the X-ray beam emerges from the crystal (usually thinner than in the Bragg case) after having delivered only a small amount of its energy, while, in the Bragg configuration, all the energy not reflected is absorbed by the crystal.
- When working at high energies. In fact, by increasing the energy, the Bragg angle (grazing) becomes smaller and, in order to keep the same angular acceptance in the Bragg geometry, longer crystals are necessary.
- When a bent crystal system is required e.g. for increasing the diffracted energy band or for focalizing the beam.

A1.5 Bent Laue crystals

In the case of thermally stressed or mechanically bent crystals, the crystal lattice planes suffer from distortions which are generally non-linear and punctually variable. In these cases, the crystal reflectivity can be calculated only by means of numerical (approximated or not) methods since there does not exist any exact algorithm for this scope.

Differentiating the Bragg's law with respect to *d*, one has:

$$\frac{\Delta d}{d} = \frac{\Delta \lambda}{\lambda} \tag{21}$$

This equation means that a variation Δd in the spacing (d) between the crystal lattice planes determines an increase of the energy acceptance $\Delta \lambda$. Therefore, deformations of the lattice planes generally cause an enlargement of the reflectivity curve with respect to the curve of a non-distorted crystal (Sanchez del Rio, Ferrero *et al.*, 1997).

Another important effect of the crystal bending is that the diffracted beam assumes a different divergence than the incident radiation. The use of bent crystal may allow for the focusing or defocusing of an X-ray beam.

In the case of cylindrically bent crystals, some approximated methods have been developed for deriving the crystal reflectivity; they are, for instance, the *lamellae model* and the *Penning-Polder method* (Authier, 2001) that given exact results only under certain conditions.

REFERENCES

A. Authier (2001). *Dynamical theory of X -ray diffraction.* New York, Oxford Press.

G. Borrmann (1950). Z. Phys. **127**.

T. Davis (1996). "X-ray diffraction imaging using perfect crystals." Journal of X-ray Science and Technology **6**: 317-342.

A. Freund (1996). "Performance of x-ray optics at the European Synchrotron Radiation Facility." Review of Scientific Instruments Supplement Cd-Rom 67.

J. P. Guigay (1999). "A simple view of the spherical wave in dynamical theory." Acta Cryst. **A55**: 561-563.

R. James (1965). *The optical principles of the diffraction of X- rays*. G. B. a. S. Ltd. London, UK.

T. Matsushita and H. Hashizume (1983). *X-Ray monochromators. Handbook on Synchrotron Radiation*. E. Koch, North Holland Publishing Company. **1A:** 261-314.

M. Sanchez del Rio, C. Ferrero and V. Mocella (1997). Computer simulations of bent perfect crystal diffraction profiles, SPIE.

M. von Laue (1931). Ergeb. Exacten Naturwissenshaft **10** (133).

W. H. Zachariasen (1945). *Theory of X-ray diffraction in crystals*. J. Wiley & Sons Inc New York.

List of the publications produced in the framework of this PhD Thesis

Phase contrast imaging developments

- Y. Nesterets, **P. Coan**, T. Gureyev, A. Bravin, P. Cloetens, S. Wilkins, "On qualitative and quantitative analysis in analyser based imaging", **Acta Crystallographica. Section A**, Vol. 62, 296-308, 2006.
- **P. Coan**, E. Pagot, S. Fiedler, P. Cloetens, J. Baruchel, A. Bravin, "Phase-contrast X-ray imaging combining free space propagation and Bragg diffraction", **Journal of Synchrotron Radiation**, Vol. 12, 241-245, 2005.
- E. Pagot, S. Fiedler, P. Cloetens, A. Bravin, **P. Coan**, K. Fezzaa, J. Baruchel, J. Härtwig, "Quantitative comparison between two phase contrast techniques: diffraction enhanced imaging and phase propagation imaging", **Physics in Medicine and Biology**, Vol. 50, 709-724, 2005.
- S. Fiedler, E. Pagot, P.Cloetens, A.Bravin, J. Baruchel, J. Härtwig, **P. Coan**, B. Salicru, W. Thomlinson, "Evaluation of two phase contrast techniques: diffraction enhanced imaging and propagation", **SPIE Proceeding**, Vol. 5030, 2003.
- E. Pagot, P. Cloetens, A. Bravin, S. Fiedler, **P. Coan**, J. Baruchel, J. Härtwig, W. Thomlinson, "A novel method to extract quantitative information in analyser-based X-ray phase contrast imaging", **Applied Physics Letters**, Vol. 82, 20, 3421-3423, 2003.

Osteoarthritis and metal implants ABI application

- A. Wagner, A. Sachse, M. Keller, O. Wagner, M. Aurich, W.D. Wetzel, R.A. Venbrocks, B. Wiederanders, P. Hortschansky, J. Horn, K. Schmuck, M. Lohmann, B. Reime, J. Metge,F. Arfelli, R. Menk, L. Rigon, C. Muehleman, A. Bravin, **P. Coan**, J. Mollenhauer, "Quality evaluation of Titanium Implant Ingrowth into Bone by Diffraction Enhanced Imaging (DEI)", **Physics in Medicine and Biology**, Vol. 51, 1313-1324, 2006.
- A. Wagner, M. Aurich, N. Sieber, M. Stoessel, W. D. Wetzel, K. Schmuck, M. Lohmann, J. Metge, B. Reime, **P. Coan**, A. Bravin, F. Arfelli, G. Heitner, R. Menk, T. Irving, Z. Zhong, C. Muehleman, J. A. Mollenhauer, "Options and Limitations of Joint Cartilage Imaging: DEI in Comparison to MRI and Sonography", **Nuclear Instruments and Methods A,** Vol. 548, 47-53, 2005.
- A. Wagner, M. Aurich, M. Stoessel, N. Sieber, W. D. Wetzel, J. Mollenhauer, K. Schmuck, C. Muehleman, M. Lohmann, B. Reime, J. Metge, **P. Coan**, A. Bravin, F. Arfelli, L. Rigon, R. H. Menk, "Chance and limit of imaging of articular cartilage in vitro in healthy arthritic joints - DEI (Diffraction Enhanced Imaging) in comparison with MRI, CT and ultrasound", **SPIE Proceeding**, Vol. 5746, 542-549, 2005.

Detector characterization

- **P. Coan**, A. Peterzol, S. Fiedler, C. Nemoz, C. Ponchut, J. C. Labiche, A. Bravin, "Evaluation of image performance of a taper optics CCD "FReLoN" camera designed for medical imaging", **Journal of Synchrotron Radiation**, Vol.13, 260-270, 2006.
- A. Peterzol, A. Bravin, **P. Coan**, H. Elleaume, "Performance of the K-edge digital subtraction angiography imaging system at the European Synchrotron Radiation Facility", **Radiation Protection Dosimetry**, Vol. 117, 44-49, 2006.
- A. Bravin, S. Fiedler, **P. Coan**, J-C Labiche, C. Ponchut, A. Peterzol, W. Thomlinson, "Comparison between a position sensitive germanium detector and a taper optics CCD "FRELON" camera for Diffraction Enhanced Imaging" camera for Diffraction Enhanced Imaging mammography", **Nuclear Instruments and Methods A,** 510, 35-40, 2003.
- A. Peterzol, A. Bravin, **P. Coan**, H. Elleaume, "Image Quality Evaluation of a germanium detector for intravenous coronary angiography at the European Synchrotron Radiation Facility", **Nuclear Instruments and Methods A,** Vol. 510, 45-50, 2003.